6-18-2015

Electrostatically Driven Large Aperture Micro-Mirror Actuator Assemblies for High Fill-Factor, Agile Optical Phase Arrays

John P. Walton

ELECTROSTATICALLY DRIVEN LARGE APERTURE MICRO-MIRROR ACTUATOR ASSEMBLIES FOR HIGH FILL-FACTOR, AGILE OPTICAL PHASE ARRAYS

THESIS

John P.K. Walton, Captain, USAF

AFIT-ENG-MS-15-J-003

DEPARTMENT OF THE AIR FORCE
AIR UNIVERSITY

AIR FORCE INSTITUTE OF TECHNOLOGY

Wright-Patterson Air Force Base, Ohio

AFIT-ENG-MS-15-J-003

ELECTROSTATICALLY DRIVEN LARGE APERTURE MICRO-MIRROR ACTUATOR ASSEMBLIES FOR HIGH FILL-FACTOR, AGILE OPTICAL PHASE ARRAYS

THESIS

Presented to the Faculty

Department of Electrical and Computer Engineering

Graduate School of Engineering and Management

Air Force Institute of Technology

Air University

Air Education and Training Command

In Partial Fulfillment of the Requirements for the

Degree of Master of Science in Electrical Engineering

John P.K. Walton, BS

Captain, USAF

June 2015

AFIT-ENG-MS-15-J-003

ELECTROSTATICALLY DRIVEN LARGE APERTURE MICRO-MIRROR ACTUATOR ASSEMBLIES FOR HIGH FILL-FACTOR, AGILE OPTICAL PHASE ARRAYS

John P.K. Walton, BS

Captain, USAF

Committee Membership:

Ronald A. Coutu, Jr., PhD
Chair

Maj Derrick Langley, PhD, USAF
Member

LaVern A. Starman, PhD
Member

AFIT-ENG-MS-15-J-003

Abstract

Aircraft laser beamsteering is accomplished using a single gimbaled mirror housed inside a turret, which protrudes from the fuselage and causes unwanted turbulence, vibrations, and weight. The U.S. Air Force is currently investigating using microelectromechanical systems (MEMS) micro-mirror arrays to replace older aircraft beamsteering technologies. MEMS micro-mirror arrays provide a unique solution to address this unique application. Unfortunately, current MEMS micro-mirror technology cannot meet all beamsteering requirements in a single assembly. These requirements include high fill-factor, large aperture, 25 degrees of out-of-plane deflection, 4-axis tilt, and actuation speeds below 1 millisecond (ms). In this research, a novel MEMS actuation scheme to address all these requirements using electrostatically driven bimorph cantilever beams was designed, fabricated, and tested. Modeling results show a linear relationship between the number of cantilever beams and maximum micro-mirror deflection. Characterization of fabricated micro-mirror assemblies supports the modeling for individual actuators, as well as, for micro-mirror platform assemblies. Fabricated devices reached vertical deflections greater than 170 μm with pull-in voltages of approximately 20 V and an optical range of 16 degrees, within the 1 mm x 1 mm spaces covered by the mirror/pillar assembly. The large deflections, low pull-in voltages, and reasonable optical range shown in this research demonstrate the feasibility of using MEMS micro-mirror arrays to address the aircraft beamsteering application.

Acknowledgments

I would like to express my sincere appreciation and eternal gratitude to all those who supported and guided me throughout this research. Without these individuals none of this would have been possible. First and foremost, I would like to thank my wife. My completion of this research is a direct result of her love and support. She not only maintained the household during the long stretches 10+ hour days and weekends spent at AFIT, but has been my pillar of support for the past 17 years. She is at the root of all my success, having been the one who first planted the seed that I was even capable of completing a college degree. For this I will be eternally grateful for her.

I would like to thank my faculty advisor, Dr. Ronald Coutu for providing me this opportunity and for being my guide and mentor throughout this journey. His patience, support, knowledge, and experience proved invaluable to my completing this thesis effort. I would also like to thank my committee members, Maj Derrick Langley and Dr. LaVern Starman, first for presiding over my thesis defense but more importantly for lending me their expertise. Their assistance was instrumental in my completion of this thesis effort. Additionally, I would like to thank the AFIT clean room technicians, Rich Johnston and Tom Stephenson for their assistance and the Air Force Research Labs Sensor Directorate for sponsoring this research.

Finally, I would like to thank Maj Jim Sattler, Maj Tod Laurvick, Capt Rob Lake, Capt Jim Lohrman, 1Lt Robert LaFleur, 1Lt Tom Donigan, 1Lt Alex Gwin, 2Lt Joe Haefner and 2Lt Chris Kodama. These individuals exemplify what it means to be a wingman. They pick me up when I stumbled and acted as my tutors when difficult topic eluded me. Ultimately, the friendships forged in this AFIT MEMS Group are ones I will carry with me the rest of my life.

John P.K. Walton

Table of Contents

Page

List of Figures

Figure Page

List of Tables

Table Page

List of Acronyms

AFIT	Air Force Institute of Technology
AFRL	Air Force Research Labs
Al	Aluminum
AlN	Aluminum Nitride
Au	Gold
CO_2	Carbon Dioxide
CTE	Coefficient of Thermal Expansion
FEM	Finite Element Model
IC	Integrated Circuit
LIGA	Lithograhie, Galvanoforming, Abforming (German) (English Translation: Lithography, Electroplating, and Molding)
MEMS	Microelectromechanical Systems
MUMPs	Multi-User MEMS Process
PZT	Lead (P), Zinconate (Z), Titanate (T)
PolyMUMPs	Polysilicon Multi-User MEMS Process
R & D	Research and Development
SEM	Scanning Electron Microscope
SiO_2	Silicon Dioxide
SOI	Silicon on Insulator
UV	Ultraviolet
ZnO	Zinc Oxide

ELECTROSTATICALLY DRIVEN LARGE APERTURE MICRO-MIRROR ACTUATOR ASSEMBLIES FOR HIGH FILL-FACTOR, AGILE OPTICAL PHASE ARRAYS

1. INTRODUCTION

1.1 Background

The microelectromechanical systems (MEMS) field is a rapidly advancing technological discipline, and the last several decades MEMS devices have been incorporated into a large number of technological applications. Used as accelerometers, gyroscopes, inertial sensors, resonators, and micro-mirrors, they can be found in nearly everything – from cellular phones to the most advanced weapon systems [1]. Simply defined, MEMS refers to miniaturized mechanical and electromechanical devices/structures, which are constructed using microfabrication methods. MEMS structures are those devices with minimum feature sizes from several millimeters (mm) to well below a micron (μm) [2]. They can vary from simple structures without moving parts, to complex structures with multiple moving components which are part of and controlled by other microelectrical components.

1.2 Motivation

Currently the U.S. Air Force is in need of agile, efficient, high power, and high accuracy beamsteering systems for integration into systems such as infrared countermeasures, laser communications, laser weapons, laser sensing for multi-target search and track capabilities. Presently, beamsteering is accomplished by a single gimbaled mirror housed inside a turret. This assembly protrudes from the aircraft and

creates drag and atmospheric turbulence. This, in turn, induces problems into other systems such as active optical steering and imaging systems, not to mention reducing the performance capabilities of the aircraft. In the ever-evolving national defense technological arena which is driven by the growing need for more advanced capabilities, systems which hinder the operational capacities of another system need to be replaced.

1.3 Problem Statement

The operational characteristics of current beamsteering systems do not allow them to be operated internally, as that would limit the system's field of view to a point as to make it operationally obsolete. Because of this, there is an immediate need to develop a new system to meet the operational needs of current and future aircraft capability requirements. One possible solution to this problem is the use of optical MEMS micro-mirror arrays.

1.4 Justification

The goal of this research is to design, model, fabricate, and test/characterize a high fill-factor, large aperture, out-of-plane, micro-mirror actuation assembly capable of reaching deflection angles of 25º with 4-axis of tilt, eventual project goal of 45º, and actuation speeds < 1 ms. This actuation assembly will be combined with a separate micro-mirror assembly, developed by researchers from the Air Force Research Laboratory (AFRL), consisting of a 1 mm x 1 mm mirror atop a 400 μm pillar; together these structures will enable the development of broadband micro-mirror arrays capable of steering large aperture laser beams across a large field of view. Ultimately, knowledge gained from this research will eliminate the need for protruding turrets housing

mechanical gimbals, thus increasing the efficiency of the optical systems as well as all the systems affected by aircraft turbulence.

1.5 Methodology

In this research, a novel electrostatic “zipper” actuation scheme was developed for the fast actuation of large aperture, large angle laser beam steering micro-mirror platform assemblies. The challenge when attempting to achieve the required deflection angles in micro-mirror actuator assemblies is due to the limited clearance, which is governed by the thickness of the sacrificial layers used during the device fabrication process. As commercially available MEMS prototyping services limit the sacrificial layers to several microns the first challenge is raising the micro-mirror assembly high enough to allow for the large initial deflections, in excess of 100 μm, necessary to reach the desired operation angles. This design addresses this problem by lifting the micro-mirror platform to an initial starting position using a series of partial-bimorph cantilever beams.

Extreme deflections have been reached using electrostatic and electrothermal actuation of high stress bimorph beams but current electrostatic designs [3, 4, 5] either have very small deflection angles or extremely long cantilever beams, which require large voltages to achieve pull-in. Electrothermal designs, however, have been shown to reach extreme deflection angles, using much shorter bimorph cantilever beams but result in much slower switching speeds [6, 7]. This “zipper” approach utilizes aspects observed in electrothermal designs, which reach the initial deflections required, incorporated into an electrostatic actuation scheme.

In an effort to achieve extreme deflection angles this “zipper” actuator design stacks bimorph cantilever beams in such a way as to allow for the deflection of each beam to be added to the previous beams. This approach has two benefits. First, beams can continue to be added to the actuator to achieve higher initial deflections, as long as the space available for the device is not exceeded. Second, this approach requires a much lower pull-in voltage than traditional electrostatic designs with comparable platform deflections. This is because the pull-in of one beam will reduce the height of subsequent beams making it much easier to actuate the entire assembly.

1.6 Summary

This chapter provides a brief background on MEMS technology as a basis of understanding the scale of the micro-mirror platform assemblies designed in this research. Following that, a discussion on the motivation driving the methodology and associated problems and then the justification for this approach was described. Subsequent chapters detail the theory and fabrication of the MEMS devices, the methodology for the design and characterization, results from the characterization of fabricated devices, analysis of the collected data, and recommendations for future work.

2. LITERATURE REVIEW

2.1 Chapter Overview

This chapter is a background and literature review of electrostatically driven, large aperture micro-mirror actuator assemblies for high fill-factor, agile optic phased arrays, and topics related to the design and fabrication of such devices. Although these topics in no way encompass all the detail needed to fully understand the complex aspects of MEMS design, fabrication, and applications they focus on those which are critical to this research. This chapter is divided into sections: MEMS Fabrication, MEMS Transducers, and MEMS Micro-mirror Actuation Schemes.

The MEMS Fabrication subsection introduces the processes involved and techniques used during the fabrication of MEMS devices and outsourced fabrication options. Specifically, it covers the Photolithography and Pattern Transfer processes, as well as the three main techniques which can be used, Microforming, Bulk Micromachining, and Surface Micromachining, and concludes with a review of two Commercial Foundry Fabrication Options. The MEMS Transducers subsection provides a brief introduction to MEMS Sensors and Actuators. It highlights their basic operations and uses, providing a simple example for each. The chapter is concluded with a brief review of the different MEMS Micro-mirror Actuation Schemes, including Electrothemal Actuation, Electrostatic Actuation, and Piezoelectric Actuation techniques currently being researched.

The complex, multi-disciplinary nature of the electrical and mechanical components of MEMS structures, which must take into consideration physics, chemistry, electrical, and mechanical effects simultaneously [8, 9] makes MEMS fabrication an

ever-evolving research area. The complexity associated with MEMS fabrication makes it vitally important fabrication be considered in the design of MEMS devices, from the beginning.

2.2 Microelectromechanical System (MEMS) Fabrication

A majority of MEMS fabrication techniques used today were adopted from established microelectronic fabrication methods. Developed during the technological revolution, they were sparked by the invention of the transistor in 1947 [10]. After an initial focus in silicon based microelectronic integrated circuits, researchers began exploring new microdevices which took advantages of the mechanical properties of silicon, in addition to its electrical properties. This innovation gave rise to microelectromechanical devices, now recognized as MEMS [11, 12, 1].

MEMS fabrication is subdivided into three processes: Microforming, Bulk Micromachining, and Surface Micromachining. Although these processes have very different approaches for producing devices, they do share some microfabrication techniques and in some cases two or more may be used to produce one device. The following sections provide background information on the procedures and processes common to MEMS microfabrication.

2.2.1 Microforming

Of the three processes, microforming is the most unique; it does not share its roots with the other two processes. It addresses the need to produce high aspect ratio devices [13, 14]. Rather than borrowing from established microfabrication techniques, it evolved from macrofabrication techniques used in processes like electroplating and injection

molding [15]. The standard microforming process used today is called the LIGA processes. LIGA, developed in Germany, is an acronym for Lithograhie, Galvanoformung, Abformung (Lithography, Electroplating, and Molding) [16]. Figure 1 is a cross sectional view of a generic LIGA process example. Figure 1(1) encompasses the lithography procedures shared by all the techniques. At this point the substrate is coated with a thick layer of photoresist which has been masked, exposed, and developed.

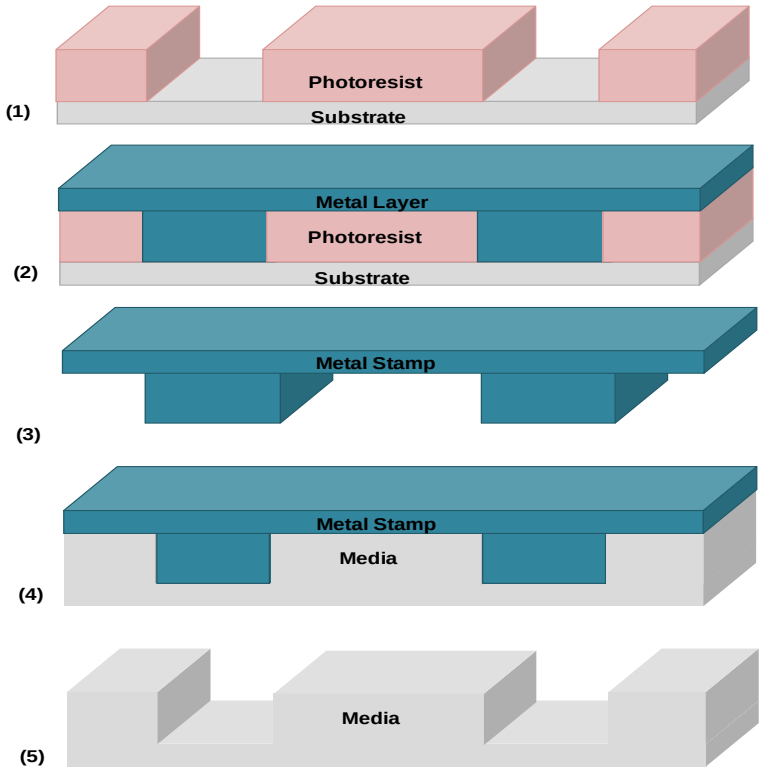

Figure 1: Cross sectional view of LIGA fabrication process: (1) patterned and developed sacrificial photoresist layer; (2) electroplated metal layer; (3) released metal mold; (4) metal mold pressed into pliable media; (5) released structure

The next image shows the results after the metal is deposited using electroplating. At this point the photoresist is removed and the metal is separated, leaving a mold to be used to create desired high aspect features. Figure 1(4) shows how the mold is then used to transfer the design to another media, as a stamp or with injection molding. Finally,

Figure 1(5) shows the finished result. Although this description is of a generic device structure the LIGA process is used to produce complex, high aspect ratio devices. Figure 2 shows much more complex examples how the LIGA process is used to create high aspect ratio MEMS devices. The Figure 2 images are all at the fabrication point depicted in Figure 1(1). At this point they can either be used to create metal devices or metal stamps, using the electroplating step discussed earlier.

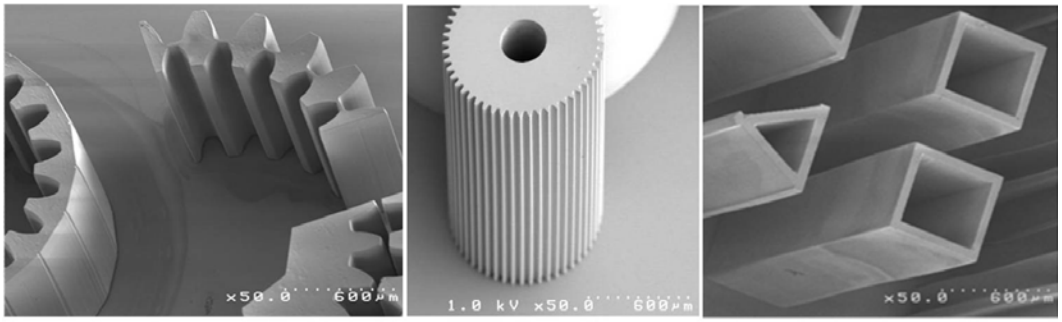

Figure 2: Scanning Electron Microscope (SEM) images of high aspect ratio MEMS structures: (a) 1.1mm gear moulds patterned in SU-8 photoresist [17]; (b) 1.78mm gear fabricated using PMMA [18]; (c) 2mm high structures with 30µm wide sidewalls patterned in SU-8 photoresist [17].

The important take way from this section is that, by combining photolithography techniques with electroplating techniques, microforming can produce micro devices with features up to the millimeter range which can be used to mold precise plastic parts or as a mechanical part, such as a gear or motor [15].

2.2.2 Bulk Micromachining

Bulk micromachining has been widely used in the production of MEMS devices since the 1970's, although the concept of MEMS came to light in the 1960's. This is a subtractive process which addresses the need for three-dimensional microstructures by removing material from the bulk substrate, usually a 300-µm to 500-µm-thick silicon

[16]. The portion of the substrate that remains forms the desired three-dimensional geometric structure. The removal of material in this process is accomplished using physical or chemical techniques, either by dry or wet etching [19]. The key factor of bulk micromachining revolves around the role the crystal orientation of the substrate plays in the etching profile. Etching can occur in two forms. It can either result in an isotropic, crystal orientation-independent, or an anisotropic, crystal orientation-dependent, profile. In most cases isotropic etches are the less desirable of the two because it etches the material evenly in all directions, making it nearly impossible to construct specific geometric structures. Anisotropic etches take advantage of the internal strength found in the substrate material's crystalline structures to create the desired geometrical structure. The materials most common to anisotropic etch techniques are those with a diamond lattice structure. Figure 3 shows a unit cell representation of a diamond structure, which

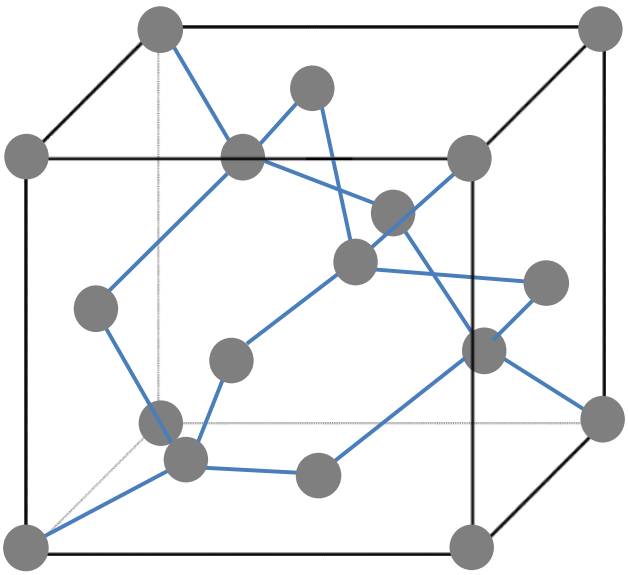

Figure 3: Diamond lattice structure fitted into a cubic unit cell [20]

describes the smallest atomic configuration that when repeated constructs a lattice [20]. The importance of this lattice structure, when etching, becomes more apparent once the

individual crystal planes are observed. This structure is much denser in some orientations. Figure 4(a-c) shows the locations of the three primary crystal planes in a unit cell of a diamond lattice structure. Top views of the individual crystal planes, as seen in Figure 4(d-f), show just how different the atomic layouts are when the perspective is shifted. The denser atomic configurations, the slower the etch rate. This fact coupled with a build up

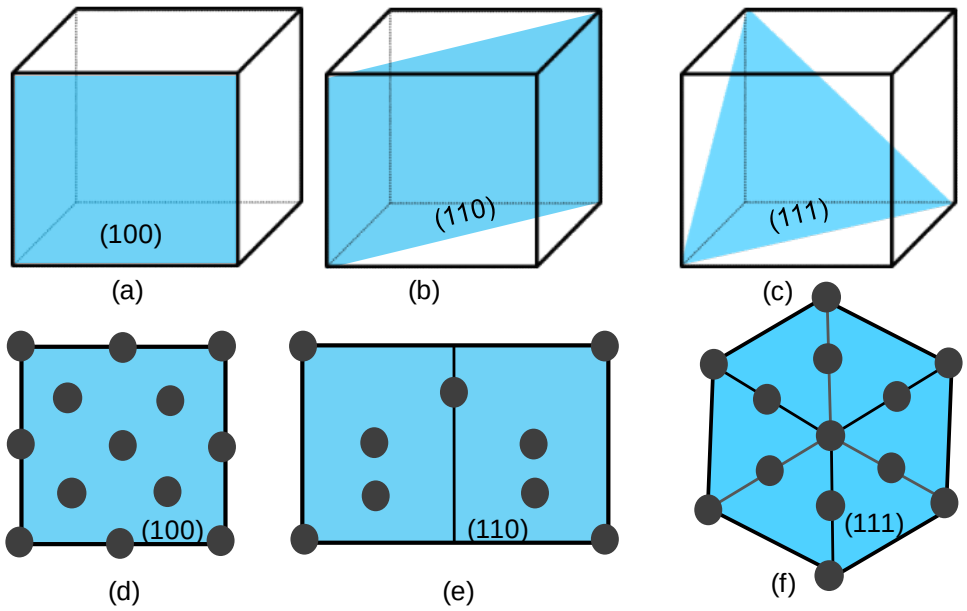

Figure 4: The three primary planes in a diamond lattice structure; (a) orientation of (100) plane, with respect to a unit cell; (b) orientation of (110) plane, with respect to a unit cell; (c) orientation of (111) plane, with respect to a unit cell; (d) top view of (100) plane showing the lattice atomic layout; (e) top view of (110) plane showing the lattice atomic layout; (f) top view of (111) plane showing the lattice atomic layout [19]

of etched material act as an etch stop to create unique etch profiles. Figure 5(1) shows an example of an anisotropic etch of a silicon wafer with a (100) crystalline orientation. In Figure 5(2) a layer of photoresist is spun onto a silicon wafer and an etch window is patterned, as described in the photolithography section. Figure 5(3) shows the etch pattern resulting from a window large enough and etch time long enough to etch through

the entire wafer. Because of the diamond crystal structure of the silicon wafer, the etchant has a much more aggressive attack in the (100) plane than in the (111) plane due to the different atomic densities of the planes. The selective etch is what makes it an anisotropic process. Figure 5(4) shows how the (111) plane, seen in Figure 4(c and f), acts as an etch stop. The different etch rates of these planes, due to their different atomic densities, produce this unique etch profile with sidewalls at a 54.74º angle.

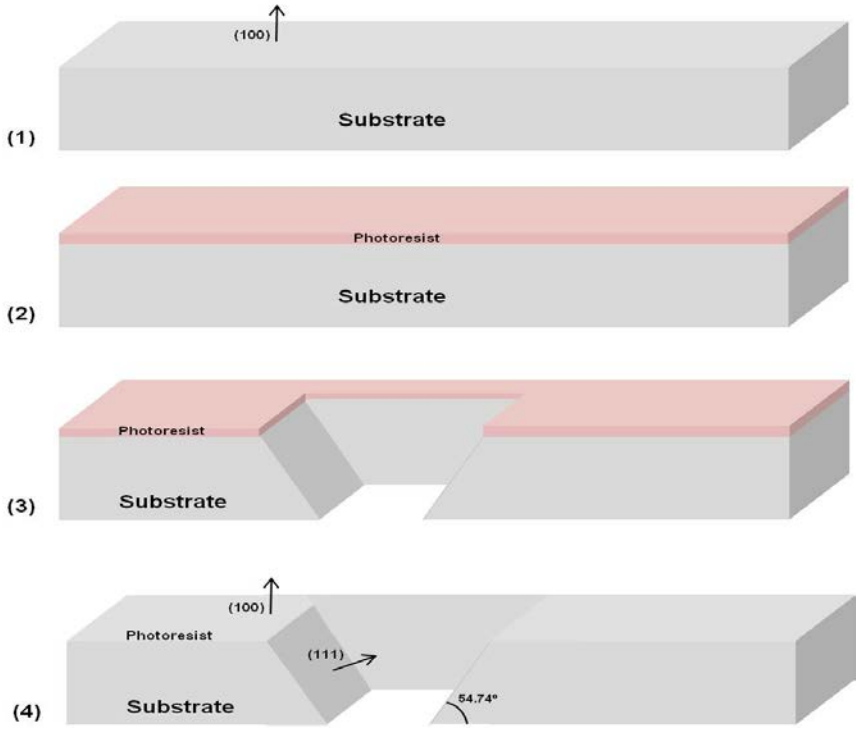

Figure 5: Cross-sectional view of an anisotropic etch profile on a silicon substrate with a (100) orientation: (1) Silicon substrate with a (100) planer orientation, (2) photoresist masking layer applied, (3) photoresist masking layer exposed and developed, the silicon substrate etched; (4) photoresist removed, unique 54.74º etch profile produced along (111) plane

Reducing the etch area, as to not allow the etchant to penetrate the bottom of the wafer, would result in an etch pattern which resembles an inverted pyramid. A reduction in the etch time, to ensure the backside of the wafer is not penetrated, would resemble an

inverted pyramid with a flat top. Additionally, if a silicon substrate wafer with a (110) orientation were used, the resulting etch patterns would produce structures with vertical sidewalls along the (111) plane. This is because the atomic density of the (110) plane is so much lower than that of the (111) plane; etching so fast that the etchant does not have the time required to etch the much denser (111) plane.

2.2.3 Surface Micromachining

Surface micromachining takes place on the surface of the wafer. Contrary to the subtractive nature of bulk micromachining, where material is removed from the substrate, surface micromachining is an additive process which uses different processing techniques to deposit thin films onto the surface of a wafer [15, 21]. These processes are repeated in order to construct complex microstructures, layer by layer. Figure 6 is an illustration of how a microdevice, in this case a basic cantilever beam, can be produced using surface micromachining techniques. Surface micromachining typically produces one of three types of layers: Insulation layers, sacrificial layers, and structural layers [19]. Insulation layers, while not shown in Figure 6, are vital to the operation of most MEMS devices; they provide a barrier between components of a microdevice, enabling electrical operation of mechanical components. Sacrificial layers, seen in Figure 6(1–4) and also referred to as spacing layers, are used to create spacing between component layers [10]. They are constructed using a material, such as silicon dioxide (SiO_2), which can be etched away without damaging other component layers of the device. Once removed (releasing the device), it creates three-dimensional components and provides the spacing required to allow the freedom of movement for the mechanical components of the device [21]. Lastly, the structural and mechanical layers are typically formed of silicon,

polysilicon, metals, or alloys [12]. As the name suggests, these are the layers which comprise the structural components of the device.

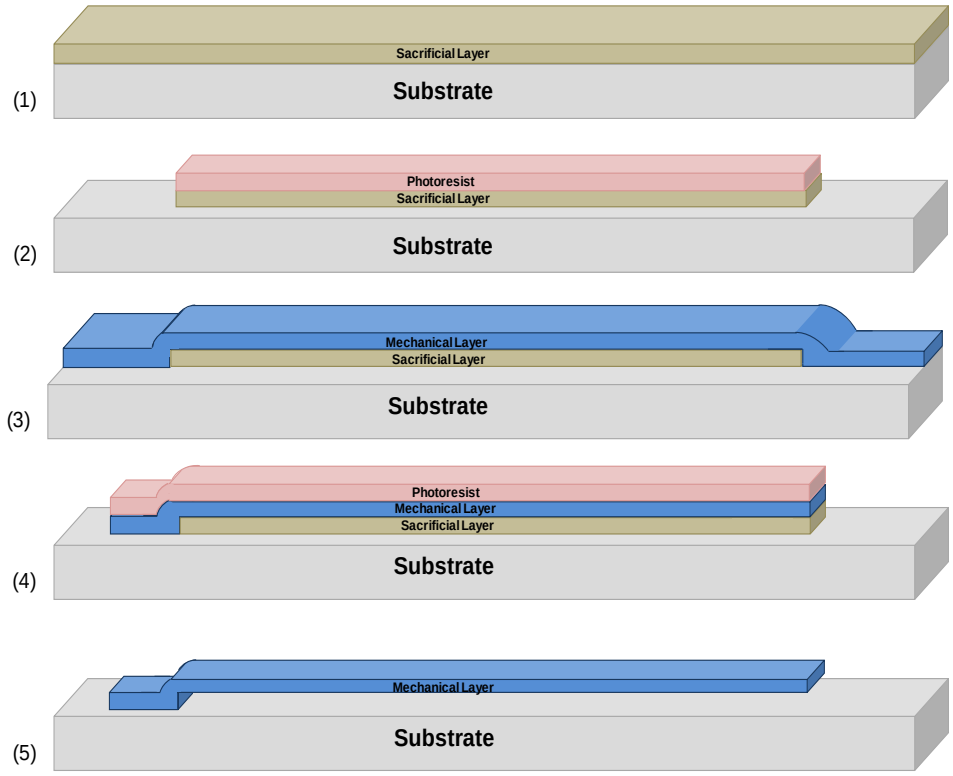

Figure 6: Cross-sectional view of a surface micromachining fabrication process for a cantilever beam: (1) sacrificial layer deposited onto a substrate; (2) photoresist masking layer applied, exposed, and developed and the sacrificial layer etched; (3) mechanical layer deposited; (4) photoresist masking layer applied, exposed, and developed and the mechanical layer etched; (5) sacrificial layer etched, device is now released

Although surface micromachining is the most commonly used MEMS fabrication technique, it brings three key challenges: Management of stress and strain, control of sacrificial layer etch, and prevention of stiction [21]. Regardless if the device is intended to minimize stress and strain, to avoid undesirable effects such as bending or buckling, or take advantage of them to provide some desired structural effect, management of the stress and strain in the structural layers are vital to the operation of all MEMS devices.

Additionally, management of the etch profiles of all the component layers is equally as vital. Component layer materials must be specifically chosen to ensure the structural layers are not inadvertently removed when the device is released during etch of the sacrificial layer. Last is the problem of stiction. This is a term used to describe the action which occurs when the surface tension of a fluid, filling the space left behind after the sacrificial layer is etched away, pulls a freestanding component into intimate contact with another layer or the substrate. While this has little effect on similar devices in the macro world, when scaled down to the micro scale it has adverse effects. Because surface tension is huge in the micro world this causes the component layer to become permanently stuck in that position [16, 21]. There are two device release methods used to prevent stiction. The first method uses a vapor etching system. This method can only be used to etch of specific materials as not all etchants can be used with this system. This method flows a gaseous form of the etchant over the device while simultaneously heating the substrate, thus removing all fluid from the release process. The second method uses a supercritical phase transition of carbon dioxide (CO_2). For this, the fluid surrounding the device is replaced with liquid CO_2 in a drying chamber. The chamber then transitions the liquid CO_2 to a critical pressure and critical temperature, creating an instantaneous change of the CO_2 from a solid to a gas, thus preventing stiction.

2.2.4 Commercial Foundry Fabrication Options

Although the fabrication techniques and procedures that were briefly discussed above may appear to be trivial tasks, they are not. In fact, fabrication is arguably the most difficult aspect of MEMS research and development. For this reason, companies have arisen to provide a much needed service. By laying out very specific design constraints

based on perfected fabrication processes, they are able to provide high quality MEMS fabrication to outside entities.

Sandia National Laboratories is a company which conducts research and development for national security applications, to include responsibilities in nuclear weapons programs [22]. In addition to research and development, they provide a service referred to as SUMMiT V™ which stands for Sandia Ultra-planar Multi-level MEMS Technology V. Described as a five-level surface micromachining technology, shown in Figure **7**, consists of a metal layer (PTNMETAL), four polysilicon mechanical layers (MMPOLY1-MMPOLY4), one non-mechanical polysilicon layer (MMPOLY0), four

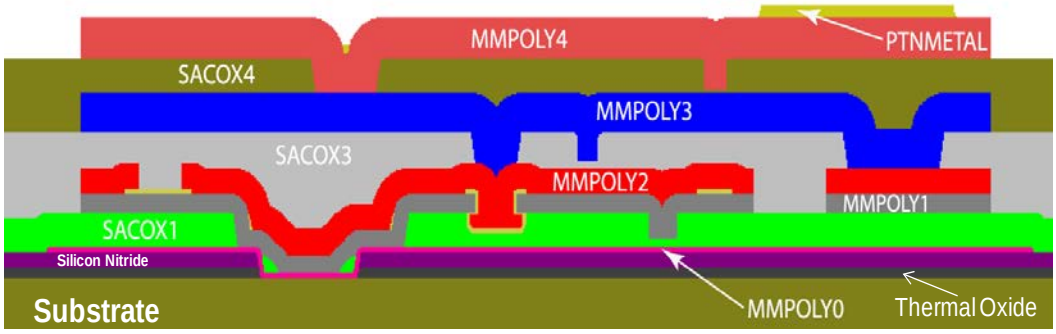

Figure 7: Cross-sectional view of the SUMMiT V™ stack showing realizable fabrication features [23]

silicon dioxide sacrificial layers (SACOX1-SACOX4), a silicon nitride electrical isolation layer, and a thermal oxide isolation layer, all atop a highly doped n-type silicon substrate [23].

MEMSCAP® Inc. is a commercial company which provides cost-effective, proof-of-concept MEMS fabrication to industry, universities, and government labs. This service is referred to as Multi-User MEMS Process (MUMPs®), and is offered in a variety of mediums which include polysilicon, silicon-on-insulator (SOI), metals, and

piezoelectric materials. One such process is PolyMUMPs™ which, as its name suggests, utilizes polysilicon to construct the structural layers. It is a conformal seven-layer polysilicon surface micromachining process [24]. Figure 8 shows a cross-sectional view of the PolyMUMPs™ process. The seven layers are made up of a nitride layer deposited across the entire wafer to electrically isolate the substrate; three polysilicon layers, which together make up the MEMS device; two oxide layers between the polysilicon layers necessary for releasing the device; and a metal layer.

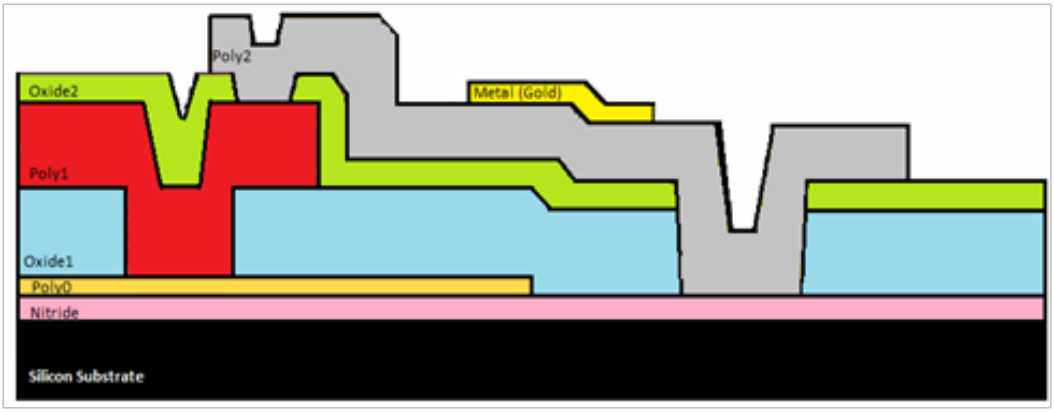

Figure 8: Cross-sectional view of the seven layers of the PolyMUMPs™ Process [24]

By allowing customers to purchase only the space of the wafer they require, companies are able to keep research and design fabrication costs down while reducing the waste produced during fabrication. Due to the multi-user nature of MUMPs®, design constraints are given to establish a single fabrication process [24]. These constraints are referred to as the PolyMUMPs™ design rules and are a set of requirements and advisements derived from the capabilities of individual process steps. For the most part, they are defined by the resolution and alignment capabilities of the lithography system. It is important to note that minimum line width and spaces are rules which ensure

compatibility between layouts and tolerances. Violation of these rules may result in missing, undersized, oversized or fused features [24].

2.3 MEMS Transducers

Transducers are extensively used for the measurement and control of instrumentation in nearly all scientific and industrial fields, from biomedical to automotive applications [25]. A transducer is a device which acts as a conduit for the transfer of energy from one domain to another (i.e., chemical to electrical or electrical to mechanical). Simply put transducers are devices which convert one form of energy to another, and in terms of MEMS devices, it refers to both sensors and actuators [9, 26].

2.3.1 Sensors

Sensors are devices which measure some type of physical quantity in their environment and output a signal, usually electrical, to relay that measured parameter change [27, 28]. There are numerous types of sensors which can be divided into categories based on their domains of operation: Electrical, measuring voltage, current, or charge; Thermal, which measures changes in temperature, heat, and heat flow; Mechanical, which measures changes in force, pressure, velocity, acceleration, or position; Chemical, which monitors changes in chemical concentration, composition, and reaction rate; Magnetic, which measures magnetic field intensity, flux density, or magnetization; Radiant, which measures magnetic wave intensity, wavelength, polarization, and phase [9]. Recognizing that there are nearly an infinite number of possible applications for sensors and the considerable overlap between categories, it is clear that there will be some cases where a sensor device will not fit into any one

category or may belong to more than one. Generally speaking, sensors take in information from the outside world and relay a signal to the system, effectively converting mechanical energy into electrical energy [9].

2.3.2 Actuators

On the other hand, actuators take a signal from the system and physically interact with the outside world (converting electrical energy into mechanical energy) [25]. Ideally, an actuator would operate using low power, be capable of fast switching speeds, maintain robustness and efficiency across all ranges of mechanical and environmental conditions, have a high power to mass ratio, and be linearly proportional between a control signal and operation parameters such as force, torque, and speed [9]. Unfortunately there is no such thing a 'perfect' actuator. In some applications one 'ideal' attribute contradicts another. In practice, actuator design is an exercise in trade-offs, maybe conceding actuation speed to reduce operating power or decreasing device robustness in order to increase the range of motion [9]. Much like sensors, there are a variety of actuation methods for actuators, the more commonly used methods are: Thermal, using the expansion of a heated material to apply a force; thermal bimorph, which takes advantage of the difference in coefficients of thermal expansion (CTE) of two bonded materials to apply a force; electrostatic, using attractive force between two oppositely charged plates; piezoelectric, using an electrically induced strain or stress proportional to an applied electric field to apply a force (opposite a sensor) [9].

2.3.3 Cantilever Beams

A common MEMS device used for transducers is cantilever beams; these are beams having one end fixed to a rigid structure while the other end is allowed to move

freely. Figure 9 shows a simple cantilever beam. These structures have been used for centuries, on the macro scale, in all types of architectural structures such as bridges and platforms. Building upon Timoshenko's work, characterizing the effects of material strengths in the early 1900's [29], cantilever structures found applications in the micro environment as sensors and actuators [8]. A few examples of typical MEMS applications of cantilever beams are electrostatically driven relays, piezoelectric sensors, and electrothermal actuators. The basic parameters to consider when characterizing the functionality of cantilever beams are the spring constant, denoted by *k*, and the resonance

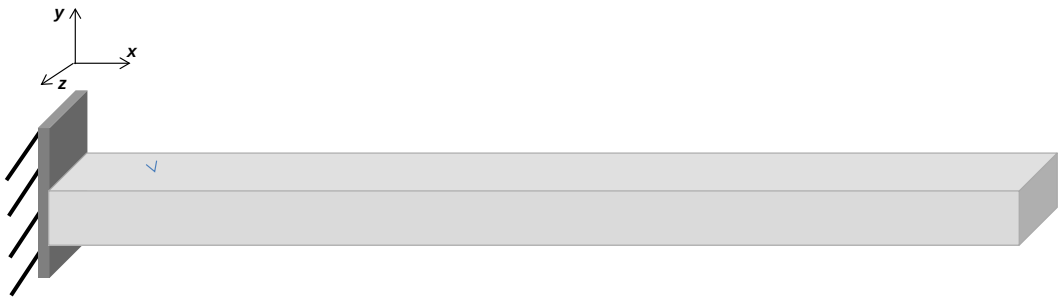

Figure 9: Simple cantilever beam

frequency, f_{res} [30]. These are used in conjunction with specific material properties of the cantilever beams in order to predict the operation characteristics of cantilever beams. Hooke's Law is used to characterize the spring constant in relation to an applied force, *F*, and the resulting deflection of the beam, denoted δ.

$$F = -k\delta \tag{1}$$

When the Young's modulus, *E*, of the material and the beam length, *l*, are considered the overall stiffness of the material (i.e. spring constant) can be written as

$$k = \frac{16}{5}\frac{EI}{l^3} \tag{2}$$

where I is the moment of inertia for a rectangular cantilever beam described by

$$I = \frac{wt^3}{12} \tag{3}$$

when w is the beam width and t is the thickness of the beam [30]. A change in surface stress at the end of the cantilever beam produces a bending moment, M, which can be expressed as:

$$M = Fl \tag{4}$$

Substituting the two previous equations into the equation for the radius of curvature, ρ, results in a formula called Stoney's equation, which also incorporates Poisson's ratio, v, for the cantilever beam material [30, 31, 32].

$$\frac{1}{\rho} = \frac{M}{EI} = \frac{6(1-v)\Delta\sigma}{Et^2} \tag{5}$$

The variable, $\Delta\sigma$, refers to the difference between the stress on the top and bottom surfaces of a cantilever beam. Expressing the resonance frequency (the natural frequency of vibration determined by the physical parameters of a given material) [33] as a function of the spring constant produces a simplified equation,

$$f_{res} = \sqrt{\frac{k}{m}} \tag{6}$$

where mass, m, is mass density times the thickness of the beam times the length of the beam times the width of the beam. Equation 6 shows how the resonance frequency increases as the spring constant increases and as the mass of the beam decreases [30]. The preceding equations illustrate how basic cantilever beam operation is closely related to the mechanical stress, as it relates to material properties and geometries of a device [34].

2.3.3.1 Electrostatic Cantilever Beam Transducer

Electrostatic actuation is based on the principle that two plates with opposing charges will attract one another [35], where one plate is fixed and the other is mobile [36]. The force generated in electrostatic devices are always attractive but can be used to actuate in a parallel fashion, when the air gap distance remains constant, or in a perpendicular fashion, where the air gap is reduced as a result of the attractive force. Figure 10 shows a parallel plate actuator with an air gap distance, *g*, and an overlap area, *A*. In this example, a voltage difference is applied across an air gap creating an electric field which draws the two sides together. Early MEMS researchers applied this simple

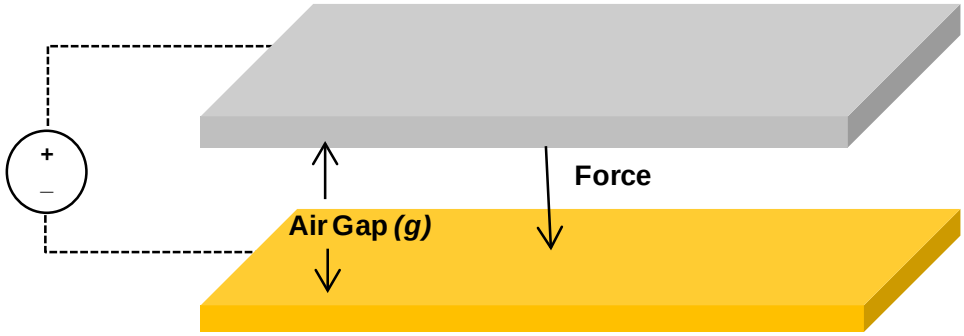

Figure 10: A simple parallel plate electrostatic actuator [35]

approach to describe cantilever beam action, using principles of superposition. However this is not a good representation as it only holds for linear systems [8]. Ignoring any fringe effects, the stored energy, *W*, at a voltage, *V*, can be expressed as:

$$W = \frac{1}{2}CV^2 = \frac{\varepsilon_0 \varepsilon_r A V^2}{2g} \tag{7}$$

with the resulting downward force between the plates expressed by [35]:

$$F = \frac{dW}{dg} = -\frac{\varepsilon_0 \varepsilon_r A V^2}{2g^2} \tag{8}$$

The fact that the attractive force is greater as the air gap is reduced demonstrates how the force is a nonlinear function of the applied voltage as well as the air gap saturation [35]. Because of this non-linearity for actuation across an air gap, numerical analysis, such as a finite element method (FEM) or a finite difference method, is used to characterize electrostatic actuation of cantilever beams. Figure 11(a) and (b) show simple 2D and 3D models of a cantilever beam. Where L is the length and undeformed position of the beam

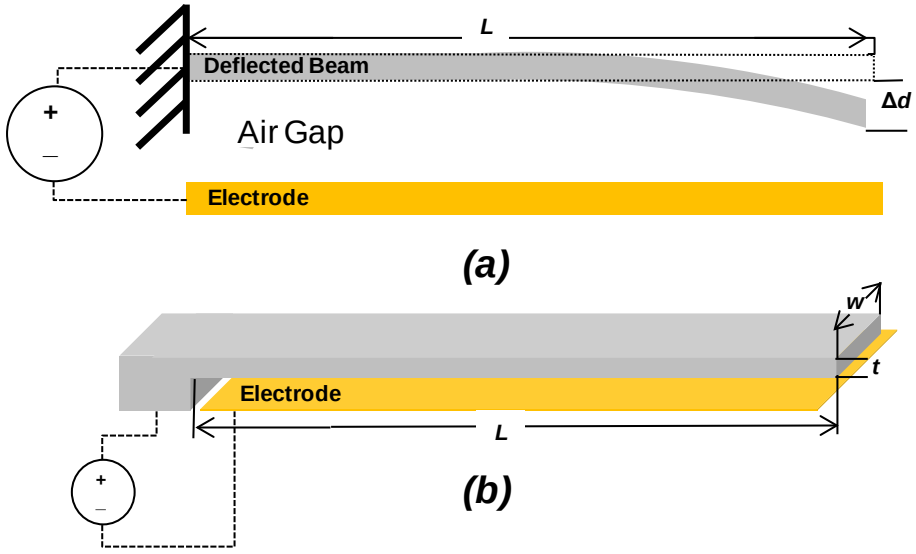

Figure 11: Simple electrostatic cantilever beam actuators: (a) 2D representation of a cantilever beam; (b) 3D representation of a cantilever beam

at rest, shown by the dotted rectangle, and Δd represents the vertical cantilever beam deflection at the free-end, w is the width of the beam, t is the beam thickness, with a voltage, V, applied across an air gap, g. If it is assumed that the cantilever beams shown in Figure 11 experiences no axial force, which is when the axial force equals zero, the beam equation is [8]:

$$EI\frac{d^4d}{dx^4}=\frac{\varepsilon wF_t^2}{2\left(g-d\right)^2} \tag{9}$$

applying boundary conditions, where the transverse force F_t and the bending moment M at $x = l$ are zero, the approximation for the deflection of a cantilever beam subjected to a uniform load distribution is [8]:

$$d_1 = \Delta d \frac{1}{3}\left(\frac{x}{l}\right)^2\left[\left(\frac{x}{l}\right)^2 - 4\left(\frac{x}{l}\right) + 6\right] = \Delta d\Psi \tag{10}$$

where Ψ is the mode shape of the beam. Substituting d_1 for d in Equation (9), then multiplying by Ψ and integrating along the beam length results in an equilibrium force, F_e equation at voltage, V [8]:

$$k\Delta d = F_e \tag{11}$$

where k is the stiffness of the beam, expressed in Equation 2. Further derivation leads to expressions for dimensionless pull-in deflection and force, as functions of an applied voltage, resulting in a required pull-in voltage, V_{pi} [8]:

$$V_{pi} = 0.6487\sqrt{\frac{kg^3}{\varepsilon A}} \tag{12}$$

where the area, A, is described by the following equation.

$$A = \frac{2}{5}wl \tag{13}$$

Once the electric field generated by an applied voltage exceeds initial air, an attractive force is experienced between the cantilever beam and electrode. When the force exceeds the equilibrium force in the cantilever beam the beam collapses to the electrode. This is because the electrostatic force is greater than the restorative force of the cantilever beam and the voltage at which this occurs is called the pull-in voltage [37, 8].

2.3.4 Bimorph Cantilever Beams

Much more complicated cantilever beam transducers are those with thermally induced mechanical stresses, commonly referred to as bimorph or bimetal cantilever beam. Bimorph cantilever beam transducers exploit the differences between the coefficients of thermal expansion (CTE) of two dissimilar materials [38, 39]. CTE is a material dependent variable, denoted as α, and is defined as the amount of thermal expansion in a material, per unit length, per degree of temperature change [19]. As the material undergoes a temperature change, the dimensions in the x, y, and z directions are changed from the original dimensions of (x, y, z) to expanded dimensions (x+Δx, y+Δy, z+Δz) [8]. These expanded dimensions is described by Equation 14, where T_0 equals the

$$\Delta x = \alpha x(T - T_0) \tag{14}$$

starting temperature and T is the ending temperature of the material. In bimorph cantilever beams, two materials are deposited at different temperatures, in contact with each other, and exposed to a change in temperature. This temperature change, coupled with the different material properties, will cause one material to expand more than the other and induce stress into the system. This stress causes the entire structure to bend or deflect [40]. Figure 12 is a cross-sectional view of a simplified bimorph cantilever beam, where l is the beam length and E_1 and E_2 are the Young's Moduli, w_1 and w_2 are the widths, and t_1 and t_2 are the thicknesses of the specific material layers.

In a common surface micromachining process, layers are deposited at elevated temperatures, well above room temperature. When the material with the lower melting temperature is deposited on top of one with a higher melting temperature, which is relaxed at the time of the second deposition, a stress is introduced into the system. This

is because as the top layer cools back to room temperature it contracts, pulling on the surface of the second layer. Upon release, the stress introduced by the top layer pulling on the surface of the bottom layer causes the bimorph cantilever beam to curl upward.

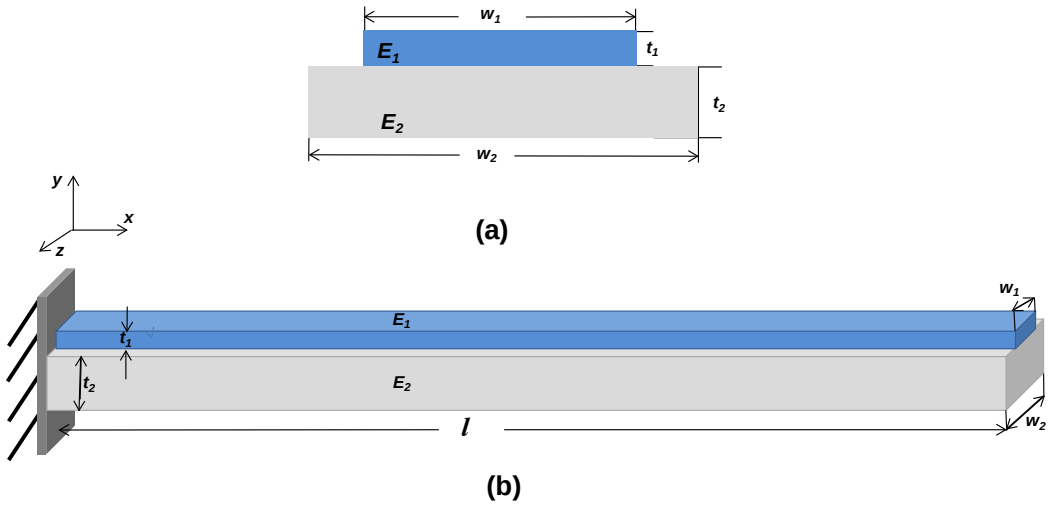

Figure 12: Cross sectional views of a bimorph a cantilever beam: (a) front view of beam; (b) side view of beam

The relationship between the driving force (e.g., change in temperature) and the beam response (e.g., deflection) must be analyzed to characterize bimorph cantilever beam transducers [8]. In order to do this, the effective flexural rigidity $(EI)_{eff}$ and the radius of curvature, R, must be obtained. The driving factors in this characterization are the Young's Modulus of the material layers, the specific beam geometries, and an applied moment M at the end of the beam. Referring to the bimorph cantilever beam shown in Figure 12, the effective flexural rigidity is described by:

$$(EI)_{eff} = E_2 \frac{w_2 t_2^3}{12} \frac{1}{1+pqr}[(1+pqr)(1+p^3qr)+3pqr(1+p)^2] \qquad (15)$$

where

$$p = \frac{t_1}{t_2}, \qquad q = \frac{w_1}{w_2}, \qquad r = \frac{E_1}{E_2} \tag{16}$$

The effective flexural rigidity of the bimorph cantilever beam, described above, can be further developed to characterize the static and dynamic response of the beam to an external force and moment [8]. From this, the following equations for the radius of curvature, ρ, can be expressed as a function of the bending moment or the moment of curvature, M, or the beam geometries and material properties. When ε is the relative strain of the bimorph beam (Equation 21) these are written as:

$$R = \frac{(EI)_{eff}}{M} = \frac{t_1 + t_2}{2\varepsilon}\left[1 + \frac{1 + pqr}{3(1+p)^2}\left(p^2 + \frac{1}{pqr}\right)\right] \tag{17}$$

Then substituting $d^2y/dx^2 = R$ into the above equation yields M [8, 37]:

$$M = (EI)_{eff}\frac{d^2y}{dx^2} = -\frac{1}{2}E_2 w_2 t_2^2 \frac{pqr(1+p)}{1+pqr}\varepsilon \tag{18}$$

For a temperature change, ΔT, the elongation of the different material layers are given as $\delta_1 = (\alpha_1 \Delta T)$ and $\delta_2 = (\alpha_2 \Delta T)$, where α refers to the coefficient of thermal expansion for the specific material layer [8]. This means the relative strain, ε, in the bimorph cantilever beam can be written as:

$$\varepsilon = \frac{\delta_2 - \delta_1}{l} = (\alpha_2 \Delta T) - (\alpha_1 \Delta T) = \Delta T(\alpha_2 - \alpha_1) \tag{19}$$

Assuming a uniform strain distribution in a bimorph cantilever beam, the two material layers are perfectly bonded at the interface, and the bottom layer length, l_2, is fully covered by the top layer, l_1, as shown in Figure 12 when $l = l_1 = l_2$, we can assume an equivalent force, F, exists at the tip of the beam, responsible for counteracting the stress- induced tip deflection [41, 42]:

$$F = \frac{3EI\Delta d}{l^3} \tag{20}$$

and by applying Castigliano's theorem the equations for beam deflection (vertical displacement), Δd, and angular displacement, θ, are as follows [8]:

$$\Delta d = \frac{l^3}{3(EI)_{eff}} F + \frac{l^2}{2(EI)_{eff}} M \tag{21}$$

and

$$\theta = \frac{l^2}{2(EI)_{eff}} F + \frac{l}{(EI)_{eff}} M \tag{22}$$

Once longitudinal stresses in the straight layers are considered the equation for the effective moment M_{eff} is expressed as [8]:

$$M_{eff} = -M = \frac{1}{2} E_2 w_2 t_2^2 \frac{pqr(1+p)}{1+pqr} \varepsilon \tag{23}$$

A majority of bimorph cantilever beam analysis, including the preceding equations, are derived from Timoshenko's work with bimetal thermostats which provided an expression for the radius of curvature in a bimorph cantilever beam nearly one hundred years ago[43]. It is often referred to as the bimetallic effect and is still used as an operating principle for thermally operated bimorph cantilever beams [34]. It assumes the length of the two material layers to be equal and expresses the tip deflection (vertical displacement) as a function of the different material properties:

$$\Delta d = \frac{3l^2}{t_1 + t_2} \left[\frac{\left(1 + \frac{t_1}{t_2}\right)^2}{3\left(1 + \frac{t_1}{t_2}\right)^2 + \left(1 + \frac{t_1 E_1}{t_2 E_2}\right) + \left(\frac{t_1^2}{t_2^2} + \frac{t_2 E_2}{t_1 E_1}\right)} \right] (\alpha_1 - \alpha_2) \Delta T \tag{24}$$

Although this equation was originally conceived to evaluate bimorph thermostat characteristics, it can be modified to predict stress-induced deformation in a multitude of MEMS bimorph cantilevers beam applications [34, 44].

2.3.4.1 Electrothermal Bimorph Cantilever Beam Transducer

One such device, used for a variety of actuation applications, is an electrothermal bimorph cantilever beam. As stated above, bimorph actuators leverage the material characteristics of two different materials to induce mechanical force, specifically different coefficients of thermal expansion of the materials. When the actuator is heated, the materials expand at different rates, causing the device to bend. Figure 13 shows an example of a basic bimorph cantilever beam. This device can be actuated in two ways, depending on which material has the higher CTE. In one case material 1 has the higher CTE and is deposited at a much higher temperature than material 2. As the cantilever beam cools to room temperature, material 1 contracts, causing the beam to deform and

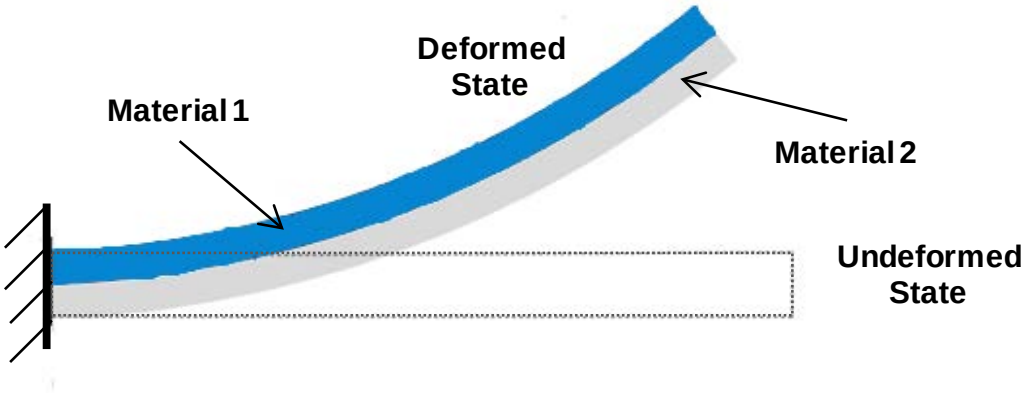

Figure 13: Schematic of a thermal bimorph cantilever beam actuator.[45]

bend upward. Once the beam is heated, heating material 1 faster than material 2, the stress contained in the system is relaxed and the beam actuates downward, to its undeformed state. The second way the beam in Figure 13 could be actuated occurs when

material 2 has a higher CTE. In this case material 2 is in its relaxed state prior to the deposition of material 1 and resulting in an undeformed initial starting position. Once the beam is heated material 2 expands more rapidly than material 1 causing the beam to actuate upward, into the deformed state.

2.3.4.2 Piezoelectric Bimorph Cantilever Beam Transducer

Piezoelectric materials are unique; they produce a predictable response dependent upon a specific applied stimulus which can be leveraged in a multitude of applications [46]. When a stress is applied to the crystalline structure of piezoelectric materials a small current is generated; inversely an applied current will produce a strain in the structure [47]. Figure 14 is an illustration of a simplified piezoelectric sensor in which this unique material characteristic is leveraged.

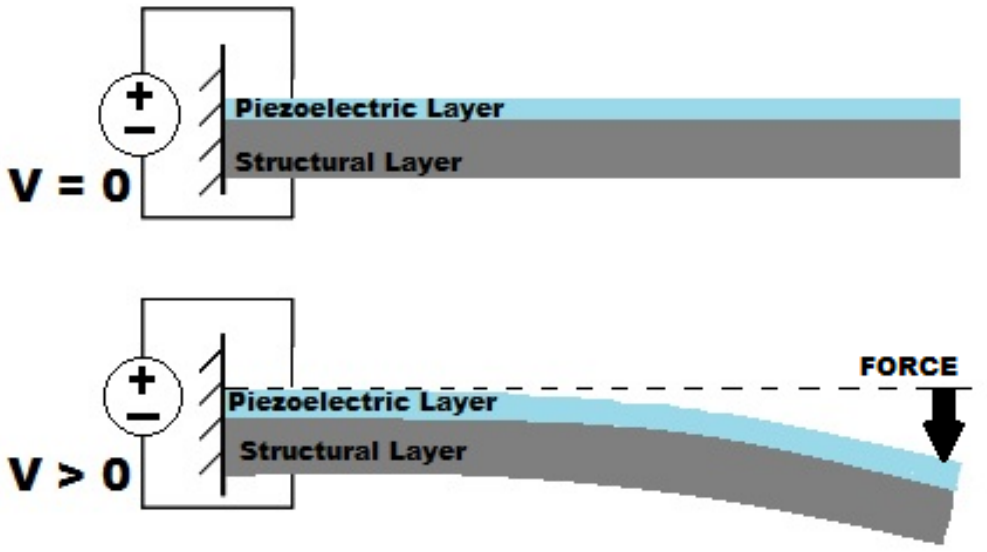

Figure 14: Schematic of a piezoelectric bimorph cantilever beam sensor. [48, 49]

In this example a force is applied, by some outside factor, which induces a stress into the system. The elongation of the piezoelectric material generates a small electrical

current in the piezoelectric layer which can be measured as a voltage difference in the system. Consequently the inverse is also true. An applied electric field, generated across a piezoelectric material, will cause the material to elongate, inducing strain between the piezoelectric and structural layers causing the beam to bend. In this case it is considered an actuator [50, 51].

2.4 MEMS Micro-mirror Actuation Schemes

When investigating actuation methods for micro-mirrors, it becomes abundantly clear there are a vast number of applications for MEMS micro-mirror arrays and nearly as many designs to meet the specific requirements of those applications. The MEMS industry has researched and developed many ways micro-mirror actuation can be accomplished, which each bring unique constraints on performance. Investigating actuation methods spanning the past 10 years, the three most heavily researched methods for actuation of micro-mirror arrays are electrothermal actuation [6, 52, 7, 53, 54, 55], electrostatic actuation [56, 3, 5, 57, 4, 58, 59], and piezoelectric actuation [60, 61, 62, 63]. While not any one method is 'better' than the next, they all have benefits and drawbacks. The challenge then becomes how to leverage the attributes of a specific actuation method, required to meet design criteria, while minimizing any drawbacks associated with that method.

2.4.1 Electrothermal Actuation

The first actuation method investigated in this thesis was electrothermal micro-mirror actuation. Electrothermal actuation is based on one of two methodologies, thermal bimorph actuation or thermal-pneumatic actuation [55, 53]. Electrothermal bimorph

actuators operate in the same manner as the bimorphs previously discussed. On the other hand, thermal-pneumatic actuators rely heavily on differing geometries, rather than depending different CTEs in the material layers, to induce actuation [8, 26]. Figure 15 is an example of both types of electrothermal concepts integrated into one design. Not only was a bimorph layer used on sections of the actuator beams, but portions of those sections were removed from the beams. This change in geometry reduced the rigidity of

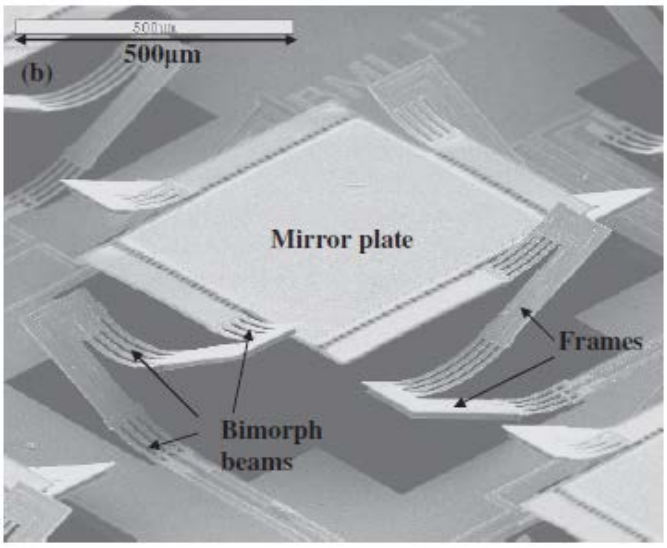

Figure 15: SEM image of an electrothermally driven bimorph micro-mirror actuator [54]

the beams in that area and assisted in the bimorph action. Of the two, electrothermal bimorph actuation tends to have a faster response time and lower power consumption than thermal-pneumatic actuation [55], because of the different properties of the two materials, and tends to produce the more desirable results in most designs.

While optical deflection angles as high as 124 degrees [7, 53] and response times as of less than 0.4 ms [6] have been observed in electrothermally driven, single-plane micro-mirror actuators, they have not successfully been implemented in a duel-plane micro-mirror actuator designs. Current electrothermal micro-mirror actuation designs

produce results with angular deflections falling from 10 degrees to just over 25 degrees, fill-factors in the range of 54% to 95% (with creative 'hidden' actuator layouts similar to the one shown in Figure 16), and response times of 8—13 ms [52, 54, 55].

2.4.2 Electrostatic Actuation

Electrostatic actuators utilize a voltage difference between the actuator assembly of the system and an electrode to induce the attractive force needed to actuate the device [8]. In most applications this method is preferred due to its low power consumption and fast response times [56]. But, as expected, it brings with it drawbacks in the forms of small actuation ranges and high actuation voltages [54]. These drawbacks are due to the proximity restrictions the system requires to generate an attractive force sufficient to actuate the device. Equation 8 shows how these negative effects are compounded by any increase in the distance between the actuator and electrode, by a factor of g^2 [3].

In addition to small actuation ranges and high actuation voltages, stiction is also a cause for concern. Recall that stiction occurs when two MEMS device elements come into intimate contact and remain stuck together, thus rendering the device inoperable. While this is a concern in all MEMS devices, it is especially worrisome for electrostatic devices since the attractive force required for actuation may inadvertently bring the device into intimate contact with the electrode [8, 21, 25]. The two most common electrostatic micro-mirror actuation methods are comb-drive (Figure 16) and parallel plate (Figure 17) actuators.

Comb-drive actuators can easily be used for micro-mirror actuation with very high fill-factors in the range from 70% to 99% in the case of the 'hidden' comb-drive

actuators, shown in Figure 16 [5, 57, 58]. This design uses two separately controlled comb-drive assemblies, an upper and a lower. This allows for quad plane actuation of

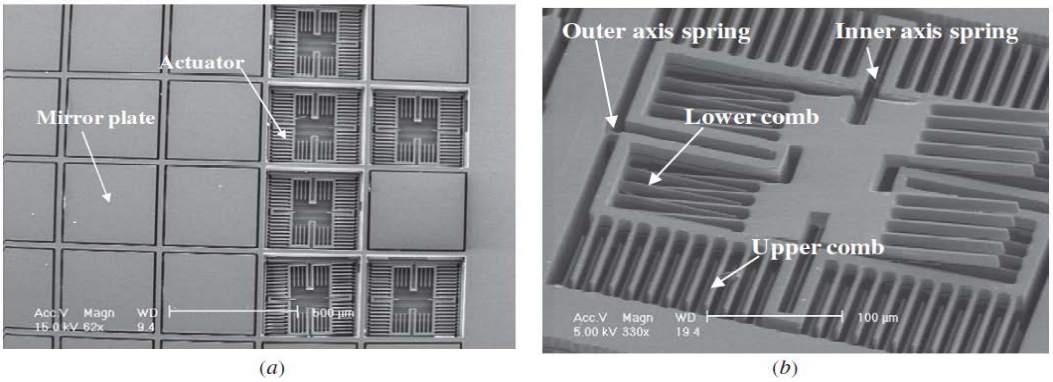

Figure 16: SEM images of comb driven electrostatic actuators: (a) micro-mirror array, (b) close-up of a comb-drive micro-mirror actuator [58]

the micro-mirror. Comb-drive actuators have very high response times of ~10 μs, the main drawback being that they only achieve deflection angles in the range of 0.2—6.7 degrees [56, 5, 57, 58].

When looking at parallel plate configurations of micro-mirror actuators, as seen in Figure 17, the significant drop in the fill-factor of these designs is immediately apparent.

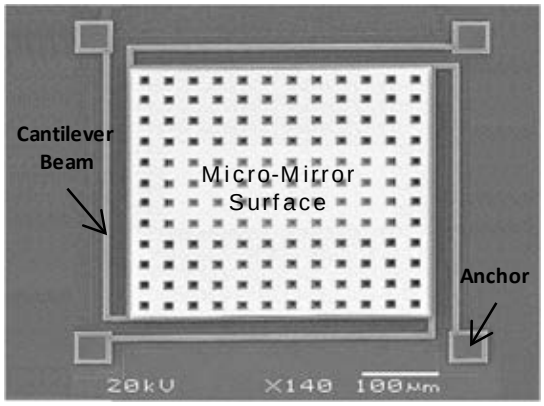

Figure 17: SEM image of parallel plate actuated micro-mirror [59]

This is due to the use of anchors and cantilever beam support elements configuration, which lay on the outer perimeter of the micro-mirror. When incorporated into an array of

micro-mirrors, these designs produce fill-factors in the range of 65%, with no significant gains in displacement angle or response time [3, 59].

2.4.3 Piezoelectric Actuation

Piezoelectric micro-mirror actuation is a relatively new field of study gaining traction with researchers in the last few years. Although there have been studies on the piezoelectric effect with respect to micro-mirror actuation, they are in no way as extensive as those in the areas of electrothermal and electrostatic. In general, the advantages piezoelectrically actuated micro-mirrors produce are considered to be the simple structures, small sizes, high scanning speed, low driving voltages and low power consumption [61]. Piezoelectric actuators are made up of multiple layers of different materials which are deposited and released, the most common being a Lead (Pb), Zinconate (Zr), and Titanate (Ti) compound called PZT [60]. Figure 18 shows an SEM

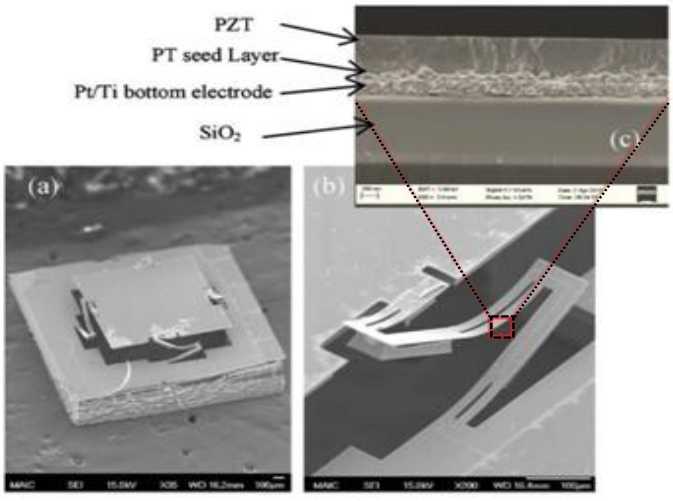

Figure 18: SEM of a Lead (Pb), Zinconate (Zr), Titanate (Ti) or PZT based piezoelectric micro-mirror: (a) single device (2 mm x 2 mm), (b) close-up of actuator, (c) cross-sectional view of unimorph layer [61]

of a piezoelectrically actuated device, which was fabricated in this way. For this design, the piezoelectric material is used to induce a stress into the structure. This stored stress is

released once the piezoelectric material is in the presence of an electric field. At that time, the piezoelectric material experiences a realignment of its crystalline structure; this relaxes the initial stress and is the driving force for the actuator [8]. The research of multiple designs were reviewed, which revealed that the majority of piezoelectrically actuated micro-mirrors can achieve deflection angles of 2.8—5 degrees and fill-factors of around 30% [60, 62, 63, 64, 65, 66].

2.5 Finite Element Modeling

Finite element modeling (FEM) refers to computer-aided design (CAD) software which is used by designers to model and simulate complex structures. It accomplishes this difficult task by first characterizing smaller element, finite element analysis (FEA), of the structure then combines those results into a single model and/or simulation. MEMS design and fabrication is a unique discipline, which often leverages FEM tools to increase the efficiency of research and development (R & D). These tools allow the modeling and simulation of all new designs prior to fabrication, reducing both time and cost of 'trial-by-fabrication'. There are many FEM tools available, but in MEMS design and fabrication there are three which appear most often ANSYS, COMSOL Multiphysics®, and CoventorWare®.

ANSYS is a comprehensive software suite expanding the entire range of physics, which simulates virtually all engineering fields. This tool provided designs scalability, from macro to micro, of the comprehensive multiphysics foundation and architecture. ANSYS Inc recently partnered with Tanner EDA to include the ability to import 3D MEMS Pro files from Tanner EDA's L-Edit design layout editor, a common tool used by

MEMS designer which is discussed in the following chapter. ANSYS's workbench framework also provides the user a simple drag-and-drop interface, with bi-directional parametric CAD software, automated meshing and project-level updates, pervasive parameter management, and integrated optimization tools [67, 68, 69].

COMSOL Multiphysics® is a multiphysics FEM software tool for electrical, mechanical, fluid flow and chemical applications. The COMSOL Multiphysics® multipurpose software platform is ideally suited for MEMS applications and boasts to contain the "Best-in-class" piezoelectric and piezoresistive FEM tools currently available. It includes modules for analyzing stationary and transient domains, fully-coupled eigenfrequency, parametric, quasi-static, and frequency responses. COMSOL Multiphysics® also allows the user to perform lumped parameter extraction of capacitance, impedance, and admittance on MEMS designs [70, 71].

CoventorWare® is a FEM tool used to predict complex, multiphysics behaviors in MEMS devices, with a focus in MEMS-specific capabilities. It is ideal for simulating the mechanical, electrostatic, piezoelectric, piezoresistive and thermal effects for MEMS sensors and actuators. The CoventorWare® suite is capable of simulating devices sensitivity, linearity, frequency response, signal-to-noise ratio, temperature stability, and actuation times. Coventor Inc. has also partnered with MEMSCAP® Inc. and Tanner EDA to include MUMP's™ specific material properties in its material library as well as the ability to import design files from Tanner EDA's L-Edit design layout editor. Additionally, CoventorWare® provides designers a 2D-to-3D model builder, automatic meshing, and field solvers [72, 73].

Each of these FEM tools provides a multiphysics based platform with the capability of simulating MEMS devices. Although slightly different, they are all capable of performing the unique multiphysics challenges, which come with the simulation of MEMS devices.

2.6 Summary

This chapter presented a background literature review of previous and current research pertaining to MEMS micro-mirror design, fabrication, and applications. Various microfabrication procedures and techniques were introduced, covering the three types of fabrication techniques common to MEMS fabrication, and commercially available fabrication options. These topics were followed by a brief review of transducers, highlighting the differences and providing simple examples for sensors and actuators. The final section of this chapter provided an extensive review of current micro-mirror research, covering electrostatic, electrothermal, and piezoelectrically actuated micro-mirror assemblies. The information presented in this chapter builds a foundation of understanding for research topics covered in the remainder of this thesis.

3. METHODOLOGY

3.1 Chapter Overview

Currently, meeting all beamsteering capability requirements of this project (high fill-factor, large aperture micro-mirrors with deflection angles of 25º, eventual goal of 45º on 4-axis, and actuation speeds < 1 ms) cannot be meet since micro-mirrors with all these functional capabilities do not exist. This chapter presents a novel design approach, analytical modeling, finite element modeling, device fabrication, post-fabrication processing, tools and equipment, and device characterization methodologies used in the evaluations of this unique design solution.

3.2 Design

To overcome the complexity of combining all these design capability requirements into a single device, each requirement was considered individually. This approach allows each design choice to be chosen to maximize the performance of that capability itself while considering the effect it has on other possible choices. The first design decision made was that MEMSCAP's® PolyMUMPs® fabrication process would be used to fabricate the prototypes for this research. This decision not only allows the research focus to be on the functional design of the device rather than fabrication, but it also affords time for three fabrication opportunities during the research timeline. It also solidified specific initial design constraints which provided a starting point for the design. Next, the requirements with limited design options were identified as being high fill-factor and fast actuation. After those design elements were identified, the remaining capability requirements were the 4-axis actuation and high deflection angles.

The first design feature determined by the capability requirements was the actuation method. Given the requirement of fast operation of the device (< 1 ms) the best choice is electrostatic actuation. Recall this micro-mirror platform actuation assembly is to be used to drive a micro-mirror atop a pillar (Figure 19), developed by AFRL researchers, which is fabricated separately and then bonded to the platform. This means

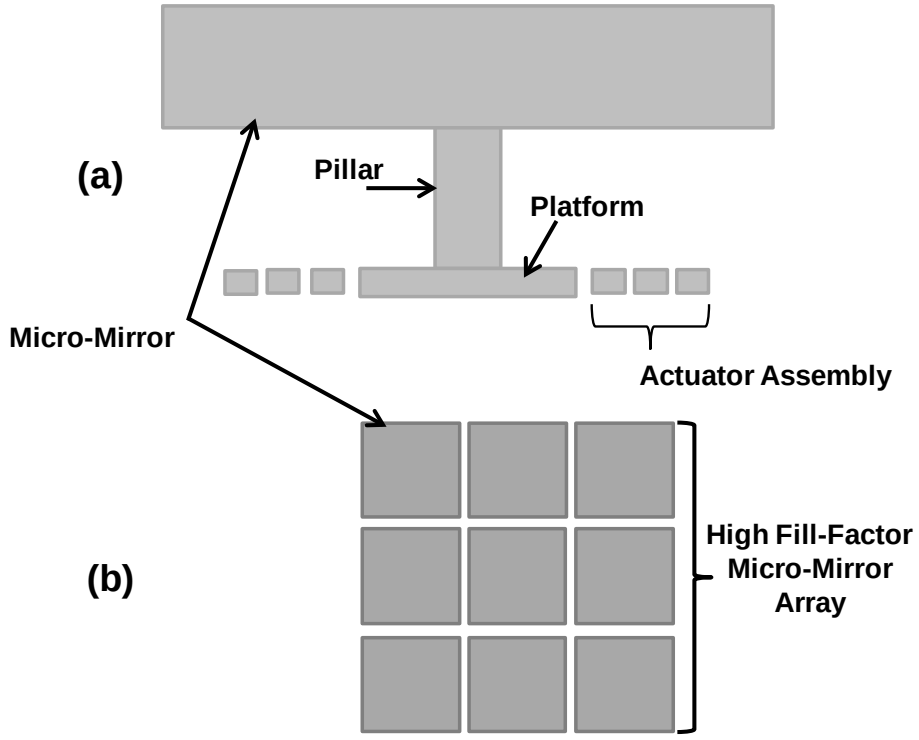

Figure 19: Illustration showing how platform actuation assembly is to be incorporated into a micro-mirror array: (a) a cross-section of a single micro-mirror element with mirror and pillar assembly bonded to micro-mirror actuation assembly, (b) a representative top view showing the high fill-factor mirror array

that in order to have a high fill-factor, also shown in Figure 19, the maximum assembly dimensions are directly tied to the size of the micro-mirror itself. To accommodate the preliminary designs of the ARFL components, the following micro-mirror platform assembly elements were chosen. Given AFRL's micro-mirrors were squares ranging from 800 μm to 1 mm, with the expected final mirror dimension choice on the higher end

of that range, and 100 μm of separation the entire assembly was designed to fit within a 1 mm square. Additionally, the pillar dimensions of the AFRL component also had a range of 200 μm x 200 μm to 500 μm x 500 μm (the latter is shown in Figure 20) which needed to be considered. This aspect proved to be a little more problematic because the dimensions of the micro-mirror platform determine the platform clearance required to

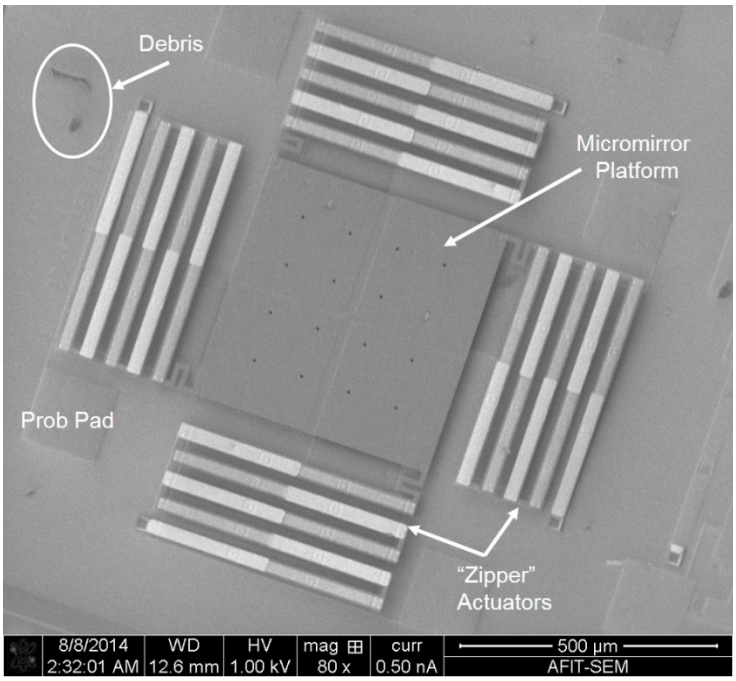

Figure 20: A top view SEM image of a micro-mirror platform actuation assembly with four 5-beam "zipper" actuators and a 500 μm x 500 μm platform

achieve high deflection angles. While it is in the best interest of this research assembly to reduce the size of the platform as much as possible, it becomes increasingly more difficult to bond a large pillar to smaller platforms. For this reason the initial designs use a 500 μm square platform, shown in Figure 20, with a 350 μm platform option to fit into the same spacing.

Given the previously identified design elements, approximately 250 μm x 500 μm of space on each side of the platform remained in which to design an electrostatically

driven actuation scheme. To address the 4-axis operational capability requirement, a four actuator design approach was chosen with one actuator assembly for each axis. Figure 20 shows how four individual actuators will be oriented to actuate a micro-mirror platform. All the design element choices made up to this point were determined rather easily, leaving the most challenging aspect of this design to consume a majority of the research efforts.

The challenge when attempting to achieve large deflection angles in micro-mirror actuator assemblies is due to the limited clearance, which is governed by the thickness of the sacrificial layers used during the device fabrication process. As standard fabrication processes limit the sacrificial layers to a couple of microns and this research requires initial deflections in excess of 150 μm, there were few options. This design addresses this problem by lifting the platform to an initial starting position upon release by using bimorph cantilever beams.

In this research, a new electrostatic “zipper” actuation assembly design is examined. This “zipper” approach utilizes aspects observed in electrothermal designs, which reach the initial deflections required, incorporated into an electrostatic actuation scheme. It uses a series of partial-bimorph cantilever beams in such a way as to allow for the deflections of each beam to be added together in order to reach extremely high deflections. This allowed the design and characterization of a single partial-bimorph cantilever beam which was then used to characterize the operation of the entire system. Figure 21 is a cross-sectional view of a partial-bimorph cantilever beam with a 50% bimorph segment, but can occupy anywhere from a 1% to 99% bimorph beam’s total length. This design approach greatly reduced the complexity for the characterization of

the entire actuation assembly and had two benefits. First, the initial deflections of each beam continue to be accumulated to achieve greater total deflections, for as long as space allows. Second, this approach requires a much lower pull-in voltage than traditional

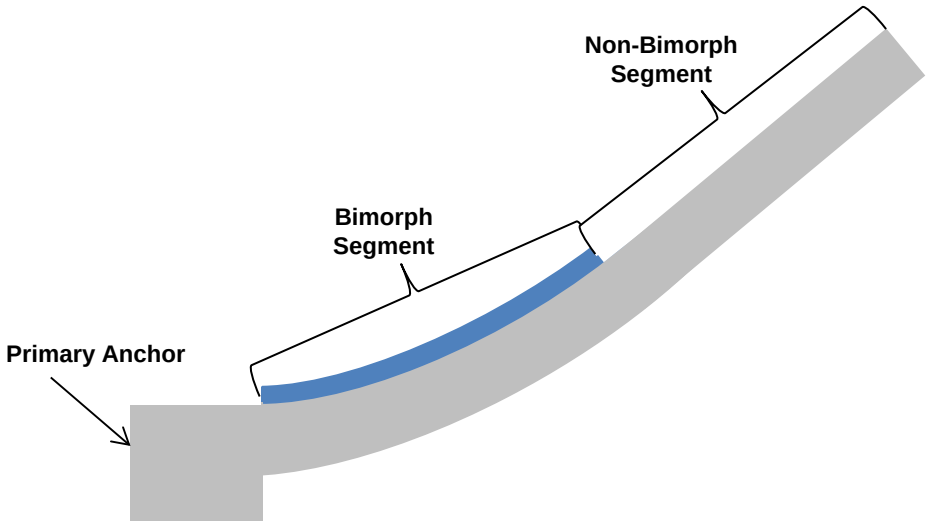

Figure 21: Cross sectional view of partial-bimorph cantilever beam

electrostatic designs with comparable platform deflections because the pull-in of one beam will reduce the height of subsequent beams, making it easier to actuate the entire assembly. This is because once one beam is actuated downward the next beam is then at the initial stating position of the first, thus requiring little to no more voltage to achieve pull-in. Figure 22 shows a simple 3-beam "zipper" actuator. The primary anchor is the portion of the actuator which is attached to the substrate. The primary anchor also performs another function, namely breeching the PolyMUMPs® nitride layer to ground the polysilicon layer through the substrate and effectively grounding the entire platform assembly. This is used in conjunction with a voltage applied to a polysilicon electrode atop the nitride to actuate the assembly. Each pair of adjacent beams is connected by a secondary anchor. These anchors are not attached to the substrate and indicate where the

top of one beam is connected to the bottom of the subsequent beam. The simple design shown in Figure 22 has two secondary anchors. Given that these devices were fabricated using PolyMUMPs®, the layer materials and thicknesses are fixed parameters [74]; therefore, the remaining design elements were chosen to fit in the available space. The

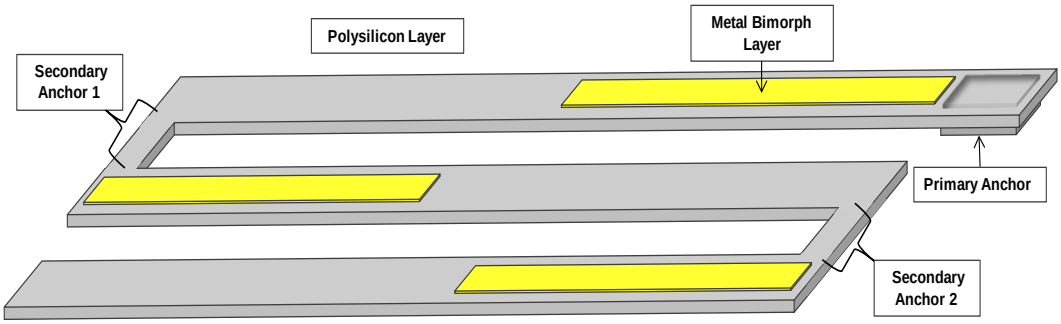

Figure 22: 3-beam polysilicon/gold bimorph "zipper" actuator design with half length bimorph layer, at the anchor end of beams.

initial bimorph actuator dimensions were as follows. The maximum beam length of 500 µm was chosen with initial widths of 30 µm (polysilicon layer) and 24 µm (metal layer). The secondary anchors were each 10 µm x 20 µm (polysilicon layer), which resulted in a 20 µm spacing between the beams. The final design consideration was the connection point between the actuator assemblies and the platform. For this, U-shaped polysilicon anchors were used. Figure 23 is a SEM image of released micro-mirror platform assemblies, showing the attachment locations for the U-shaped. Actuator assemblies with an odd number of partial-bimorph beams are connected at the corners of the platform while those with an even number of beams are connected at the center of the platform, using a 250-µm-long, full-bimorph beam to reach the center of the platform.

Using the initial design choices described above and recalling that the elements which have the largest effect on bimorph beam deflection are the beam thickness and length (Equation 26) only the metal layer length remained to be examined for optimal

design options. At this point analytical modeling was used to determine the optimal length of the metal bimorph layer.

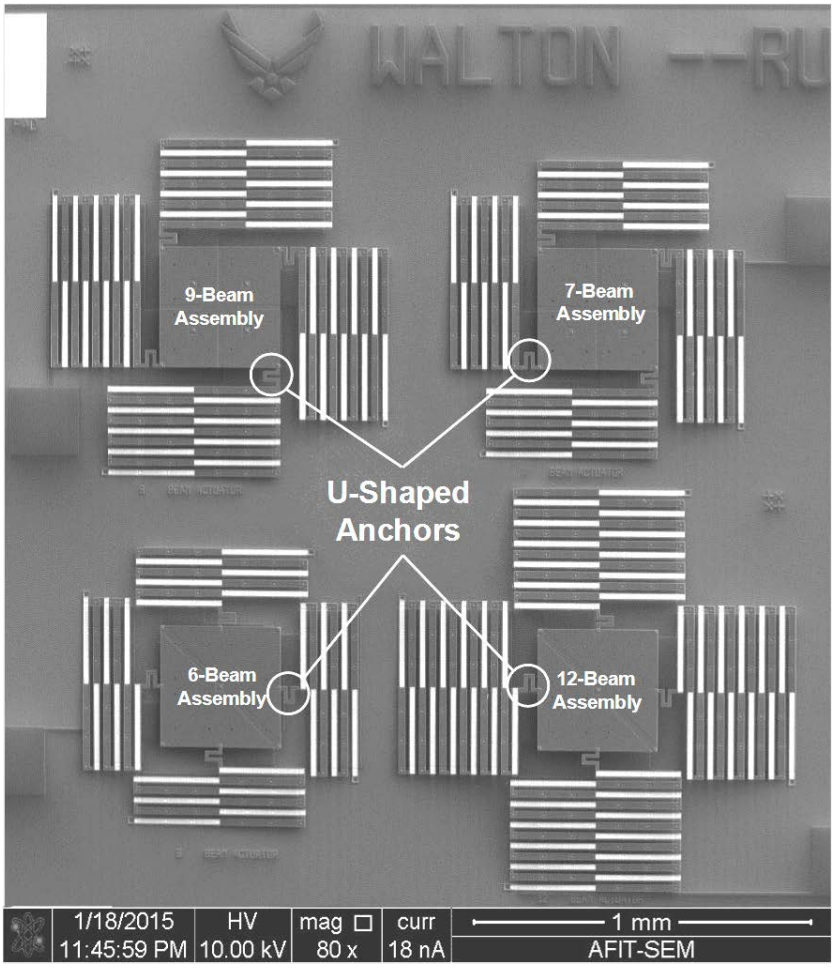

Figure 23: SEM image of released micro-mirror platform assemblies showing the attachment locations for U-shaped anchors, which connect "zipper" actuators with both an even number and an odd numbers of partial bimorph beams to the micro-mirror platform: (Top/Left) a 9-beam actuation assembly; (Top/Right) a 7-beam actuation assembly; (Bottom/Left) a 6-beam actuation assembly; (Bottom/Right) a 12-beam actuation assembly

3.3 Analytical Modeling

Analytical modeling was used to evaluate the effect metal layer lengths has on the overall initial deflection of a partial-bimorph cantilever beam. This was accomplished in order to determine the optimal layer length needed to produce the highest initial

deflections. Additional, analytical modeling was used to calculate the expected pull-in voltages associated with partial-bimorph beams with different initial deflections.

3.3.1 Initial Deflections

In an 'at-rest' state, the partial-bimorph actuator is deflected upward (deformed), as described previously. The methodology for calculating the maximum initial deflection of a partial-bimorph cantilever beam is presented here; to do this the beam will be analyzed in two parts. Part one uses Equation 24 and provides the portion of the beam deflection resulting from the bimorph segment of the cantilever beam, d_1. Part two calculates the deflection of the non-bimorph segment of the beam, $d_2 = l_2 sin\theta$. Figure 24 is a cross-sectional view of a partial-bimorph cantilever beam illustrating how d_2 is to be

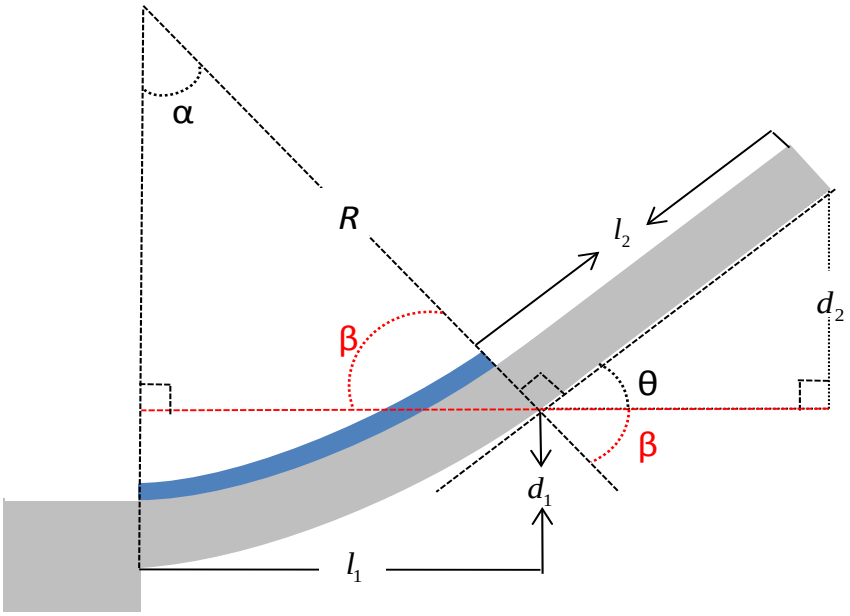

Figure 24: Cross-sectional view of a partial bimorph cantilever beam illustrating how initial beam deflection will be calculated

calculated. To calculate the deflection of the non-bimorph segment of the beam, d_2, the following process is used. First, the radius of curvature, R (Equation 17), is calculated using the effective flexural rigidity, from Equation 15, and the effective moment

Equation 23. At this point two assumptions are made about the cantilever beam being analyzed. First, l_1 is not significantly changed as a result of the contraction of the metal layer, meaning l_1 equals the arch length; and second, the beam segment, l_2, has no significant internal stress and is therefore perfectly straight. Working with these assumptions, α is found by first calculating it in radians, expressed as $\alpha_r = l_1 / R$, and then converting to degrees, where $\alpha = (\alpha_r\ 180)/\pi$. Figure 24 clearly shows $\alpha = 90-\beta$ and also $\theta = 90-\beta$. This means $\alpha = \theta$, therefore

$$d_2 = l_2 \sin\theta = l_2 \sin\left(\alpha_r \frac{180}{\pi}\right) = l_2 \sin\frac{l_1}{R} \tag{25}$$

This value is then added to d_1 in order to get the total cantilever deflection

$$\Delta d = d_1 + d_2 \tag{26}$$

3.3.2 Pull-in Voltages

In addition to the initial deflection, the expected voltage required to pull-in the partial-bimorph cantilever beam will also be modeled analytically. Figure 25 is a cross-sectional view of a partial-bimorph cantilever beam illustrating how pull-in voltage will be calculated. Recalling the previous declaration that the non-bimorph section of the beam is perfectly straight, it follows that pull-in of the bimorph segment will also pull-in the non-bimorph section, and thus the non-bimorph segment can be ignored in this model. In order to simplify this calculation three assumptions are made: The deflection at $^1/_2\ l_l$ occurs at $^1/_2\ d_l$; the pull-in of the first half of the bimorph segment will bring the second half of the bimorph segment down to the starting position of the first, allowing for pull-in of the entire segment; and lastly, the pull-in models for simple cantilever beam are adequate to represent this small bimorph segment.

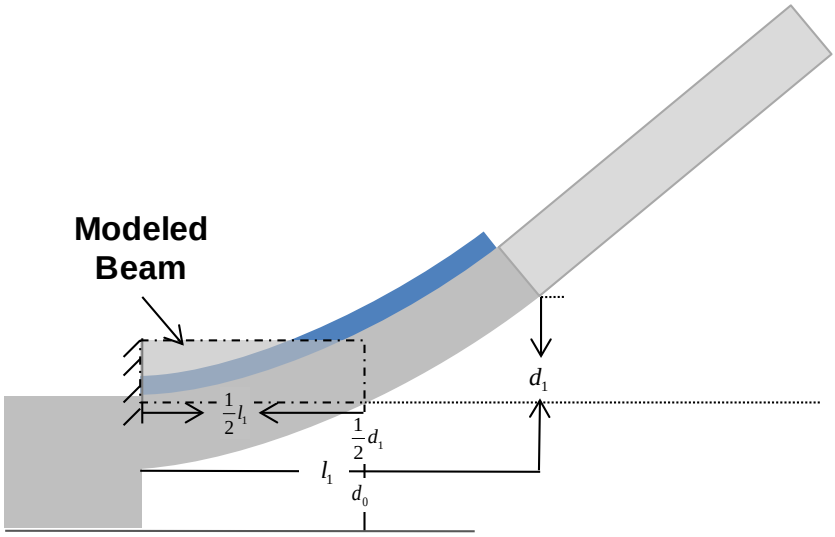

Figure 25: Cross-sectional view of a partial bimorph cantilever beam illustrating how pull-in voltage will be calculated

These assumptions allow the use of Equation 12. This equation allows the model to account for the bimorph nature of this cantilever beam design, when the effective flexural rigidity (Equation 15) is used to calculate the stiffness (Equation 2) and the relative strain (Equation 19) of one bimorph cantilever beam.

3.4 Finite Element Modeling

For the computer-aided actuator modeling portion of this research, the actuator dimensions were as follows: 1.5 µm-thick polysilicon (Poly2) beams measuring 30 µm wide x 500 µm long; 10 µm wide x 20 µm long secondary anchors; and 0.5 µm thick x 24 µm wide gold bimorph layer. These were the maximum allowable dimensions, as suggested by the PolyMUMPs™ design rules [75] and established initial design constraints. Figure 26 shows three example 3-beam partial-bimorph configurations modeled in this research.

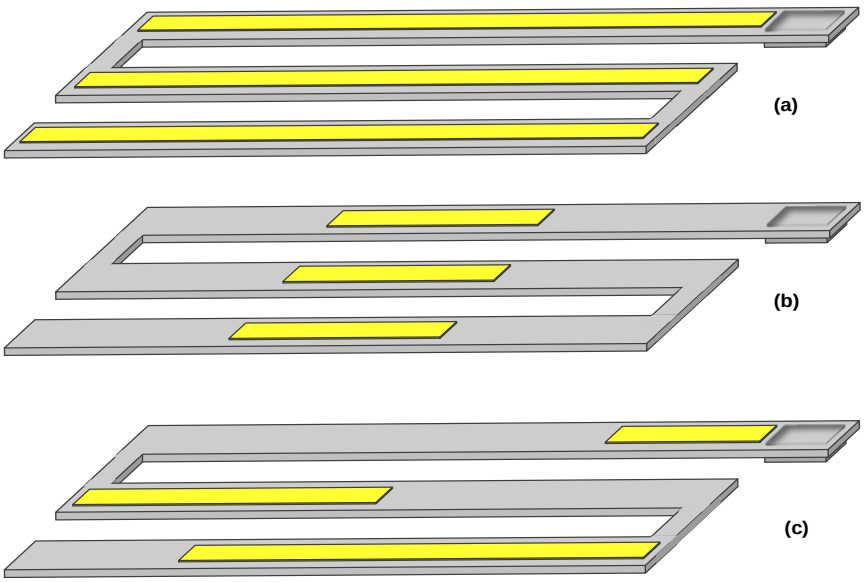

Figure 26: 3-beam polysilicon/gold bimorph zipper actuator designs: (a) full length gold, (b) one third length gold, centered on beam, (c) varied length gold located at bottom of beams.

There were three phases to the modeling of the designs. For all phases, static modeling of designs were conducted using MEMS specific CoventorWare® software and captured the total deflection obtained by each actuator configuration, in order to determine the optimal bimorph cantilever beam configuration.

During phase I of the modeling, the length and location of the metal layer were varied with respect to the underlying polysilicon beam. Research of similar designs found that bimorph layer lengths of approximately one-half the total length of the cantilever beam maximizes the end point deflection [76]. This was verified by modeling multiple lengths for comparison. Additionally, these different bimorph lengths were modeled at different locations on the polysilicon beam. This phase established the optimal bimorph geometry and partial-bimorph beam configuration, which produced the highest initial deflection in the actuator.

Phase II of the modeling varied the number of beams in the actuator and the material stress in the bimorph layer. This phase characterized the effects additional beams have on the structure and also observed the effect on the system due to changing the bimorph material and/or deposition characteristics.

Lastly, a space-saving design was evaluated along with modeling of a full micro-mirror platform actuation assembly. For the space-saving design, beam widths and spacing widths were reduced and modeled in hopes of reducing the actuator footprint, thus allowing for additional beams to be added to the assembly without exceeding the maximum allotted space for the actuator. The full platform actuation assembly was modeled to ensure that the results for an individual actuator would hold true once incorporated into an actuation assembly.

3.5 Device Fabrication

As previously stated, prototype fabrication of these device designs was accomplished using PolyMUMPs™. Using this fabrication option greatly reduced the risks of failed fabrication processes and afforded three design fabrication opportunities during the time allotted for this research. Each fabrication run consisted of 15 copies of one 1 cm x 1 cm area of design space called a die site. MEMSCAP® required that each die site layout be designed using Tanner EDA's L-Edit MEMS software.

L-Edit MEMS layout editor software was created by Tanner EDA and designed specifically to simplify the difficult task of preparing a design layout for fabrication. Figure 27 shows the L-Edit design layout for the third and final 1 cm x 1 cm die site, on the left. On the right is an SEM image of a full die site with fabricated devices released

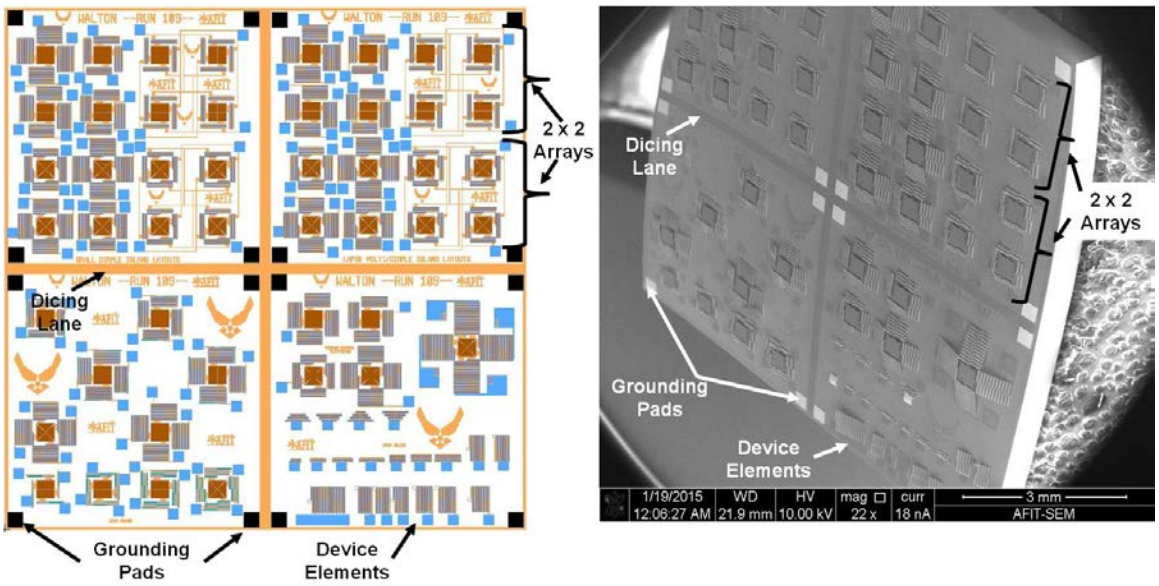

Figure 27: Full 1 cm x 1 cm die site: (Left) L-Edit Layout ready to submit for device fabrication; (Right) is a SEM image of a die site fabricated in PolyMUMPs®with devices released for testing

for testing. The die site layouts were segmented into quarters, by dicing lane. Each quarter had enough space for a 4 x 4 array of devices or 16 individual devices. This allowed the option to dice it into smaller pieces in the event only a few assemblies needed to be released and tested. Otherwise all the devices would be released and the unused devices would then be wasted. Figure 28 shows an L-Edit design for an individual micro-mirror platform actuation assembly (shown in Figure 27) with 7-beam “zipper” actuators developed for this research. Each quadrant contains four breached nitride grounding pads to easily ground assemblies for testing and a mix of individual micro-mirror platform actuation assemblies. Included among the three design layouts were assemblies driven by 1, 2, 3, 4, 5, 6, 7, 8, 9, 10, 11, 12, and 22 beam “zipper” actuators.

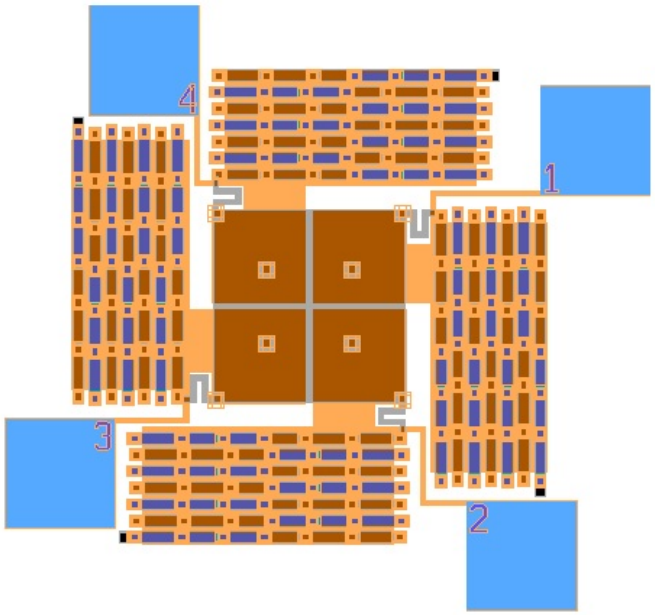

Figure 28: L-Edit layout of a micro-mirror platform assembly with four 7-beam "zipper" actuators

Even with duplicate copies of the modeled device configurations above, there was still space available on the die. To take advantage of this remaining space a couple un-conventional design ideas were fabricated. Those devices were deemed ‘corrugated’ beam designs. These designs attempted to reduce the rigidity of the partial-bimorph beams mechanically in the actuation plane, to produce greater initial deflections and/or reduce actuation voltages. There were two corrugated design fabricated for comparison to the original (modeled) designs. Figure 29 shows cross-sectional views of both corrugated designs that were fabricated using PolyMUMPs®.

Corrugated design 1, Figure 29(a), replaced the solid POLY2 layer of the original partial-bimorph beam design with alternating POLY1/POLY2 layers. These segments maintained the same beam width as the original designs, with lengths of 15 μm. This allowed for a 5 μm overlapped, bonded with a POLY1/POLY2/VIA, and a 5 μm gap.

Corrugated design 2, Figure 29(b), took a much different approach. Using the conformal nature of the PolyMUMPs® fabrication process, a wave in the solid POLY2 layer was created. This was accomplished by strategically placing 15 μm gaps between 15 μm segments of the POLY0 layer being used as the electrode.

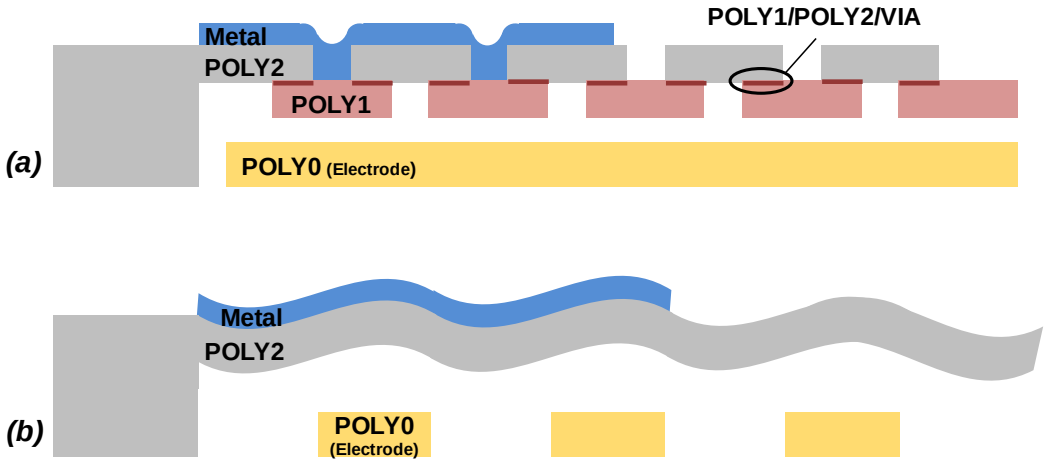

Figure 29: Cross-section views of corrugated partial-bimorph beam designs: (a) corrugated design 1, stacked POLY1 and POLY2 layers bonded with POLY1/POLY2/VIA layer; (b) corrugated design 2, conformal POLY2

3.5.1 Post Fabrication Processing (Post-Processing)

The post-process fabrication of these devices were conducted in two class 100 cleanrooms located at AFIT and AFRL's Sensor Directorate, on Wright-Patterson Air Force Base, Ohio.

Understanding and accepting the limitations of the PolyMUMPs® fabrication, this research explored the post-processing of the devices in an effort to increase device performance. For this, procedures were developed to examine different bimorph layers, which would induce higher stresses into the system and produce greater initial deflections in the "zipper" actuators. Choosing materials with higher CTEs than the gold layer and/or

depositing the bimorph material at a higher deposition temperature than that used by MEMSCAP® induces additional stress into the system, thus producing higher initial deflections. After post-processing, devices were then release for comparison to unmodified devices.

Post-fabrication processing activities were quite involved and included photolithography, etching, evaporation, and sputtering. Background on these processes can be found in the photolithography and pattern transfer appendix, APPENDIX A and APPENDIX B respectively. Post-fabrication processing was accomplished by first creating mask sets for patterning. Then the PolyMUMPs® gold and chrome adhesion layers were removed to allow the deposition of new partial-bimorph layer with different materials and/or deposition methods. Figure 30 shows a micro-mirror platform assembly,

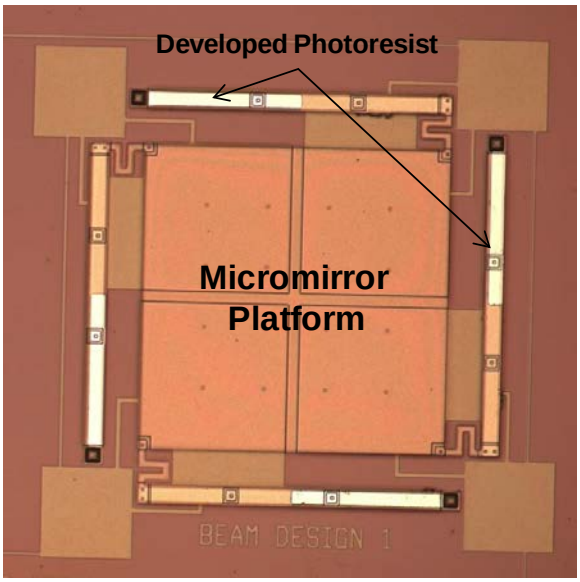

Figure 30: Optical image of a single-beam electrostatic partial-bimorph actuator in the midst of post-fabrication processing

electrostatically driven by four single-beam partial-bimorph actuators, in the midst of post-fabrication processing procedures. At this point, the device seen in Figure 30 has the

PolyMUMPs® gold and chrome layers removed and a layer of photoresist applied, masked, exposed, and developed. The brighter portion of the beams indicates the developed area of photoresist, ready for metal evaporative deposition. For this portion of the research, devices were post-processed with bimorph material layers of gold (Au) and aluminum (Al), 0.5 μm thick, using both evaporative and sputtering deposition techniques at temperatures of 100º C and 125º C. The process followers for those procedures are contained in APPENDIX C and APPENDIX D respectively.

3.6 Tools and Equipment

Other than device fabrication conducted through PolyMUMPs® and at AFRL facilities, all device fabrication, characterization, and testing were conducted in AFIT's Cleanroom and Device Characterization Lab. For this there were four main pieces of equipment used: a Hitachi S-4700 SEM, used to image devices; a Micromanipulator probe station, used to optically observe device condition and actuation; Karl Suss MJB3 Mask Aligner, used during the post-processing photolithography steps; and a 3D optical surface profiler, ZYGO® NewView™ 7300 white light interferometer, to measure initial device deflections as well as step measurements of devices as voltage was increased to the point of pull-in.

The first two pieces of equipment were used throughout this research to provide visual verification of the device condition and provide the high quality imagery of the fabricated devices. The MJB3 mask aligner was exclusively used during the post-fabrication portion of this research. This tool was used to align the pattern transfer masks to the existing device features and expose the photoresist layer to ultraviolet (UV) light.

The results of this process are clearly visible in Figure 30. The final piece of equipment used was by far the most important piece of equipment to this research. The ZYGO® NewView™ 7300 is an optical profiler uses reflected light to produce non-destructive, fast, and high-precision 3D measurements of devices. It can be used for characterizing surface roughness, step heights, critical dimensions (i.e. slopes), and topographical features covering heights ranging from less than 1 nm to 20,000 μm [77].

3.7 Device Characterization and Testing

Fabricated devices were evaluated in two parts, using the ZYGO NewView™ 7300 series white light interferometer. First the initial deflections for devices were characterized, recording initial deflection height measurements for all secondary anchors

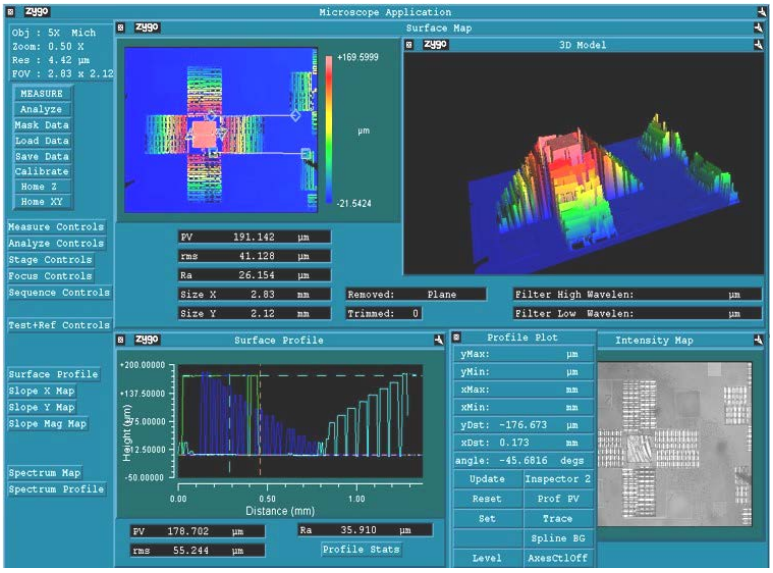

Figure 31: Screenshot of ZYGO white light interferometer measurement for the initial deflection (0 V) of a micro-mirror platform actuation assembly, actuated by four 22-beam "zipper" actuators

and their associated micro-mirror platforms. Four of each "zipper' actuator configuration measured during the device characterization portion of this research. Figure 31 is a

screenshot of a measurement taken of an un-energized micro-mirror platform actuation assembly with four 22-beam “zipper” actuators. The top left image in the screenshot shows a top-down view (measurement angle) of the device and the line segments indicating the physical locations for the measurements indicated in the lower left image. The image on the top right is a 3D rendering (model) of the measurements taken in the top left image. Note that it shows solid columns under the individual partial-bimorph cantilever beams; this is because the measurement is taken from directly above the devices and when the model is generated it assumes a solid structure. Figure 32 is a SEM image of a released micro-mirror platform assembly actuated by four 8-beam "zipper" actuators, showing the air gap under the “zipper” actuators.

In addition to the device characterization conducted in this research, the devices were also operationally tested. The purpose for this testing was to evaluate the pull-in voltage requirements of the “zipper” actuator assemblies. The procedures for this were very similar to those conducted in the device characterization phase. The difference being that the steps previously described were repeated numerous times for each actuator tested. During device testing, two samples of each “zipper’ actuator assemblies were tested. A power supply was used to apply a voltage difference between the polysilicon layer of the structure (grounded) and a polysilicon electrode (voltage). Under the optics

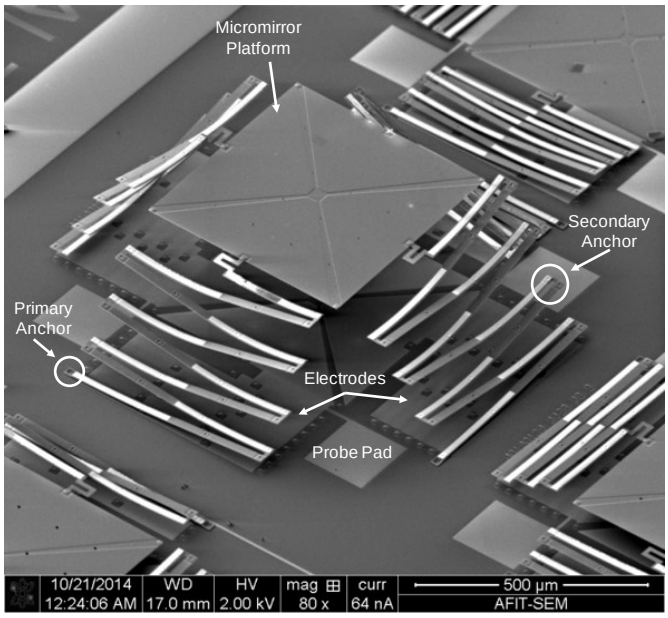

Figure 32: SEM image of a released micro-mirror platform assembly actuated by four 8-beam "zipper" actuators

of the ZYGO NewView™ 7300 probes were placed on the probe pads (Figure 32) and the grounding pads (Figure 27). Then a voltage was applied (0v, 10v, 15v, 18v, 19v, and 20v) terminating once the device achieved pull-in. At each voltage step a ZYGO measurement was taken, recording the same data points as used in the device characterization. Additionally, Platform deflections were taken on the actuation side and the side opposite of the actuation to capture platform tilt.

3.8 Summary

This chapter detailed the design approach, modeling, device fabrication, post-fabrication processing, tools and equipment, and characterization and testing methodologies used in this research. The following chapters will present the data results collected during the evaluation of this unique design as well as the analysis of that data.

4. DATA

4.1 Chapter Overview

Previous chapters provided background, discussing fabrication techniques and device characterization methods used to evaluate the "zipper" actuator design introduced in this research. In this chapter, the analytical modeling, finite element modeling, device characterization/testing, and post-fabrication processing results are presented. The analytical modeling provide calculated results for the expected initial beam deflections and voltages required for pull-in of a single partial-bimorph cantilever beam, while finite element modeling evaluated the expected initial deflections of "zipper" actuators constructed from multiple partial-bimorph cantilever beams. Device characterization and testing provided measured results for the initial deflections and pull-in voltage requirements of the PolyMUMPs® fabricated micro-mirror platform assemblies. Post-fabrication processing results provided an evaluation of the evaporative and sputtering post-processing efforts conducted on the PolyMUMPs® fabricated devices.

4.1 Analytical Modeling Results

The analytical modeling results presented in this section were obtained using the methodologies explained in the previous chapter (Section 3.3). For this modeling, there were two variables which needed to be evaluated. First was the length of the metal bimorph segment to be used on the modeled partial-bimorph cantilever beam. For this, the bimorph segment was modeled at lengths from 100 μm to 450 μm, in increments of 50 μm, and 496 μm (to avoid multiplying by zero). The second variable was the change in temperature (deposition to room temperature). Although it is known that

PolyMUMPs® depositions are conducted at low temperatures, those deposition temperatures are not publicized and would inevitably vary from process to process. For this reason the change in temperature, ΔT in Equation 24, was also varied. All partial-bimorph cantilever configurations were modeled at 10º C, 50º C, 100º C, 150º C, 200º C, and 250º C.

4.1.1 Partial-Bimorph Cantilever Beam Initial Deflections

Below is one example of the analytical initial deflection modeling results calculated. For this modeling, initial deflections of nine partial-bimorph beam configuration were calculated with respect to six different changes in temperature. Table 1 shows the resulting initial deflection calculations for beams fabricated at 150º C above room temperature. The bimorph column indicates the length of the bimorph segment while the non-bimorph column indicates the remaining portion of the cantilever beam.

Table 1: Calculated initial deflection results for a 500 µm partial-bimorph cantilever beam with varied bimorph segments and a temperature change of 150º C

Bimorph	Non-Bimorph	d_1	d_2	Δd_1
1.00E-04	4.00E-04	3.56E-06	2.35E-05	2.70E-05
1.50E-04	3.50E-04	8.01E-06	3.08E-05	3.88E-05
2.00E-04	3.00E-04	1.42E-05	3.52E-05	4.94E-05
2.50E-04	2.50E-04	2.23E-05	3.66E-05	5.88E-05
3.00E-04	2.00E-04	3.20E-05	3.51E-05	6.71E-05
3.50E-04	1.50E-04	4.36E-05	3.06E-05	7.42E-05
4.00E-04	1.00E-04	5.70E-05	2.33E-05	8.02E-05
4.50E-04	5.00E-05	7.21E-05	1.31E-05	8.52E-05
4.96E-04	4.00E-06	8.76E-05	1.15E-06	8.87E-05

Notice the final bimorph segment length is not the full length of the beam. This is because PolyMUMPs® design rules suggest a minimum of 3 µm between the metal layer and the edge of the beam and also to avoid multiplying by zero (Equation 25) when l_2 is

zero. Equation 24 was used to calculate the deflection on the bimorph segment, d_1. The deflection associated with the non-bimorph segment, d_2 was calculated using Equation 25 and the processes discussed in Section 3.3.1. Those two deflections were then added to calculate the total initial deflection of the partial-bimorph cantilever beam. Figure 33 is a graph of the calculated initial deflections for partial-bimorph cantilever beams with a change in deposition temperature of 150º C. This graph shows the total initial deflections

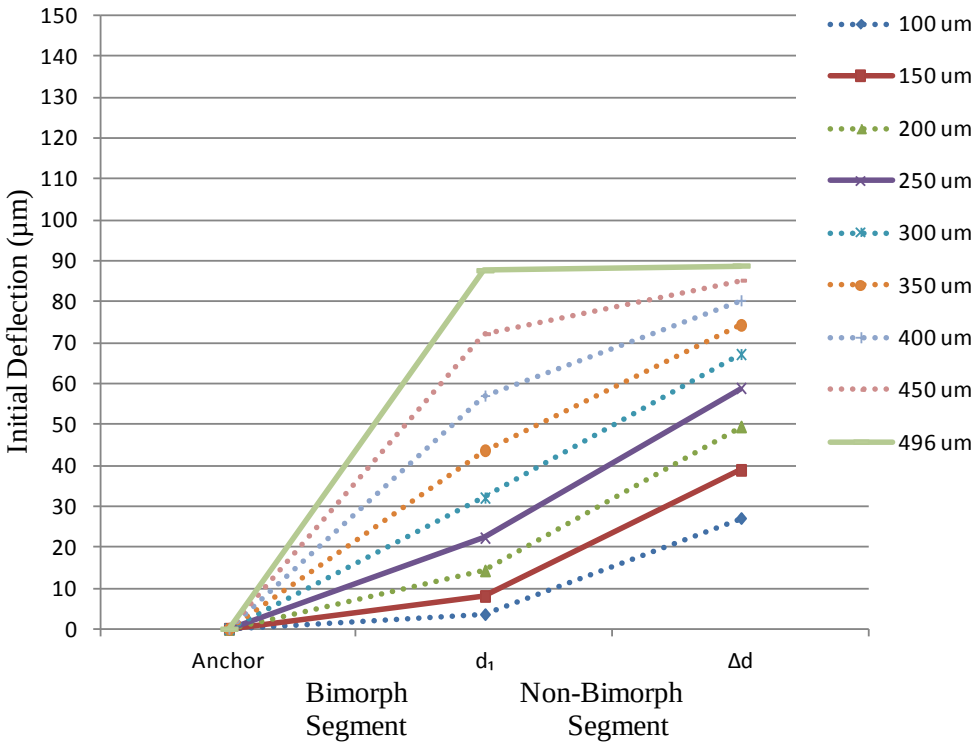

Figure 33: Graph of calculated initial deflection results for a 500 µm partial-bimorph cantilever beam with varied bimorph segments and a temperature change of 150º C

achieved by each of partial-bimorph cantilever beam configurations, as well as the amount of initial deflection associated with the two segments of that beam configuration. A full set of the analytical modeling results showing the initial deflection calculation for all nine beam configurations at six different temperatures is included in APPENDIX E.

4.1.2 Partial- Bimorph Cantilever Beam Pull-in Voltages

Recall from the modeling methodology discussed in Section 3.3.2 that the non-bimorph segment of the beam is to be ignored in this portion of the analytical modeling, given the assumptions that the non-bimorph segment of the beam was perfectly straight and would achieve pull-in once the bimorph segment exceeding its pull-in voltage. An example of the calculated pull-in voltage results for partial-bimorph cantilever beams fabricated at 150º C above room temperature is shown in Table 2. For this modeling, the same bimorph segment lengths were modeled at the temperatures used to model initial

Table 2: Calculated voltages required for pull-in of a 500 µm partial-bimorph cantilever beam with varied bimorph segments and a temperature change of 150º C

Bimorph Segment Length (µm)	Modeled Segment Length (µm)	Pull-in Voltage
100	50	38.7
150	75	31.3
200	100	31.1
250	125	33.2
300	150	30.3
350	175	39.9
400	200	43.8
450	225	47.9
496	248	51.8

deflections. Additionally, Figure 34 is a graph of the data presented above, which shows the relationship between the bimorph segment length and the voltage required to

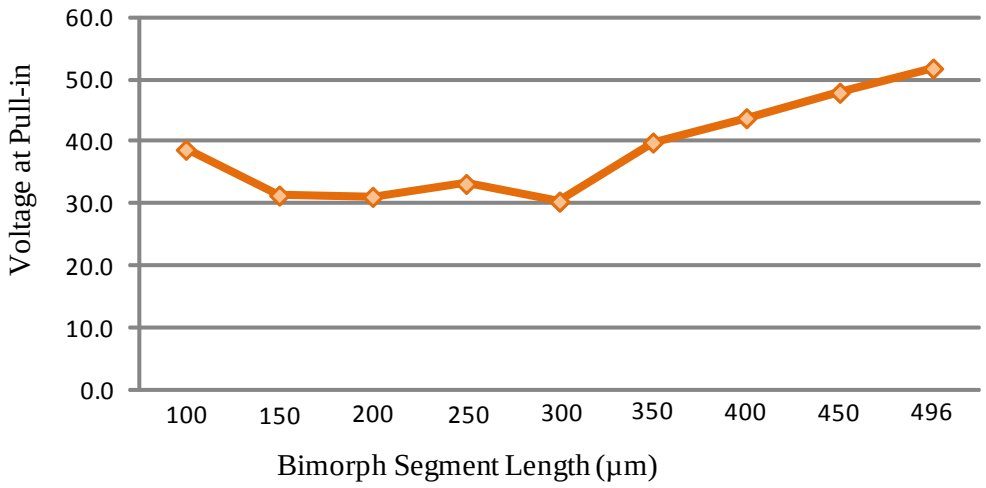

Figure 34: Graph of calculated voltages required for pull-in of a 500 µm partial-bimorph cantilever beam with varied bimorph segments and a temperature change of 150º C

pull-in the beams. In this section, one-half the length of the bimorph segments at a height of one-half the deflection achieved by that bimorph segment was used to construct a basic cantilever beam model. From this, the required pull-in voltage was calculated using Equation 12 and the procedures discussed in Section 3.3.2. This model produced voltage requirements from 10 V (10º C model) to more than 80 V (250º C model). A full set of the analytical modeling results showing the initial deflection calculation for all nine beam configurations at the six different temperatures is included in APPENDIX F.

4.2 Finite Element Modeling Results

Finite element modeling was conducted using CoventorWare® and ANSYS Multi-Physics modeling software, to evaluate different partial-bimorph cantilever beam geometries and configurations effects on the operation of the "zipper" designs used to actuate micro-mirror platforms. The FEM guided the evolution of this design and

consisted of three modeling phases, which culminated in the optimized design fabrication using PolyMUMPs®.

4.2.1 Initial Deflection Modeling Using CoventorWare®

In this portion of the research CoventorWare® software was used to model the initial deflection behavior of stacked partial-bimorph cantilever beams. Design geometries and configurations were varied over three phases in order to optimize the design prior to fabrication.

Phase 1 of FEM began with the predetermined materials and geometries discussed in Section 3.4 and inputs determined by the commercial fabrication process and AFRL compatibility requirements. Recall that this initial design focused the FEM on optimizing the bimorph layer length and location to optimize actuator deflections. For this, bimorph layer lengths of 150 μm, 250 μm, and 500 μm were modeled at the bottoms, centers, and tops of all cantilever beams in the actuator. FEM quickly eliminated center and top bimorph segment locations as viable options. Figure 35 shows a 3-beam "zipper" actuator with 250-μm-long bimorph segments oriented at the center of the cantilever beams. This configuration produced a maximum deflection of 14 μm, observed at secondary anchor 1 and the end of beam three. Beam two actually produced a deflection of – 14 μm, returning secondary anchor 2 to the starting height at the primary anchor. This allows beam three to produce the same deflection as beam one. Similar results were observed with the 150-μm and 500-μm-long bimorph layers centered on the cantilever beams; the only difference being the maximum deflections obtained.

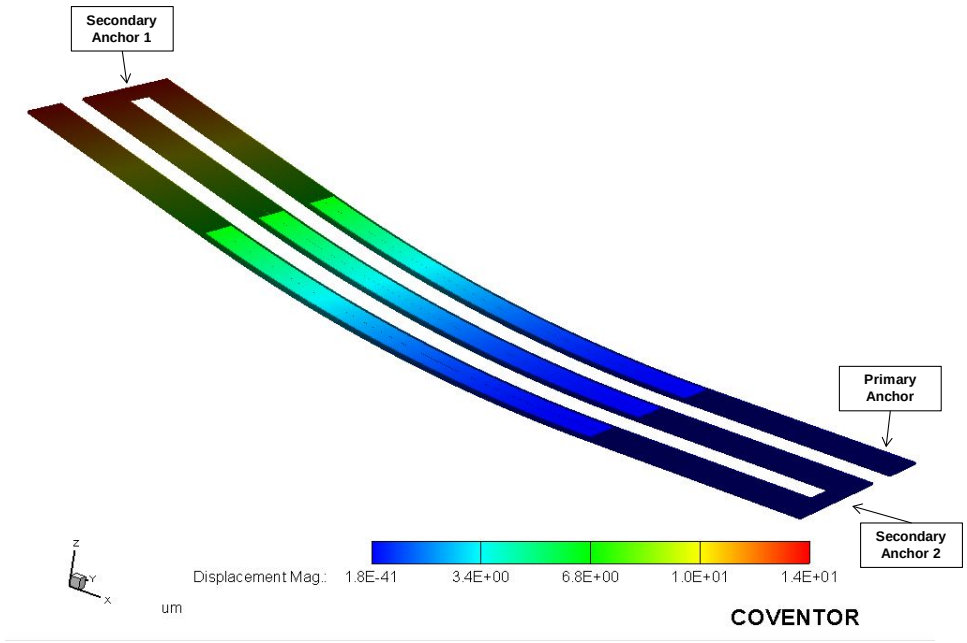

Figure 35: CoventorWare® simulation of a 3-beam "zipper" actuator with 250-µm-long gold bimorph segments centered on cantilever beams

When the bimorph layer was modeled at the bottom of each beam in the actuator the results are much more promising, seen in Figure 36 and Figure 37. This configuration resulted in a maximum actuator deflection more than double that of the first models, clearly visible in the 3D image, seen in Figure 36. Not only did this configuration of the partial-bimorph beam add an additional 6 µm deflection to the first beam, but the actuator also zipped open, producing a greater maximum deflection in the actuator. A 20 µm deflection was observed at secondary anchor 1. A deflection of 14 µm (- 6 µm in the actuator) was observed at secondary anchor 2. With an additional 19 µm added by the final partial-bimorph beam to produce a total actuator deflection of 33 µm, observed at the end of beam three. The graph in Figure 37 shows the deflection gain at secondary

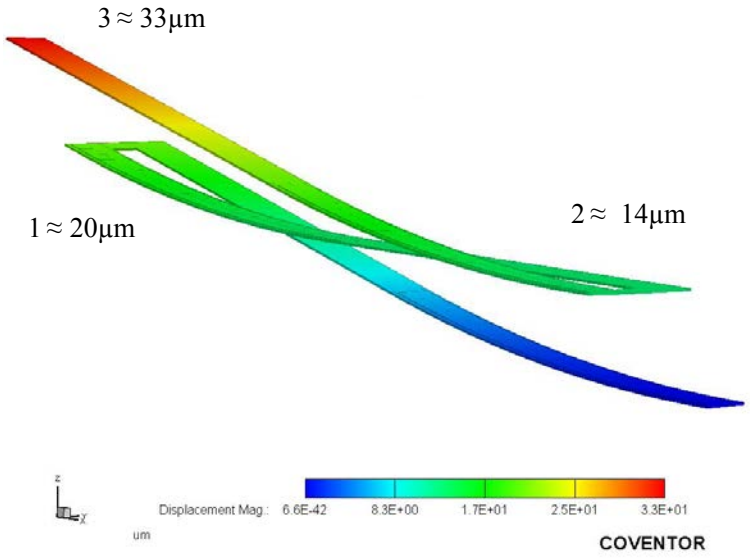

Figure 36: CoventorWare® simulation of a 3-beam "zipper" actuator with 250-µm-long gold bimorph segments located at the bottom of the cantilever beams, 3D deformation model

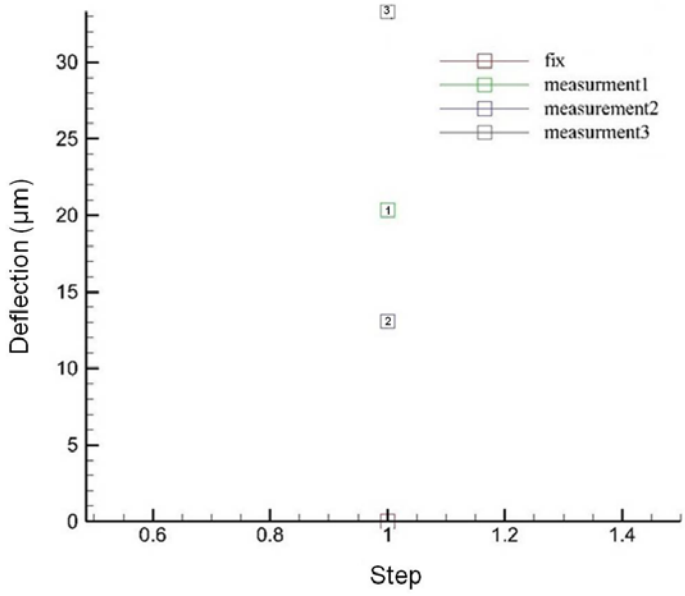

Figure 37: CoventorWare® simulation of a 3-beam "zipper" actuator with 250-µm-long gold bimorph segments located at the bottom of the cantilever beams, graph of deflections at each secondary anchor and end of the last partial-bimorph cantilever beam

anchor 1, loss at secondary anchor 2, and gain at the end of beam three. Similar results were observed in the model with 150 μm bimorph segments in this configuration, again the difference being a reduction in the maximum actuator deflection. There was no need to model the 500 μm bimorph segments in this configuration as this would produce the same results as the center configured models.

In an effort to overcome the negative deflection observed between secondary anchor 1 and secondary anchor 2, the "zipper" actuator assembly was modeled with varied lengths of bimorph segments. Starting with the smallest bimorph segment on beam one and getting progressively longer on each subsequent beam, shown in Figure 38 and Figure 39. Figure 39 shows a deflection gain at secondary anchor 1, a gain at secondary

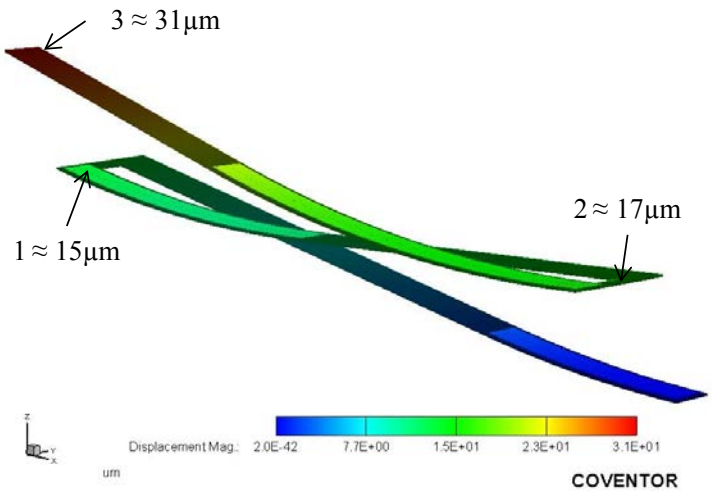

Figure 38: CoventorWare® simulation a 3-beam "zipper" actuator with varied length gold bimorph segments (150μm, 225μm, and 300μm) located at the bottom of the cantilever beams, 3D deformation model

anchor 2, and a gain at the end of beam three. While this approach did indeed overcome the negative deflection observed in beam two of the previous models, it also resulted in less maximum deflection for the actuator. This reduction in initial deflections coupled with the fact that the optimal bimorph segment lengths have to be recalculated each time a partial-bimorph beam is added to the actuator makes this solution impracticable for this application. Similar results were observed in other varied length configurations, none of which produced greater deflections than those observed in previous models.

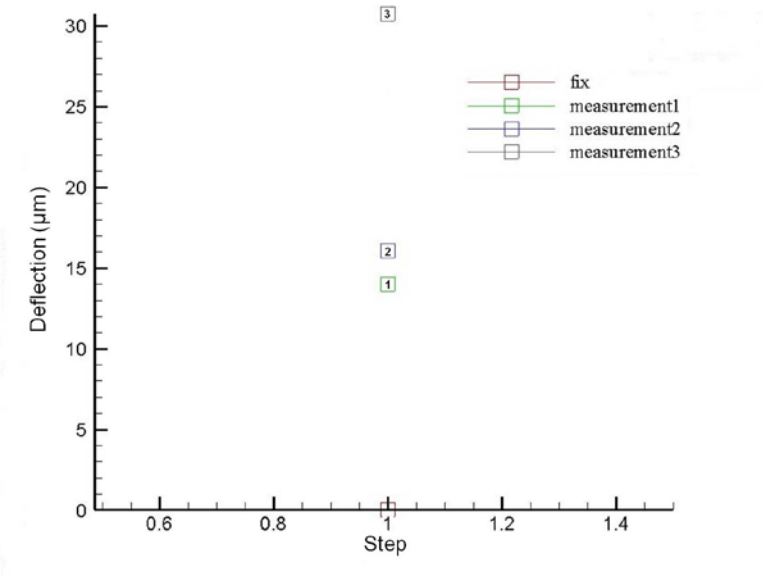

Figure 39: CoventorWare® simulation a 3-beam "zipper" actuator with varied length gold bimorph segments (150µm, 225µm, and 300µm) located at the bottom of the cantilever beams, graph of deflections at each secondary anchor and end of the last partial-bimorph cantilever beam

As a result of the findings in FEM phase I, it was determined that the "zipper" actuator design with 250-µm-long bimorph segments located at the bottom of the cantilever beams was the best design to meet the unique needs of this research.

Phase II FEM examined the effect adding additional partial-bimorph cantilever beams has on the "zipper" actuator assembly. Additionally, an aluminum bimorph material with a higher coefficient of thermal expansion was modeled to observe the impact on the maximum initial deflection of the actuator. For modeling of actuators with gold bimorph segments, 4-beam, 5-beam (Figure 40 and Figure 41), 7-beam and 10-beam (Figure 42 and Figure 43) actuator configurations were modeled. Actuator configurations with gold bimorph segments produced approximately 14 μm of deflection per pair of partial-bimorph cantilever beams. Odd numbered beams added approximately 20 μm

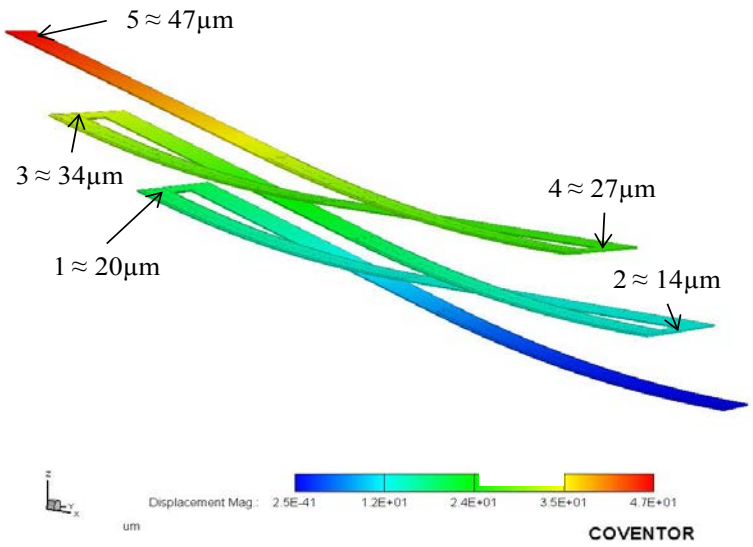

Figure 40: CoventorWare® simulation of a 5-beam "zipper" actuator with 250-μm-long gold bimorph segments located at the bottom of the cantilever beams: (Left) 3D deformation model

deflection, while even numbered beams subtracted approximately 6 μm from the total actuator deflection. Figure 40 shows the 3D deformation model and Figure 41 the graph of the modeled initial deflection measurements for a 5-beam "zipper" actuator with gold

partial-bimorph cantilever beams. The deflection steps observed in this example were also reflected in the 4-beam, 7-beam, and 10-beam models with gold bimorph segments.

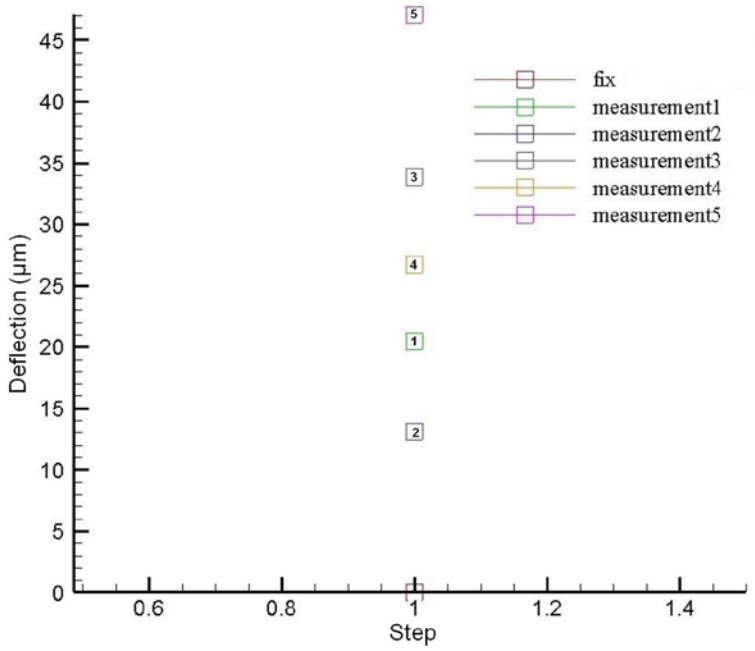

Figure 41: CoventorWare® simulation of a 5-beam "zipper" actuator with 250-µm-long gold bimorph segments located at the bottom of the cantilever beams, graph of deflections at each secondary anchor and end of the last partial-bimorph cantilever beam

Next, these models were repeated for "zipper" actuators with aluminum partial-bimorph cantilever beams. Figure 42 shows the 3D deformation model and Figure 43 shows the graph of the modeled initial deflection measurements for a 10-beam "zipper" actuator with aluminum partial-bimorph cantilever beams. This example shows how these devices produce approximately 18 µm of deflection per pair. The "zipper' actuators

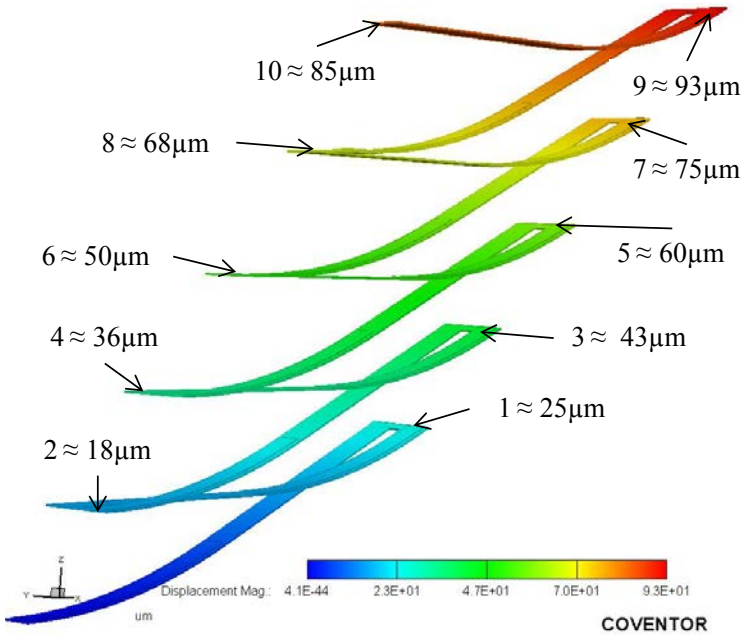

Figure 42: CoventorWare® simulation of a 10-beam "zipper" actuator with 250-µm-long aluminum bimorph segments located at the bottom of the cantilever beams, 3D deformation model

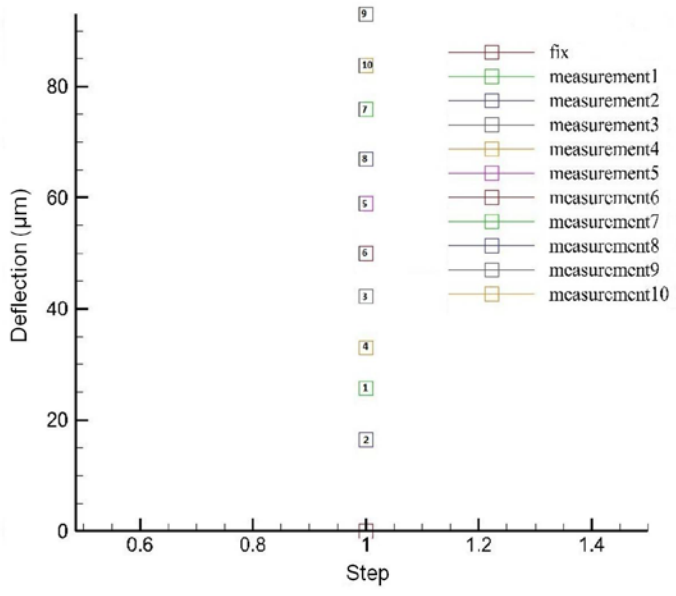

Figure 43: CoventorWare® simulation of a 10-beam "zipper" actuator with 250-µm-long aluminum bimorph segments located at the bottom of the cantilever beams, graph of deflections at each secondary anchor and end of the last partial-bimorph cantilever beam

modeled with aluminum partial-bimorph cantilever beams produced a gain of approximately 25 µm in deflection for every odd numbered beam and a loss of approximately 7 µm in the even numbered beams. Table 3 gives modeled deflections measured at each secondary anchor and the last partial-bimorph cantilever for the actuators seen in Figure 41 and Figure 42/Figure 43.

Table 3: Modeled initial deflections results for a 5-beam "zipper" actuator with gold bimorph segments and a 10-beam "zipper" actuator with aluminum bimorph segments

Actuator Design	Secondary Anchors	Deflection (µm)	Max Actuator Delfection (µm)
5-Beams	1	+20	**47** (~14 per pair
	2	-6	
	3	+20	
	4	-7	
	5	+20	
10-Beam	1	+25	**93** (~18 per pair)
	2	-7	
	3	+25	
	4	-7	
	5	+24	
	6	-10	
	7	+25	
	8	-7	
	9	+25	
	10	-8	

Combined, they highlight that each odd numbered beam produces a net gain in the actuator, while even numbered beams produce a net loss. This phase verified that the “zipper” actuation scheme continues to add deflection as additional beam pairs are added and identified a predictable pattern which can be exploited. Given that each pair of beams adds additional deflection to the system, the number of beams needed to reach specific

design criteria is easily determined. It also showed that materials with different CTEs (bimorph material) will produce different deflection, yet follow the same step pattern.

Phase III of the FEM also had two parts. First, a "zipper" actuator design with smaller partial-bimorph cantilever beam widths and spacing was examined, to increase the number of pairs of beams which can fit in the available space. Figure 45 shows the modeling results for a 5-beam "zipper" actuator with gold bimorph segments widths reduced from 24 µm to 16 µm, partial-bimorph cantilever beam widths reduced from 30 µm to 20 µm, and the spacing between beams reduced from 20 µm to 10 µm. This minor adjustment to the geometry reduces the footprint of the actuator by 15 µm for each pair of

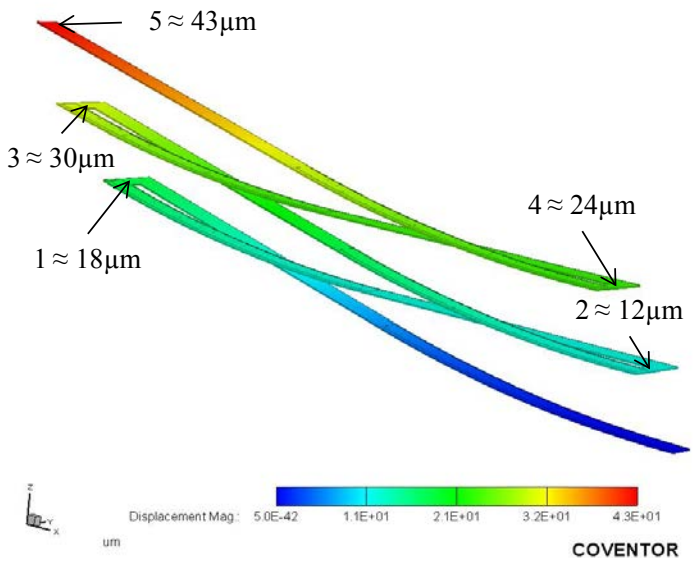

Figure 44: CoventorWare® simulation of 5-beam "zipper" actuator with 250-µm-long gold bimorph segments located at the bottom of 20-µm-wide cantilever beams: (Left) 3D deformation model

beams, with minimal loss of beam deflection. Actuators modeled with this new geometry produced approximately 12 µm of deflection for each pair of beams. When compared to

the results seen Figure 41, this geometry produced a maximum deflection of 4 µm less (5-beam “zipper” actuators). For the second part of this phase, and final FEM modeling,

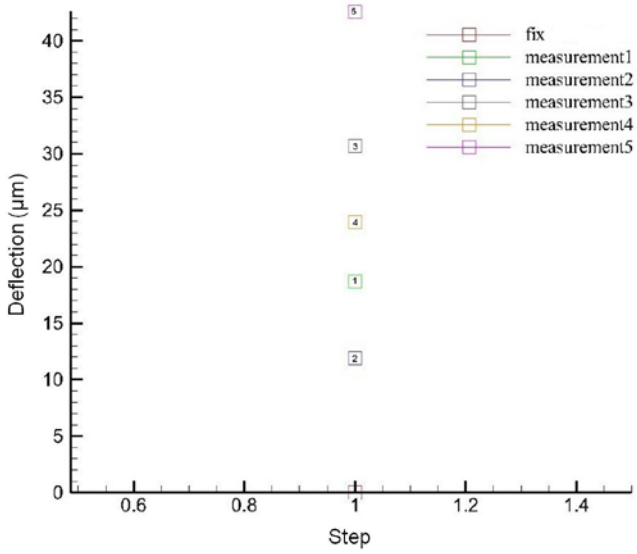

Figure 45: CoventorWare® simulation of 5-beam “zipper” actuator with 250-µm-long gold bimorph segments located at the bottom of 20-µm-wide cantilever beams, graph of deflections at each secondary anchor and end of the last partial-bimorph cantilever beam

micro-mirror platform assemblies were modeled with four 3-beam and four 4-beam “zipper” actuators to ensure the previous actuator modeling results held once the actuators are incorporated into a device. Figure 46 is a 3D static deformation model of a micro-mirror platform assembly driven by four 3-beam “zipper” actuators, resulting in

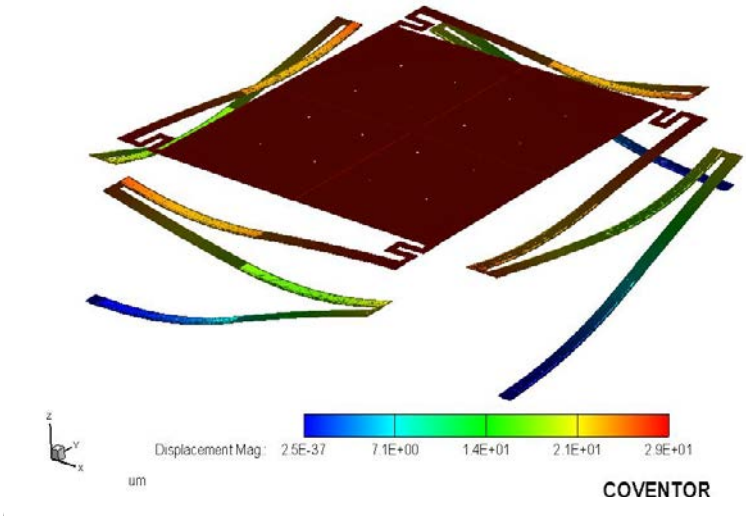

Figure 46: CoventorWare® simulation of four 3-beam "zipper" actuators with 250-µm-long gold bimorph segments located at the bottom of cantilever beams, connected to a 500 µm x 500 µm micro-mirror platform assembly

a total initial deflection for the micro-mirror platform assembly of 29µm. When compared to the 3-beam actuator modeled in phase I, which had the wider partial-bimorph cantilever beams, the result show that little-to-no deflection will be lost when the four actuators are connected to a micro-mirror platform. These results were also shared by the micro-mirror assembly modeled with four 4-beam actuators.

As a direct result of the FEM completed in this portion of the research, 3-beam through 12-beam and 22-beam "zipper" actuators, with reduced geometries, were submitted to MEMSCAP Inc. for fabrication using their PolyMUMPs® process.

4.2.2 Initial Deflection Modeling Using ANSYS

The purpose for this portion of the research was to evaluate ANSYS Multi-physics software for possible implementation in the AFIT MEMS Lab because its relatively low academic licensing cost may make it a more effective tool for AFIT. As

this software is new to AFIT the goal for this modeling was to compare ANSYS results to those obtained using CoventorWare®.

The first thing to be accomplished was the construction of a material database for the PolyMUMPs™ material layers. As ANSYS was originally designed to model the macro environment and has added its micro capabilities in recent years, thin film material properties have to be added to the model. Figure 47 shows a screen capture of the Data Source library that was built for the PolyMUMPs™ specific material properties. Because

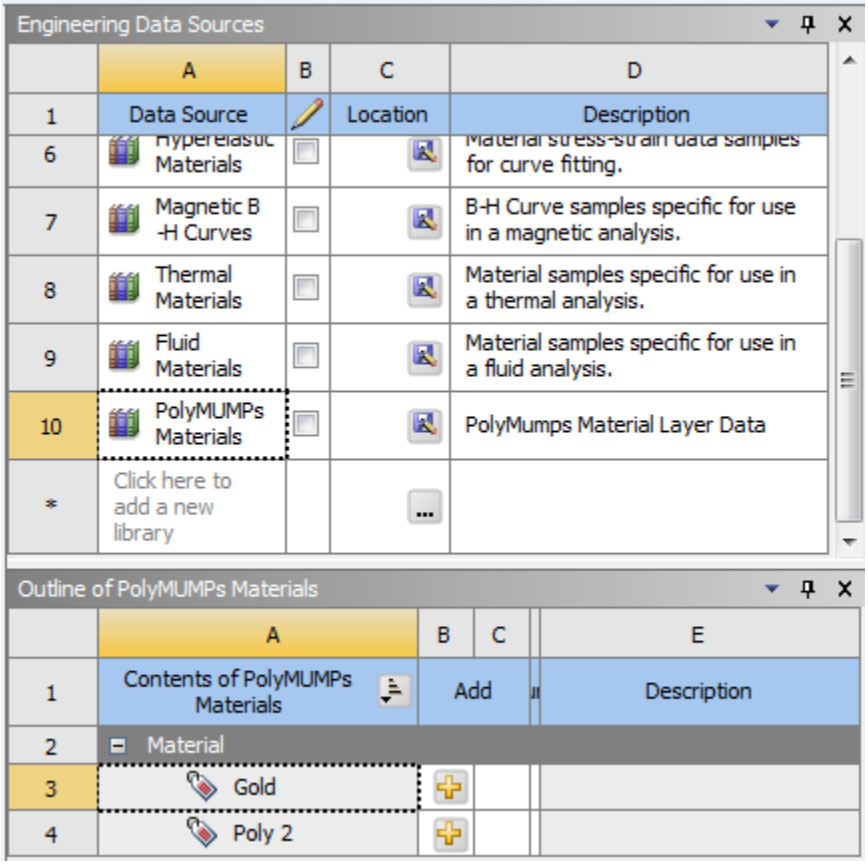

Figure 47: Screen capture of ANSYS Engineering Data Source containing newly created PolyMUMPs Materials Data Source and outline of PolyMUMPs Data Source contents

this model is to be compared with those in the previous section, the gold and polysilicon material property values used were the same as those in the CoventorWare® models.

Once this was done, the next step was to build the geometry file which consisted of the design to be modeled. This can be accomplished either by building (sketching) the design directly in the geometry module or by importing the design file from L-edit. Both are relatively straight forward but if the L-edit design file already exists it is much quicker to import the design. Figure 48 is a screen capture of the 5-beam actuator design, which was

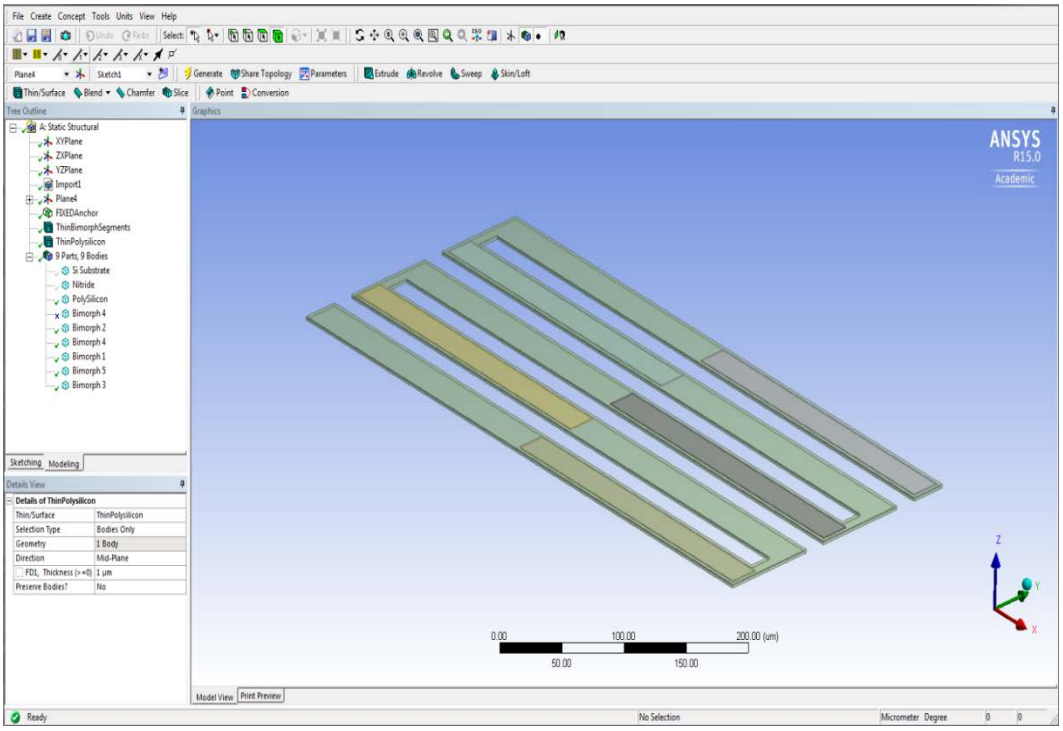

Figure 48: Screen capture of 5-beam "zipper" actuator geometry in ANSYS, imported from L-edit design file using MEMS Pro 3D Modeler

imported from L-edit. To accomplish this, a 3D model is built in L-edit, using the MEMS Pro tool bar. That 3D model is exported as a *.sat file and saved. The saved file was then imported into the geometry module of the ANSYS file. After the design is in the geometry module all the layers can be renamed and material properties assigned. Next the model was meshed in preparation for simulation. Figure 49 shows a screen capture of the 5-beam design after it had been meshed.

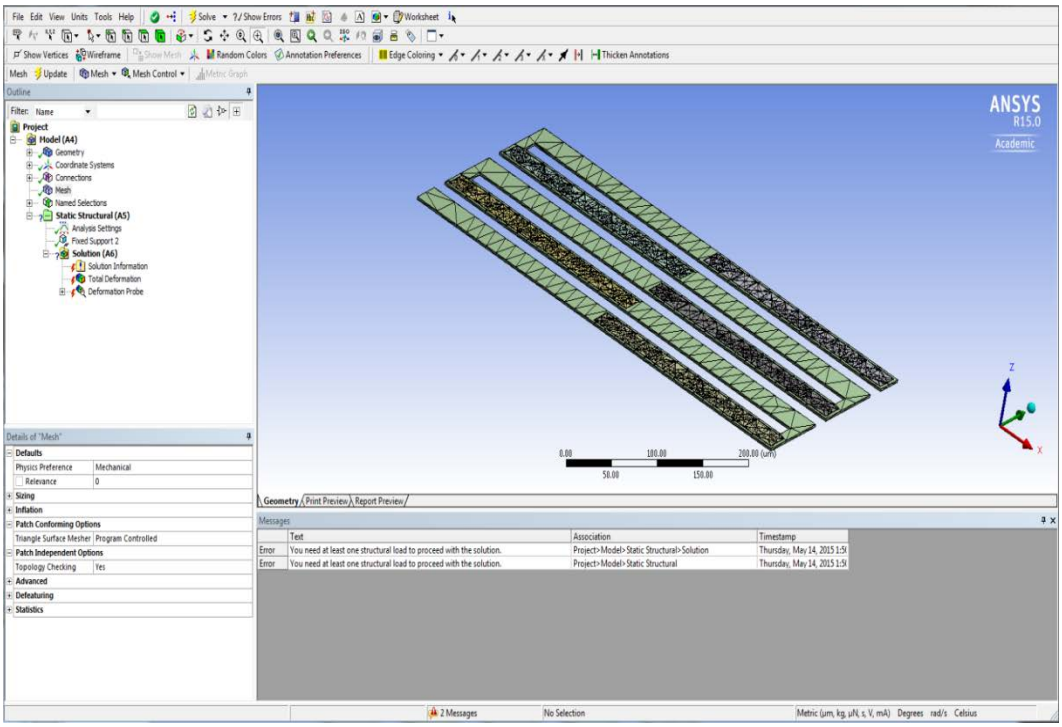

Figure 49: Screen capture of Meshed 5-Beam “zipper” actuator geometry in ANSYS

This was the extent of the results of this portion of the research. Recall that the purpose for this model was to determine the expected initial deflections resulting from the stresses introduced by the stacked partial-bimorph. Where CoventorWare® automatically accounts for this internal stress ANSYS does not. It required the types of forces affecting the model be set within the model. Unsure of what settings to use, I contacted ANSYS support but was still unable to resolve this issue during the course of this research. While a full design simulation using ANSYS was not accomplished, this research did make headway toward reaching that goal.

4.3 Characterization and Testing Results

Device characterizations and testing began immediately upon the receipt of the PolyMUMPs® fabricated devices. Figure 50 is an SEM image of a fabricated micro-mirror platform assembly driven by four 7-beam "zipper" actuators. It clearly shows how

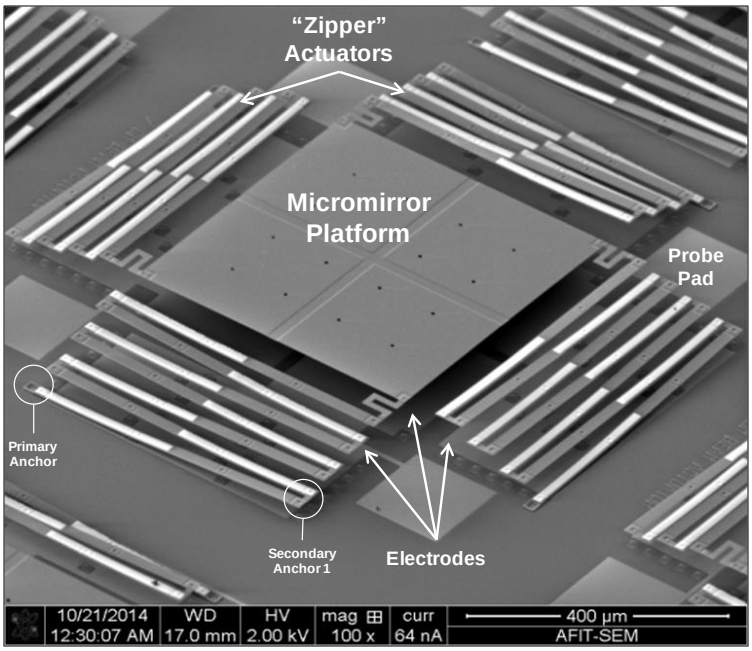

Figure 50: Scanning Electron Microscope (SEM) image of four 7-beam "zipper" actuators with 250-µm-long gold bimorph segments located at the bottom of cantilever beams, connected to a 500 µm x 500 µm micro-mirror platform assembly

each pair of beams produce additional positive deflection in the assembly. In this portion of the research, initial deflection characterization and required pull-in voltage testing of the fabricated devices were conducted using a ZYGO® NewView™ 7300 3D optical white light interferometer, following the procedures outlined in Section 3.7.

4.3.1 Initial Deflection Characterizations

For the device characterization portion of this research, static initial deflections of all actuator configurations (four of each) were measured at all secondary anchors and the platform/last cantilever beam. Table 4 contains the measured initial deflection results for

four 5-beam “zipper” actuators. The first four columns each represent an individual actuator, while the rows provide the location of the measurement. The last column of the

Table 4: Measured initial deflection results for PolyMUMPs® fabricated, 5-beam “zipper” actuators; 500 µm partial-bimorph cantilever beams with 250 µm bimorph segments

Secondary Anchors	Actuator Deflections (µm)				Average Deflection
1	21.7	21.5	24.8	23.7	22.93
2	23.3	23.5	26	25.8	24.65
3	31.7	31.5	35	34.1	33.08
4	42	43.2	47	46.9	44.78
5	42.2	40.8	45.3	45.3	43.40

table is an average measurement for the deflection height of that location, taken across the four measured actuators, showing an average maximum deflection of approximately 43 µm. This set of data was unusual because the measurements showed a net positive

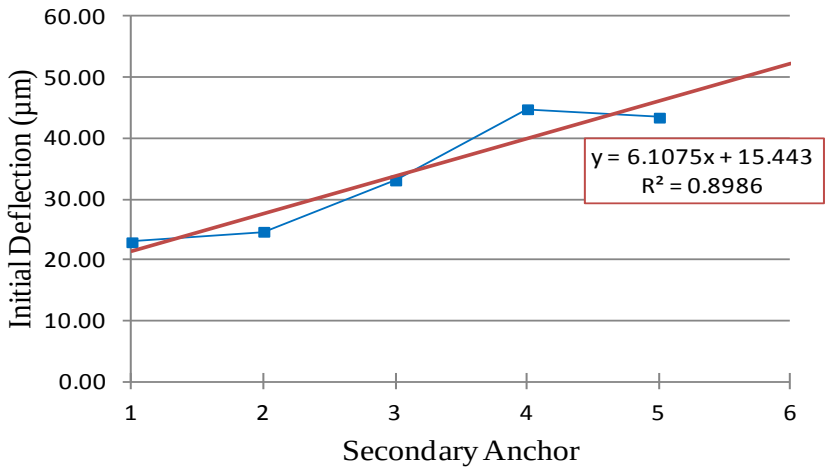

Figure 51: Graph of measured initial deflection results for PolyMUMPs® fabricated, 5-beam “zipper” actuators; 500 µm partial-bimorph cantilever beams with 250 µm bimorph segments

deflection added to the system at each secondary anchor, contrary to the FEM results. This can also be seen in Figure 51, which shows a graphical representation of the average

deflections measured. It is important to note that all four actuators showed this, and that the only other actuator configurations to demonstrate this unexpected deflection profile were the 3-beam actuator and the corrugated design configurations. Table 5 and Figure 52 show the measured initial deflections for the 10-beam "zipper actuators. This measured data set is more representative of the remaining data collected in this portion of the research and closely agrees with the expected deflection of the system, as predicted during the FEM of this research. There are net positive deflections measured at all odd numbered secondary anchors, while there are net negative deflections measured at all

Table 5: Measured initial deflection results for PolyMUMPs® fabricated, 10-beam "zipper" actuators; 500 µm partial-bimorph cantilever beams with 250 µm bimorph segments

		Actuator Deflections (µm)				Average Deflection
Secondary Anchors	1	25	23.8	23.7	24.1	24.15
	2	19.4	20	20.1	20.5	20.00
	3	37.4	36.7	36.9	36.7	36.93
	4	34.2	34.3	36.1	36.1	35.18
	5	51	51.2	51.2	51.3	51.18
	6	50	48.3	50.7	50.7	49.93
	7	66.3	65.2	66.4	66	65.98
	8	62	61.3	64.5	64.3	63.03
	9	82.2	81.1	83.1	82.9	82.33
	10	76	76.1	76.7	76.6	76.35

even numbered secondary anchors. This device produced an average maximum deflection measured to be approximately 76 µm.

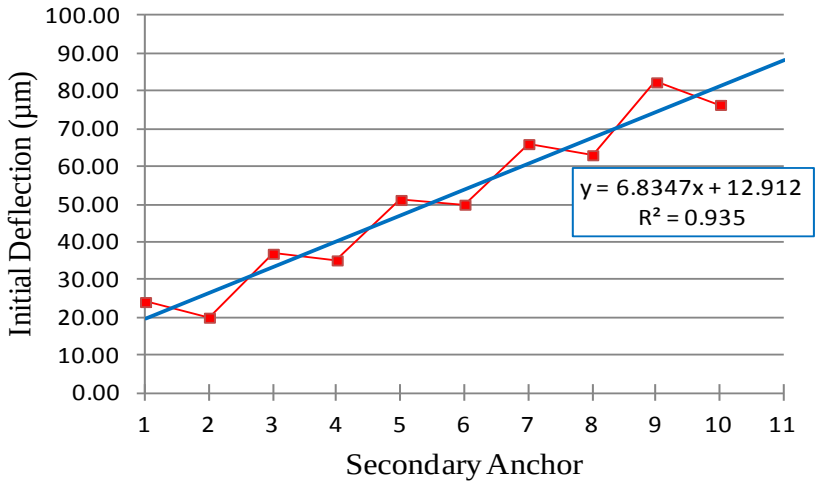

Figure 52: Graph of measured initial deflection results for PolyMUMPs® fabricated, 10-beam "zipper" actuators; 500 µm partial-bimorph cantilever beams with 250 µm bimorph segments

The most impressive example of this trend is observed in the 22-beam micro-mirror platform assembly, presented in Table 6 and Figure 53. While all the devices characterized in this portion of the research (excluding the 3-beam, 5-beam, and corrugated beam devices previously discussed) responded this way, significant variations in deflections did occur. Table 6 shows a maximum initial deflection difference of approximately 11 µm between the first two assemblies and the last two assemblies measured. This resulted in a range of maximum initial deflection from 165 µm to 176.3 µm with an average maximum of nearly 171 µm.

Table 6: Measured initial deflection results for PolyMUMPs® fabricated, 22-beam "zipper" actuators; 500 µm partial-bimorph cantilever beams with 250 µm bimorph segments

Secondary Anchors	Actuator Deflections (µm)				Average Deflection
1	23.3	24.5	29.1	27.7	26.15
2	20.3	21.4	21.9	21.7	21.33
3	36.7	37.4	42.9	41.8	39.70
4	36.1	37.5	39.6	38.6	37.95
5	50.5	51.1	56.9	56	53.63
6	52.1	53.3	56.9	55	54.33
7	64.1	65.3	71.6	70.9	67.98
8	67.2	68.2	72.9	70.8	69.78
9	78.5	79.1	86.8	86.2	82.65
10	82.5	83.6	90.2	86.5	85.70
11	93	93.4	102.7	101.2	97.58
12	94.8	97.6	105.5	103.1	100.25
13	106.5	108.1	118.1	117.2	112.48
14	109.6	111.9	121.1	117.4	115.00
15	121.8	123.3	133.9	132.8	127.95
16	124.1	125.5	135.4	132.9	129.48
17	137.4	138.5	150	149.8	143.93
18	138	139.2	150.3	147.1	143.65
19	152.8	154.5	166.1	166.9	160.08
20	151.7	152.6	164.8	161.8	157.73
21	169.2	170	182.9	184.1	176.55
22	165	165.8	176.3	176.2	170.83

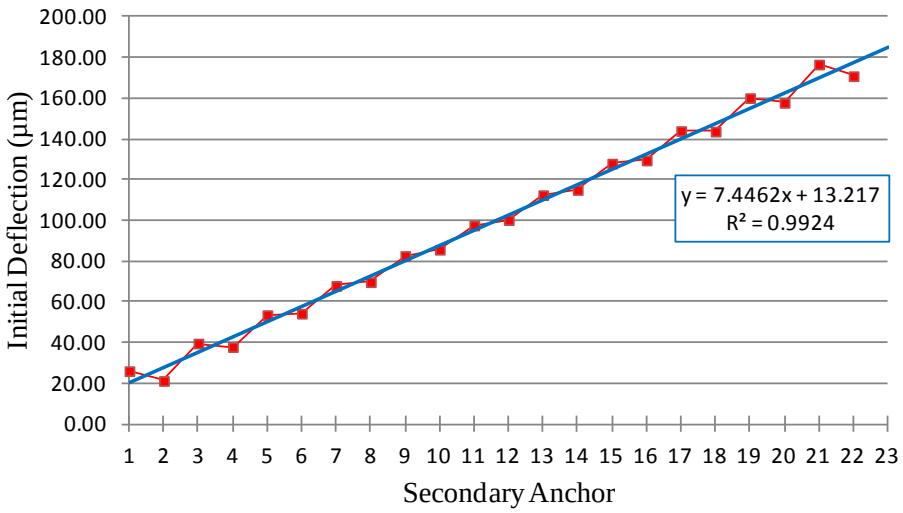

Figure 53: Graph of measured initial deflection results for PolyMUMPs® fabricated, 22-beam "zipper" actuators; 500 µm partial-bimorph cantilever beams with 250 µm bimorph segments

In addition to the modeled designs there were "corrugated" designs fabricated, seen in Figure 29. Unfortunately, none of the corrugated design 1 devices (stacked POLY1/POLY2 layers) survived the release process. Figure 54 shows POLY1/POLY2/VIA stacked beam fragments (corrugated design 1). Each time a set of devices were released, all corrugated design 1 devices were destroyed. The fragmentation

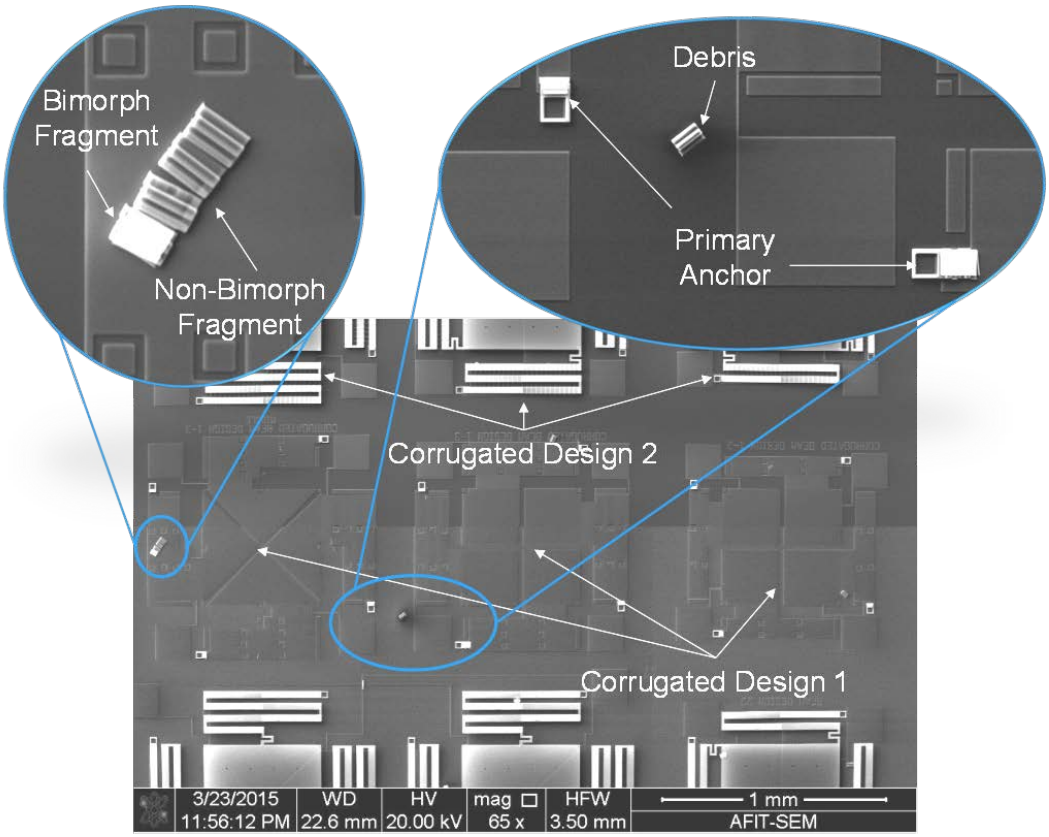

Figure 54: SEM image of released POLY1/POLY2 stacked beam fragments atop an adjacent device

deposited debris across every other device. Figure 55 clearly shows the debris field produced by the disintegration of the corrugated design 1 beam. All devices released with this beam configuration had fragments of POLY1/POLY2 beams on them, which interfered with the release and/or operation of those devices. For this reason, these devices were removed from the final fabrication run. Corrugated design 2 devices however did not experience the same reaction. This is also observed in Figure 55. The corrugated design 1 device (bottom right) is missing, fragmenting into small pieces of debris, while the device with corrugated design 2 (top right) is released and fully intact.

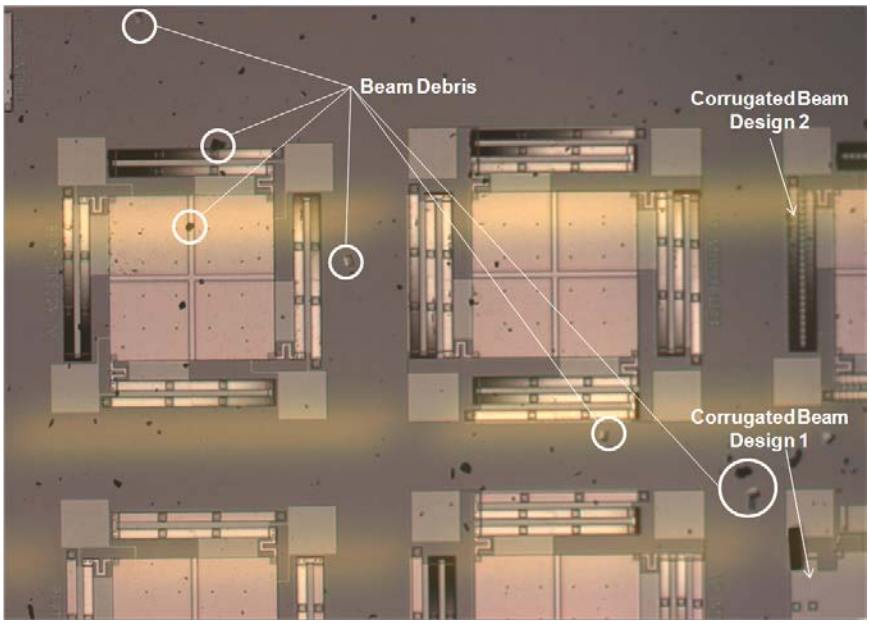

Figure 55: Optical microscope image of debris field from released POLY1/POLY2 stacked beam devices

Initial deflection characterizations were also conducted for devices with 5-beam, 7-beam, 9-beam, and 11-beam corrugated design 2 partial-bimorph cantilever beams. Table 7 and Figure **56** show the 11-beam corrugated design 2 measured initial deflection data and graph respectfully. This design produced an average maximum initial deflection of approximately 88 μm. Also it illustrates that this device also experienced a net positive deflection gain at almost all secondary anchors and a loss of deflection at the end of the final beam/platform. This unexpected result was also shared by the other fabricated corrugated device configurations measured. Additionally, all corrugated designs averaged maximum deflection results were very close to those measured for their flat counterparts. The largest difference being 5μm, observed between the 11-beam device configurations.

Table 7: Measured initial deflection results for PolyMUMPs® fabricated, corrugated 11-beam "zipper" actuators; 500 µm partial-bimorph cantilever beams with a 250 µm bimorph segments

Secondary Anchors	Actuator Deflections (µm)				Average Corrugated Deflection
1	26.7	24.1	24.8	25.9	25.38
2	24.1	22	23.6	23.6	23.33
3	39	37.8	37.2	39.4	38.35
4	42	38.4	41.3	41.7	40.85
5	51.1	46.5	50	52.6	50.05
6	59.2	55.3	57.3	59.9	57.93
7	63.4	58.9	64.2	65.4	62.98
8	74.7	71.8	76.1	75.8	74.60
9	74.7	71.7	77.4	77.9	75.43
10	91.4	86.5	93.3	94.2	91.35
11	87.5	85	89.3	90.1	87.98

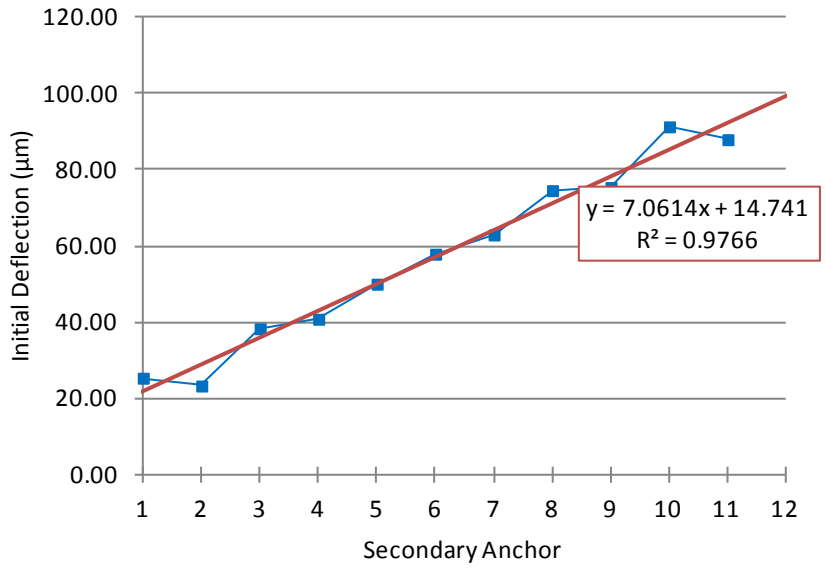

Figure 56: Graph of measured initial deflection results for PolyMUMPs® fabricated, corrugated 11-beam "zipper" actuators; 500 µm partial-bimorph cantilever beams with 250 µm bimorph segments

A full set of the characterization results showing the initial deflections measured for the different "zipper" actuator configurations is included in APPENDIX G**.**

4.3.2 Pull-in Voltage Testing

Pull-in voltage testing proved to be very difficult. There were two major challenges to overcome. The first issue encountered was that AFIT's ZYGO® NewView™ 7300 was not set up to measure an actuated device (applied power). To overcome this challenge a vacuum chuck for the NewView™ 7300 table was fabricated and a power generation station, using portable probes, was set up. The second issue encountered was due to the layout of the design. When working in this confined space it was clear that these devices are too close together. Figure 57 is an SEM of a full set of devices released for testing. It shows an example of the largest area of devices which can

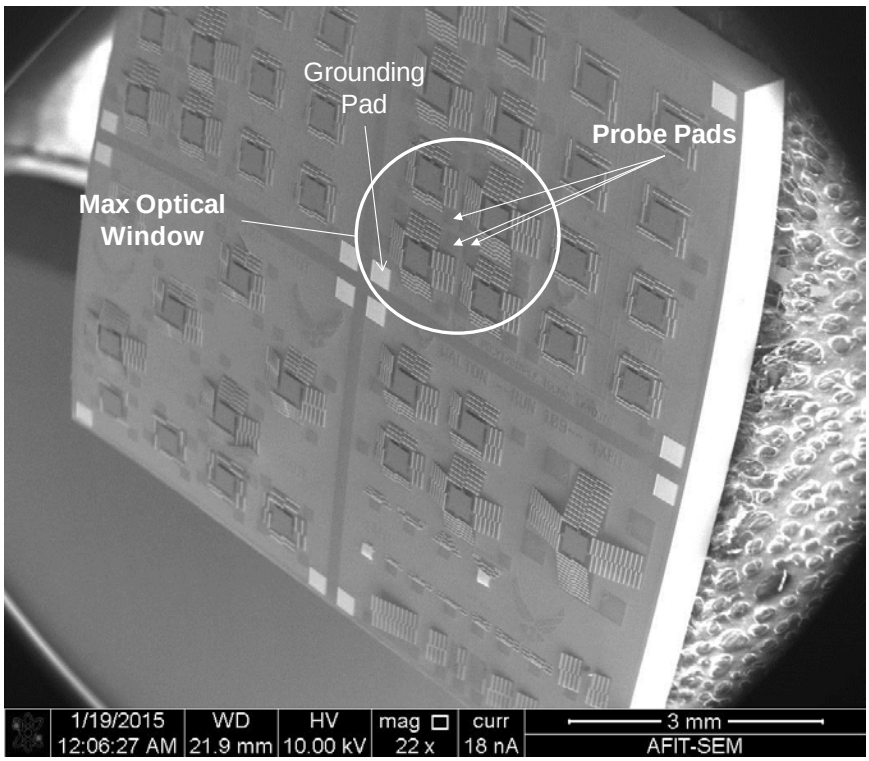

Figure 57: SEM image of a full PolyMUMPs® fabricated die site released for testing

be measured at any given time, the circle representing the optical view window. The issue being the space needed to allow for freedom of movement of the probes, within

that viewing area. A probe needed to be placed on a ground pad and one on the probe pad of the actuator to be tested. While this was not too difficult for devices close to the ground pad (bottom left of circle) it became increasingly more difficult the further the test device was from the ground pad (top right of circle).

Additionally, the deflections of surrounding devices also posed an issue. At times, they inadvertently made contact with the probe and shorted the devices. To overcome this, micro-mirror assemblies were strategically and very carefully removed to allow adequate space for probe movement. Even after this extreme measure, there were four devices which were not fully tested. The 11-beam flat configuration and the corrugated 5-beam and 9-beam configurations were positioned in areas which could not be tested. Additionally, only a single 10-beam configuration was tested because of the difficult locations. For all other device configurations, a minimum of two actuators were tested.

With the exceptions of the 3-beam, 4-beam and 5-beam "zipper" actuator configurations, most of the devices tested achieved pull-in between 18 V and 20 V. One 7-beam and one 9-beam actuator achieved pull-in at 15 V and one 11-beam actuator required 25 V to pull-in. Table 8 shows the measured test data collected during the test of two 12-beam assemblies. Each data point collected reflects the deflection height of a secondary anchor, the last beam, the actuation side of the platform (PF_a), and the side of the platform opposite the actuation (PF_o) for each step in applied voltage. Figure 58 is a graphical representation of the actuator deflection data seen in Table 8(b). It shows how the actuator experienced little pull-in until 18 V, then snapped down at 19 V. This example was unique from most of the other tests. Additional pull-in was achieved by

Table 8: Measured deflection results for pull-in of PolyMUMPs® fabricated micro-mirror platform assembly with four 12-beam "zipper" actuators; (a) device 1 test results, (b) device 2 test results

	1	2	3	4	5	6	7	8	9	10	11	12	PFa	PFo
0v	21.6	19.5	34.3	33.7	47.9	47.2	60.8	60.4	75.4	73.1	90.0	83.8	84.5	84.9
10v	20.7	18.5	32.8	31.6	45.8	45.2	59.2	58.3	73.7	71.1	88.9	82.8	83.7	84.9
(a) 15v	19.4	15.7	30.7	29.0	43.6	42.8	57.6	56.2	72.1	69.7	87.8	81.9	82.6	84.1
19v	3.8	3.8	3.4	3.8	3.4	3.8	14.9	15.7	35.3	33.8	57.8	53.2	55.4	75.2
20v	3.5	3.7	3.8	3.9	3.8	3.5	14.4	14.6	34.6	32.8	56.6	53.6	56.1	75.4
0v	21.7	19.7	33.7	33.2	46.8	47.5	60.2	59.8	74.5	72.5	90.2	85.2	84.3	84.4
10v	20.8	18.3	32.0	32.0	44.8	45.6	58.0	58.7	72.2	70.6	87.7	82.5	82.6	84.4
(b) 15v	19.5	15.5	30.0	28.8	42.7	42.4	56.1	55.6	70.9	68.3	86.6	81.6	82.3	83.9
18v	4.8	4.4	3.7	11.5	16.1	22.7	33.7	36.9	52.2	51.7	72.2	66.7	68.9	80.2
19v	3.9	3.7	3.7	3.7	3.9	3.8	3.9	3.5	23.3	23.5	47.9	42.2	45.0	71.9
20v	3.5	3.3	3.8	3.3	3.9	3.2	4.0	3.1	3.8	16.1	36.4	33.8	42.6	68.9

increasing voltage. In most cases the addition of additional voltage (up to 10v) either caused the platform to snap down (short) or had no effect on the pull-in.

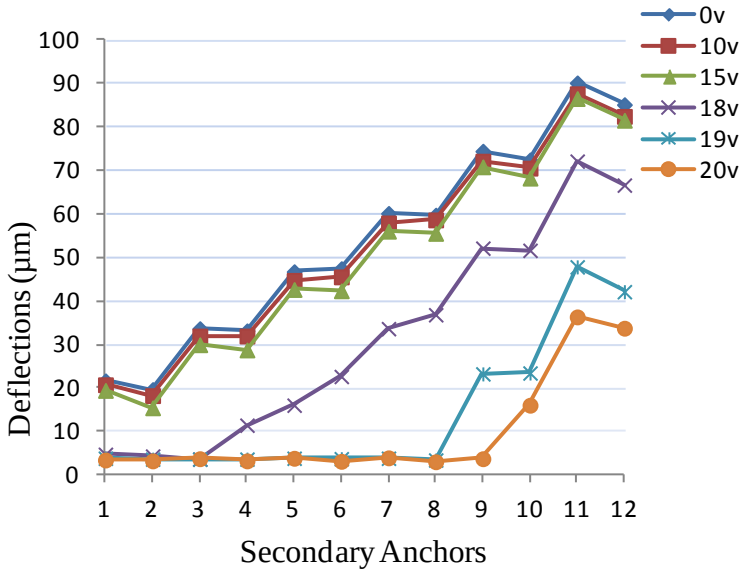

Figure 58: Graph of measured deflection results for pull-in test of PolyMUMPs® fabricated micro-mirror platform assembly 2, with 12-beam "zipper" actuator deflections measured at each secondary anchor

Figure 59 is a graphical representation of the platform deflection data seen in Table 8(b). It shows the tilt actuation of the platform. Notice that the side opposite the actuation

experienced a little pull-in as the actuator pulls down and with a large drop at pull-in. While the different actuator configurations tended to produce similar profiles, the

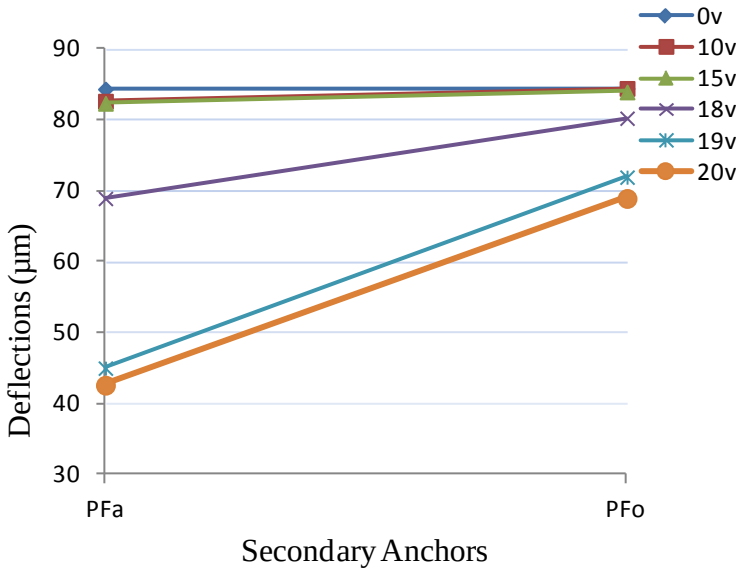

Figure 59: Graph of measured deflection results for pull-in test of PolyMUMPs® fabricated 12-beam micro-mirror platform assembly 2, with micro-mirror platform deflection, measured on actuation side (PF_a) and side opposite actuation (PF_o)

deflection differences seen between the two sides of the platform ranged from 0 µm to as much as 26 µm. As previously mentioned the 3-beam, 4-beam and 5-beam configurations did not achieve pull-in. Figure 60 and Figure 61 are graphs showing the measured pull-in data for a 4-beam actuator, also representative of the 3-beam configurations tested. These devices never achieved full pull-in (up to 10 V). While the actuators are seen to have had some pull-in, the platform did not achieve any significant tilt. This result was also seen in the 5-beam actuators test, except that in those cases the platform snapped in and shorted.

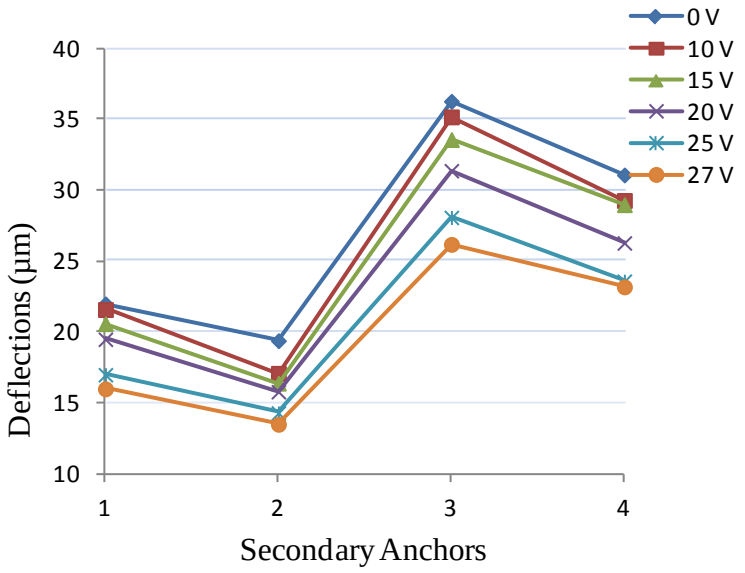

Figure 60: Graph of measured deflection results for pull-in test of PolyMUMPs® fabricated micro-mirror platform assembly 1; 4-beam "zipper" actuator deflections, measured at each secondary anchor

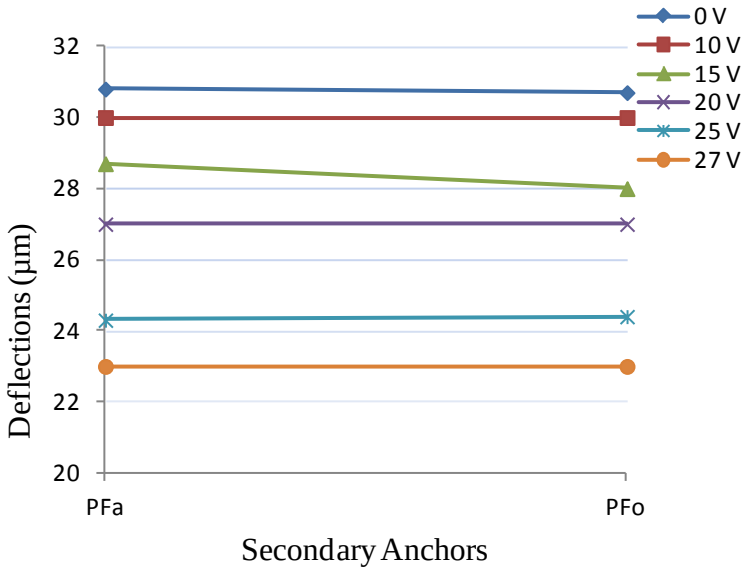

Figure 61: Graphs of measured deflection results for pull-in test of PolyMUMPs® fabricated 4-beam micro-mirror platform assembly 1; micro-mirror platform deflection, measured on actuation side (PF_a) and side opposite actuation (PF_o)

4.4 Post-Fabrication Processing Results

Working closely with AFRL researchers, two post-fabrication processing attempts were made during this portion of this research. Both attempts consisted of the same initial preparation of the devices which consisted of the removal of the PolyMUMPs® metal and adhesion layers.

The first attempt used an evaporative deposition method. Figure 62 is an image of one of the many failed attempts at mask alignment. In this instance the photoresist layer was removed and the alignment re-accomplished. Once this channel of developed photoresist was properly aligned to within a couple microns, the devices were sent to AFRL for metallization. Two full dye sites were taken to AFRL at a time, one for gold

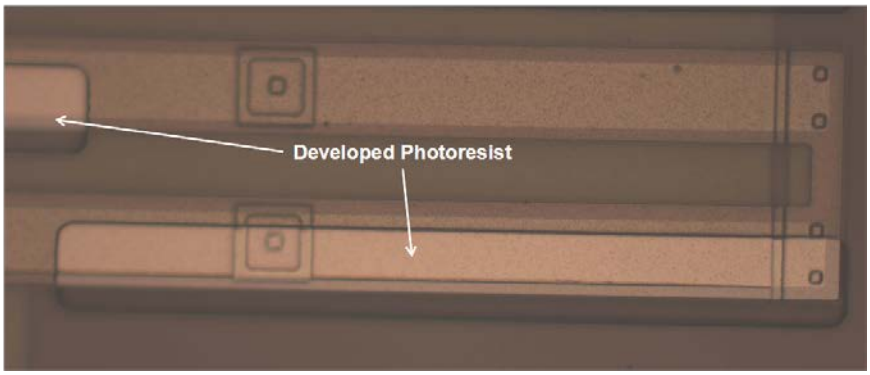

Figure 62: Optical microscope image of a fabricated device during post-fabrication processing

evaporation and one for aluminum evaporation, both at 120º C. Multiple attempts were made with the same outcome. For all the evaporated devices the lift off was perfect, however the resulting released devices were all less than desirable. All the devices with post-processed evaporated gold (seen in Figure 63) produced very little deflection. This is

clearly seen in the image because all the beams of the actuator are in the same focal range. If this 5-beam assembly had any significant deflection some of the beams would

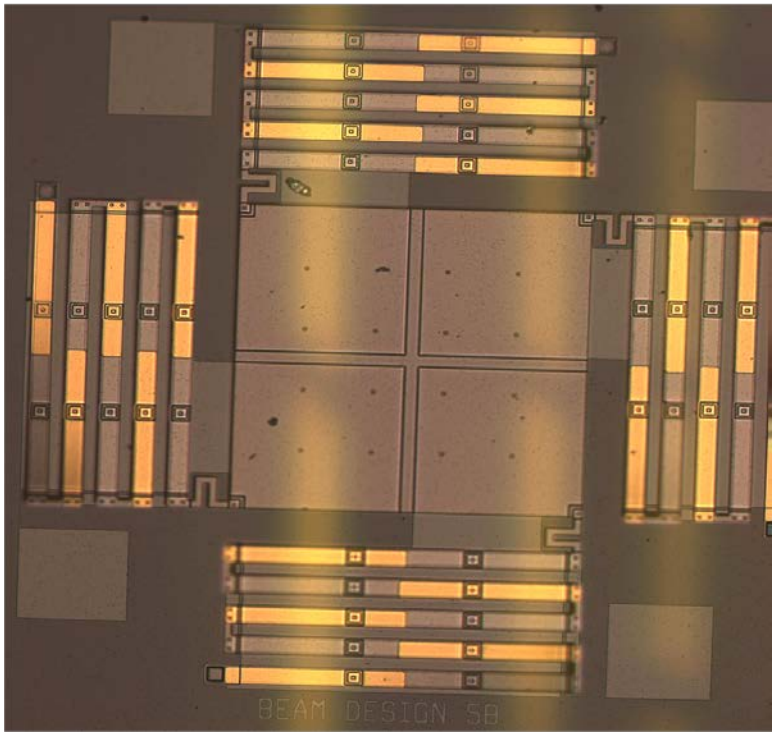

Figure 63: Optical microscope image of a release device, post-processed with evaporated gold bimorph segment

be blurred. As for the aluminum results, they were even worse. None of the aluminum devices deflected at all.

The second post-fabrication processing attempt used sputter deposition. This deposition was also conducted at AFRL. This process differed in that the prepared devices were immediately sent to AFRL for metallization. The material was sputtered on, patterned and back etched, and then a protective layer of photoresist was applied prior to release. Figure 64 shows a device with a protective layer of photoresist applied over the beams. Unfortunately, the results from this post-processing attempt were similar to the

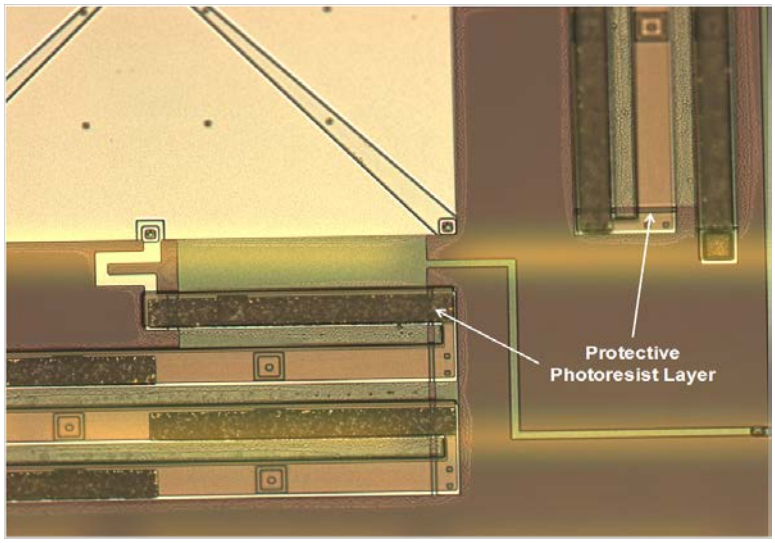

Figure 64: Optical microscope image of a fabricated device in the midst of post-fabrication processing

previous attempts using evaporation. The device in Figure 65 shows one of the few instances where the sputtered bimorph segment survived the release of the device. In this example four of the sixteen bimorph segments can be seen. Three appear to still be

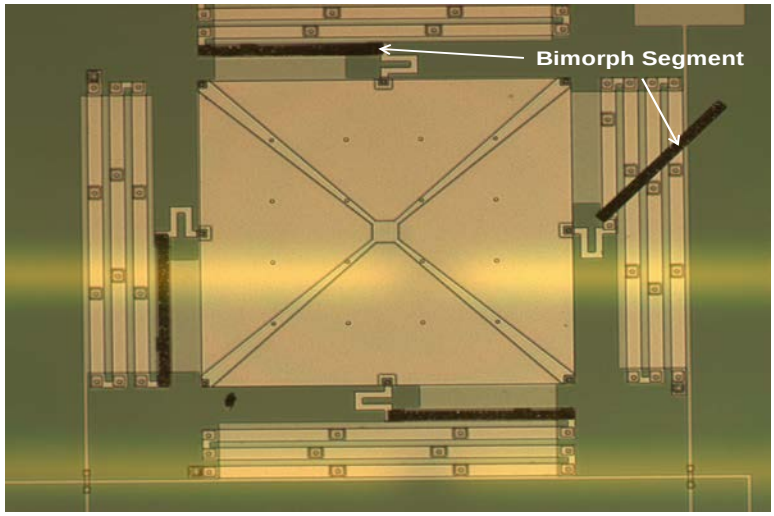

Figure 65: Optical microscope image of a release device, post-processed with sputtered aluminum bimorph segment

attached to the cantilever but one has clearly detached from the cantilever beam, leading to the conclusion that the other bimorph segments also detached and floated away. The

results for the sputtered gold were also similar to those observed in the evaporative process, producing little to no deflection in the assemblies.

4.5 Summary

In this chapter, data results were presented for the evaluation of 15 “zipper” actuator design configurations introduced in this research. Evaluations of these designs were conducted using analytical modeling, finite element modeling, and experimental characterization and testing. Additionally, results from post-fabrication processing attempts were discussed.

5. ANALYSIS

5.1 Chapter Overview

In this chapter, data collected during the evaluation of the “zipper” actuator design and presented in the previous chapter is analyzed. Modeled and fabricated devices operations are discussed, unusual or unexpected observations are explained, and hypothesis as to the causes are provided.

5.2 Analytical Modeling Analysis

5.2.1 Initial Deflections

Two factors were observed to affect the initial deflection during the evaluation of partial-bimorph cantilever beams, the length of the bimorph segment and the temperature variation associated with material depositions. Figure 66 and Figure 67 show graphs for the calculated initial deflection data with a 50º C and a 250º C temperature changes respectively. A full set of calculated initial deflection data is located in APPENDIX E.

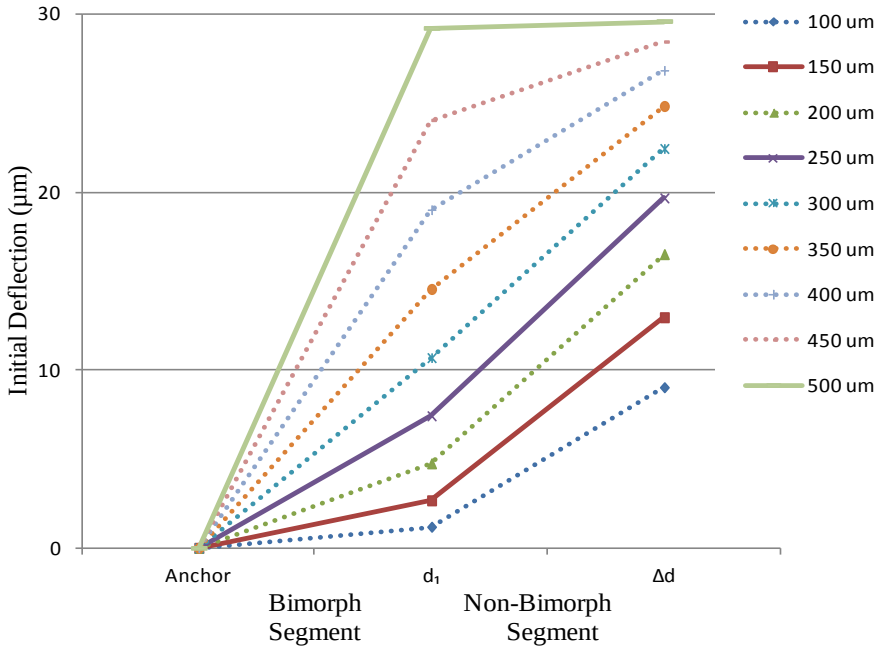

Figure 66: Graph of calculated initial deflection results for a 500 µm partial-bimorph cantilever beam with varied bimorph segments; a temperature change of 50º C, max deflection scale 0 µm 30 µm;

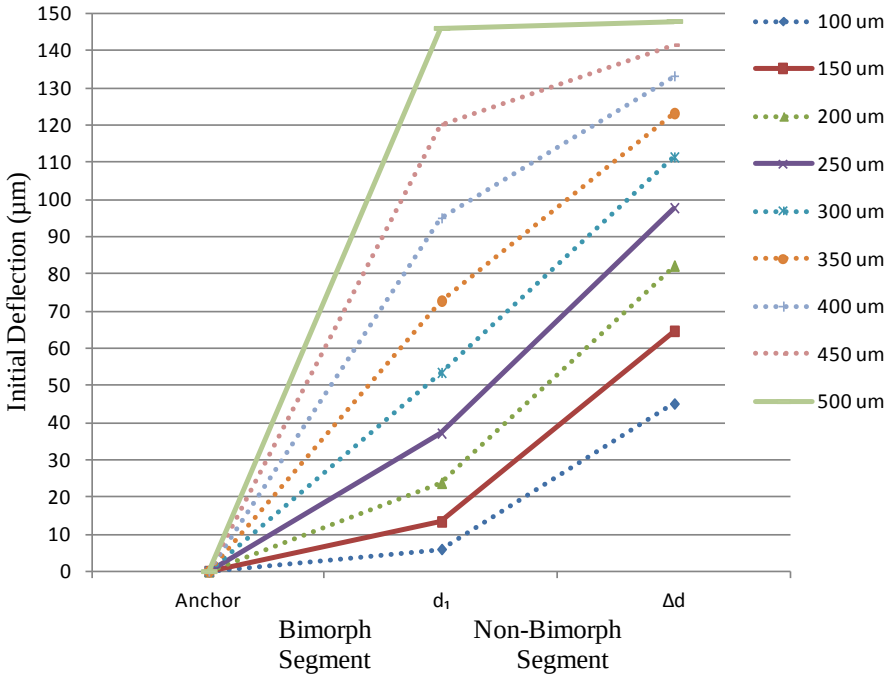

Figure 67: Graph of calculated initial deflection results for a 500 µm partial-bimorph cantilever beam with varied bimorph segments; a temperature change of 250º C, max deflection scale 0 µm to 150 µm

There were a few results from this modeling that are relevant to this research. First, the calculated data verified that longer bimorph segments produce higher deflections in partial-bimorph cantilever beams and second, an increase in the deposition temperature will produce greater deflections in all bimorph segment lengths. Additionally, looking at the data across the six temperatures, the relationship between the bimorph segments with different lengths remains unchanged regardless of the deposition temperature. This proves post-fabrication processing is a viable operational improvement option for these devices.

Another interesting observation was made once fabricated devices were received. The partial-bimorph cantilever beam with a 250 μm bimorph segments and a change in temperature of 50º C (seen in Table 9) produced a total deflection comparable to those

Table 9: Calculated initial deflection results for a 500 μm partial-bimorph cantilever beam with varied bimorph segments and a temperature change of 50º C

Bimorph	Non-Bimorph	d_1	d_2	Δd_1
1.00E-04	4.00E-04	1.19E-06	7.83E-06	9.02E-06
1.50E-04	3.50E-04	2.67E-06	1.03E-05	1.30E-05
2.00E-04	3.00E-04	4.75E-06	1.17E-05	1.65E-05
2.50E-04	2.50E-04	7.42E-06	1.22E-05	1.97E-05
3.00E-04	2.00E-04	1.07E-05	1.17E-05	2.24E-05
3.50E-04	1.50E-04	1.45E-05	1.03E-05	2.48E-05
4.00E-04	1.00E-04	1.90E-05	7.83E-06	2.68E-05
4.50E-04	5.00E-05	2.40E-05	4.40E-06	2.84E-05
4.96E-04	4.00E-06	2.92E-05	3.88E-07	2.96E-05

measured from fabricated devices, approximately 20 μm. It shows that the likely PolyMUMPs® metal deposition occurred around 50º C above room temperature.

5.2.2 Pull-in Voltages

The calculated pull-in voltage data was also affected by the bimorph segment length and the bimorph deposition temperature. The data graphs shown in

Figure 68, Figure 69, and Figure 70 represent the voltage required to achieve pull-in of partial-bimorph cantilever beams with changes in temperature of 10º C, 50º C, and 250º C. As expected, bimorph layers deposited at lower temperatures require much less voltage to achieve pull-in. This is true for all but the smallest bimorph segments because cantilever beam stiffness is directly related to the length of the beam and this model used half of the

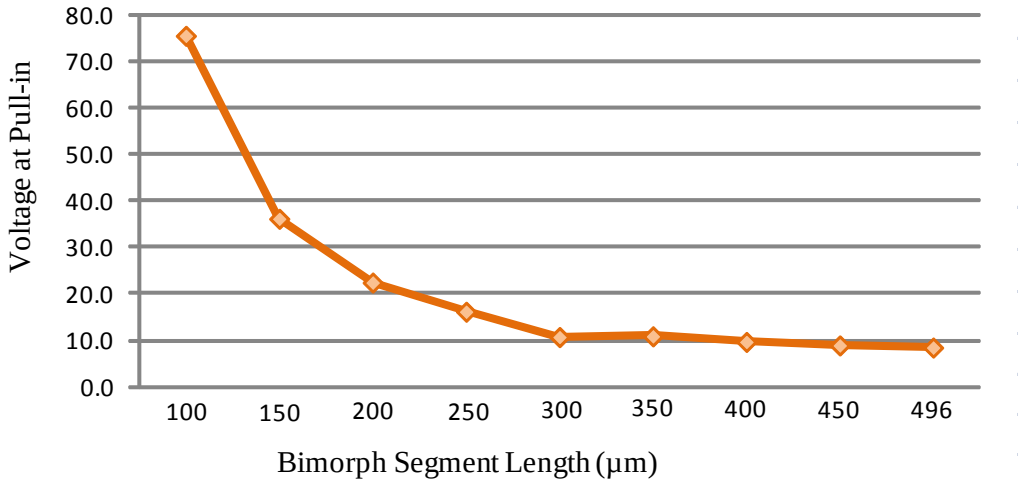

Figure 68: Graphs of calculated pull-in voltages for a 500 µm partial-bimorph cantilever beam with varied bimorph segments, a temperature change of 10º C

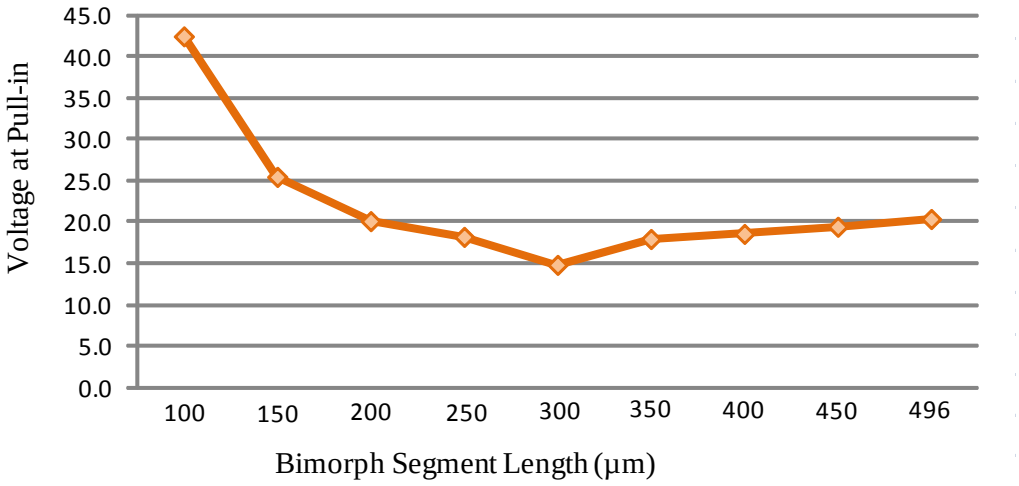

Figure 69: Graphs of calculated pull-in voltages for a 500 µm partial-bimorph cantilever beam with varied bimorph segments, a temperature change of 50º C

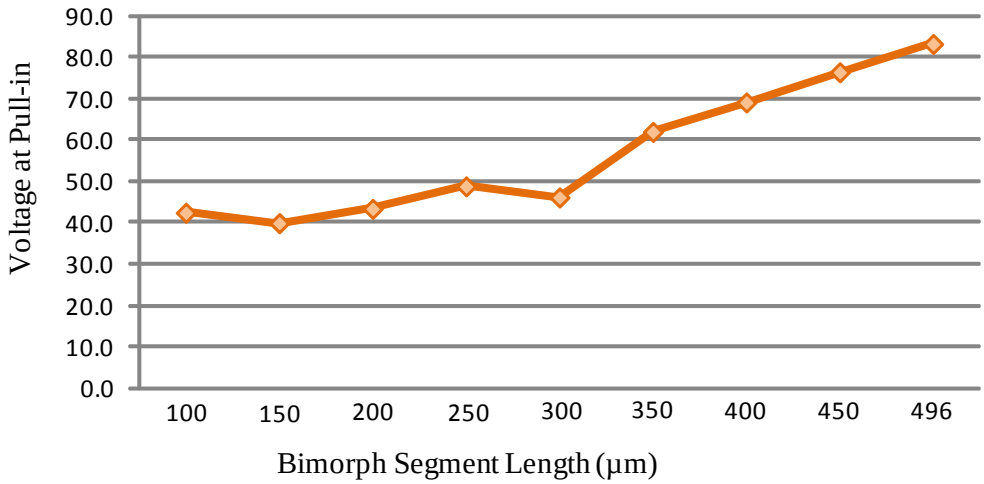

Figure 70: Graphs of calculated pull-in voltages for a 500 µm partial-bimorph cantilever beam with varied bimorph segments, a temperature change of 250º C

bimorph segment length to model a cantilever. For this reason, the small bimorph segments produced little deflection and little change in pull-in voltage requirements. Similar logic explains the reason for such a large swing seen in the partial-cantilever

beams with longer bimorph segments. Like the analytical models for initial deflections, the data for a change in temperature of 50º C (shown in Figure 70(Middle)) matches the data measured from fabricated devices. Given the data calculated using a 10º C change in temperature is below that of fabricated devices, it was excluded from further analysis. The remaining data, available in APPENDIX F, shows a swing of 20 V (for bimorph segments between 150 μm and 300 μm) and 40 V – 60 V (for bimorph segments over 300 μm) across the range of temperatures. Additionally, the partial-bimorph cantilever beams with bimorphs segment lengths of 250 μm and 300 μm experienced the smallest shift in required pull-in voltage across the range of temperatures.

All the modeling calculations point to an optimal bimorph segment length of between 250 μm and 300 μm. These lengths would allow for post-fabrication processing of devices with the least impact of pull-in voltage requirements.

5.3 Finite Element Modeling Analysis

5.3.1 Initial Deflection Using CoventorWare®

Very early into the FEM it was apparent that the angle (relative to the substrate) produced by a deflected odd numbered partial-bimorph cantilever beam (observed at the end of the beam) had a direct effect on the deflection of the following beam. Because the end of the odd beam is connected to the start of the even beam (via a secondary anchor) the even beam must overcome its negative starting position (angle) to achieve a positive deflection. This was most evident in actuators with centered bimorph segments, like the example in Figure 35.

The most interesting finding in this modeling, and arguably most important, occurred once the bimorph segment was modeled at the bottom of the beam. In this configuration the actuator exhibited the desired “zipper” action and produced an interesting reaction in the even numbered beams. Although this beam produced a net negative deflection in the actuator, it brought secondary anchor nearly parallel to the substrate. This acted like a reset which proved vital to the “zipper” function of the actuator, enabling almost 75% of the deflection for odd numbered beams to add to the total deflection of the actuator.

Actuators modeled with increasing bimorph segment lengths proved not to be the most optimal design for this research. While each beam yielded a net gain in deflection between its starting and ending points, the shorter bimorph segment lengths significantly reduce the actuator deflection. Additionally, none of the secondary anchors return to near parallel with the substrate, which required more bimorph segment length in subsequent beams to overcome ever increasing negative angles at the secondary anchors. Given that increasing bimorph segment lengths in an actuator produced less deflection and the complex recalculations required (optimal bimorph segment step size) when the number of beams actuator is changed this design approach was abandoned. All FEM modeling to this point confirmed that maximum deflection of this “zipper” actuator assembly is driven by the number of beams in that system.

The final FEM examined an actuator design with smaller partial-cantilever beam geometries. This ‘space saving’ option reduced the space required for each pair of beams by 15 µm and produce 4 µm less of total system deflection. The additional 15 µm of space (per pair of beams) far outweighs the loss of less than 1µm of deflection per beam.

For every two beams in the actuator, the space saving adjustments allow for an additional beam to be added to the system without increasing the fill-factor. While this adjustment will reduce the maximum initial deflection by approximately 1 μm per beam, the addition of another (odd numbered) partial-bimorph beam adds approximately 19 μm to the system and each pair of beams adds approximately 12 μm. For this reason the 'space saving' geometries were fabricated.

5.4 Characterization and Testing Analysis

Due to the debris of fragmented devices with corrugated design 1, all device characterization and testing was performed on the third and final PolyMUMPs® fabrication run. Even with the additional POLY1/POLY2/VIA overlap on the second fabrication run, devices with corrugated design 1 actuators did not survive the release process. This is likely due to an inefficient VIA adhesion layer, which was not strong enough to withstand the stress introduced by the partial-bimorph cantilever beams.

5.4.1 Initial Deflection Characterization

Figure 71 is a graph showing a sample of the initial deflections of "zipper" actuators with 6-beam, 7-beam, 11-beam, 12-beam, and 22-beam configurations. It shows the linear step deflections of this design as well as an approximate 7 μm deflection gain per beam (14 μm per beam-pair). These observations match the results from the analytical and FEM modeling. Additionally, the R^2 values for the data trendlines show that more beams in the actuator result in a more linear step deflections. It is also clear at which point this trend starts to break down. Devices with less than seven beams in the actuators produce significantly less desirable results. This is mainly due to the connection

at the platform. All devices produce less deflection in the beam attached to the platform. In actuators with few beams this is noticeable because that final beam deflection is a larger percentage of the total deflection.

While on average, the initial deflections of all devices agreed with the modeled results, there was some noticeable variation in deflections of actuators with the same number of beams. It is well known that the slightest variations in deposition temperatures, pressures, humidity, and many other factors can affect the material properties and/or characteristics of the deposited material. This is the likely cause of these variations, given the fact that the 15 (1 cm x 1 cm) PolyMUMPs® fabricated die sites can be produce on as many wafers and use as many depositions per layer.

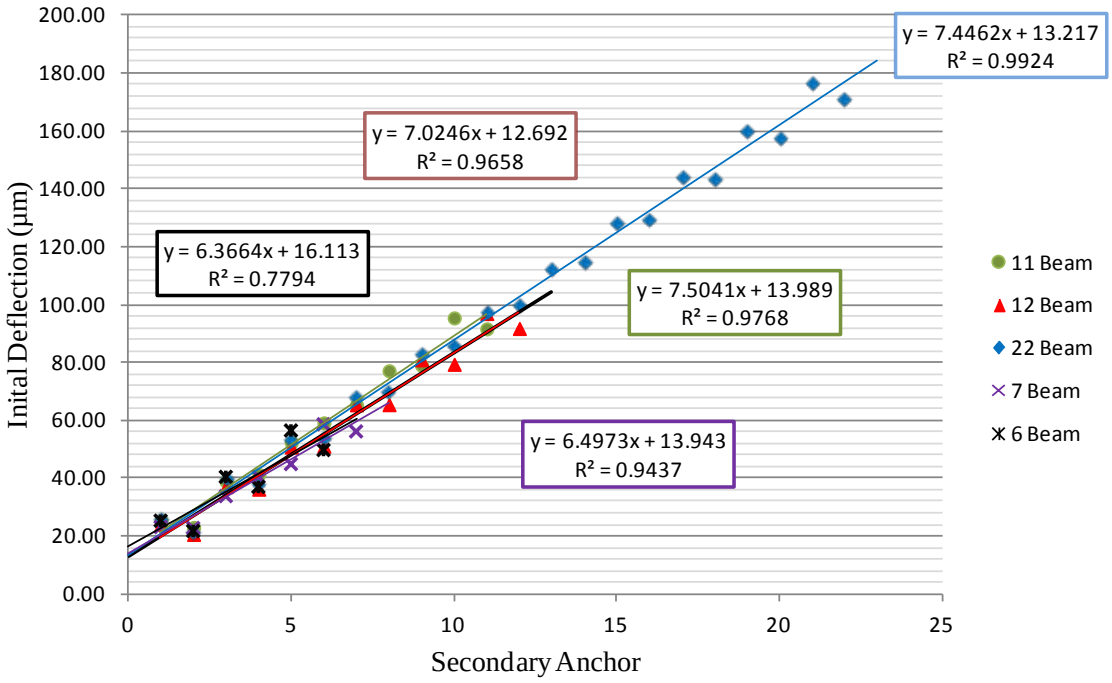

Figure 71: Graph of average initial deflection characterizations for “zipper” actuators

When comparing the corrugated designs to their non-corrugated counterparts they produced 1 μm to 3 μm less deflection. While it is not significant, this is likely a result of the corrugation in the beam. As the bimorph material is also conformal, it is inducing different amounts of stress into the system base on its location on the wave. While the stress from on top of the wave helps the beam to curl upward, the stress from the bottom of the wave causes the beam to curl back downward and cancels some of the deflection.

5.4.2 Pull-in Voltage Testing

With the exception of a few tested actuators, the pull-in responses can be parsed into three categories. In all probability, the causes for the few outliners previously discussed were one or more of the following factors. There could have been something different in the fabrication of that device, it was damaged (either during release or during testing), or there could have been an oxide buildup on the device. All tests were conducted within 12 days of release to minimize the chance for oxide buildup, but it is still possible. Based on the results presented for beams with more than five beams, actuators with this partial-bimorph cantilever geometry will achieve pull-in at/or below 20 v. Although true, that did not translate to an equal amount of micro-mirror platform tilt across the range of "zipper" actuator configurations. Figure 72 shows the micro-mirror deflection results to the second 22-beam actuator tested. This example shows the tilt experienced during actuator pull-in.

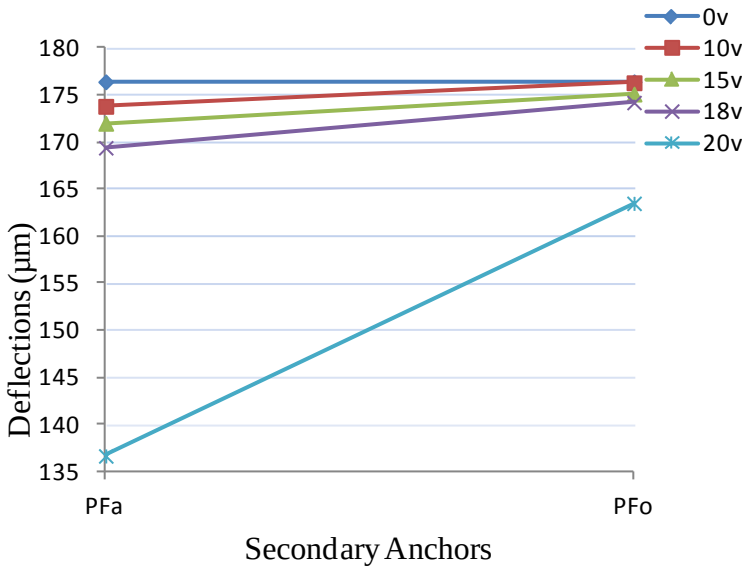

Figure 72: Graph of measured micro-mirror platform deflection results for pull-in test of PolyMUMPs® fabricated 22-beam micro-mirror platform assembly 2; measured on actuation side (PF_a) and side opposite actuation (PF_o)

Actuators with less than five beams produce no tilt in the platform and snapped in, all at the same time. Actuator configurations with six to nine beams produced a maximum deflection difference (tilt deflection, between PF_a and PF_o) of 20 µm, which equated to approximately 3.3º of mechanical tilt. The best results were measured in actuators with more than nine beams. These actuators produced a maximum tilt deflection of 27 µm, or approximately 4.4º. There was a limiting factor observed in all actuators tested, which directly limited the maximum amount of tilt in the assemblies. The likely cause for this is due to a dynamic spring constant of the micro-mirror platform assembly. As one actuator is pulled down, the three others are actively pushing the platform up, which causes the spring constant of the assembly to increases. The test data clearly illustrates the pull-in steps of the actuator, as well as how that actuation affects the platform. However, the dynamic affect of the three other actuators on the pull-in and tilt

of the platform was not immediately apparent. This effect can most easily be observed in the test data graphs. Figure 73 shows the deflection results for a 10-beam actuator. All

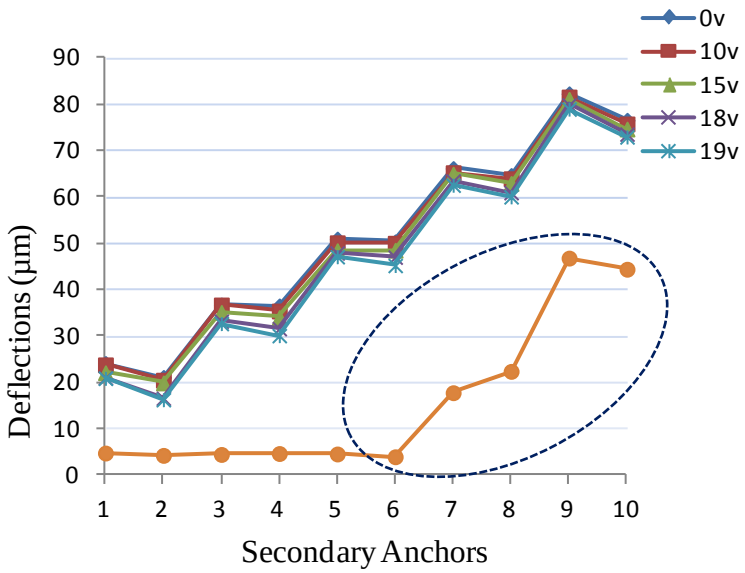

Figure 73: Graph of measured 10-beam "zipper" actuator deflection results for pull-in test of PolyMUMPs® fabricated micro-mirror platform assembly 1, measured at each secondary anchor

tested devices which demonstrated a step pull-in reacted in a similar manner, only a portion of the actuator beams achieved pull-in. The beams nearest the platform remained up. This is due to the stiffness added to the assembly by the other actuators. As the actuated beams pull down on the platform, the beams of the three remaining actuators are pushing the platform up. At some point an equilibrium state is reached, resulting in a maximum tilt deflection from 20 µm to 24 µm (3.3º to 4.4º). Given that the angles produced are very close, it appears that no matter the number of beams in a configuration, the maximum mechanical platform tilt which can be achieved with this design is approximately 4º.

5.5 Post-Fabrication Processing Analysis

Despite best efforts to achieve greater deflections in post-processed devices, this portion of the research was not successful. There were two main contributing factors which hindered post-fabrication processing. It was discovered during the third post-processing attempt that the evaporated aluminum bimorph layer was missing. As the aluminum and chrome adhesion layer are very similar in color it is not definite, but the likely cause for this is that the aluminum was inadvertently etched away. While aluminum etches much slower in 49% hydrofluoric acid (HF) than the doped PolyMUMPs® sacrificial oxide layers, this design required a 15 minute release in HF because of the lack of etch holes in the platform (simulating a pillar/mirror assembly bonded to platform). This extended exposure to HF was sufficient to etch .5 μm of aluminum. Devices with evaporated gold bimorph layers results weren't much better. While the gold survived the release process they did not produce the expected higher deflection, in fact the results were worse than the PolyMUMPs® fabricated devices. Upon further inquiry, it was discovered that AFRL does not possess the capability to evaporate metal at elevated temperatures (i.e. the requested 125º C).

For these reasons, new post-processing procedures were developed for using sputtering deposition techniques. This process yielded similar results. Although some aluminum bimorph segments survived the release most were etched away. It would appear that the protective layer of photoresist used was insufficient. The likely cause for the poor results seen in the sputtered gold devices is that the devices are not being adequately heated during the sputtering process. As most sputter chambers are calibrated for use with 3" – 6" wafers and this research requires metallization of 1 cm x 1cm piece,

the heat measurements are likely not accurately representing the temperature of the devices during metallization.

5.6 Summary

This chapter presented analysis of the data collected during the modeling and evaluation of the “zipper” actuator design. Modeled, fabricated device operations, and post-fabrication results were discussed. Observations were explained and suspected causes for all observations were provided. Conclusions found during this research, the significance of this research, and recommendations for future research are provided in the following chapter.

6. CONCLUSIONS AND RECOMMENDATIONS

6.1 Chapter Overview

This chapter provides a summary of the research conducted on the "zipper" actuator design, the significance of the research, and recommendations for future research on this topic.

6.2 Conclusions of Research

The work presented in this thesis provided the framework for a novel electrostatically driven "zipper" actuator capable of achieving extreme initial deflections with relatively low actuation voltages. This device is intended to be used for the actuation of a micro-mirror platform assembly. Multiple avenues of design characterization were conducted which resulted in the validation of this design as a viable approach to the implementation of a micro-mirror array capable of agile laser beamsteering.

The analytical modeling provided a foundation to evaluate the implementation of different bimorph material layers. These models determined the effects material and/or deposition variations have on the initial deflection and the pull-in voltage requirements of partial-bimorph cantilever beams. Additionally, it showed that partial-bimorph cantilevers with bimorph segments of 50% to 60% of the total beam length will produce the optimal beam deflection, relative to pull-in voltage requirements.

Finite element modeling validated the initial deflections of partial-bimorph cantilever beam and the optimal bimorph segment length calculated during that analytical modeling. It determined that locating the bimorph segment at the bottom of the partial-bimorph cantilever will produce the maximum deflections in the actuator by minimizing

the negative angle observed between beams. FEM showed how stacked partial-bimorph cantilever beams add the deflections of the individual beams and produce higher deflection in the system. Finally, it was used to optimize the geometry to reduce the space requirements of the actuator and proved that" zipper" actuator deflections will not be significantly diminished once incorporated into a micro-mirror platform assembly.

Characterization and testing of fabricated devices verified the results of the analytical and finite element modeling. Although there were variations in the measured data, the assumption is that these variations are due to minor variations in the fabrication process. This proved the vital role fabrication plays in the operation of MEMS devices. Additionally, the measured data showed the liner relationship between the number of partial-bimorph cantilever beam and the maximum deflection of the "zipper" actuator and the voltage required to achieve pull-in of the devices is approximately 20 V, regardless of the number of beams in the actuator. Unfortunately, the additional actuators were observed to have an adverse affect on the ability to pull the platform downward on the actuation side. The additional upward force produced by the un-actuated "zipper" actuators coupled with the rigid actuator-to-platform anchor resulted in all the tested actuators reaching a pull-in equilibrium state long before expected, which produced a dismal 4.4º maximum mechanical tilt of the platform.

Demonstration of the extreme deflection with lower actuation voltage requirements shown in this research illustrates the potential of this novel "zipper" actuation design for agile laser beamsteering micro-mirror array applications, currently of interest to the U.S. Air Force.

6.3 Significance of Research

4-axis tilt, electrostatically driven MEMS micro-mirror arrays, while of particular interest to the U.S. Air Force have possible applications within many other technological industries outside the traditional military applications. The design explored in this research will guide future work toward the realization of an agile MEMS micro-mirror laser beam steering capability. The following are the significant findings of this research which will benefit AFRL research toward the development of an electrostatically driven, large aperture, micro-mirror actuation assembly for high fill-factor, agile optical phase arrays.

The demonstration of the “zipper” actuator design as a suitable structure for the electrostatic actuation of MEMS micro-mirrors.

The demonstration of high-fill factor arrays micro-mirror platform assemblies designed with fill-factors of 95% or better, when implemented with AFRL mirror and pillar assembly.

The demonstration of extreme micro-mirror platform deflections of up to 175 μm with level deflection of platform and low actuation voltages of approximately 20 V is achievable with this design.

The development and validation of analytical models to characterize the deflections achievable from a partial-bimorph cantilever beam and the pull-in voltage requirement associated with that deflection. These models can be used to quickly evaluate the effects of bimorph material and/or deposition variations on the operation of partial-bimorph cantilever beams.

The demonstration of the important role the deposition temperature of the bimorph layer plays in the maximum deflection and the pull-in voltage requirements of a partial bimorph cantilever beam.

The discovery of the adverse affects of the un-actuated “zipper” actuators have on the tilt of the micro-mirror platform.

The demonstration of the ability to bond mirror and pillar assembly to an array of micro-mirror platform actuation assemblies without damage to the platform actuation assemblies or the mirror and pillar assemblies (seen in Figure 74).

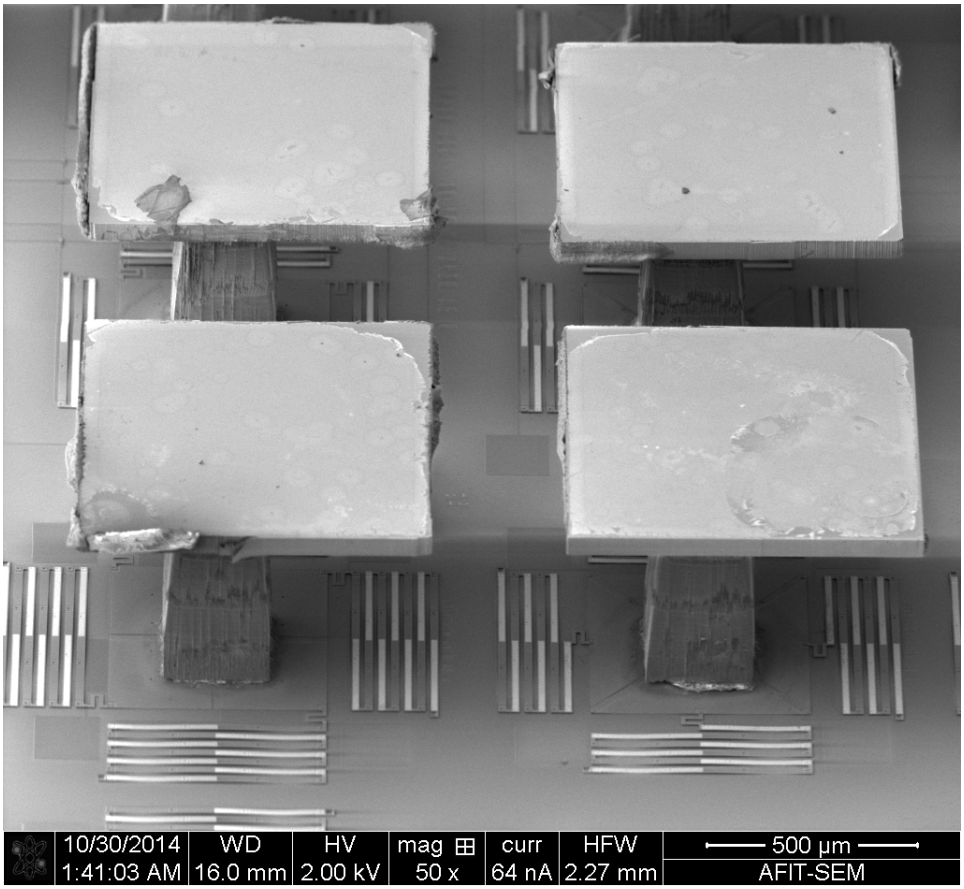

Figure 74: SEM image of AFRL designed and fabricated micro-mirror on pillar, flip bonded onto a 2 x 2 “zipper” actuator array

The demonstration that this “zipper” actuator design is capable of achieving full release and lift the mirror and pillar assembly, once it has been flip bonded to a micro-mirror platform (seen in Figure 75).

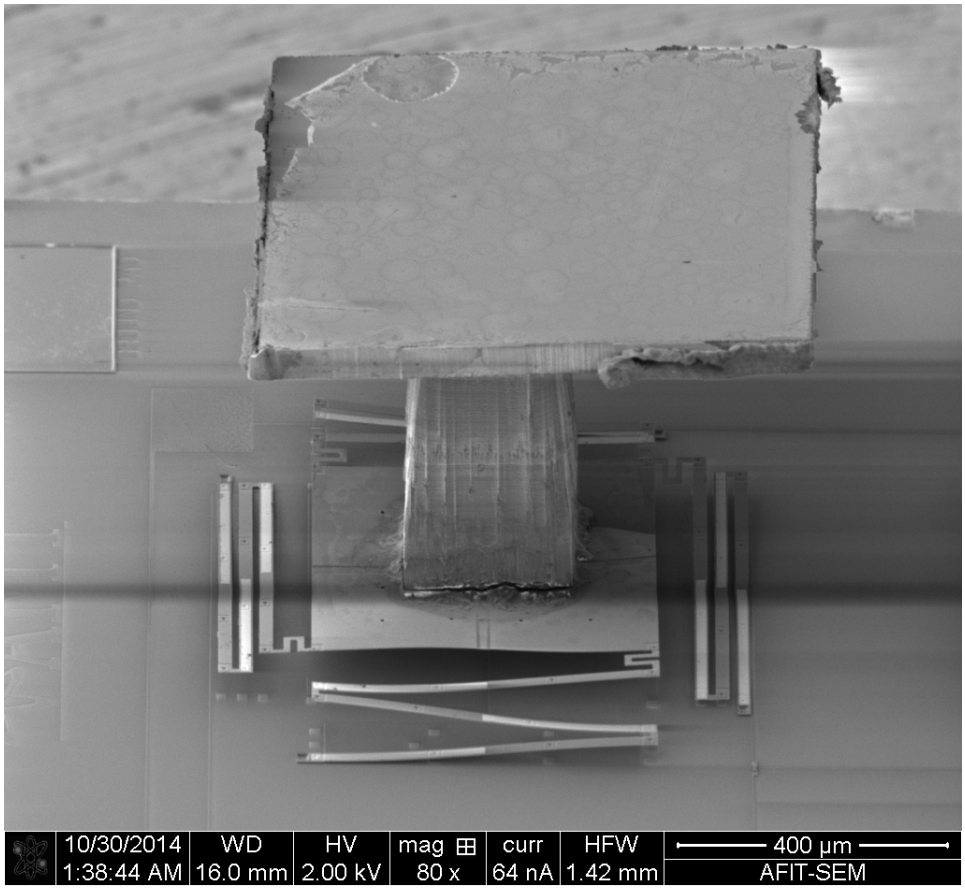

Figure 75: SEM image of AFRL designed and fabricated micro-mirror on pillar, flip bonded onto a 2 x 2 “zipper” actuator array

6.4 Recommendations for Future Research

Unfortunately, due to the time and fabrication constraints of this research full optimization of this “zipper” actuation design could not be accomplished. While a majority of the stated goals for this research were met, further research is needed to optimize the mechanical tilt of the micro-mirror platform in order to reach those goals.

For this reason, the following recommendations for future work are presented based on knowledge gained during this research.

Analytical modeling of static spring constant in micro-mirror platform assembly, as well as the dynamic change in the spring constant of the assembly as the platform is actuated. This will need to be modeled for the pull-in of a single actuator and multiple actuators, as this will likely change the dynamic response in the assembly.

Additional device testing to examine the extent of variation between deflections of devices, initial and during actuation and what fabrication processes steps may be the cause for the observed variations.

Fabrication of devices with 300 μm bimorph segments for comparison to the 250 μm bimorph segments studied in this research.

Further exploration of post-fabrication processing to elevate the issues identified in this research. Specifically, explore the deposition technique used in this research to identify possible cause and make adjustments which will increase sample temperature. Additionally, explore different back etch techniques in an effort to protect aluminum bimorph layer during device release.

Research and development of a better actuator-to-platform anchor, which would allow for more flexibility in the joint and ultimately produce more platform tilt. Maybe a hinge or pair of hinges which operate like a U-joint type mechanism.

Examine the possible use of a piezoelectric material for the bimorph segment in a partial-bimorph cantilever beam or in addition to a bimorph segment. This could provide a piezo-assist to the pull-in of the beam and/or add a position sensing capability to the device.

6.5 Summary

This chapter concluded this research by highlighting the conclusions and the significance of this research, and providing recommendations for future research topics.

APPENDIX A. Additional Background: Photolithography

In microfabrication, the term photolithography refers to a process which consists of five basic steps used to transfer device layer patterns to a photosensitive material called photoresist by means of selective exposure to a radiation source such as ultraviolet (UV) light [78]. Using a spinner, a wafer is prepared (cleaned) and a layer of photoresist is applied. Next, the wafer is softbaked to set the photoresist and ensure all excess liquid is removed. At this point the photoresist is masked with the desired pattern and exposed to a radiation source, using a system like the one depicted in Figure 76. In this example

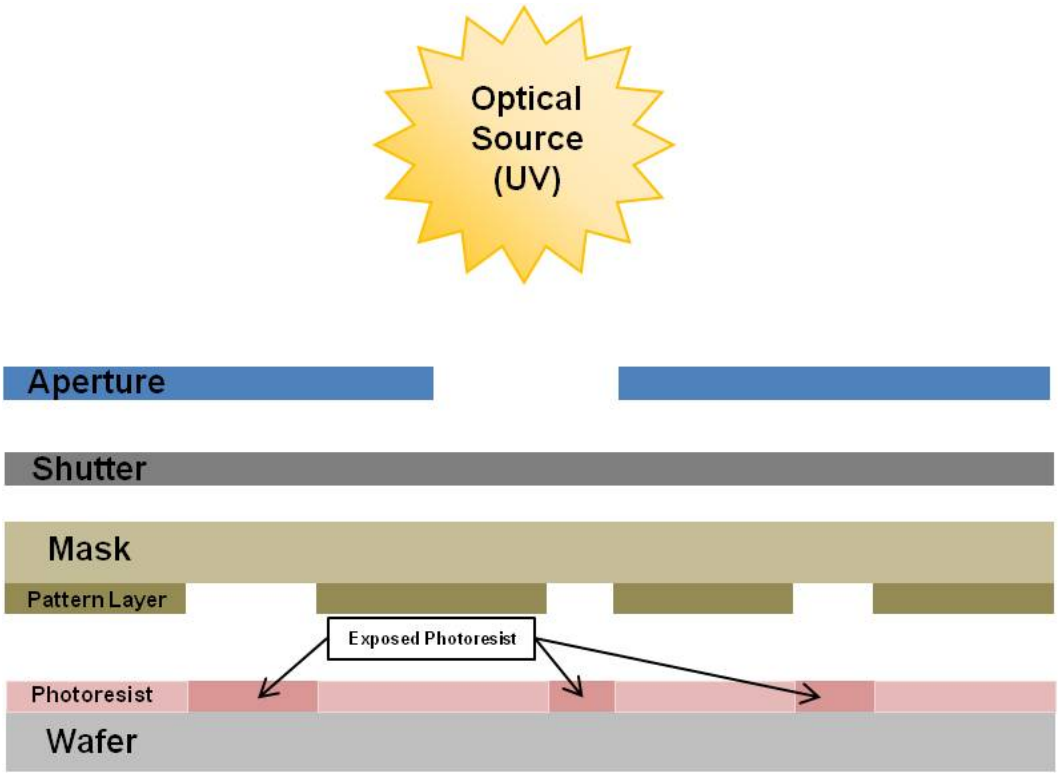

Figure 76: Diagram of simple photolithography system

the shutter is removed allowing UV light to pass through the open areas of the mask pattern layer, which transfers the pattern to the photoresist. Once exposed, the unwanted photoresist is developed away leaving the desired pattern in the photoresist. The final step is to hard bake the wafer, which further hardens the photoresist and removes any remaining liquid [15].

Photoresist is a material that undergoes a physical change, on the molecular level, when exposed to UV light. There are many types of photoresists but they are parsed into two categories, based on how they respond to UV exposure. Positive photoresists are polymers with strong molecular bonds; exposure to UV light breaks down the chemical bond, weakening it, making the exposed area soluble. So when using a positive photoresist, what is visible through the mask pattern layer (Figure 76) is removed during the development step. Negative photoresist is the inverse of positive photoresist. It is a polymer with weak molecular bond. When exposed to UV light long chains of molecules are formed, making the polymer much more robust [78]. This means the area visible through the mask pattern layer (Figure 76) remains.

Once the unwanted photoresist is developed away, leaving the pattern to be transferred, the device layer is manufactured. This is accomplished either though an additive process (material growth or deposition) or a subtractive process (etching).

APPENDIX B. Additional Background: Pattern Transfer

The fabrication of a MEMS device happens layer by layer. For each layer one or more photolithography masks are used to define device features. After each photolithography step, in order to construct three dimensional structures, the device wafer will either undergo the addition or the removal of material [16].

To add material, it must be grown or deposited. To grow a layer of material a gas, a mixture of gasses, or materials evaporated into a gaseous form are flowed over the substrate wafer. In doing this, layers of atoms settle and bond to the wafer, stacking up until the desired device layer thickness is reached. Using slightly different processes, this can produce amorphous layers, polycrystalline, or monocrystalline layers. A monocrystalline epitaxial growth is shown in Figure 77.

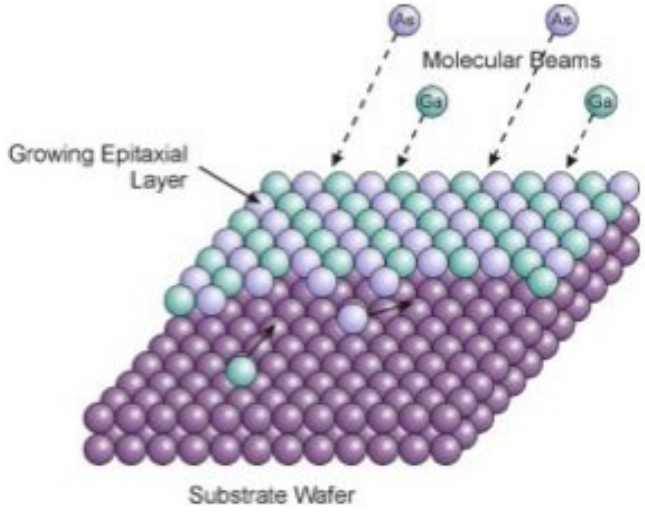

Figure 77: Molecular beam epitaxial (MBE) growth of gallium-arsenide (GaAs) on a substrate [79]

In addition to material growth, physical deposition of material can be used to add material to the layer as well. This is accomplished either through the evaporation of the target material or a process called sputtering. Evaporative deposition is one of the oldest methods for depositing films. Much like the growing process described above, it starts with the heating of the target to the point of vaporization [80]. Figure 78(a) is an illustration of a generalized evaporation deposition process showing how, rather than flowing the material across the substrate as seen in the growth method, the material is allowed to naturally settle onto the wafer. Because of the 'straight' path of the target material's atoms, this process produces a non-conformal deposition layer. On the other hand, the simplified sputtering method, shown in Figure 78(b), is a process by which the target material is bombarded by energetic ions, usually argon [80]. When the high-energy

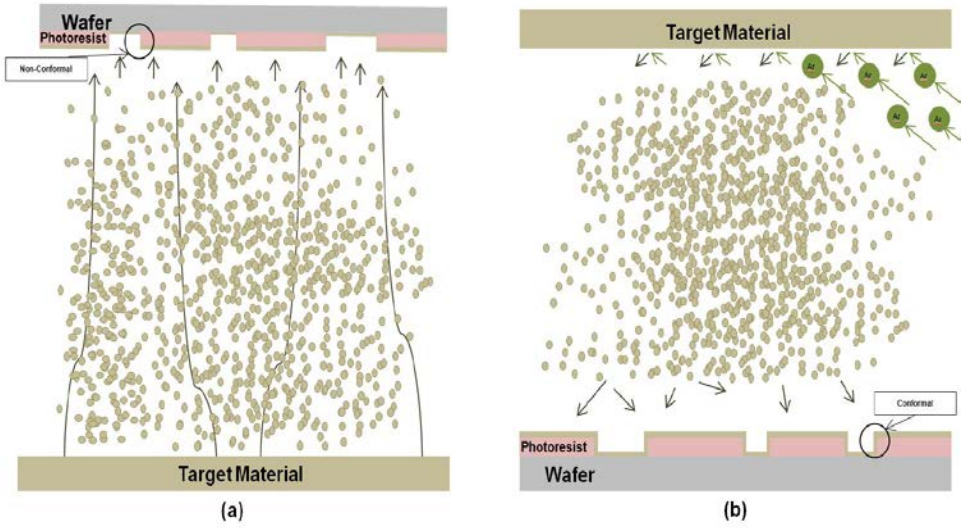

Figure 78: Simplified material deposition methods; (a) Evaporation, (b) Sputtering

ions impact the target, there is a ballistic exchange of momentum, which knocks the target atoms free. The kinetic energy generated from that initial exchange results in many

other collisions between atoms as they move toward the wafer. This means that those target atoms are deposited onto the wafer from every angle, resulting in a conformal deposition layer.

Subtracting material is another way to produce three-dimensional features in a device layer. There are many ways this can be accomplished, but they all fall into one of two categories. They are either a dry etch method, in which material is removed by causing physical damage, a wet etch method which removes material through a chemical reaction, or some combination of both [15]. These methods are all referred to as etching. Figure 79 is a simplified example of an etching process to illustrate how etching a portion of a device layer, regardless of etching method used, will produce three dimensional

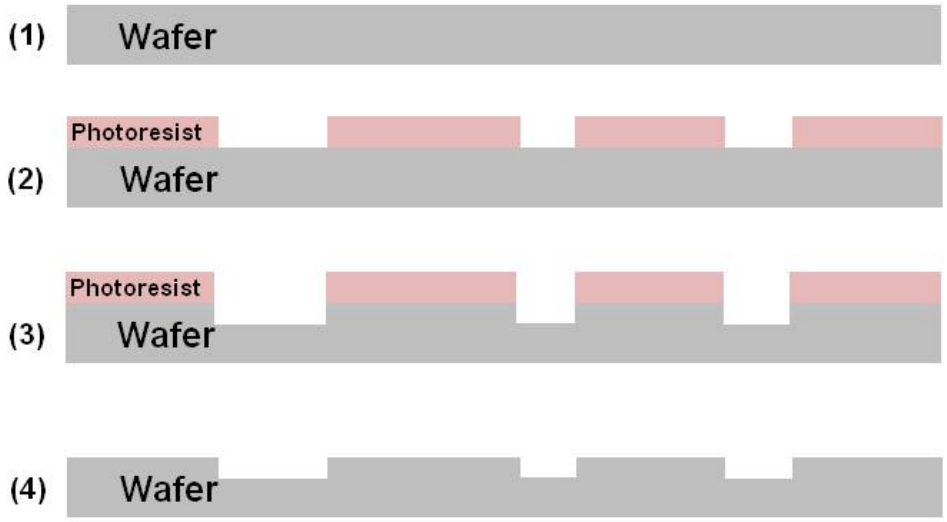

Figure 79: Cross-sectional view of a simplified etch process for one device layer: (1) cleaned wafer substrate, (2) photoresist layer applied, patterned, exposed, and developed (3) source wafer etched, (4) photoresist layer removed to reveal device layer etch profile

features in that layer. The photoresist layer in step (2) is the result of photolithography process and is used to protect the area of the wafer which is not to be etched. Step (3)

shows how the photoresist, chosen to withstand the particular etchant method to be used, protects areas of the wafer while allowing the removal of material from the exposed areas. In step (4) the remaining photoresist has been removed. At this point in the fabrication and as long as additional device layers are required, this photolithography process would repeat.

APPENDIX C. Post PolyMUMPs™ Fabrication Process Follower: Evaporation

Post-Fabrication Processing of PolyMUMPs™ Devices (Evaporative Deposition & Lift-Off) (1 of 2)			
Initials	**Process Step**	**Notes**	**Date/ Time**
	Remove PolyMUMPs™ Protective Photoresist Layer (Solvent Hood) □ Submerge sample in Acetone • Soak for 25-30 minutes (Agitate sample every 3-5 minutes)	**Start Date** **Start Time**	
	Cleaning of Sample (Solvent Hood) □ Rinse/spin (500 rpm) with Acetone, Methanol, and DI water (30 sec ea) □ Dry with Nitrogen □ Inspect sample using Optical Microscope; repeat as necessary □ Bake at 110°C for 2 min		
	1818 Photoresist (Solvent Hood) □ Flood wafer with 1818 photoresist using dropper □ Spin wafer for 30 sec at 4,000 rpm; Ramp at 200 rpm/sec □ Bake wafer on hot plate for 75 sec at 110°C		
	Cleaning of Mask (Solvent Hood) □ Rinse with Acetone for 30 sec □ Rinse with Methanol for 30 sec □ Rinse with De-Ionized (DI) water for 30 sec □ Dry with Nitrogen on Texwipes		
	Alignment & Exposure (MJB-3 Mask Aligner) □ Align mask and Sample in x, y, and theta directions □ Expose for 7 sec		
	Developing of Photoresist (Base Hood) □ Place sample on spinner (500 rpm) spray with 351 Developer (45 sec) □ Rinse sample with DI water for approx. 30 sec □ Dry with nitrogen on Texwipes		
	Inspection of Lithographic Process (Optical Microscope) □ How is the alignment? Focus on the smallest features. □ Are the features clean and open with sharp definition? □ If necessary, strip photoresist using acetone or re-develop		
	Pre-metallization Cleaning (Plasma Asher) □ Place wafer in O_2 Plasma Asher for 2 min at 75 W (default setting)		
	Contact Cleanroom Technician to schedule metallization **Evaporation Criteria:** **Adhesion Layer** **Bimorph Layer**		
	Metal Lift-off □ Adhere Scotch tape to wafer and pull metal from surface		

Post-Fabrication Processing of PolyMUMPs™ Devices (Evaporative Deposition & Lift-Off) (2 of 2)			
Initials	**Process Step**	**Notes**	**Date/ Time**
	Ultrasonic (AS NEEDED) □ Place sample in a Petri dish and place the dish in ultrasonic bath □ Using a beaker, fill the bath with water until the Petri dish floats □ Submerge the sample in acetone (in Petri dish) □ Ultrasonic for approximately 3-5 min; continue longer if needed □ Rinse/spin (500 rpm) with acetone, methanol, and DI water (30 sec ea) □ Dry with nitrogen		
	Device Release (Acid Hood) □ Submerge sample in 49% Hydrofluoric acid (49% HF) • Soak for 15 minutes *(Use sample holder if available)* □ Submerge sample in 3-Stage Methanol Dip (1-2 min each stage) □ Place sample in transport beaker, submerged in Methanol		
	CO_2 Dry (Breezeway) □ Place sample in drying chamber *(Use sample holder if available)* □ Fill chamber with enough Methanol to cover sample □ Close chamber and run dry cycle		
		Finish Date Finish Time	

APPENDIX D. Post PolyMUMPs™ Fabrication Process Follower: Sputtering

Post-Fabrication Processing of PolyMUMPs™ Devices (Sputter Deposition & Back Etch) (1 of 3)			
Initials	**Process Step**	**Notes**	**Date/ Time**
	Remove PolyMUMPs™ Protective Photoresist Layer (Solvent Hood) □ Submerge sample in Acetone • Soak for 25-30 minutes (Agitate sample every 3-5 minutes)	**Start Date** **Start Time**	
	Remove PolyMUMPs™ Gold (Au) Layer (Acid Hood) □ Submerge sample in Gold Etchant • Soak for 1-2 min □ Rinse with De-Ionized (DI) water for 30 sec		
	Remove PolyMUMPs™ Chrome (Cr) Adhesion Layer (Acid Hood) □ Submerge sample in Nicrome • Soak for 30 sec (≈200Å) □ Rinse with De-Ionized (DI) water for 30 sec		
	Pre-metallization Cleaning (Plasma Asher) □ Place wafer in O_2 Plasma Asher for 2 min at 75 W (default setting)		
	Contact Cleanroom Technician to schedule metallization **Sputter Criteria:** **Adhesion Layer** **Bimorph Layer**		
	HMDS Photoresist Adhesion Layer (Solvent Hood) □ Flood wafer with HMDS using dropper □ Spin wafer for 30 sec at 4,000 rpm; Ramp at 200 rpm/sec □ Bake wafer on hot plate for 75 sec at 110°C		
	1818 Photoresist (Solvent Hood) □ Flood wafer with 1818 photoresist using dropper □ Spin wafer for 30 sec at 4,000 rpm; Ramp at 200 rpm/sec □ Bake wafer on hot plate for 2 min at 110°C		
	Cleaning of Mask 1 (Solvent Hood) □ Rinse with Acetone for 30 sec □ Rinse with Methanol for 30 sec □ Rinse with De-Ionized (DI) water for 30 sec □ Dry with Nitrogen on Texwipes		
	Alignment & Exposure (MJB-3 Mask Aligner) □ Align mask and Sample in x, y, and theta directions □ Expose for 7 sec		
	Developing of Photoresist (Base Hood) □ Place sample on spinner (500 rpm) spray with 351 Developer (45 sec) □ Rinse sample with DI water for approx. 30 sec □ Dry with nitrogen on Texwipes		

Post-Fabrication Processing of PolyMUMPs™ Devices (Sputter Deposition & Back Etch) (2 of 3)			
Initials	**Process Step**	**Notes**	**Date/ Time**
	Inspection of Lithographic Process (Optical Microscope) □ How is the alignment? Focus on the smallest features. □ Are the features clean and open with sharp definition? □ If necessary, strip photoresist using acetone or re-develop		
	Back Etch Bimorph and Adhesions Layers (Acid Hood) □ ***GOLD***--Submerge sample in Gold Etchant (1-2 min) □ Rinse with De-Ionized (DI) water for 30 sec □ ***ALUMINUM***--Heat Al etchant to >60° C; Submerge for 20 sec (125Å per sec) □ Rinse with De-Ionized (DI) water for 30 sec □ ***Chrome***--Submerge sample in Nicrome (30 sec) (400Å per min) □ Rinse with De-Ionized (DI) water for 30 sec		
	Remove Photoresist Layer (Solvent Hood) □ Submerge sample in Acetone (2-3 min) • Agitate sample □ Rinse with Acetone for 30 sec □ Rinse with Methanol for 30 sec □ Rinse with De-Ionized (DI) water for 30 sec □ Dry with Nitrogen on Texwipes		
	HMDS Photoresist Adhesion Layer (Solvent Hood) □ Flood wafer with HMDS using dropper □ Spin wafer for 30 sec at 4,000 rpm; Ramp at 200 rpm/sec □ Bake wafer on hot plate for 75 sec at 110°C		
	1818 Photoresist (Solvent Hood) □ Flood wafer with 1818 photoresist using dropper □ Spin wafer for 30 sec at 4,000 rpm; Ramp at 200 rpm/sec □ Bake wafer on hot plate for 2 min at 110°C		
	Cleaning of Mask 2 (Solvent Hood) □ Rinse with Acetone for 30 sec □ Rinse with Methanol for 30 sec □ Rinse with De-Ionized (DI) water for 30 sec □ Dry with Nitrogen on Texwipes		
	Alignment & Exposure (MJB-3 Mask Aligner) □ Align mask and Sample in x, y, and theta directions □ Expose for 7 sec		
	Developing of Photoresist (Base Hood) □ Place sample on spinner (500 rpm) spray with 351 Developer (45 sec) □ Rinse sample with DI water for approx. 30 sec □ Dry with nitrogen on Texwipes		
	Inspection of Lithographic Process (Optical Microscope) □ How is the alignment? Focus on the smallest features. □ Are the features clean and open with sharp definition? □ If necessary, strip photoresist using acetone or re-develop		

Post-Fabrication Processing of PolyMUMPs™ Devices (Sputter Deposition & Back Etch) (3 of 3)			
Initials	**Process Step**	**Notes**	**Date/ Time**
	Device Release (Acid Hood) □ Submerge sample in 49% Hydrofluoric acid (49% HF) • Soak for 15 minutes *(Use sample holder if available)* □ Submerge sample in 3-Stage Methanol Dip (1-2 min each stage) □ Place sample in transport beaker, submerged in Methanol		
	Remove Photoresist Layer (Solvent Hood) □ Submerge sample in Acetone (2-3 min) • DO NOT Agitate sample □ Submerge sample in Methanol • For Transfer to CO_2 Dryer		
	CO_2 Dry (Breezeway) □ Place sample in drying chamber *(Use sample holder if available)* □ Fill chamber with enough Methanol to cover sample □ Close chamber and run dry cycle		
		Finish Date Finish Time	

APPENDIX E. Analytical Modeling Data Tables and Graphs: Bimorph Cantilever Beam Initial Deflections

Table 10: Calculated initial deflection results for a 500 µm partial-bimorph cantilever beam with varied bimorph segments and a temperature change of 10° C

Bimorph	Non-Bimorph	d_1	d_2	Δd_1
1.00E-04	4.00E-04	2.37E-07	1.57E-06	1.80E-06
1.50E-04	3.50E-04	5.34E-07	2.06E-06	2.59E-06
2.00E-04	3.00E-04	9.49E-07	2.35E-06	3.30E-06
2.50E-04	2.50E-04	1.48E-06	2.45E-06	3.93E-06
3.00E-04	2.00E-04	2.14E-06	2.35E-06	4.49E-06
3.50E-04	1.50E-04	2.91E-06	2.06E-06	4.96E-06
4.00E-04	1.00E-04	3.80E-06	1.57E-06	5.36E-06
4.50E-04	5.00E-05	4.81E-06	8.81E-07	5.69E-06
4.96E-04	4.00E-06	5.84E-06	7.77E-08	5.92E-06

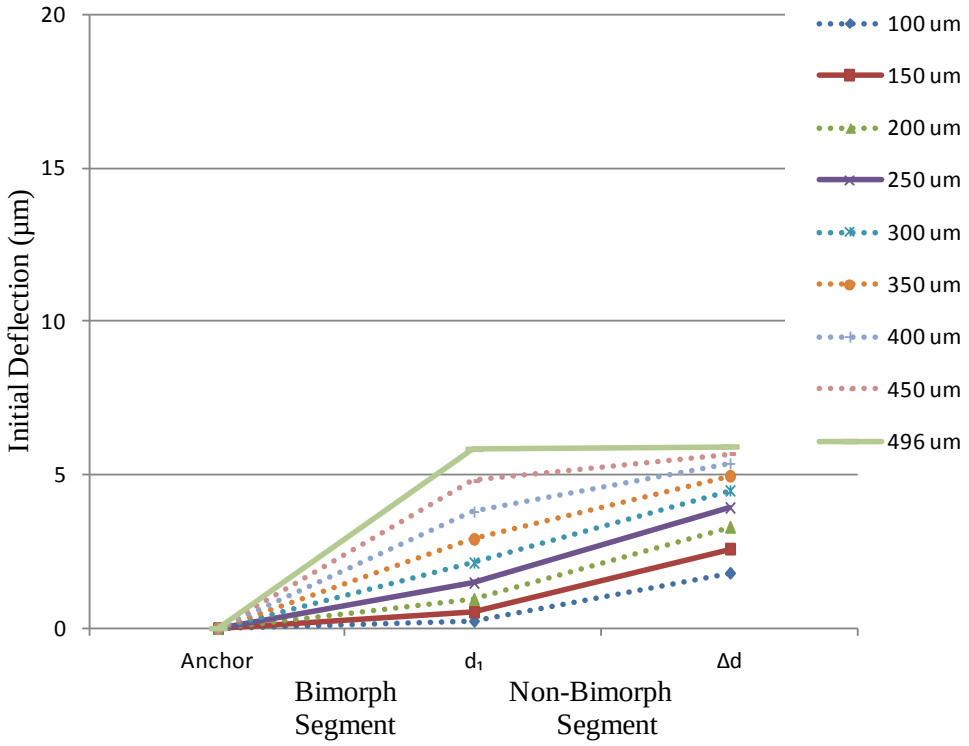

Figure 80: Graph of calculated initial deflection results for a 500 µm partial-bimorph cantilever beam with varied bimorph segments and a temperature change of 10° C

Table 11: Calculated initial deflection results for a 500 µm partial-bimorph cantilever beam with varied bimorph segments and a temperature change of 50° C

Bimorph	Non-Bimorph	d_1	d_2	Δd_1
1.00E-04	4.00E-04	1.19E-06	7.83E-06	9.02E-06
1.50E-04	3.50E-04	2.67E-06	1.03E-05	1.30E-05
2.00E-04	3.00E-04	4.75E-06	1.17E-05	1.65E-05
2.50E-04	2.50E-04	7.42E-06	1.22E-05	1.97E-05
3.00E-04	2.00E-04	1.07E-05	1.17E-05	2.24E-05
3.50E-04	1.50E-04	1.45E-05	1.03E-05	2.48E-05
4.00E-04	1.00E-04	1.90E-05	7.83E-06	2.68E-05
4.50E-04	5.00E-05	2.40E-05	4.40E-06	2.84E-05
4.96E-04	4.00E-06	2.92E-05	3.88E-07	2.96E-05

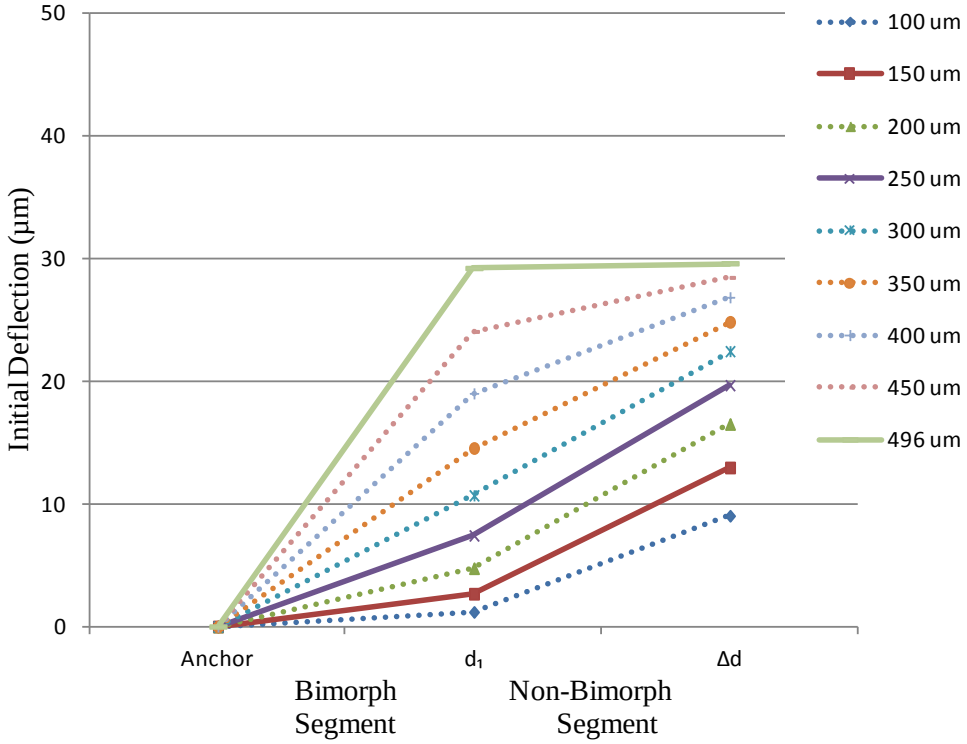

Figure 81: Graph of calculated initial deflection results for a 500 µm partial-bimorph cantilever beam with varied bimorph segments and a temperature change of 50° C

Table 12: Calculated initial deflection results for a 500 µm partial-bimorph cantilever beam with varied bimorph segments and a temperature change of 100º C

Bimorph	Non-Bimorph	d_1	d_2	Δd_1
1.00E-04	4.00E-04	2.37E-06	1.57E-05	1.80E-05
1.50E-04	3.50E-04	5.34E-06	2.06E-05	2.59E-05
2.00E-04	3.00E-04	9.49E-06	2.35E-05	3.30E-05
2.50E-04	2.50E-04	1.48E-05	2.44E-05	3.93E-05
3.00E-04	2.00E-04	2.14E-05	2.34E-05	4.48E-05
3.50E-04	1.50E-04	2.91E-05	2.05E-05	4.96E-05
4.00E-04	1.00E-04	3.80E-05	1.56E-05	5.36E-05
4.50E-04	5.00E-05	4.81E-05	8.77E-06	5.68E-05
4.96E-04	4.00E-06	5.84E-05	7.72E-07	5.92E-05

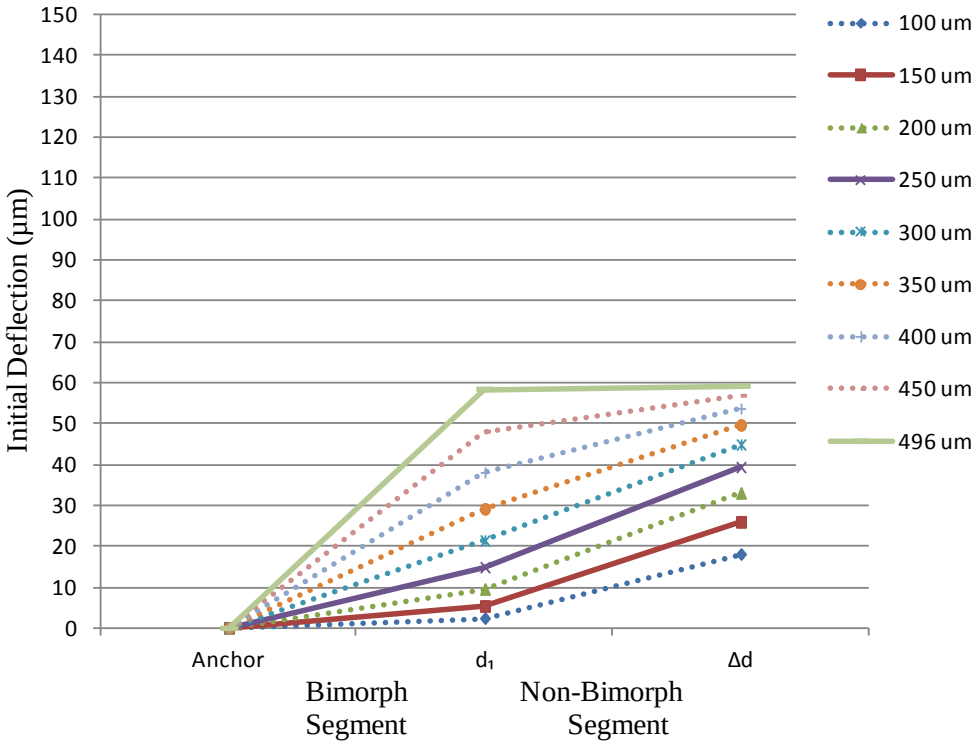

Figure 82: Graph of calculated initial deflection results for a 500 µm partial-bimorph cantilever beam with varied bimorph segments and a temperature change of 100º C

Table 13: Calculated initial deflection results for a 500 µm partial-bimorph cantilever beam with varied bimorph segments and a temperature change of 150° C

Bimorph	Non-Bimorph	d_1	d_2	Δd_1
1.00E-04	4.00E-04	3.56E-06	2.35E-05	2.70E-05
1.50E-04	3.50E-04	8.01E-06	3.08E-05	3.88E-05
2.00E-04	3.00E-04	1.42E-05	3.52E-05	4.94E-05
2.50E-04	2.50E-04	2.23E-05	3.66E-05	5.88E-05
3.00E-04	2.00E-04	3.20E-05	3.51E-05	6.71E-05
3.50E-04	1.50E-04	4.36E-05	3.06E-05	7.42E-05
4.00E-04	1.00E-04	5.70E-05	2.33E-05	8.02E-05
4.50E-04	5.00E-05	7.21E-05	1.31E-05	8.52E-05
4.96E-04	4.00E-06	8.76E-05	1.15E-06	8.87E-05

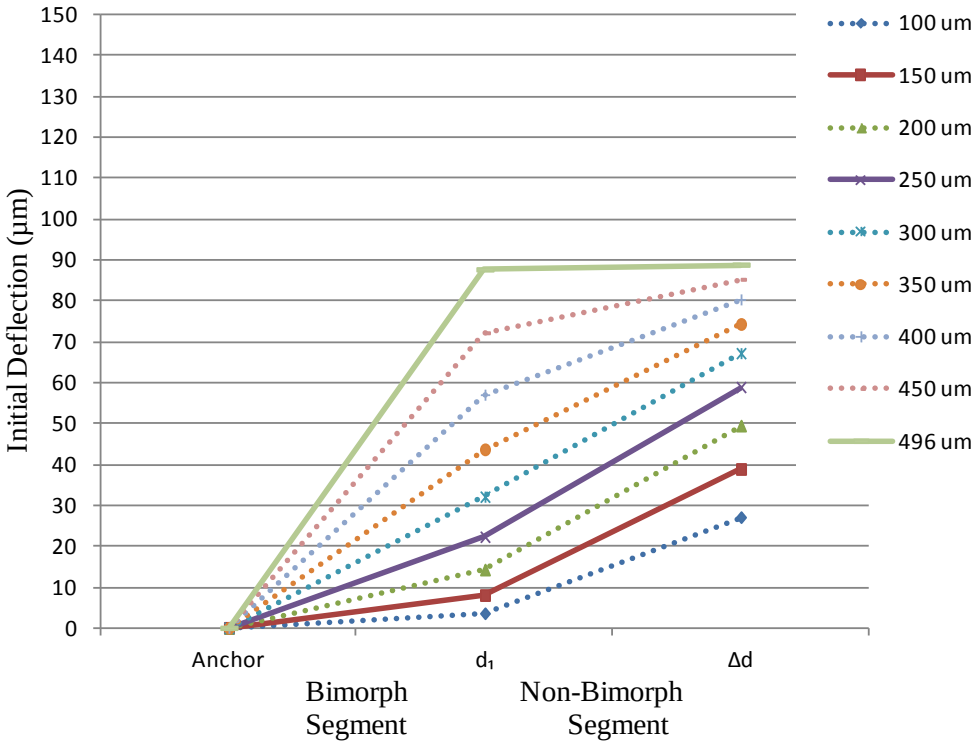

Figure 83: Graph of calculated initial deflection results for a 500 µm partial-bimorph cantilever beam with varied bimorph segments and a temperature change of 150° C

Table 14: Calculated initial deflection results for a 500 µm partial-bimorph cantilever beam with varied bimorph segments and a temperature change of 200º C

Bimorph	Non-Bimorph	d_1	d_2	Δd_1
1.00E-04	4.00E-04	4.75E-06	3.13E-05	3.60E-05
1.50E-04	3.50E-04	1.07E-05	4.10E-05	5.17E-05
2.00E-04	3.00E-04	1.90E-05	4.68E-05	6.58E-05
2.50E-04	2.50E-04	2.97E-05	4.86E-05	7.83E-05
3.00E-04	2.00E-04	4.27E-05	4.66E-05	8.93E-05
3.50E-04	1.50E-04	5.82E-05	4.06E-05	9.88E-05
4.00E-04	1.00E-04	7.60E-05	3.08E-05	1.07E-04
4.50E-04	5.00E-05	9.61E-05	1.73E-05	1.13E-04
4.96E-04	4.00E-06	1.17E-04	1.52E-06	1.18E-04

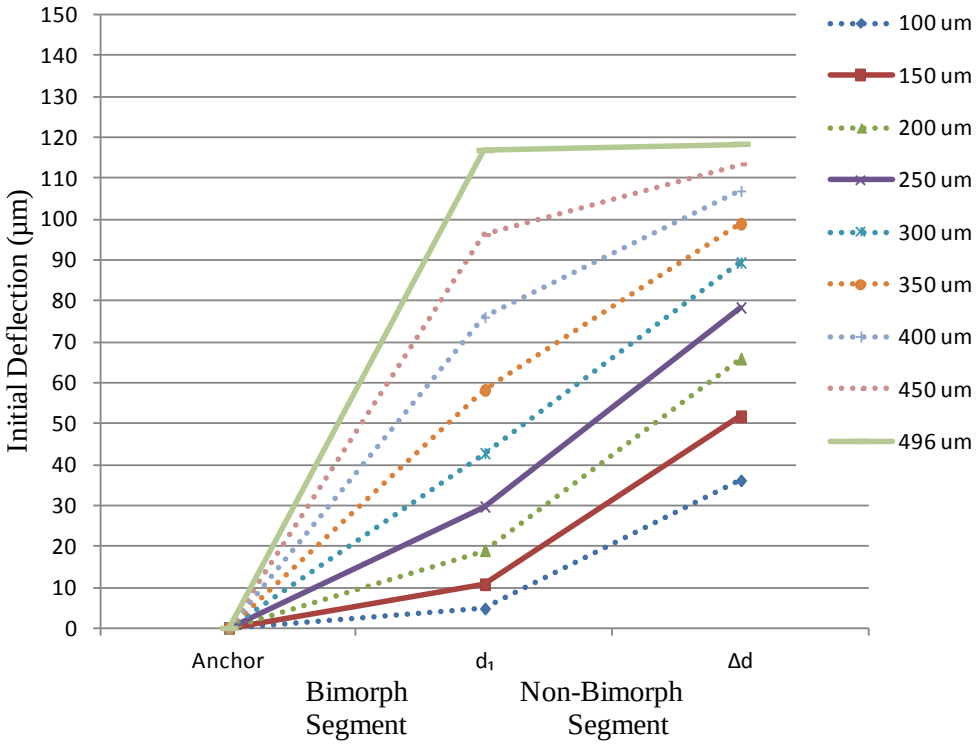

Figure 84: Graph of calculated initial deflection results for a 500 µm partial-bimorph cantilever beam with varied bimorph segments and a temperature change of 200º C

Table 15: Calculated initial deflection results for a 500 µm partial-bimorph cantilever beam with varied bimorph segments and a temperature change of 250º C

Bimorph	Non-Bimorph	d_1	d_2	Δd_1
1.00E-04	4.00E-04	5.93E-06	3.91E-05	4.50E-05
1.50E-04	3.50E-04	1.34E-05	5.12E-05	6.46E-05
2.00E-04	3.00E-04	2.37E-05	5.84E-05	8.21E-05
2.50E-04	2.50E-04	3.71E-05	6.06E-05	9.77E-05
3.00E-04	2.00E-04	5.34E-05	5.79E-05	1.11E-04
3.50E-04	1.50E-04	7.27E-05	5.04E-05	1.23E-04
4.00E-04	1.00E-04	9.49E-05	3.82E-05	1.33E-04
4.50E-04	5.00E-05	1.20E-04	2.13E-05	1.41E-04
4.96E-04	4.00E-06	1.46E-04	1.87E-06	1.48E-04

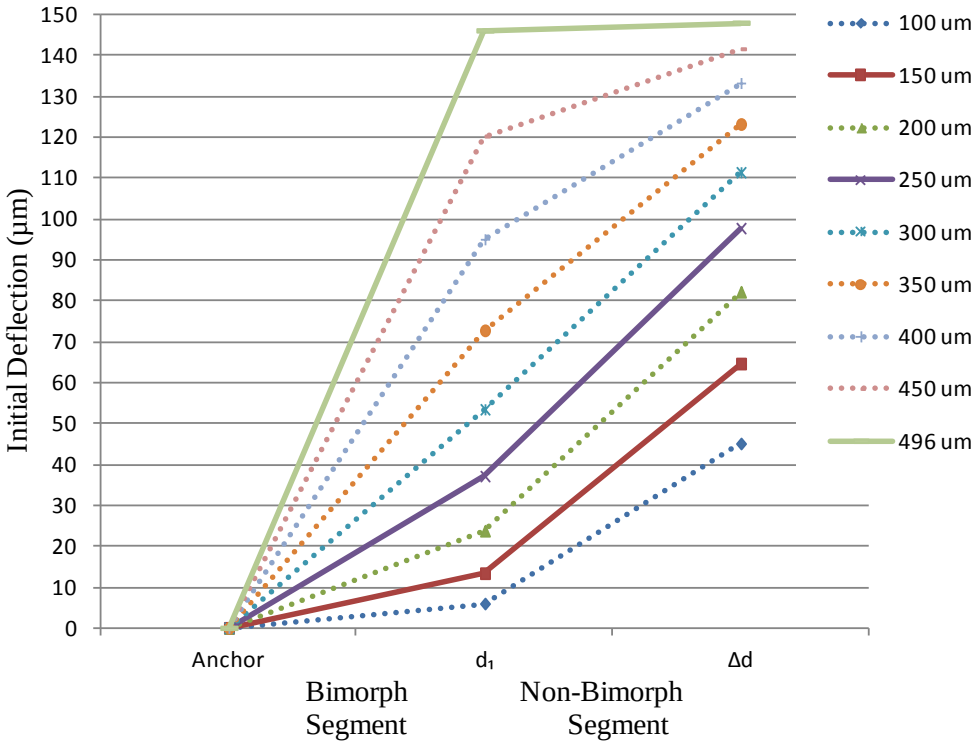

Figure 85: Graph of calculated initial deflection results for a 500 µm partial-bimorph cantilever beam with varied bimorph segments and a temperature change of 250º C

APPENDIX F. Analytical Modeling Data Tables and Graphs: Bimorph Cantilever Beam Pull-in Voltages

Table 16: Calculated voltages required for pull-in of a 500 µm partial-bimorph cantilever beam with varied bimorph segments and a temperature change of 10° C

Bimorph Segment Length (µm)	Modeled Segment Length (µm)	Pull-in Voltage
100	50	75.5
150	75	36.2
200	100	22.5
250	125	16.2
300	150	10.8
350	175	10.9
400	200	9.7
450	225	9.0
496	248	8.5

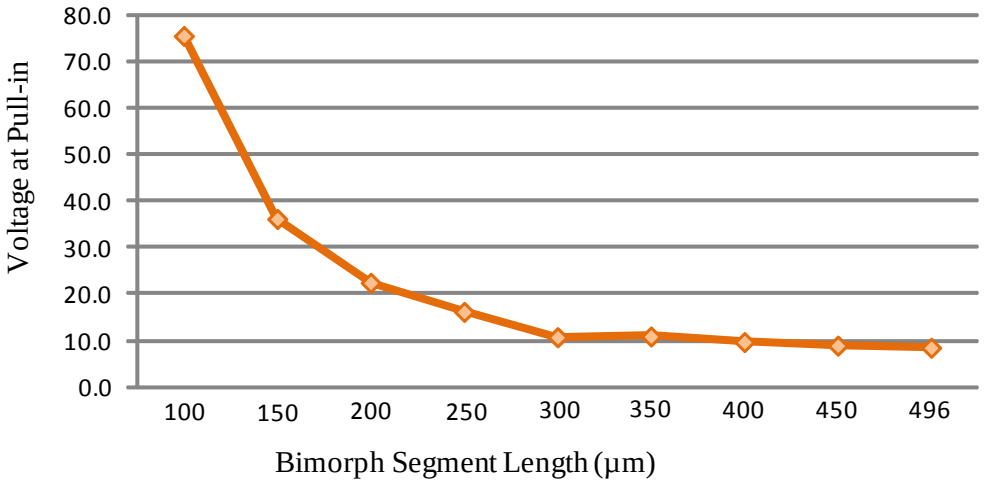

Figure 86: Calculated voltages required for pull-in of a 500 µm partial-bimorph cantilever beam with varied bimorph segments and a temperature change of 10° C

Table 17: Calculated voltages required for pull-in of a 500 µm partial-bimorph cantilever beam with varied bimorph segments and a temperature change of 50º C

Bimorph Segment Length (µm)	Modeled Segment Length (µm)	Pull-in Voltage
100	50	42.5
150	75	25.5
200	100	20.2
250	125	18.3
300	150	14.9
350	175	18.0
400	200	18.6
450	225	19.5
496	248	20.4

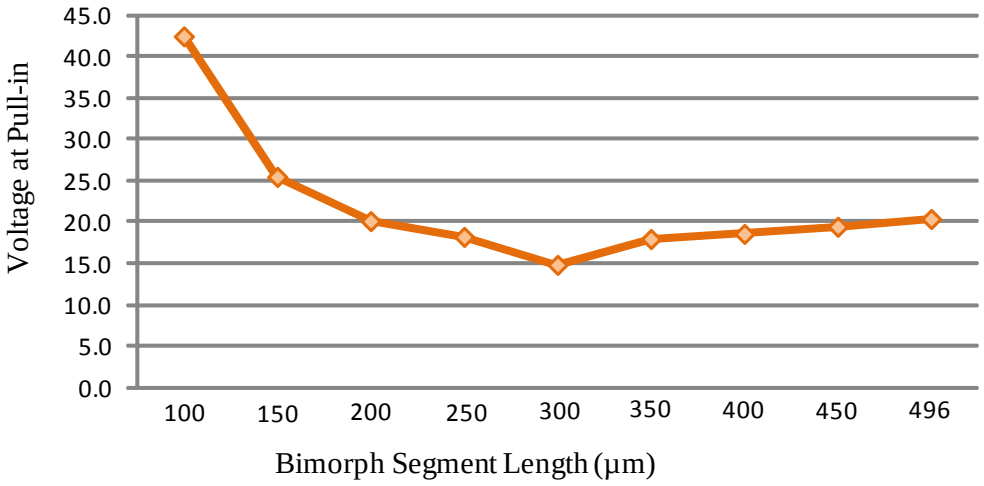

Figure 87: Calculated voltages required for pull-in of a 500 µm partial-bimorph cantilever beam with varied bimorph segments and a temperature change of 50º C

Table 18: Calculated voltages required for pull-in of a 500 µm partial-bimorph cantilever beam with varied bimorph segments and a temperature change of 100º C

Bimorph Segment Length (µm)	Modeled Segment Length (µm)	Pull-in Voltage
100	50	38.4
150	75	27.6
200	100	25.2
250	125	25.5
300	150	22.5
350	175	28.8
400	200	31.1
450	225	33.6
496	248	36.1

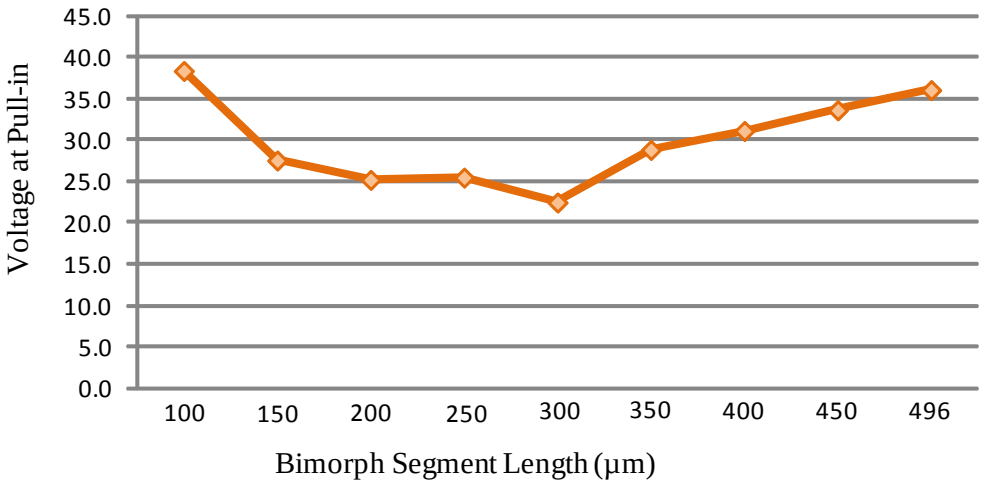

Figure 88: Calculated voltages required for pull-in of a 500 µm partial-bimorph cantilever beam with varied bimorph segments and a temperature change of 100º C

Table 19: Calculated voltages required for pull-in of a 500 µm partial-bimorph cantilever beam with varied bimorph segments and a temperature change of 150° C

Bimorph Segment Length (µm)	Modeled Segment Length (µm)	Pull-in Voltage
100	50	38.7
150	75	31.3
200	100	31.1
250	125	33.2
300	150	30.3
350	175	39.9
400	200	43.8
450	225	47.9
496	248	51.8

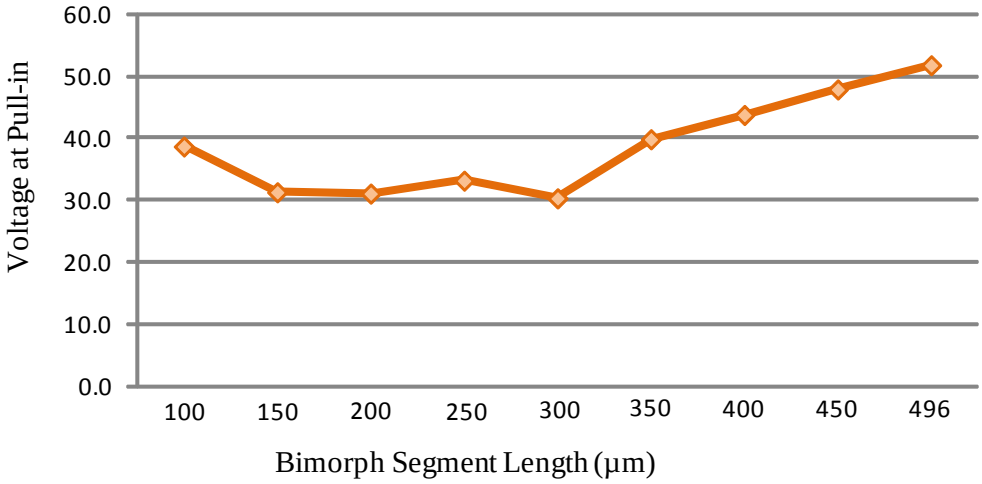

Figure 89: Calculated voltages required for pull-in of a 500 µm partial-bimorph cantilever beam with varied bimorph segments and a temperature change of 150° C

Table 20: Calculated voltages required for pull-in of a 500 µm partial-bimorph cantilever beam with varied bimorph segments and a temperature change of 200º C

Bimorph Segment Length (µm)	Modeled Segment Length (µm)	Pull-in Voltage
100	50	40.3
150	75	35.5
200	100	37.2
250	125	41.0
300	150	38.2
350	175	50.9
400	200	56.4
450	225	62.2
496	248	67.5

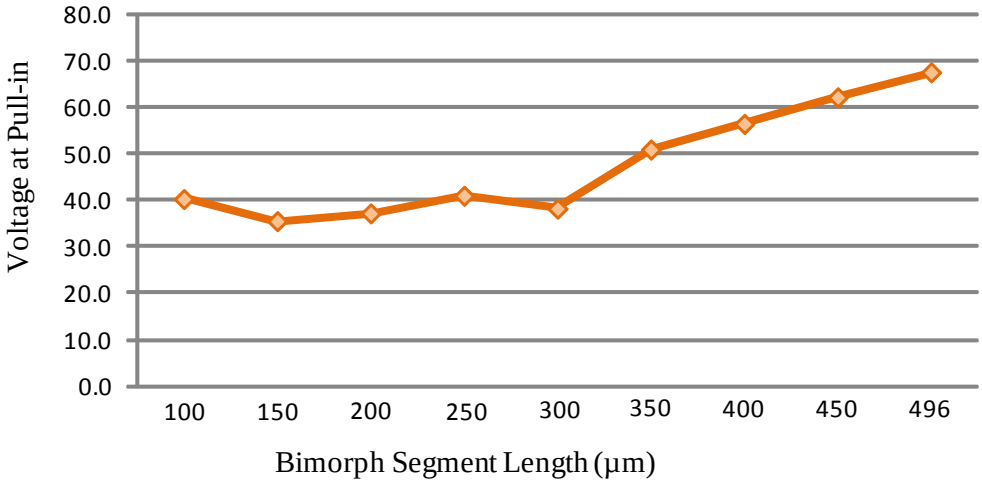

Figure 90: Calculated voltages required for pull-in of a 500 µm partial-bimorph cantilever beam with varied bimorph segments and a temperature change of 200º C

Table 21: Calculated voltages required for pull-in of a 500 µm partial-bimorph cantilever beam with varied bimorph segments and a temperature change of 250º C

Bimorph Segment Length (µm)	Modeled Segment Length (µm)	Pull-in Voltage
100	50	42.5
150	75	40.0
200	100	43.4
250	125	48.9
300	150	46.2
350	175	62.0
400	200	69.1
450	225	76.4
496	248	83.3

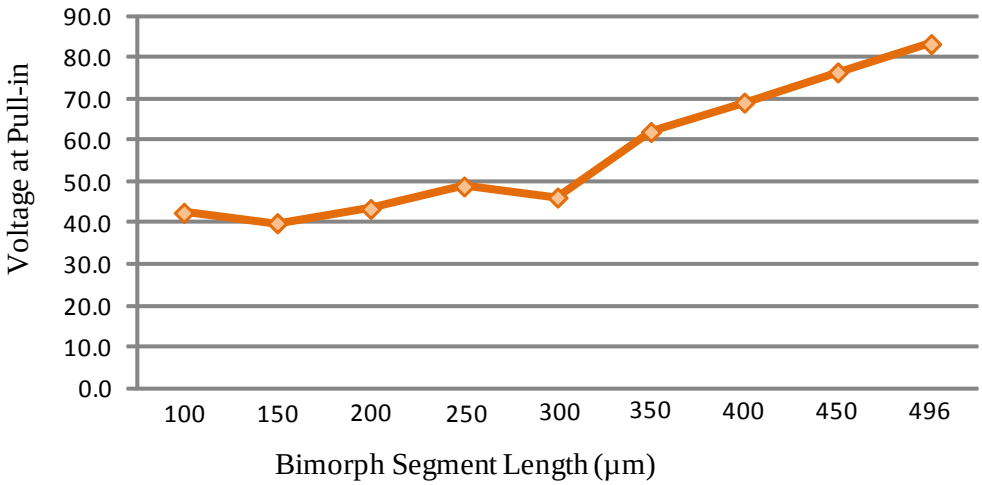

Figure 91: Calculated voltages required for pull-in of a 500 µm partial-bimorph cantilever beam with varied bimorph segments and a temperature change of 250º C

APPENDIX G. Experimental Data Tables and Graphs: "Zipper" Actuator Assembly Initial Deflections

Table 22: Measured initial deflection results for PolyMUMPs® fabricated, 22-beam "zipper" actuators; 500 µm partial-bimorph cantilever beams with 250 µm bimorph segments

Secondary Anchors	Actuator Deflections (µm)				Average Deflection
1	23.3	24.5	29.1	27.7	26.15
2	20.3	21.4	21.9	21.7	21.33
3	36.7	37.4	42.9	41.8	39.70
4	36.1	37.5	39.6	38.6	37.95
5	50.5	51.1	56.9	56	53.63
6	52.1	53.3	56.9	55	54.33
7	64.1	65.3	71.6	70.9	67.98
8	67.2	68.2	72.9	70.8	69.78
9	78.5	79.1	86.8	86.2	82.65
10	82.5	83.6	90.2	86.5	85.70
11	93	93.4	102.7	101.2	97.58
12	94.8	97.6	105.5	103.1	100.25
13	106.5	108.1	118.1	117.2	112.48
14	109.6	111.9	121.1	117.4	115.00
15	121.8	123.3	133.9	132.8	127.95
16	124.1	125.5	135.4	132.9	129.48
17	137.4	138.5	150	149.8	143.93
18	138	139.2	150.3	147.1	143.65
19	152.8	154.5	166.1	166.9	160.08
20	151.7	152.6	164.8	161.8	157.73
21	169.2	170	182.9	184.1	176.55
22	165	165.8	176.3	176.2	170.83

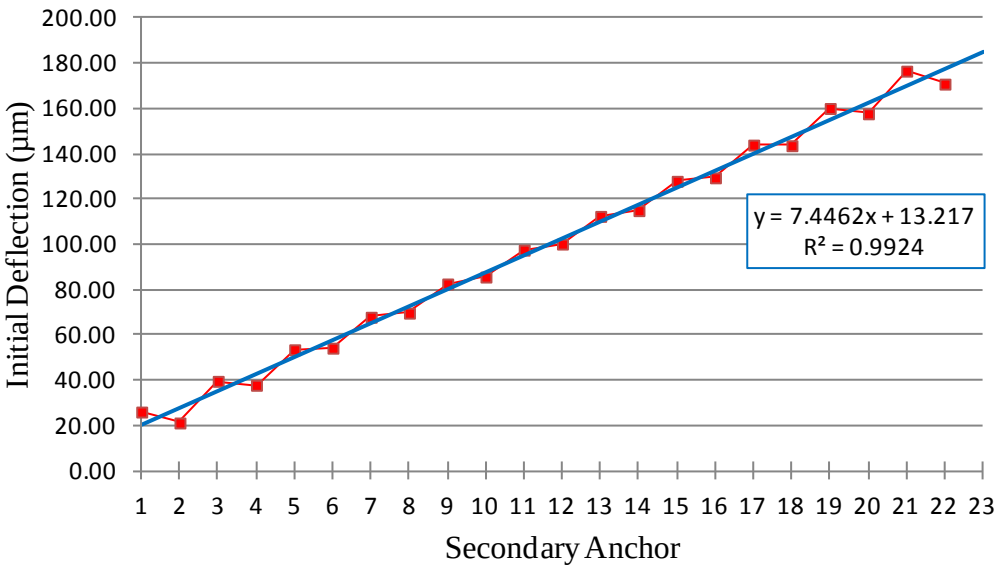

Figure 92: Graph of measured initial deflection results for PolyMUMPs® fabricated, 22-beam "zipper" actuators; 500 µm partial-bimorph cantilever beams with 250 µm bimorph segments

Table 23: Measured initial deflection results for PolyMUMPs® fabricated, 12-beam "zipper" actuators; 500 µm partial-bimorph cantilever beams with 250 µm bimorph segments

Secondary Anchors	Actuator Deflections (µm)				Average Deflection
1	24	24	24.2	24.3	24.13
2	20.3	21.4	20.3	20.6	20.65
3	37.8	36.8	37	37	37.15
4	36.5	37.1	35.7	35.8	36.28
5	51.4	50.5	50.7	50.7	50.83
6	51.4	52	50.4	50.7	51.13
7	66.1	65.1	65.2	65.3	65.43
8	66.1	66.2	64.5	65.1	65.48
9	81.3	81	80.7	80.9	80.98
10	80.4	80.5	78.1	78.7	79.43
11	98	97.2	96.4	96.3	96.98
12	92.6	92	91.7	90.9	91.80

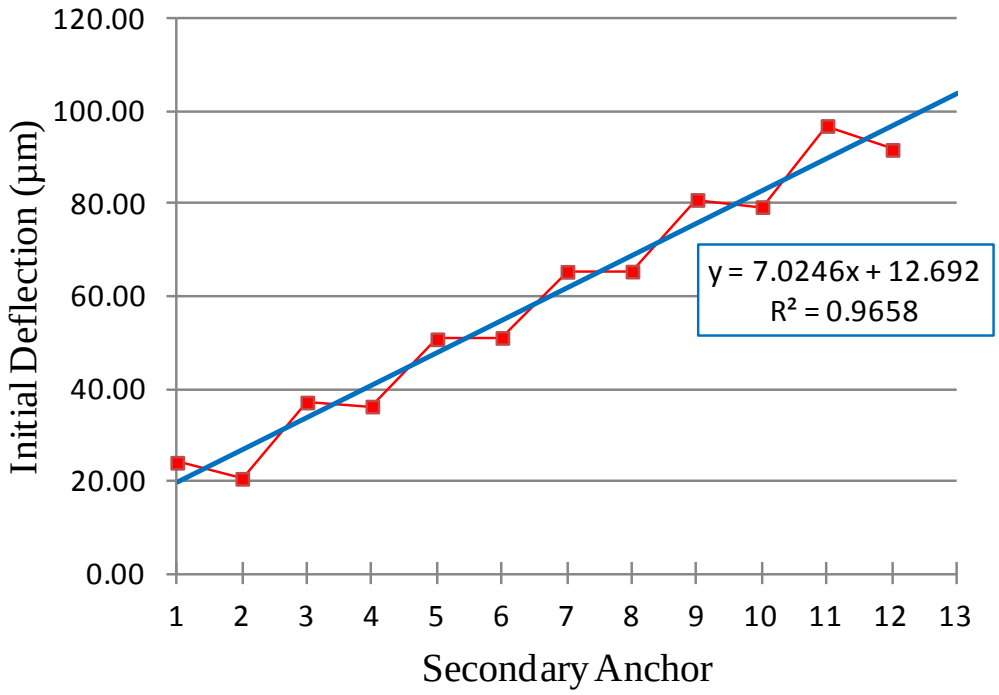

Figure 93: Graph of measured initial deflection results for PolyMUMPs® fabricated, 12-beam "zipper" actuators; 500 µm partial-bimorph cantilever beams with 250 µm bimorph segments

Table 24: Measured initial deflection results for PolyMUMPs® fabricated, 11-beam "zipper" actuators; 500 µm partial-bimorph cantilever beams with 250 µm bimorph segments

Secondary Anchors	Actuator Deflections (µm)				Average Deflection
1	26.8	25.1	25.2	24.9	25.50
2	23.4	22.5	23.3	23	23.05
3	40.3	37.9	39	38.5	38.93
4	42.5	41.6	41.3	40	41.35
5	54.4	51.6	52	51.7	52.43
6	59.2	58.6	59.7	59.2	59.18
7	67.8	64.2	64.6	64.9	65.38
8	77.9	75.9	77.5	77.4	77.18
9	80	78.9	78.5	78.8	79.05
10	96.2	93.8	95.9	95.9	95.45
11	92.1	91.6	91.7	91.3	91.68

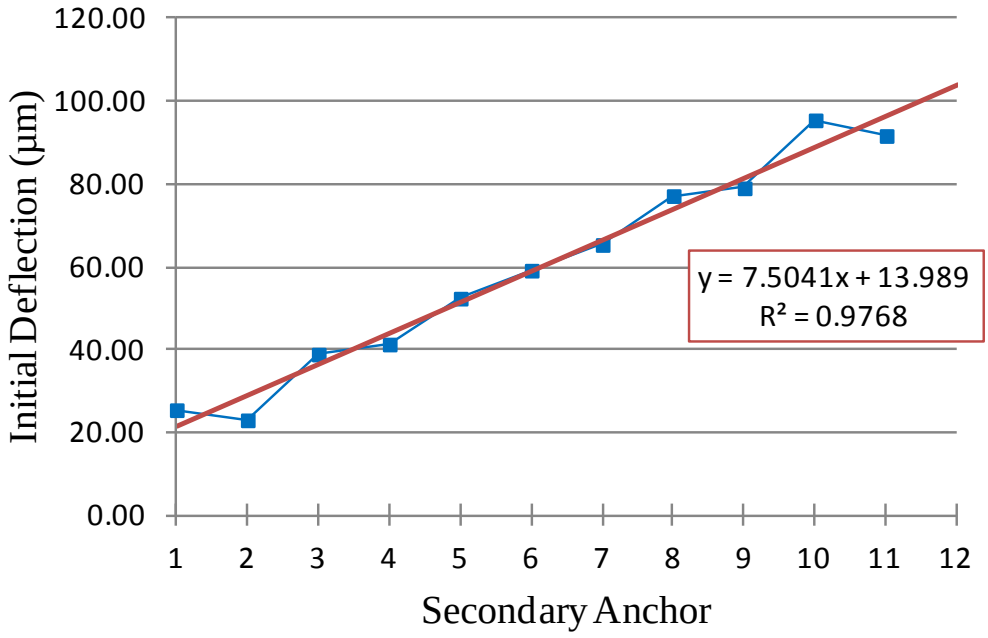

Figure 94: Graph of measured initial deflection results for PolyMUMPs® fabricated, 11-beam "zipper" actuators; 500 µm partial-bimorph cantilever beams with 250 µm bimorph segments

Table 25: Measured initial deflection results for PolyMUMPs® fabricated, 10-beam "zipper" actuators; 500 µm partial-bimorph cantilever beams with 250 µm bimorph segments

Secondary Anchors	Actuator Deflections (µm)				Average Deflection
1	25	23.8	23.7	24.1	24.15
2	19.4	20	20.1	20.5	20.00
3	37.4	36.7	36.9	36.7	36.93
4	34.2	34.3	36.1	36.1	35.18
5	51	51.2	51.2	51.3	51.18
6	50	48.3	50.7	50.7	49.93
7	66.3	65.2	66.4	66	65.98
8	62	61.3	64.5	64.3	63.03
9	82.2	81.1	83.1	82.9	82.33
10	76	76.1	76.7	76.6	76.35

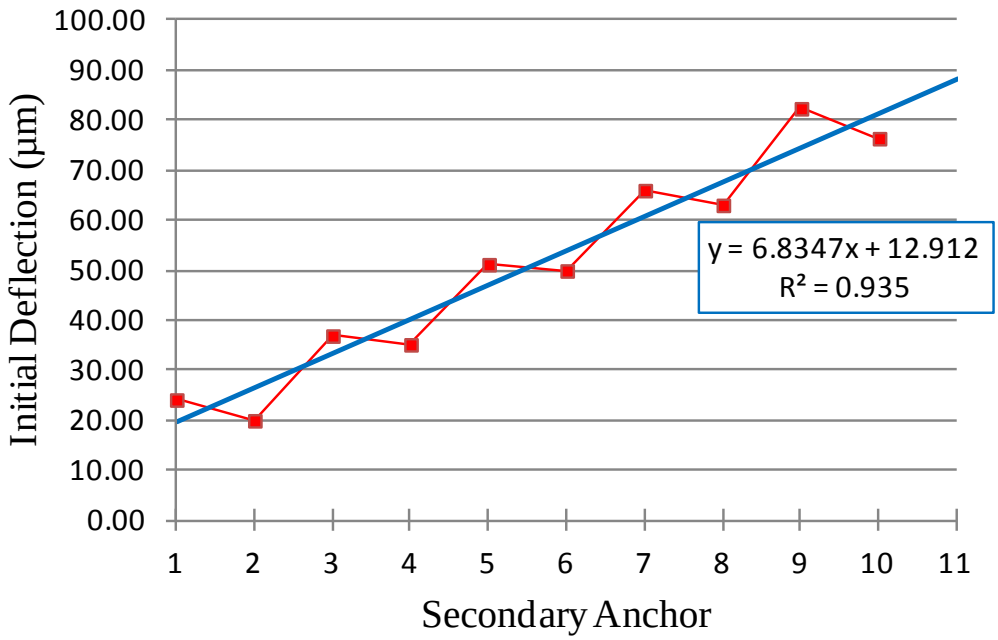

Figure 95: Graph of measured initial deflection results for PolyMUMPs® fabricated, 10-beam "zipper" actuators; 500 µm partial-bimorph cantilever beams with 250 µm bimorph segments

Table 26: Measured initial deflection results for PolyMUMPs® fabricated, 9-beam "zipper" actuators; 500 µm partial-bimorph cantilever beams with 250 µm bimorph segments

Secondary Anchors	Actuator Deflections (µm)				Average Deflection
1	23.3	23.2	24.7	25.1	24.08
2	22.2	21.6	23.7	23.7	22.80
3	35.3	34.5	28.3	37.2	33.83
4	39.2	39.4	42.6	42.3	40.88
5	46.9	46.7	50.6	49.5	48.43
6	56.7	56.7	61.6	61	59.00
7	58.3	58.6	63.2	62	60.53
8	74.3	74.2	80.3	79.6	77.10
9	70.5	70.1	75.3	74.3	72.55

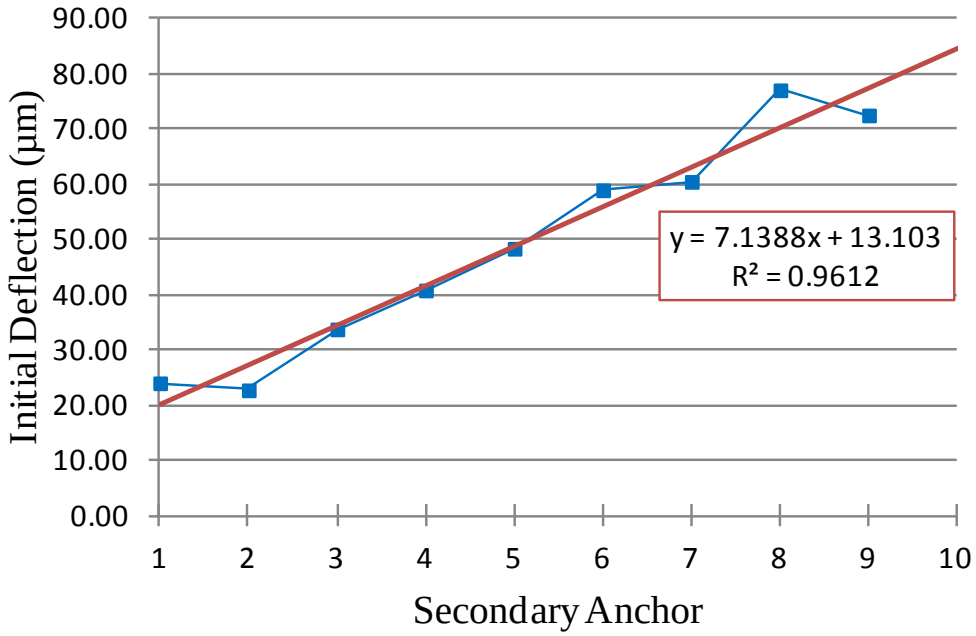

Figure 96: Graph of measured initial deflection results for PolyMUMPs® fabricated, 9-beam "zipper" actuators; 500 µm partial-bimorph cantilever beams with 250 µm bimorph segments

Table 27: Measured initial deflection results for PolyMUMPs® fabricated, 8-beam "zipper" actuators; 500 µm partial-bimorph cantilever beams with 250 µm bimorph segments

Secondary Anchors	Actuator Deflections (µm)				Average Deflection
1	23.5	24.1	23.9	23.2	23.68
2	20.3	20.3	20.4	20.2	20.30
3	36.6	36.9	36.9	37	36.85
4	35.2	35.3	35.6	35.3	35.35
5	51.5	51.7	51.9	52.2	51.83
6	49	49.1	49.5	49.7	49.33
7	67	67.1	67.5	68.2	67.45
8	61.5	60.6	61.6	61.6	61.33

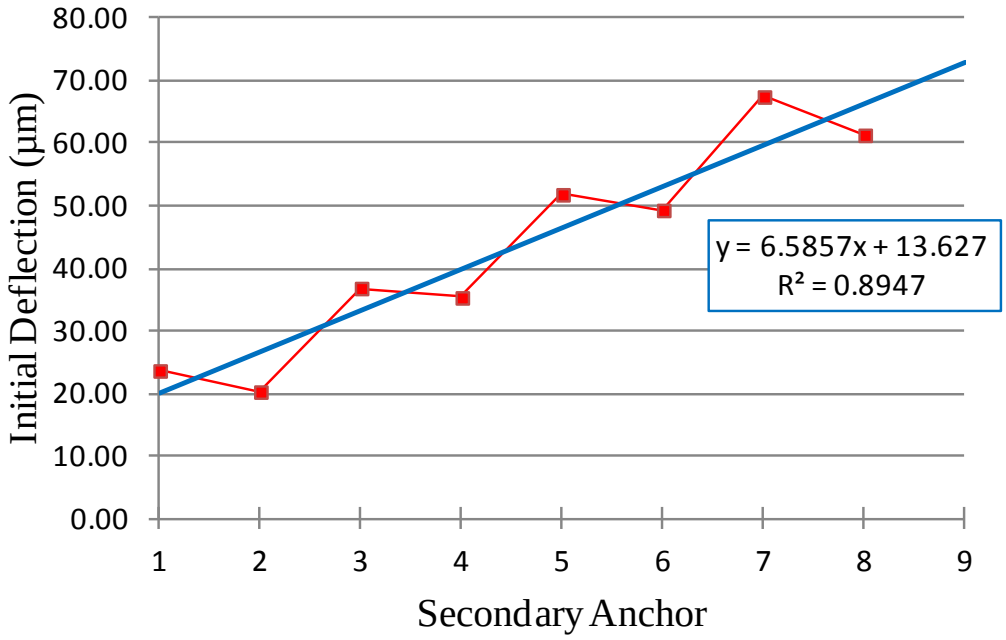

Figure 97: Graph of measured initial deflection results for PolyMUMPs® fabricated, 8-beam "zipper" actuators; 500 µm partial-bimorph cantilever beams with 250 µm bimorph segments

Table 28: Measured initial deflection results for PolyMUMPs® fabricated, 7-beam "zipper" actuators; 500 µm partial-bimorph cantilever beams with 250 µm bimorph segments

Secondary Anchors	Actuator Deflections (µm)				Average Deflection
1	22.9	23	22.8	23.5	23.05
2	22.6	22.3	22.8	23.2	22.73
3	33.5	33.7	33.9	33.9	33.75
4	40.6	40.2	40.7	40.5	40.50
5	44.4	44.4	45.1	45.4	44.83
6	58.7	58.2	58.9	58.5	58.58
7	55.8	56	56.2	56.4	56.10

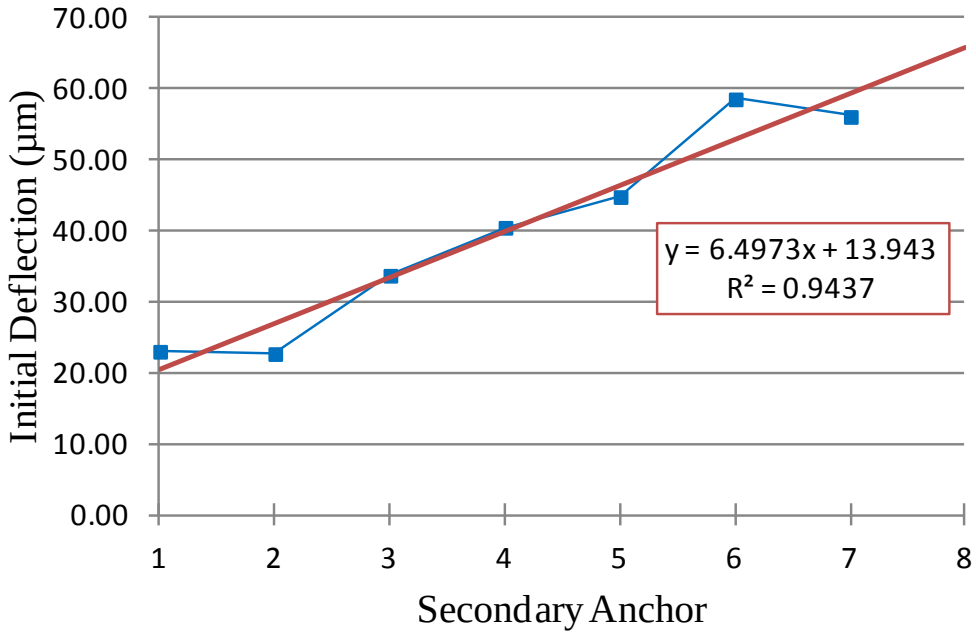

Figure 98: Graph of measured initial deflection results for PolyMUMPs® fabricated, 7-beam "zipper" actuators; 500 µm partial-bimorph cantilever beams with 250 µm bimorph segments

Table 29: Measured initial deflection results for PolyMUMPs® fabricated, 6-beam "zipper" actuators; 500 µm partial-bimorph cantilever beams with 250 µm bimorph segments

Secondary Anchors	Actuator Deflections (µm)				Average Deflection
1	26.5	26.7	23.6	24.2	25.25
2	22.3	22.6	20.7	21.2	21.70
3	42.9	42.8	37.9	38	40.40
4	38.4	38.6	35	35.7	36.93
5	59.5	59.5	53.5	53.2	56.43
6	52.3	52.5	47.1	46.8	49.68

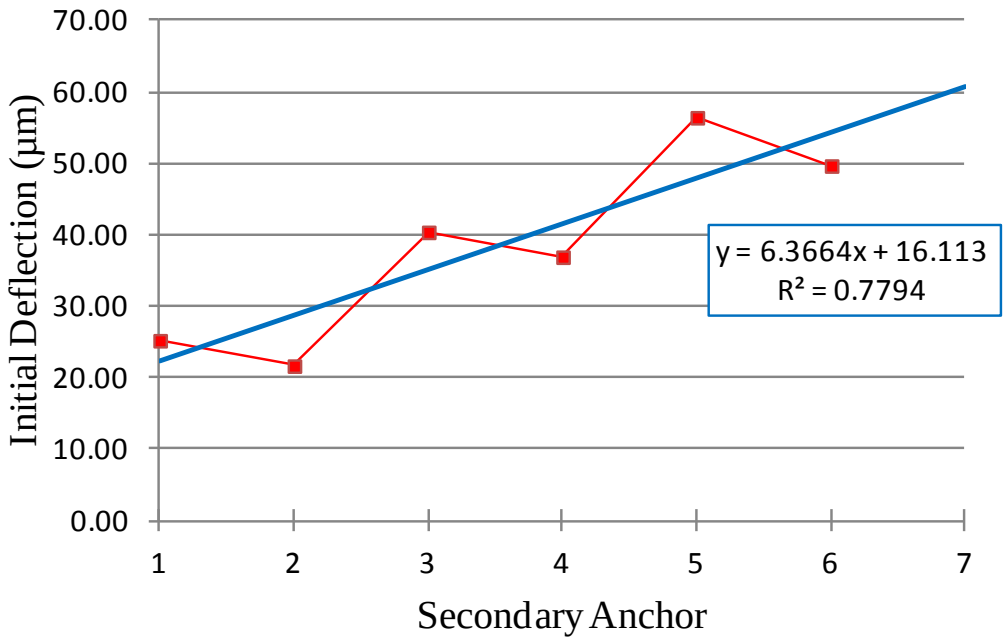

Figure 99: Graph of measured initial deflection results for PolyMUMPs® fabricated, 6-beam "zipper" actuators; 500 µm partial-bimorph cantilever beams with 250 µm bimorph segments

Table 30: Measured initial deflection results for PolyMUMPs® fabricated, 5-beam "zipper" actuators; 500 µm partial-bimorph cantilever beams with 250 µm bimorph segments

Secondary Anchors	Actuator Deflections (µm)				Average Deflection
1	21.7	21.5	24.8	23.7	22.93
2	23.3	23.5	26	25.8	24.65
3	31.7	31.5	35	34.1	33.08
4	42	43.2	47	46.9	44.78
5	42.2	40.8	45.3	45.3	43.40

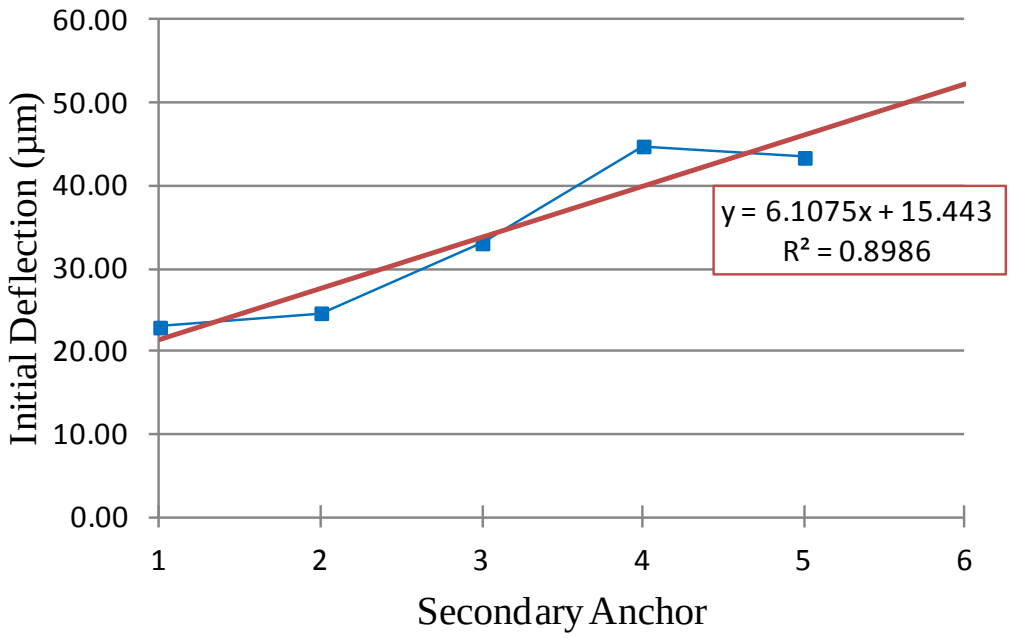

Figure 100: Graph of measured initial deflection results for PolyMUMPs® fabricated, 5-beam "zipper" actuators; 500 µm partial-bimorph cantilever beams with 250 µm bimorph segments

Table 31: Measured initial deflection results for PolyMUMPs® fabricated, 4-beam "zipper" actuators; 500 µm partial-bimorph cantilever beams with 250 µm bimorph segments

Secondary Anchors	Actuator Deflections (µm)				Average Deflection
1	24.1	24.1	24.3	24.4	24.23
2	20.2	20.2	19.4	19.5	19.83
3	38.5	38.8	38.8	38.8	38.73
4	32.6	32.7	32.6	32.5	32.60

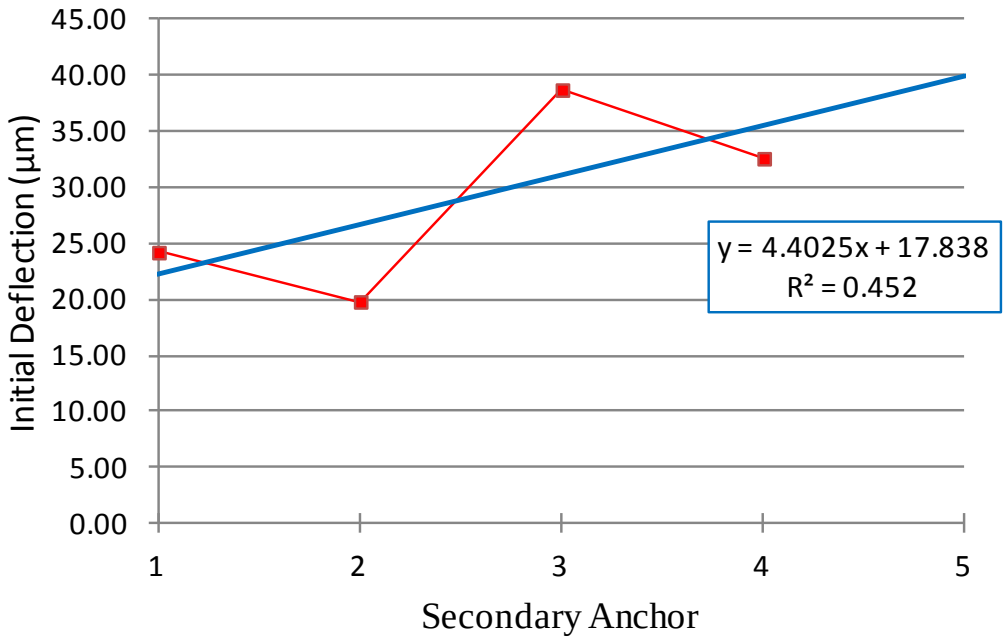

Figure 101: Graph of measured initial deflection results for PolyMUMPs® fabricated, 4-beam "zipper" actuators; 500 µm partial-bimorph cantilever beams with 250 µm bimorph segments

Table 32: Measured initial deflection results for PolyMUMPs® fabricated, 3-beam "zipper" actuators; 500 µm partial-bimorph cantilever beams with 250 µm bimorph segments

Secondary Anchors	Actuator Deflections (µm)				Average Deflection
1	21.3	21.1	21.1	21.3	21.20
2	27.5	26.2	27.2	26.8	26.93
3	28.5	28.5	28.7	28.7	28.60

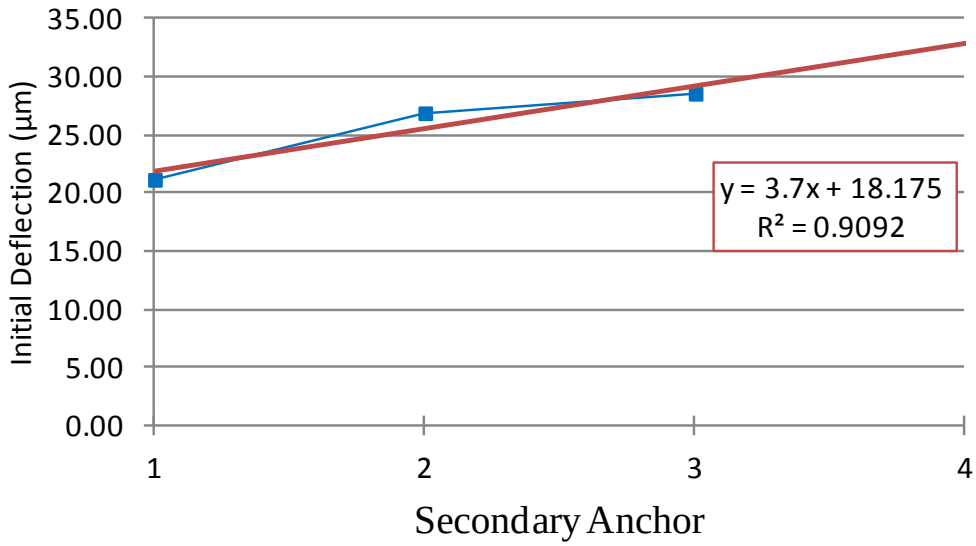

Figure 102: Graph of measured initial deflection results for PolyMUMPs® fabricated, 3-beam "zipper" actuators; 500 µm partial-bimorph cantilever beams with 250 µm bimorph segments

Table 33: Measured initial deflection results for PolyMUMPs® fabricated, corrugated 11-beam "zipper" actuators; 500 µm partial-bimorph cantilever beams with 250 µm bimorph segments

Secondary Anchors	Actuator Deflections (µm)				Average Corrugated Deflection
1	26.7	24.1	24.8	25.9	25.38
2	24.1	22	23.6	23.6	23.33
3	39	37.8	37.2	39.4	38.35
4	42	38.4	41.3	41.7	40.85
5	51.1	46.5	50	52.6	50.05
6	59.2	55.3	57.3	59.9	57.93
7	63.4	58.9	64.2	65.4	62.98
8	74.7	71.8	76.1	75.8	74.60
9	74.7	71.7	77.4	77.9	75.43
10	91.4	86.5	93.3	94.2	91.35
11	87.5	85	89.3	90.1	87.98

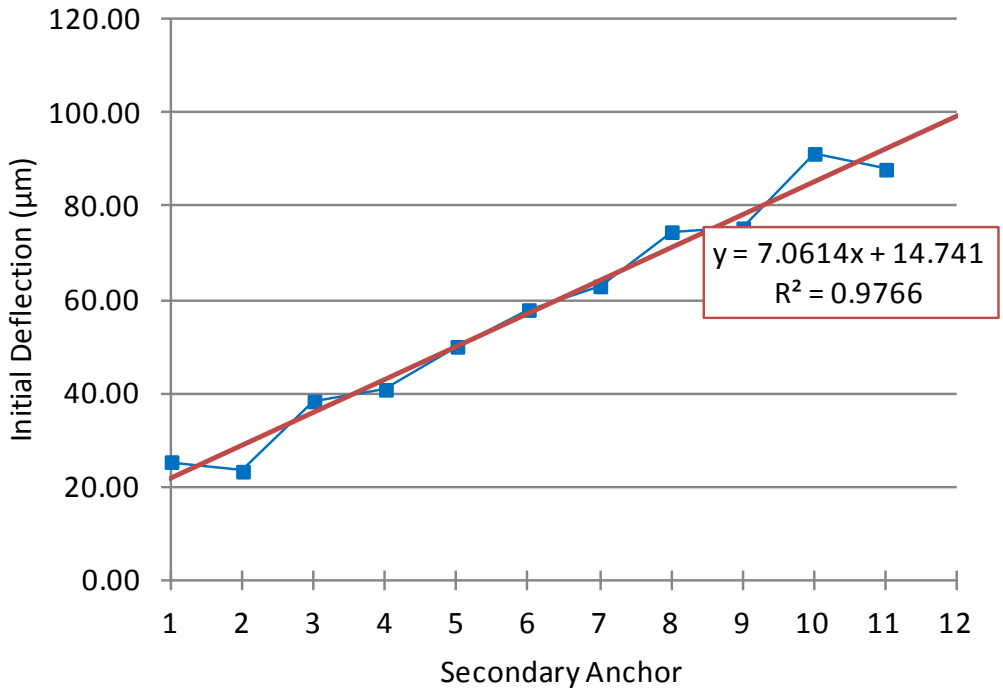

Figure 103: Graph of measured initial deflection results for PolyMUMPs® fabricated, corrugated 11-beam "zipper" actuators; 500 µm partial-bimorph cantilever beams with 250 µm bimorph segments

Table 34: Measured initial deflection results for PolyMUMPs® fabricated, corrugated 9-beam "zipper" actuators; 500 µm partial-bimorph cantilever beams with a 250 µm bimorph segments

Secondary Anchors	Actuator Deflections (µm)				Average Corrugated Deflection
1	24.7	23	24.8	23.5	24.00
2	24.3	23	23.7	23.5	23.63
3	35	33	37.1	34.6	34.93
4	41.9	40.5	41.6	41.9	41.48
5	47	44.6	49.1	46.4	46.78
6	59.1	57.2	59.3	59.7	58.83
7	59.3	56.9	61.4	59.4	59.25
8	75.9	74.2	76.6	76.8	75.88
9	70.3	70	72.2	73.4	71.48

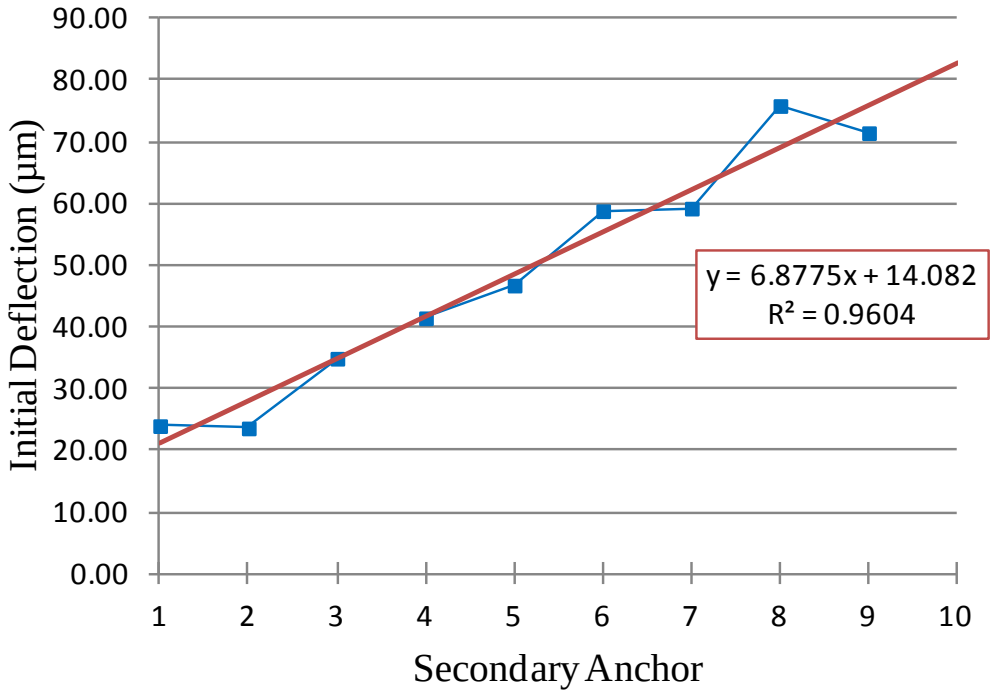

Figure 104: Graph of measured initial deflection results for PolyMUMPs® fabricated, corrugated 9-beam "zipper" actuators; 500 µm partial-bimorph cantilever beams with 250 µm bimorph segments

Table 35: Measured initial deflection results for PolyMUMPs® fabricated, corrugated 7-beam "zipper" actuators; 500 µm partial-bimorph cantilever beams with a 250 µm bimorph segments

		Actuator Deflections (µm)				Average Corrugated Deflection
Secondary Anchors	1	24.2	23.4	25.7	24	24.33
	2	23.9	23.6	25	24.4	24.23
	3	34.8	33.2	37.3	35	35.08
	4	42.6	42.4	43.5	44.6	43.28
	5	46.5	44.1	48.5	46.7	46.45
	6	60.2	59.1	62.2	63.7	61.30
	7	56.9	54.8	58.9	58.1	57.18

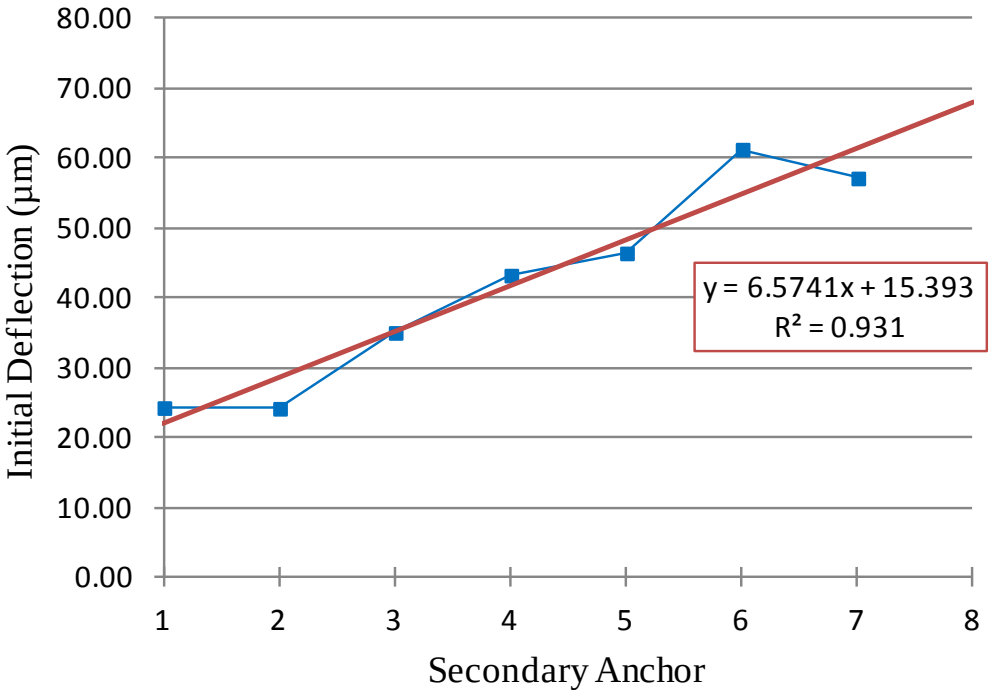

Figure 105: Graph of measured initial deflection results for PolyMUMPs® fabricated, corrugated 7-beam "zipper" actuators; 500 µm partial-bimorph cantilever beams with 250 µm bimorph segments

Table 36: Measured initial deflection results for PolyMUMPs® fabricated, corrugated 5-beam "zipper" actuators; 500 µm partial-bimorph cantilever beams with a 250 µm bimorph segments

		Actuator Deflections (µm)				Average Corrugated Deflection
Secondary Anchors	1	24	22.5	23.6	22.9	23.25
	2	24.8	25.1	24.8	25.7	25.10
	3	33.1	31.5	33.8	32.7	32.78
	4	45.7	45.1	46.8	45.8	45.85
	5	42.5	40.7	42.9	44.3	42.60

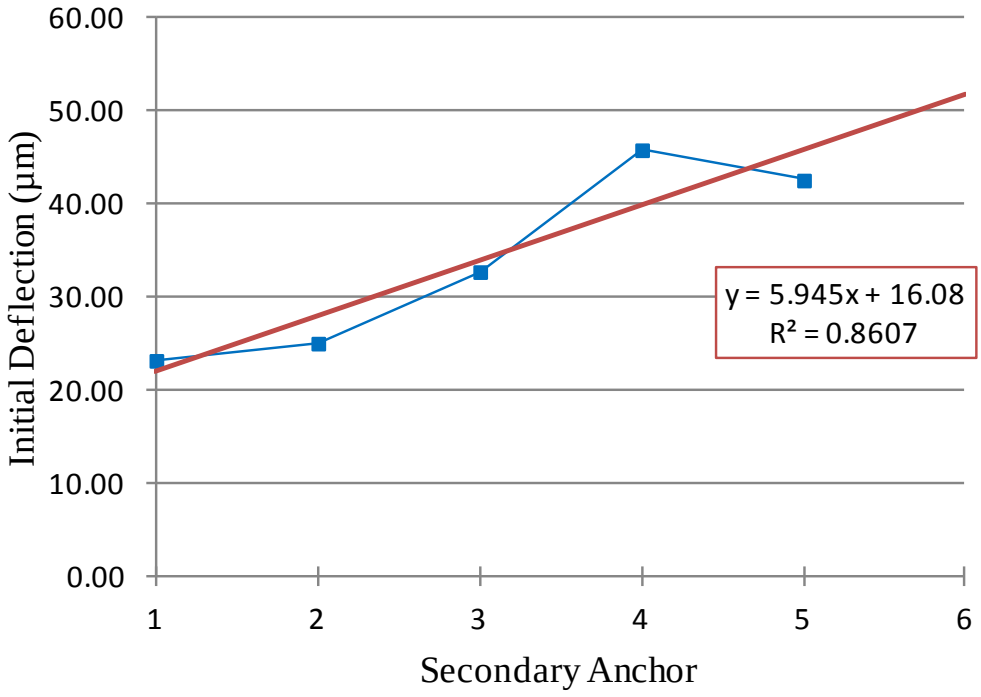

Figure 106: Graph of measured initial deflection results for PolyMUMPs® fabricated, corrugated 5-beam "zipper" actuators; 500 µm partial-bimorph cantilever beams with 250 µm bimorph segments

APPENDIX H. Experimental Data Tables and Graphs: "Zipper" Actuator Assembly Pull-in Voltages

Table 37: Measured deflection results for pull-in of PolyMUMPs® fabricated micro-mirror platform assembly with four 22-beam "zipper" actuators; (a) device 1 test results, (b) device 2 test results

	1	2	3	4	5	6	7	8	9	10	11	12	13	14	15	16	17	18	19	20	21	22	PFa	PFo
0 V	29	30	43	40	57	57	72	73	87	90	103	106	118	121	134	135	150	150	166	165	183	176	177	177
10 V	26	21	40	38	54	53	68	70	83	86	99	100	114	116	130	131	148	146	164	160	183	174	174	177
(a) 15 V	24	19	37	33	51	51	65	66	79	82	95	98	111	113	128	129	145	143	162	158	180	172	173	176
18 V	24	15	35	30	49	46	62	62	77	78	93	93	109	110	126	124	143	140	160	155	179	170	171	175
19 V	8	8	8	8	8	8	7	5	19	18	36	35	55	55	76	75	77	95	120	116	144	136	139	164
20 V																								
0 V	28	22	42	39	56	55	71	71	86	87	101	103	117	117	133	133	150	147	167	162	184	176	176	176
10 V	26	19	40	38	53	53	68	68	82	84	97	98	112	114	130	129	146	145	164	153	184	174	174	176
(b) 15 V	23	17	39	34	50	51	65	65	79	82	94	97	110	111	127	127	144	142	163	153	180	173	172	175
18 V	22	16	35	28	48	46	63	63	78	78	91	91	111	111	125	124	142	142	160	149	179	172	169	174
20 V	6	6	6	6	6	6	6	7	19	17	35	34	53	53	75	75	76	96	119	115	146	136	137	164

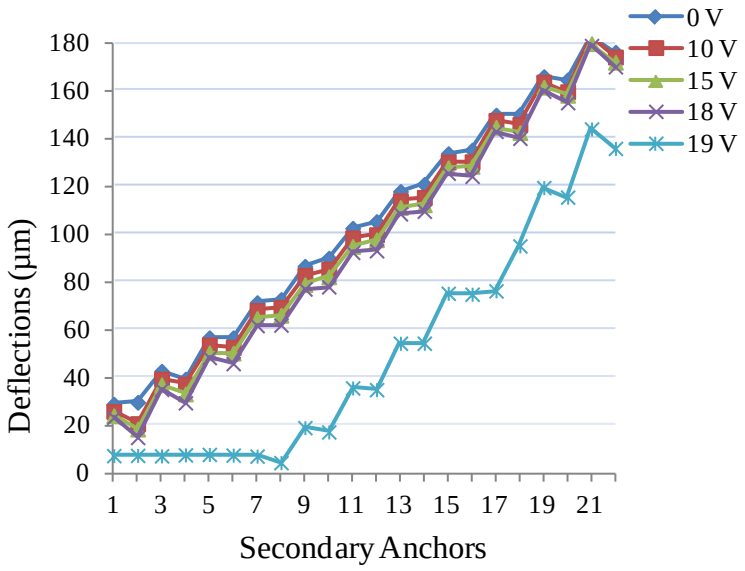

Figure 107: Graph of measured 22-beam "zipper" actuator deflection results for pull-in test of PolyMUMPs® fabricated micro-mirror platform assembly 1; measured at each secondary anchor

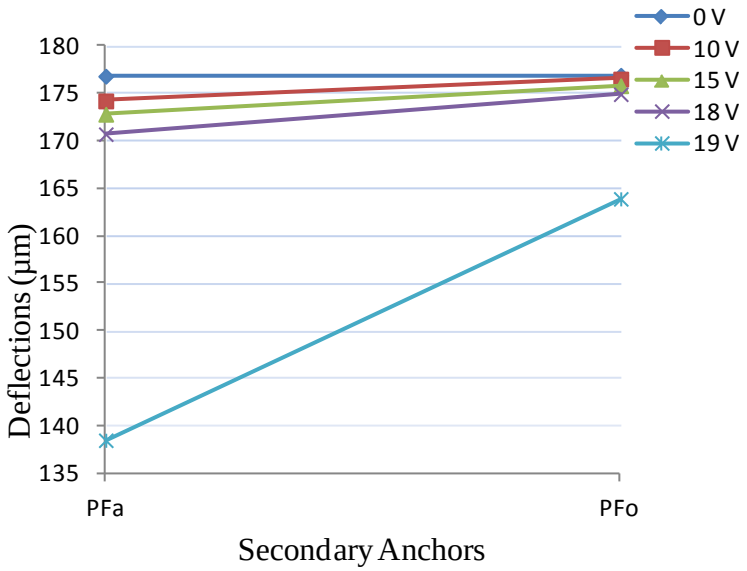

Figure 108: Graph of measured micro-mirror platform deflection results for pull-in test of PolyMUMPs® fabricated 22-beam micro-mirror platform assembly 1; measured on actuation side (PF_a) and side opposite actuation (PF_o)

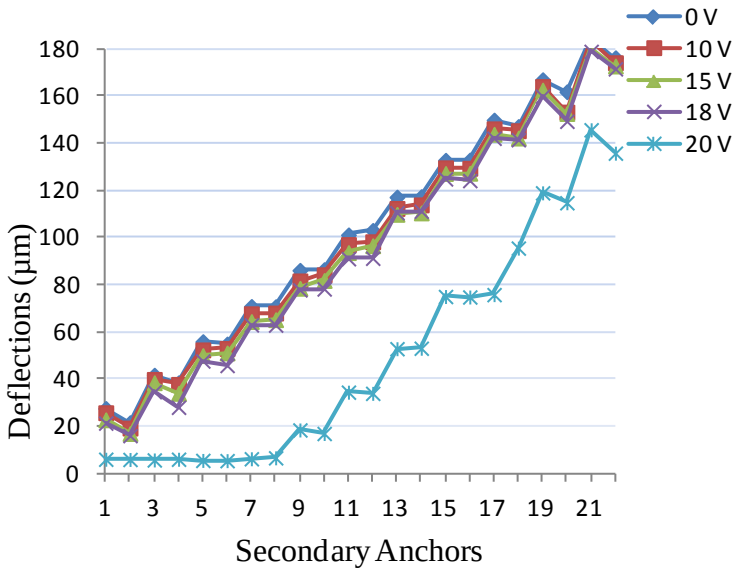

Figure 109: Graph of measured 22-beam "zipper" actuator deflection results for pull-in test of PolyMUMPs® fabricated micro-mirror platform assembly 2; measured at each secondary anchor

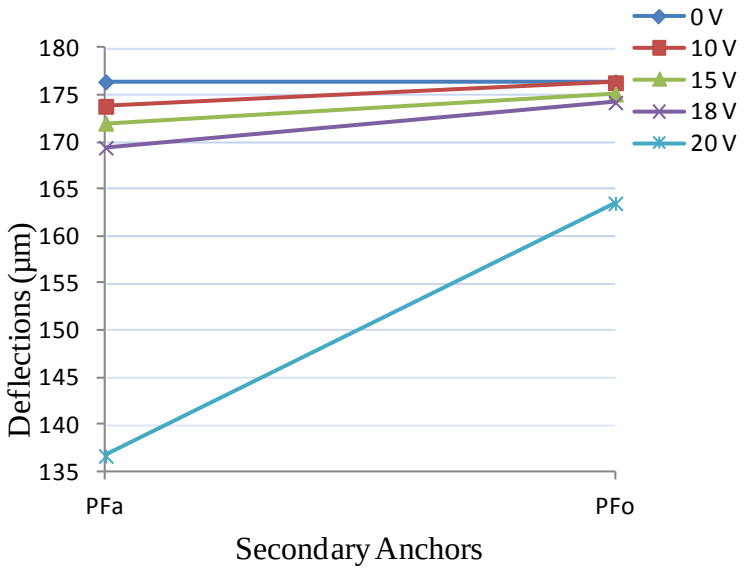

Figure 110: Graph of measured micro-mirror platform deflection results for pull-in test of PolyMUMPs® fabricated 22-beam micro-mirror platform assembly 2; measured on actuation side (PF_a) and side opposite actuation (PF_o)

Table 38: Measured deflection results for pull-in of PolyMUMPs® fabricated micro-mirror platform assembly with four 12-beam "zipper" actuators; (a) device 1 test results, (b) device 2 test results

	1	2	3	4	5	6	7	8	9	10	11	12	PFa	PFo
0 V	22	20	34	34	48	47	61	60	75	73	90	84	85	85
10 V	21	19	33	32	46	45	59	58	74	71	89	83	84	85
(a) 15 V	19	16	31	29	44	43	58	56	72	70	88	82	83	84
19 V	4	4	3	4	3	4	15	16	35	34	58	53	55	75
20 V	4	4	4	4	4	4	14	15	35	33	57	54	56	75
0 V	22	20	34	33	47	48	60	60	75	73	90	85	84	84
10 V	21	18	32	32	45	46	58	59	72	71	88	83	83	84
(b) 15 V	20	16	30	29	43	42	56	56	71	68	87	82	82	84
18 V	5	4	4	12	16	23	34	37	52	52	72	67	69	80
19 V	4	4	4	4	4	4	4	4	23	24	48	42	45	72
20 V	4	3	4	3	4	3	4	3	4	16	36	34	43	69

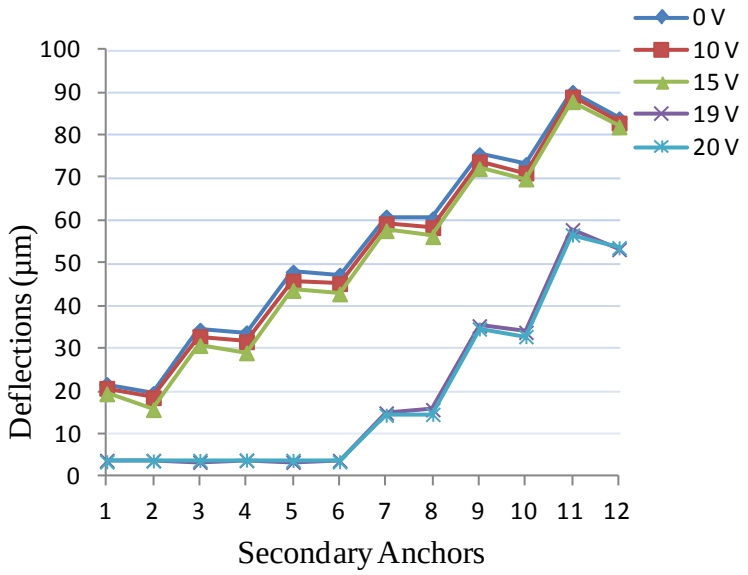

Figure 111: Graph of measured 12-beam "zipper" actuator deflection results for pull-in test of PolyMUMPs® fabricated micro-mirror platform assembly 1; measured at each secondary anchor

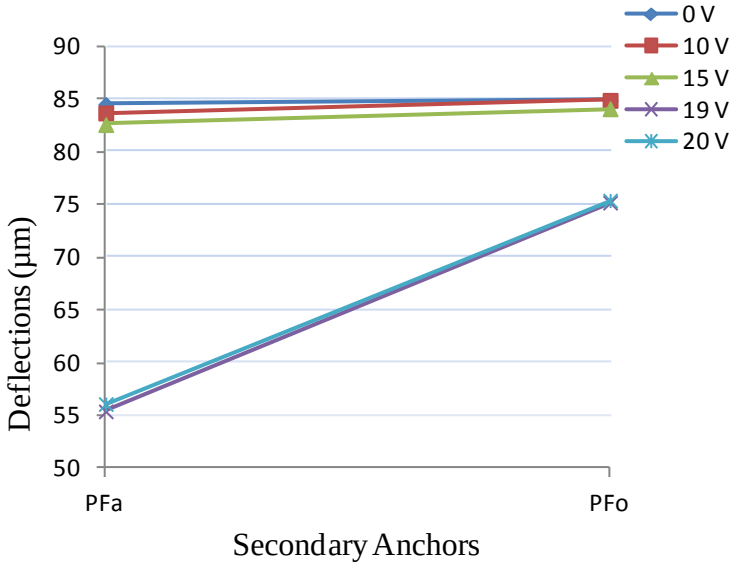

Figure 112: Graph of measured micro-mirror platform deflection results for pull-in test of PolyMUMPs® fabricated 12-beam micro-mirror platform assembly 1; measured on actuation side (PF_a) and side opposite actuation (PF_o)

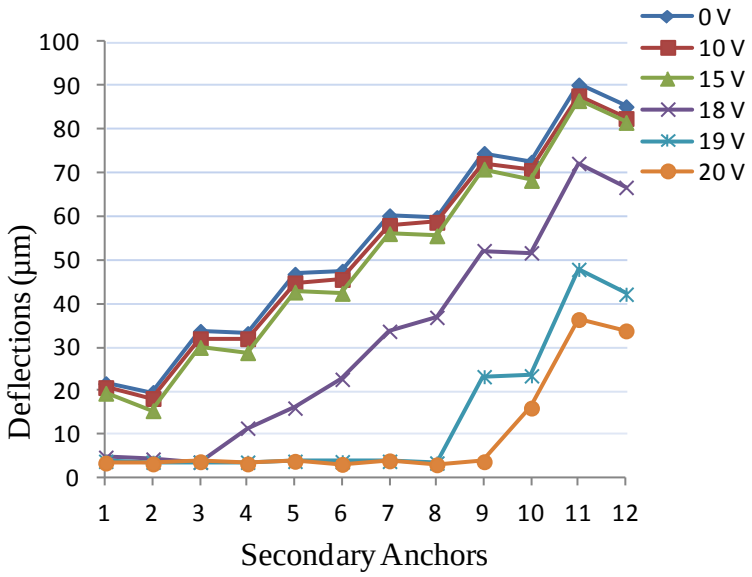

Figure 113: Graph of measured 12-beam "zipper" actuator deflection results for pull-in test of PolyMUMPs® fabricated micro-mirror platform assembly 2; measured at each secondary anchor

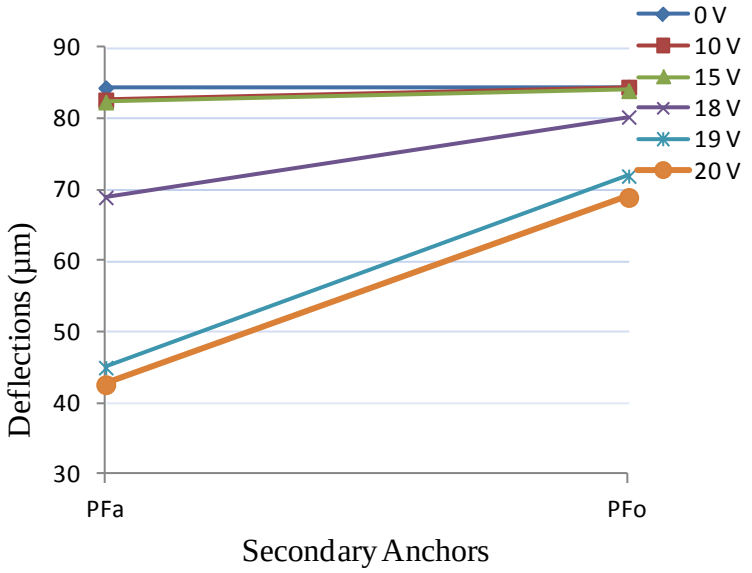

Figure 114: Graph of measured micro-mirror platform deflection results for pull-in test of PolyMUMPs® fabricated 12-beam micro-mirror platform assembly 2; measured on actuation side (PF_a) and side opposite actuation (PF_o)

Table 39: Measured deflection results for pull-in of PolyMUMPs® fabricated micro-mirror platform assembly with four 10-beam "zipper" actuators

	1	2	3	4	5	6	7	8	9	10	PFa	PFo
0 V	24	21	37	37	51	50	66	65	82	77	76	76
10 V	24	21	37	35	50	50	65	64	82	76	74	76
15 V	22	20	35	34	48	49	65	63	81	75	73	75
18 V	21	17	33	32	48	47	63	61	80	74	59	73
19 V	21	16	33	30	47	45	63	60	79	73	38	63
20 V	5	4	5	5	5	4	18	22	47	44	34	60

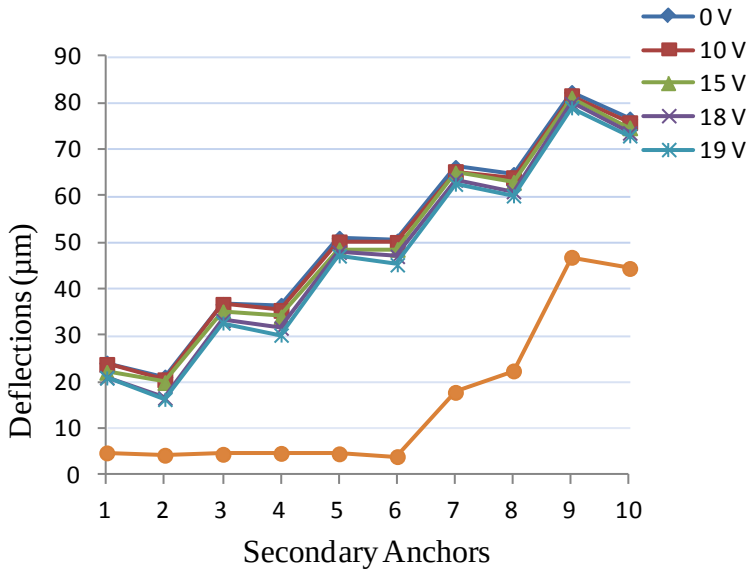

Figure 115: Graph of measured 10-beam "zipper" actuator deflection results for pull-in test of PolyMUMPs® fabricated micro-mirror platform; measured at each secondary anchor

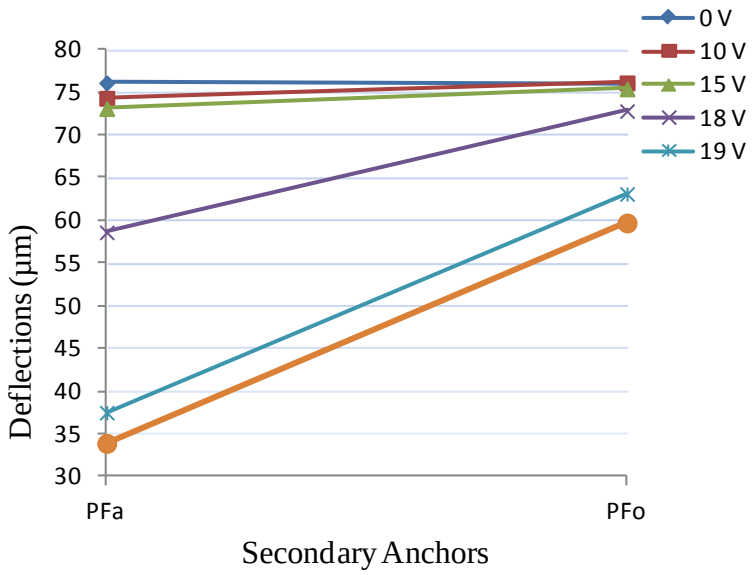

Figure 116: Graph of measured micro-mirror platform deflection results for pull-in test of PolyMUMPs® fabricated 10-beam micro-mirror platform; measured on actuation side (PF_a) and side opposite actuation (PF_o)

Table 40: Measured deflection results for pull-in of PolyMUMPs® fabricated micro-mirror platform assembly with four 9-beam "zipper" actuators; (a) device 1 test results, (b) device 2 test results

	1	2	3	4	5	6	7	8	9	PFa	PFo
0 V	18	18	28	31	37	45	46	58	55	56	56
(a) 10 V	8	9	12	13	15	18	19	24	23	23	28
15 V	5	6	7	6	7	8	9	9	11	11	13
0 V	23	20	34	36	45	51	56	67	67	67	66
10 V	22	19	33	34	44	49	56	65	66	66	67
(b) 15 V	21	16	31	31	42	46	54	63	65	65	68
18 V	6	5	6	3	14	19	30	39	48	49	56
19 V	6	6	6	3	16	18	30	36	48	49	56
20 V	4	5	4	5	4	5	4	5	9	11	17

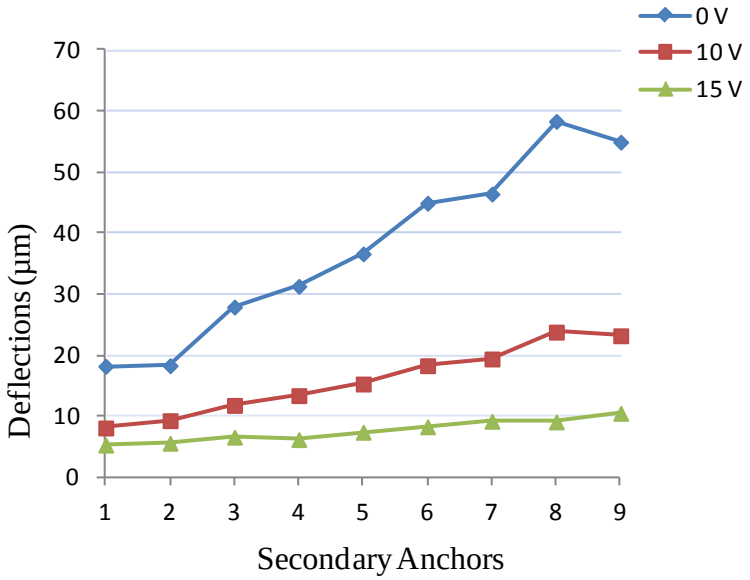

Figure 117: Graph of measured 9-beam "zipper" actuator deflection results for pull-in test of PolyMUMPs® fabricated micro-mirror platform assembly 1; measured at each secondary anchor

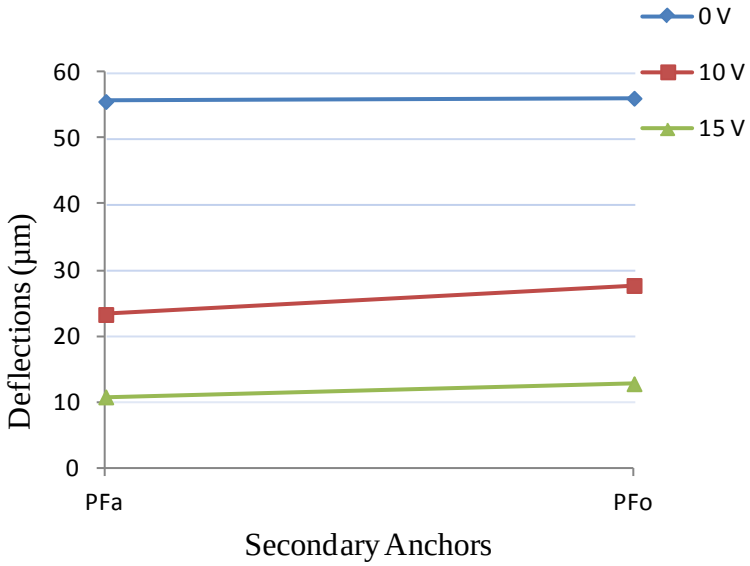

Figure 118: Graph of measured micro-mirror platform deflection results for pull-in test of PolyMUMPs® fabricated 9-beam micro-mirror platform assembly 1; measured on actuation side (PF_a) and side opposite actuation (PF_o)

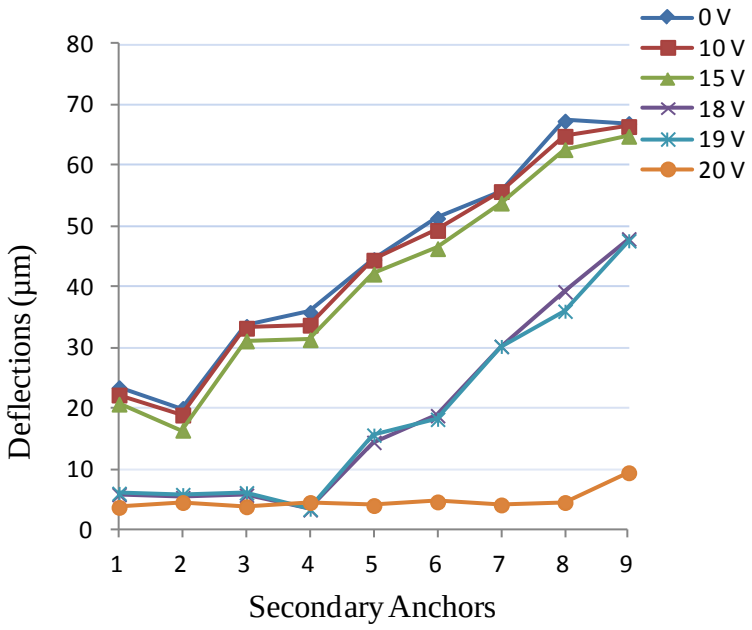

Figure 119: Graph of measured 9-beam "zipper" actuator deflection results for pull-in test of PolyMUMPs® fabricated micro-mirror platform assembly 2; measured at each secondary anchor

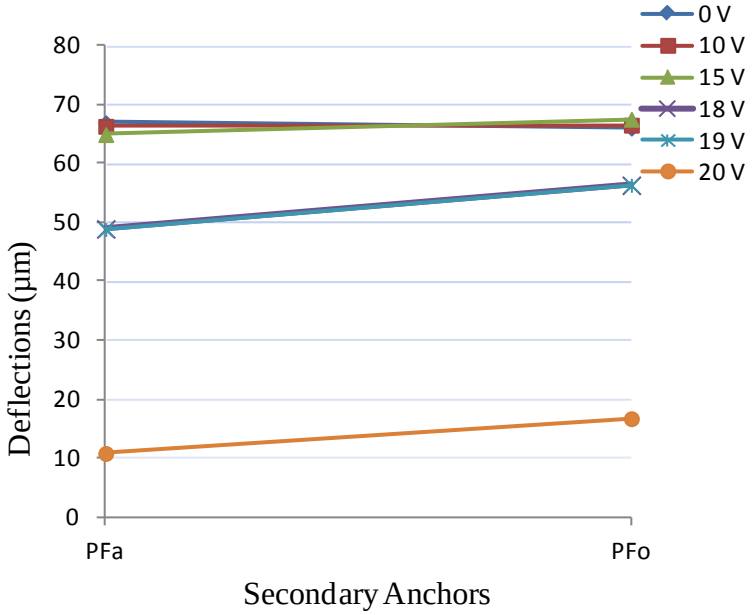

Figure 120: Graph of measured micro-mirror platform deflection results for pull-in test of PolyMUMPs® fabricated 9-beam micro-mirror platform assembly 2; measured on actuation side (PF_a) and side opposite actuation (PF_o)

Table 41: Measured deflection results for pull-in of PolyMUMPs® fabricated micro-mirror platform assembly with four 8-beam "zipper" actuators; (a) device 1 test results, (b) device 2 test results

	1	2	3	4	5	6	7	8	PFa	PFo
0 V	22	19	35	33	48	46	63	57	57	56
10 V	20	18	33	31	47	45	61	57	56	57
(a) 15 V	19	16	30	29	44	43	59	49	55	57
18 V	18	14	30	27	44	40	59	47	54	57
20 V	5	4	4	4	16	18	38	34	35	52
0 V	22	19	34	33	47	47	62	57	57	58
10 V	20	19	32	32	46	45	60	56	56	56
(b) 15 V	20	17	31	29	45	42	60	50	55	57
18 V	4	4	4	3	16	18	39	34	38	52
20 V	4	3	3	3	14	17	37	35	35	52

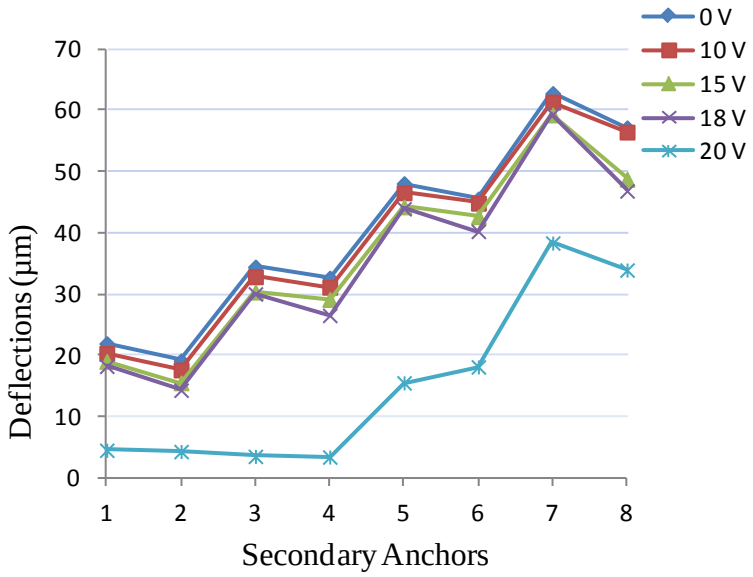

Figure 121: Graph of measured 8-beam "zipper" actuator deflection results for pull-in test of PolyMUMPs® fabricated micro-mirror platform assembly 1; measured at each secondary anchor

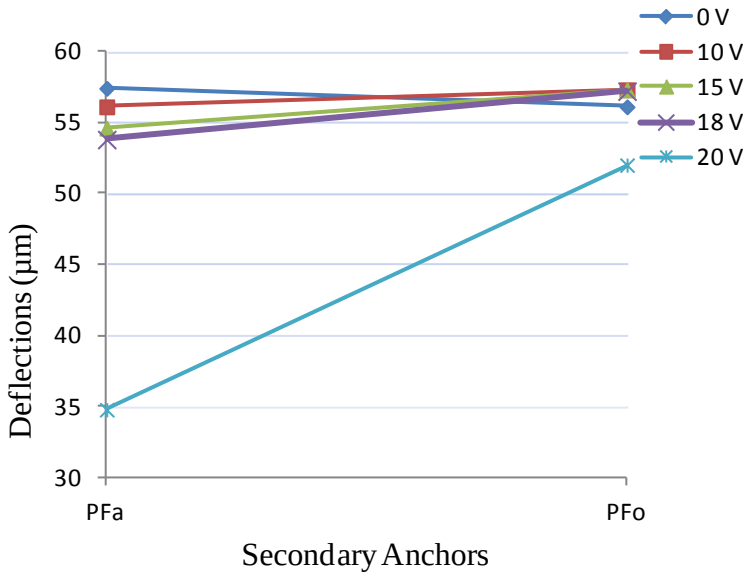

Figure 122: Graph of measured micro-mirror platform deflection results for pull-in test of PolyMUMPs® fabricated 8-beam micro-mirror platform assembly 1; measured on actuation side (PF_a) and side opposite actuation (PF_o)

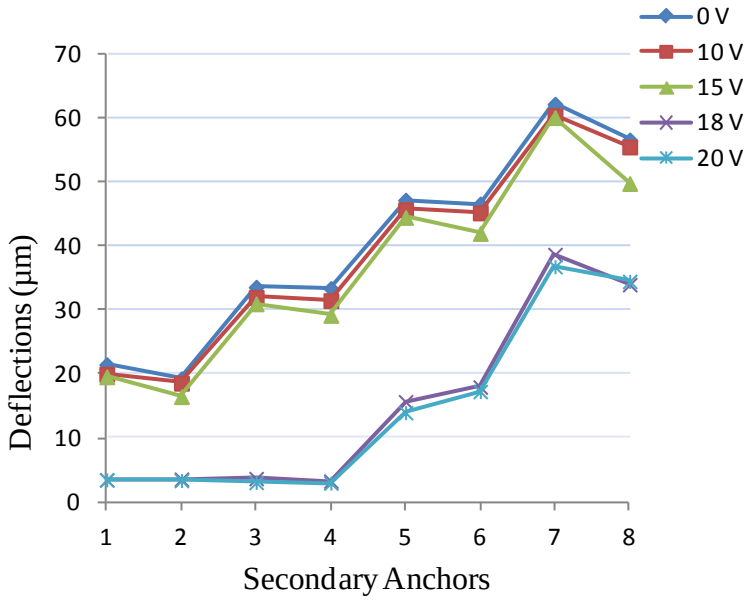

Figure 123: Graph of measured 8-beam "zipper" actuator deflection results for pull-in test of PolyMUMPs® fabricated micro-mirror platform assembly 2; measured at each secondary anchor

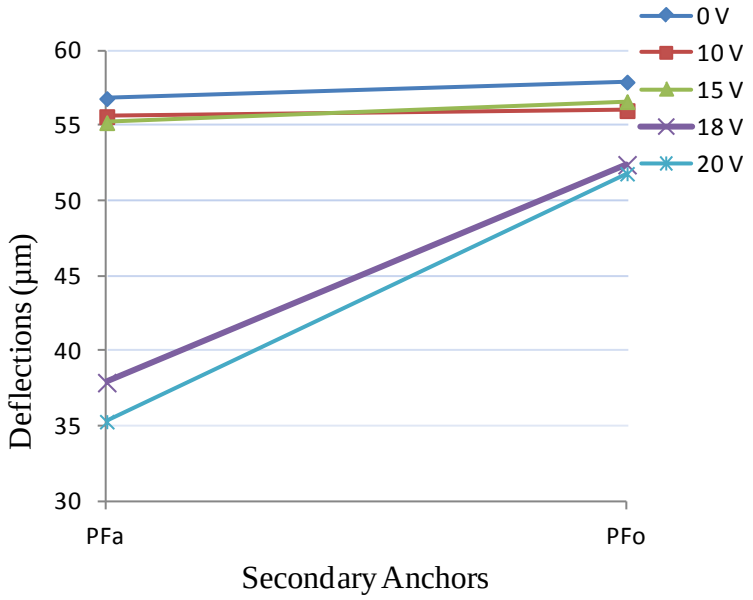

Figure 124: Graph of measured micro-mirror platform deflection results for pull-in test of PolyMUMPs® fabricated 8-beam micro-mirror platform assembly 2; measured on actuation side (PF_a) and side opposite actuation (PF_o)

Table 42: Measured deflection results for pull-in of PolyMUMPs® fabricated micro-mirror platform assembly with four 7-beam "zipper" actuators; (a) device 1 test results, (b) device 2 test results, (c) device 3 test results

		1	2	3	4	5	6	7	PFa	PFo
(a)	0 V	20	19	28	33	37	47	46	46	45
	10 V	18	16	25	29	33	43	41	41	42
	15 V	6	6	6	5	4	11	18	19	30
(b)	0 V	19	21	28	35	38	51	49	49	49
	10 V	18	19	27	34	37	50	47	48	49
	15 V	16	17	24	32	34	47	46	46	48
	18 V	6	4	4	5	5	4	19	21	41
(c)	0 V	20	20	29	35	39	51	49	49	49
	10 V	19	19	28	34	38	49	48	48	50
	15 V	18	17	27	31	36	47	46	46	50
	18 V	6	5	6	6	5	10	3	3	14

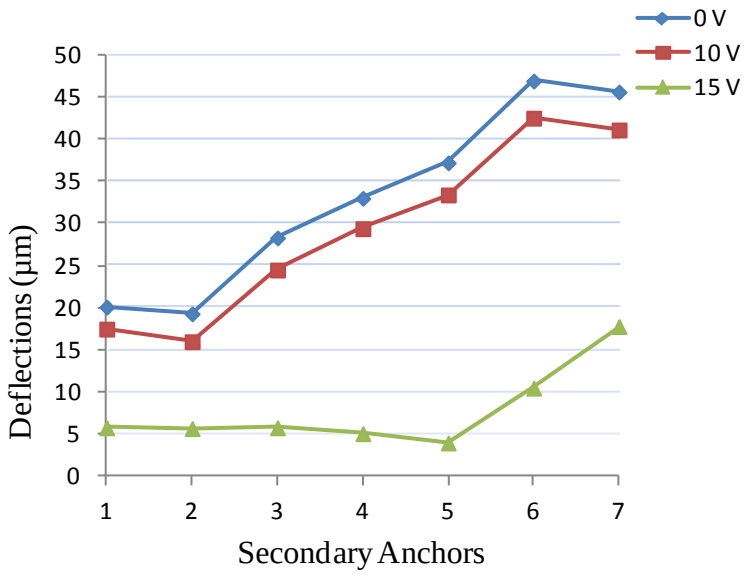

Figure 125: Graph of measured 7-beam "zipper" actuator deflection results for pull-in test of PolyMUMPs® fabricated micro-mirror platform assembly 1; measured at each secondary anchor

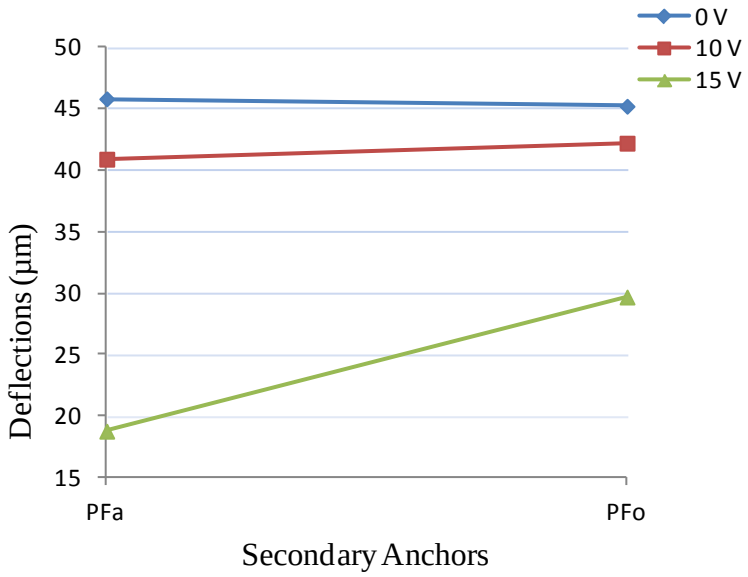

Figure 126: Graph of measured micro-mirror platform deflection results for pull-in test of PolyMUMPs® fabricated 7-beam micro-mirror platform assembly 1; measured on actuation side (PF_a) and side opposite actuation (PF_o)

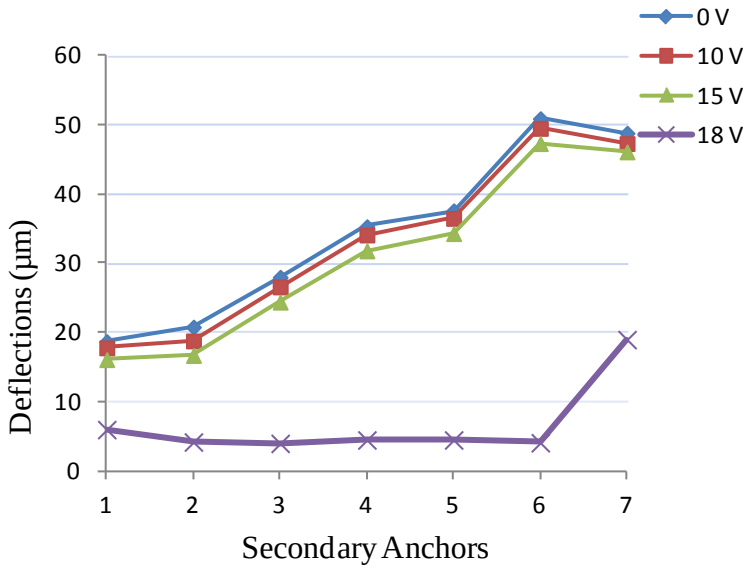

Figure 127: Graph of measured 7-beam "zipper" actuator deflection results for pull-in test of PolyMUMPs® fabricated micro-mirror platform assembly 2; measured at each secondary anchor

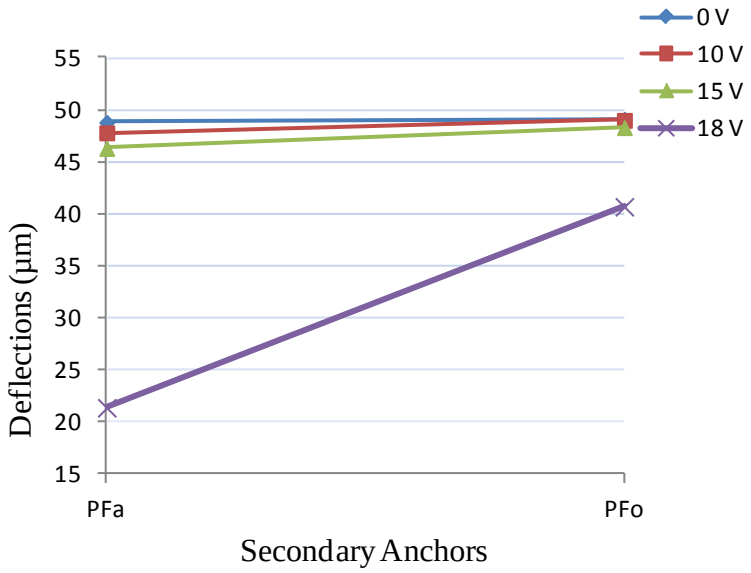

Figure 128: Graph of measured micro-mirror platform deflection results for pull-in test of PolyMUMPs® fabricated 7-beam micro-mirror platform assembly 2; measured on actuation side (PF_a) and side opposite actuation (PF_o)

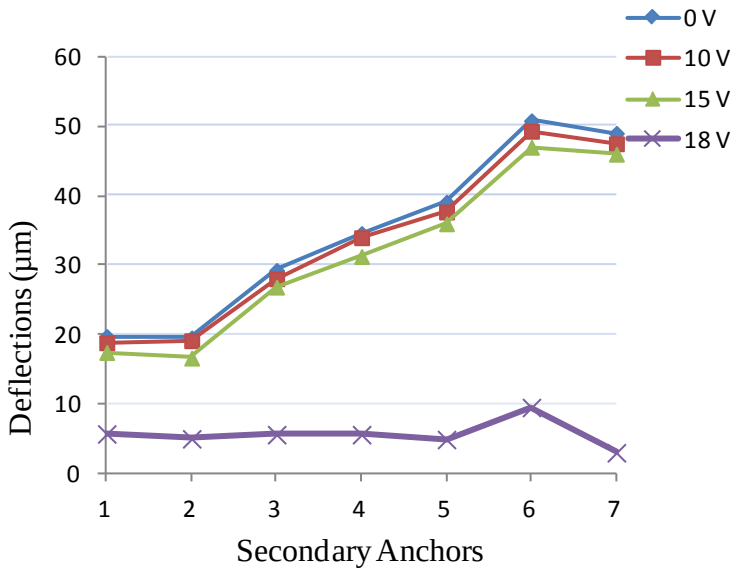

Figure 129: Graph of measured 7-beam "zipper" actuator deflection results for pull-in test of PolyMUMPs® fabricated micro-mirror platform assembly 3; measured at each secondary anchor

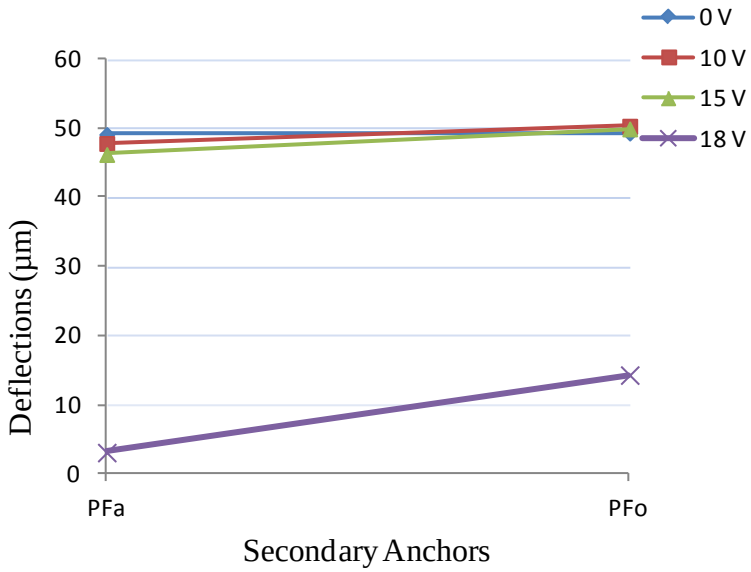

Figure 130: Graph of measured micro-mirror platform deflection results for pull-in test of PolyMUMPs® fabricated 7-beam micro-mirror platform assembly 3; measured on actuation side (PF_a) and side opposite actuation (PF_o)

Table 43: Measured deflection results for pull-in of PolyMUMPs® fabricated micro-mirror platform assembly with four 6-beam "zipper" actuators; (a) device 1 test results, (b) device 2 test results

	1	2	3	4	5	6	PFa	PFo
0 V	21	18	33	30	46	41	41	42
10 V	19	16	32	28	45	40	41	41
(a) 15 V	18	12	28	23	42	37	37	40
18 V	6	6	6	5	24	20	22	35
19 V	5	5	5	5	21	19	21	34
0 V	4	20	23	29	42	41	40	43
10 V	4	16	21	27	40	37	38	42
(b) 15 V	4	14	18	25	39	35	36	42
18 V	3	13	17	24	37	34	36	41
19 V	4	4	4	4	9	17	20	34

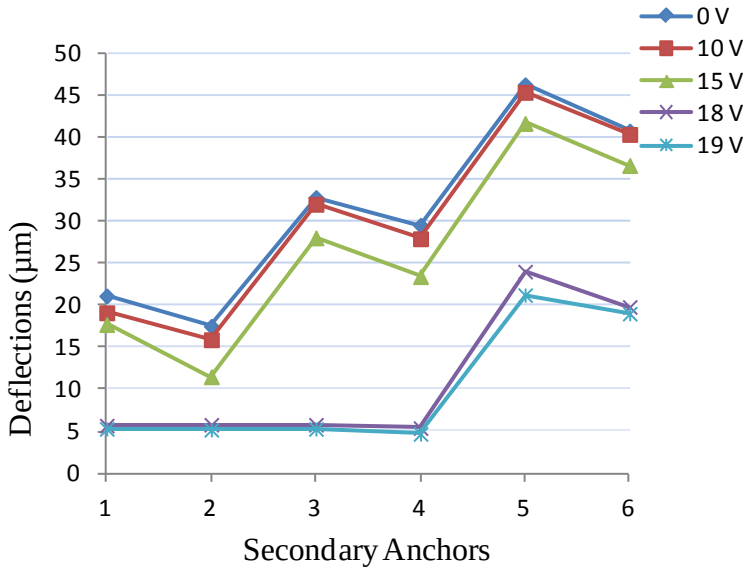

Figure 131: Graph of measured 6-beam "zipper" actuator deflection results for pull-in test of PolyMUMPs® fabricated micro-mirror platform assembly 1; measured at each secondary anchor

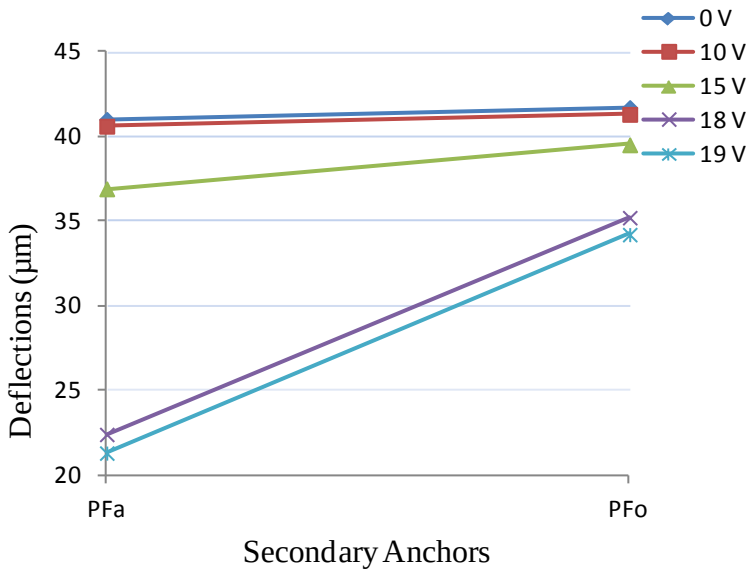

Figure 132: Graph of measured micro-mirror platform deflection results for pull-in test of PolyMUMPs® fabricated 6-beam micro-mirror platform assembly 1; measured on actuation side (PF_a) and side opposite actuation (PF_o)

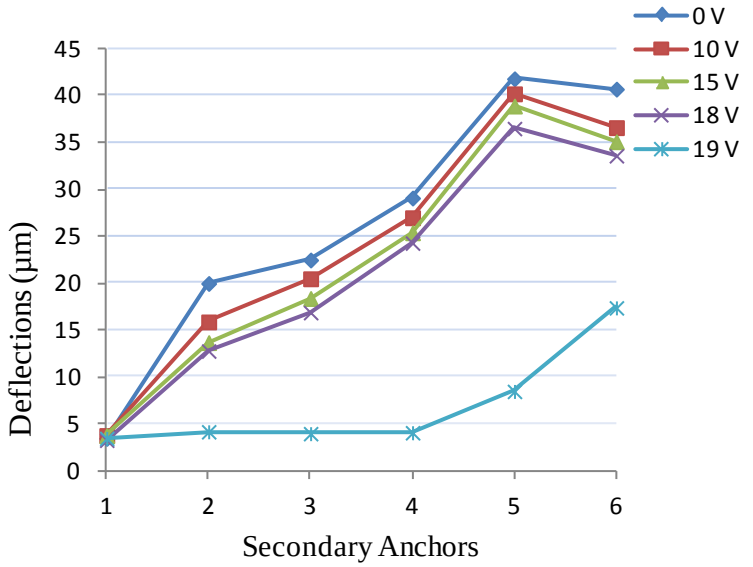

Figure 133: Graph of measured 6-beam "zipper" actuator deflection results for pull-in test of PolyMUMPs® fabricated micro-mirror platform assembly 2; measured at each secondary anchor

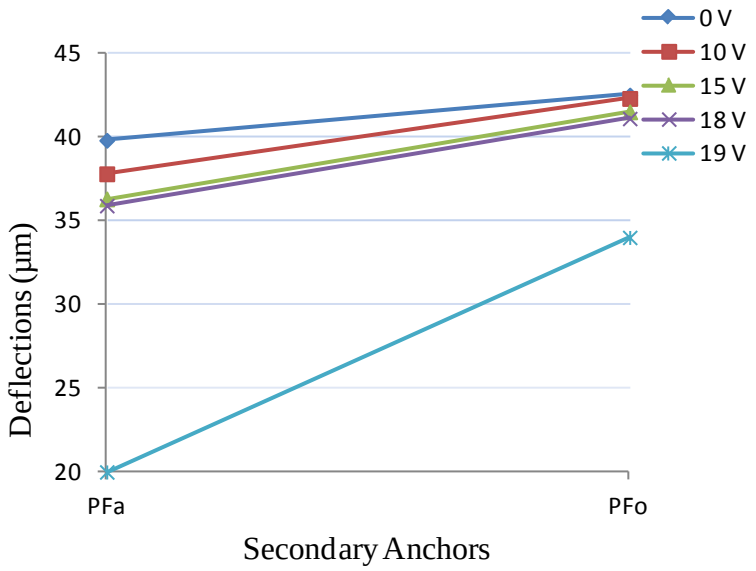

Figure 134: Graph of measured micro-mirror platform deflection results for pull-in test of PolyMUMPs® fabricated 6-beam micro-mirror platform assembly 2; measured on actuation side (PF_a) and side opposite actuation (PF_o)

Table 44: Measured deflection results for pull-in of PolyMUMPs® fabricated micro-mirror platform assembly with four 5-beam "zipper" actuators; (a) device 1 test results, (b) device 2 test results

	1	2	3	4	5	PFa	PFo
0 V	20	23	29	41	39	39	40
10 V	19	22	28	40	38	38	40
(a) 15 V	18	21	27	39	37	37	39
18 V	17	19	26	37	36	36	39
20 V	3	3	3	3	3	3	6
0 V	20	24	29	43	42	42	41
10 V	19	23	29	41	41	41	42
(b) 15 V	19	22	26	40	39	39	42
18 V	18	20	25	39	38	37	41
20 V	3	4	3	3	3	4	7

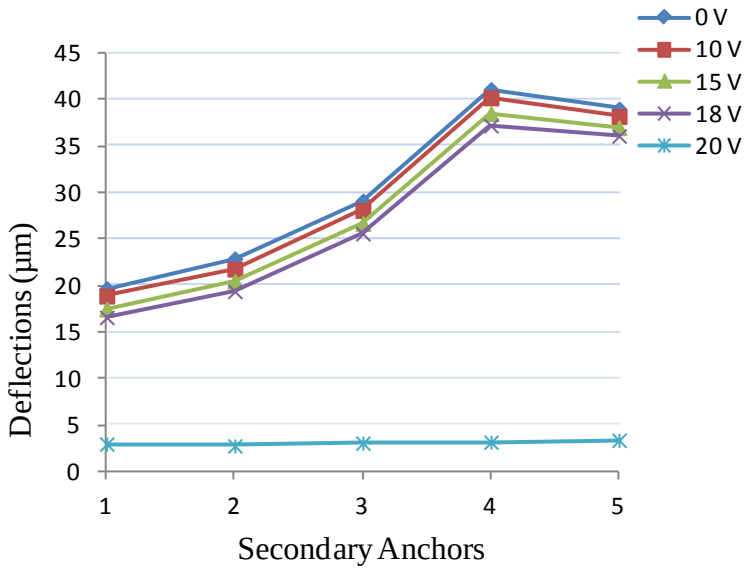

Figure 135: Graph of measured 5-beam "zipper" actuator deflection results for pull-in test of PolyMUMPs® fabricated micro-mirror platform assembly 1; measured at each secondary anchor

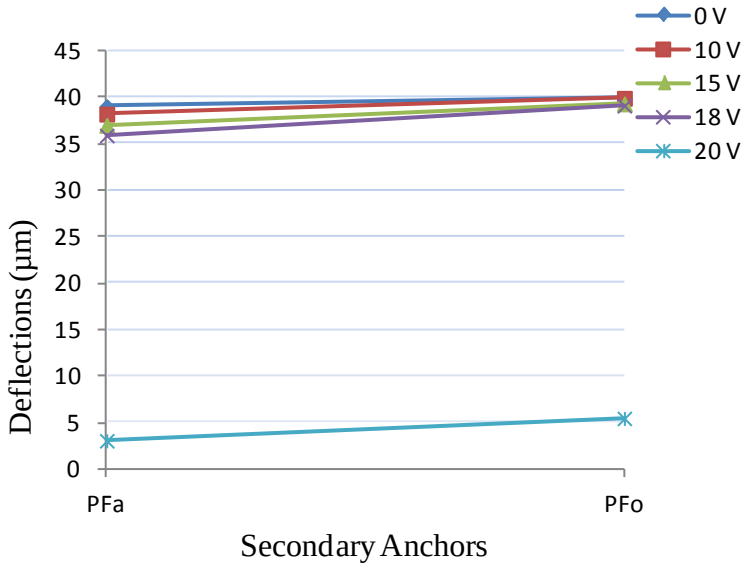

Figure 136: Graph of measured micro-mirror platform deflection results for pull-in test of PolyMUMPs® fabricated 5-beam micro-mirror platform assembly 1; measured on actuation side (PF_a) and side opposite actuation (PF_o)

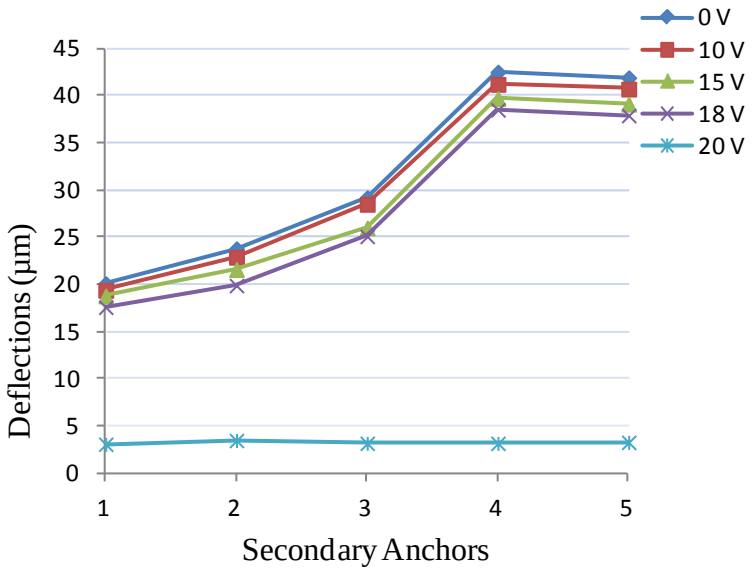

Figure 137: Graph of measured 5-beam "zipper" actuator deflection results for pull-in test of PolyMUMPs® fabricated micro-mirror platform assembly 2; measured at each secondary anchor

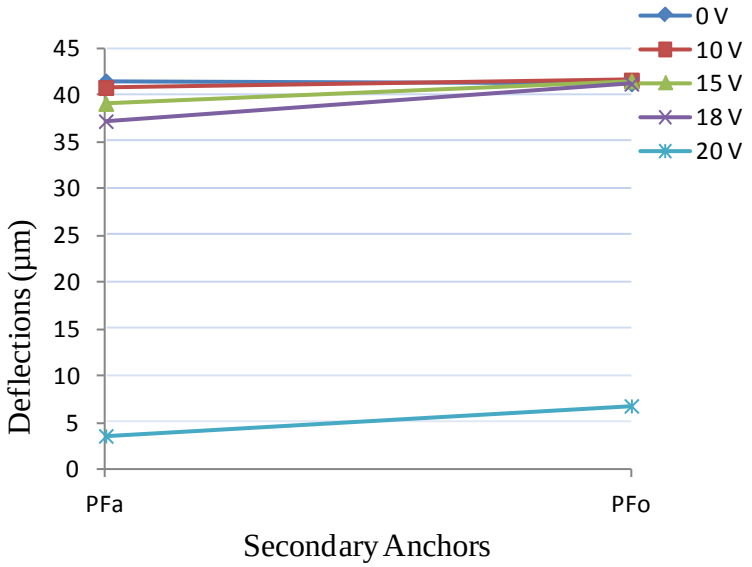

Figure 138: Graph of measured micro-mirror platform deflection results for pull-in test of PolyMUMPs® fabricated 5-beam micro-mirror platform assembly 2; measured on actuation side (PF_a) and side opposite actuation (PF_o)

Table 45: Measured deflection results for pull-in of PolyMUMPs® fabricated micro-mirror platform assembly with four 4-beam "zipper" actuators; (a) device 1 test results, (b) device 2 test results

	1	2	3	4	PFa	PFo
0 V	22	19	36	31	31	31
10 V	22	17	35	29	30	30
(a) 15 V	21	16	34	29	29	28
20 V	20	16	31	26	27	27
25 V	17	14	28	24	24	24
27 V	16	14	26	23	23	23
0 V	22	18	36	31	31	31
10 V	22	18	35	29	30	30
(b) 15 V	20	17	33	28	29	29
20 V	19	16	31	26	27	27
25 V	17	15	28	23	24	24
27 V	16	13	26	23	23	23

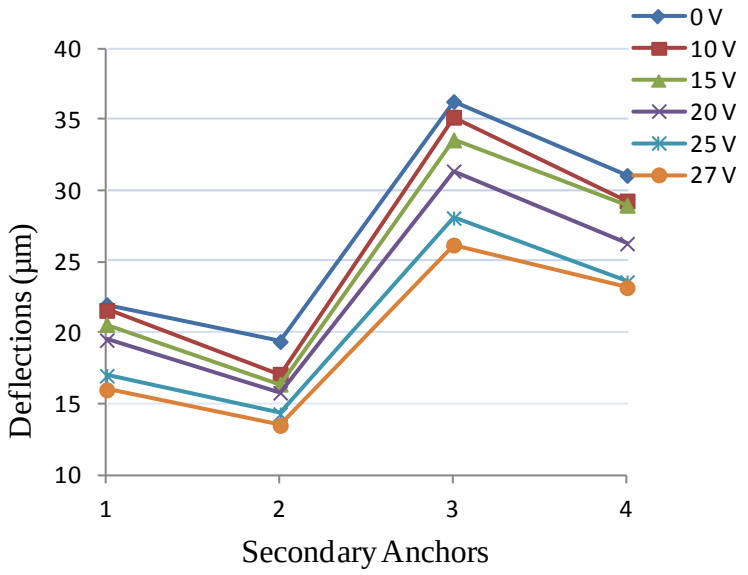

Figure 139: Graph of measured 4-beam "zipper" actuator deflection results for pull-in test of PolyMUMPs® fabricated micro-mirror platform assembly 1; measured at each secondary anchor

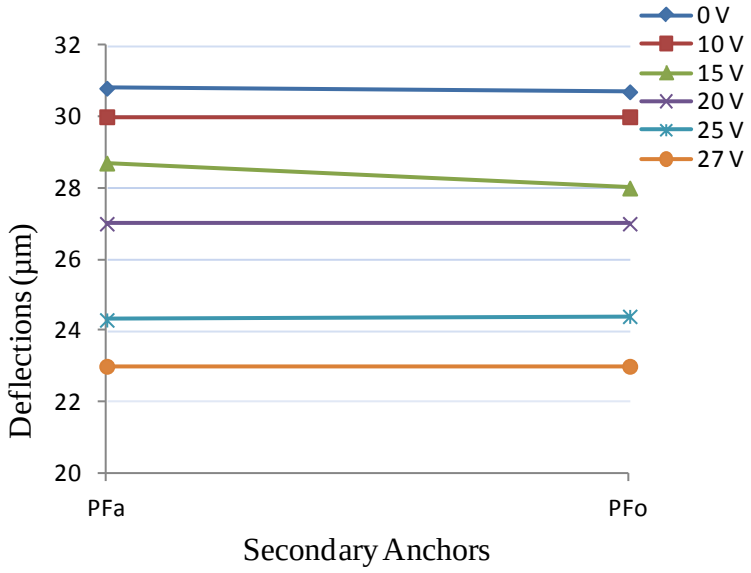

Figure 140: Graph of measured micro-mirror platform deflection results for pull-in test of PolyMUMPs® fabricated 4-beam micro-mirror platform assembly 1; measured on actuation side (PF_a) and side opposite actuation (PF_o)

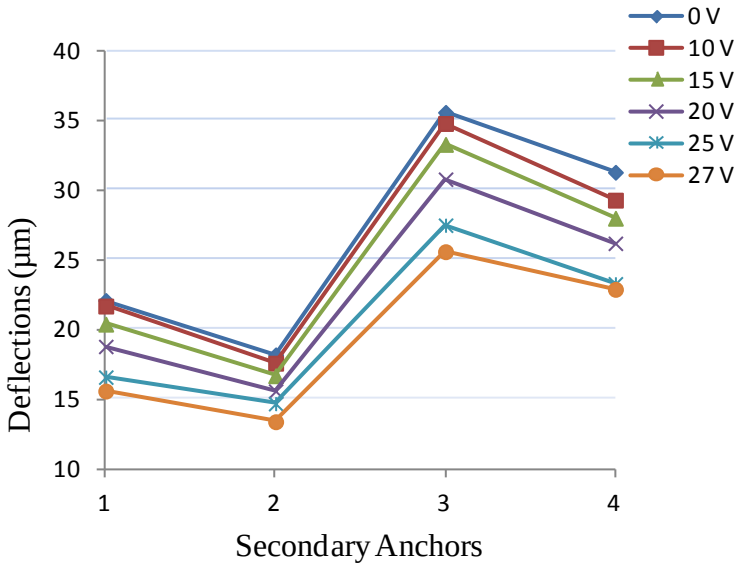

Figure 141: Graph of measured 4-beam "zipper" actuator deflection results for pull-in test of PolyMUMPs® fabricated micro-mirror platform assembly 2; measured at each secondary anchor

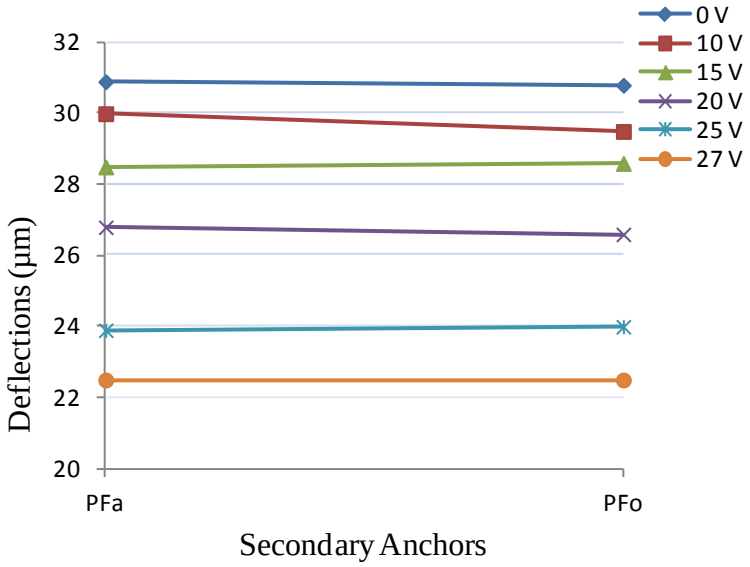

Figure 142: Graph of measured micro-mirror platform deflection results for pull-in test of PolyMUMPs® fabricated 4-beam micro-mirror platform assembly 2; measured on actuation side (PF_a) and side opposite actuation (PF_o)

Table 46: Measured deflection results for pull-in of PolyMUMPs® fabricated micro-mirror platform assembly with four 3-beam "zipper" actuators; (a) device 1 test results, (b) device 2 test results, (c) device 3 test results

	1	2	3	PFa	PFo
0 V	19	25	26	27	27
10 V	19	25	26	26	26
(a) 15 V	18	24	24	25	25
18 V	17	22	23	23	23
25 V	16	21	22	22	22
28 V	15	19	20	21	20
0 V	20	25	27	27	27
10 V	19	24	25	26	26
15 V	19	24	25	25	25
(b) 18 V	17	22	23	24	24
25 V	17	22	22	23	23
28 V	16	21	21	22	22
0 V	19	25	26	27	26
10 V	19	24	25	26	26
(c) 15 V	18	23	24	25	25
18 V	17	22	23	24	24
25 V	17	21	22	22	22
28 V	15	19	20	20	20

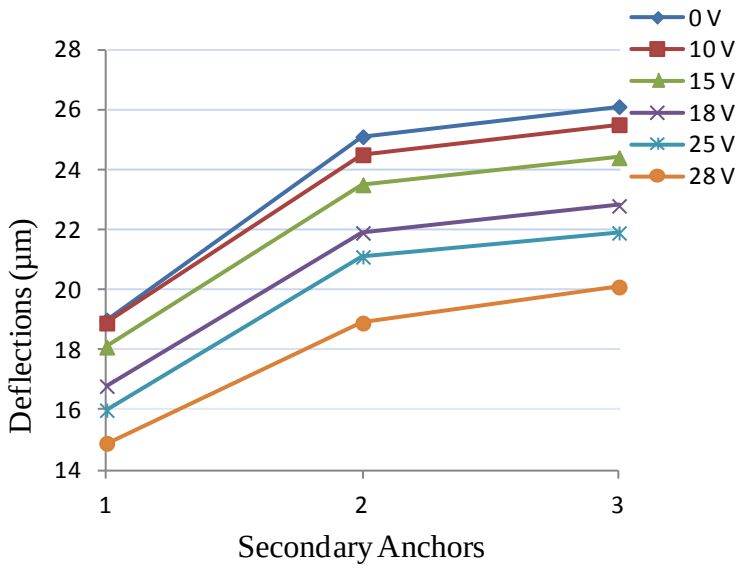

Figure 143: Graph of measured 3-beam "zipper" actuator deflection results for pull-in test of PolyMUMPs® fabricated micro-mirror platform assembly 1; measured at each secondary anchor

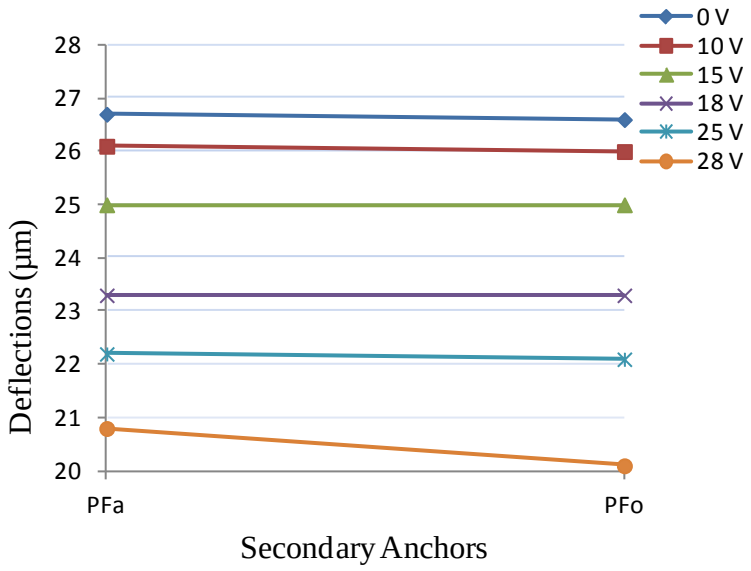

Figure 144: Graph of measured micro-mirror platform deflection results for pull-in test of PolyMUMPs® fabricated 3-beam micro-mirror platform assembly 1; measured on actuation side (PF_a) and side opposite actuation (PF_o)

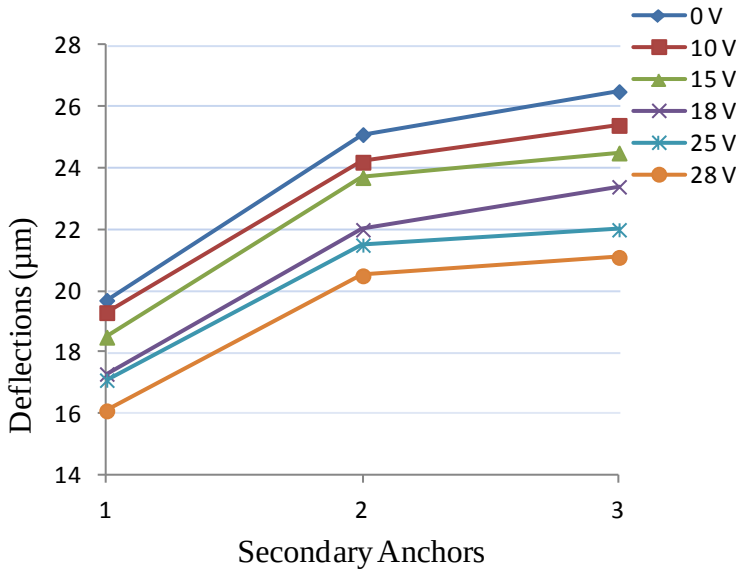

Figure 145: Graph of measured 3-beam "zipper" actuator deflection results for pull-in test of PolyMUMPs® fabricated micro-mirror platform assembly 2; measured at each secondary anchor

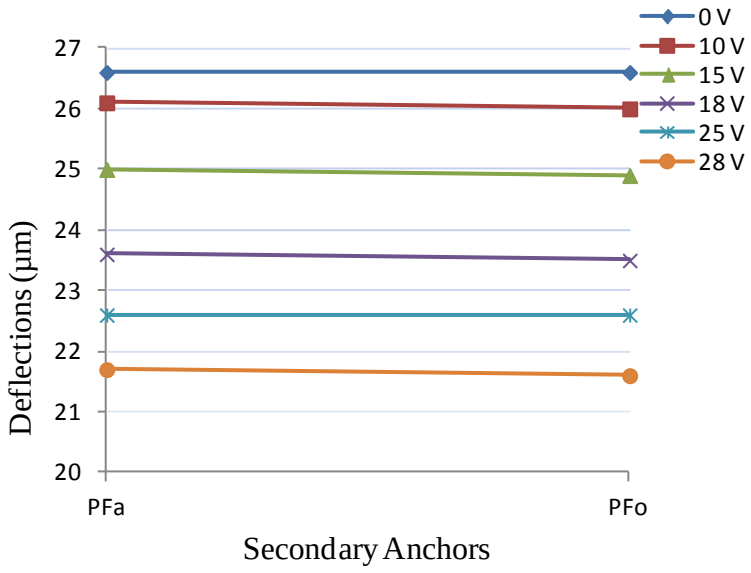

Figure 146: Graph of measured micro-mirror platform deflection results for pull-in test of PolyMUMPs® fabricated 3-beam micro-mirror platform assembly 2; measured on actuation side (PF_a) and side opposite actuation (PF_o)

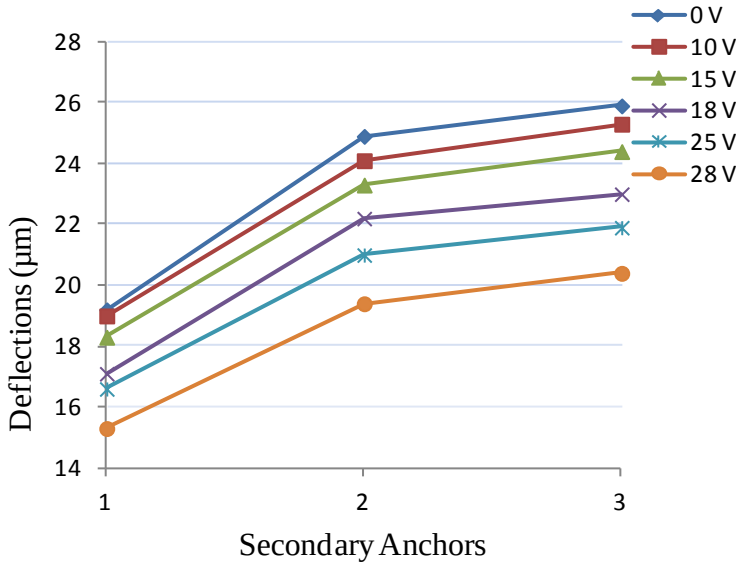

Figure 147: Graph of measured 3-beam "zipper" actuator deflection results for pull-in test of PolyMUMPs® fabricated micro-mirror platform assembly 3; measured at each secondary anchor

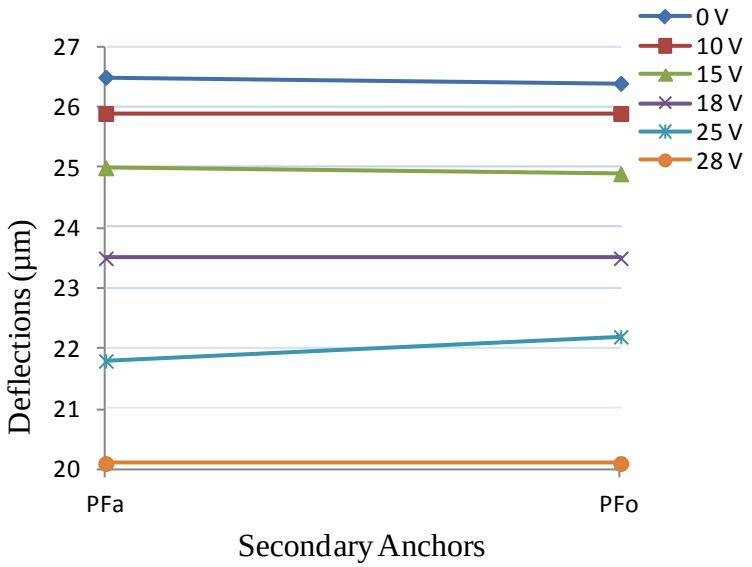

Figure 148: Graph of measured micro-mirror platform deflection results for pull-in test of PolyMUMPs® fabricated 3-beam micro-mirror platform assembly 3; measured on actuation side (PF_a) and side opposite actuation (PF_o)

Table 47: Measured deflection results for pull-in of PolyMUMPs® fabricated micro-mirror platform assembly with four 11-beam (corrugated) "zipper" actuators; (a) device 1 test results, (b) device 2 test results, (c) device 3 test results

	1	2	3	4	5	6	7	8	9	10	11	PFa	PFo
0 V	23	21	33	35	43	50	53	66	64	83	76	76	77
10 V	13	4	9	21	22	31	34	44	47	58	60	61	73
(a) 15 V	6	3	3	19	14	29	25	37	36	46	48	49	64
18 V	4	3	3	18	11	25	20	31	29	36	42	43	59
19 V	3	3	3	18	10	24	19	29	27	33	39	39	57
20 V	3	3	3	17	9	23	17	27	25	30	36	37	55
0 V	21	18	32	33	41	47	52	61	63	76	75	75	75
10 V	11	3	13	3	25	18	34	33	44	48	58	59	69
15 V	6	3	4	19	13	26	24	33	35	39	48	49	62
(b) 18 V	4	3	3	17	11	23	20	27	29	31	40	42	57
19 V	3	2	2	16	9	22	18	25	26	28	38	39	56
20 V	3	2	3	16	9	21	17	22	25	26	36	37	54
0 V	15	8	20	19	32	36	43	52	55	68	68	69	69
10 V	14	4	9	18	20	30	33	42	45	54	58	58	64
15 V	7	4	3	20	13	29	24	34	35	39	47	48	58
(c) 18 V	5	3	3	19	10	26	20	30	29	34	40	41	54
19 V	4	3	3	19	10	25	18	29	26	30	37	38	51
20 V	10	3	3	11	3	15	10	18	18	21	29	30	45
25 V	3	3	3	10	3	11	3	14	10	15	21	23	39

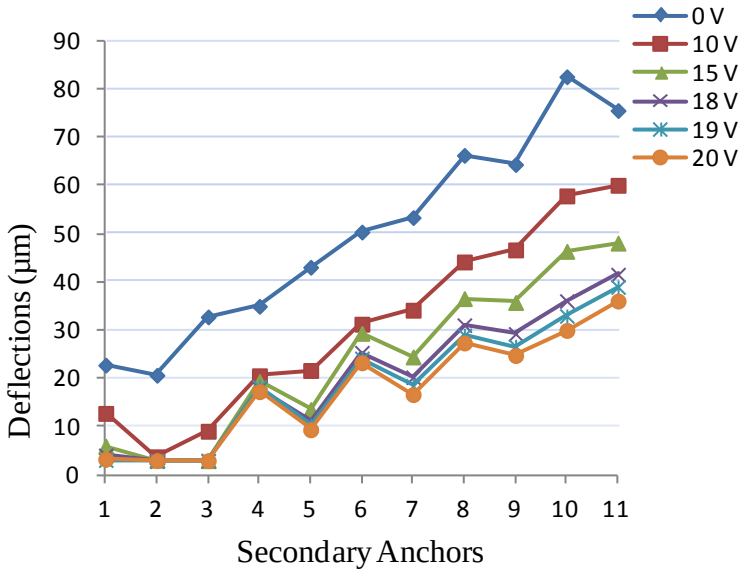

Figure 149: Graph of measured 11-beam (corrugated) "zipper" actuator deflection results for pull-in test of PolyMUMPs® fabricated micro-mirror platform assembly 1; measured at each secondary anchor

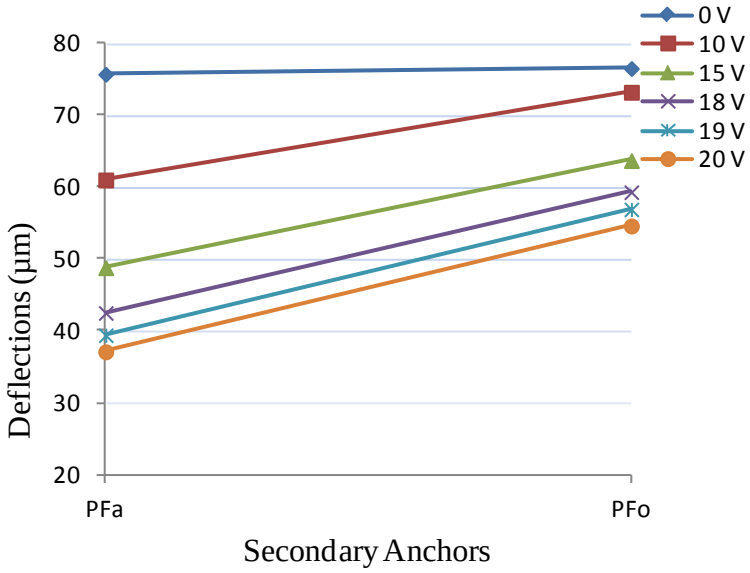

Figure 150: Graph of measured micro-mirror platform deflection results for pull-in test of PolyMUMPs® fabricated 11-beam (corrugated) micro-mirror platform assembly 1; measured on actuation side (PF_a) and side opposite actuation (PF_o)

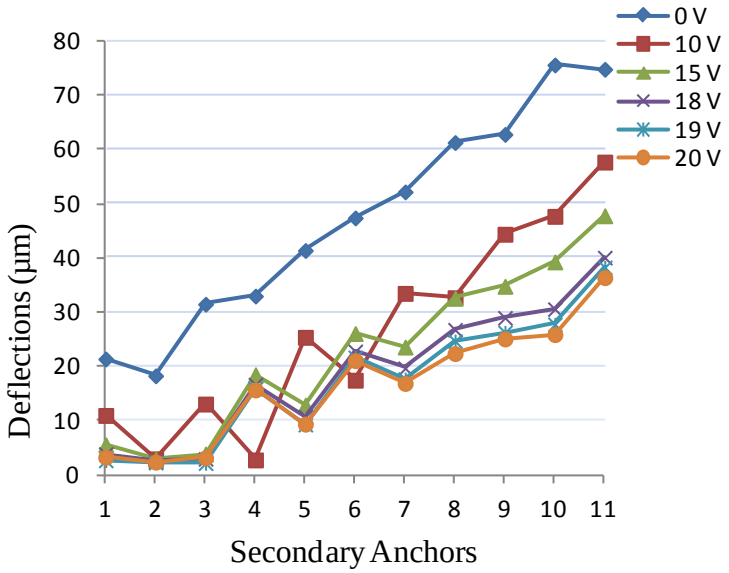

Figure 151: Graph of measured 11-beam (corrugated) "zipper" actuator deflection results for pull-in test of PolyMUMPs® fabricated micro-mirror platform assembly 2; measured at each secondary anchor

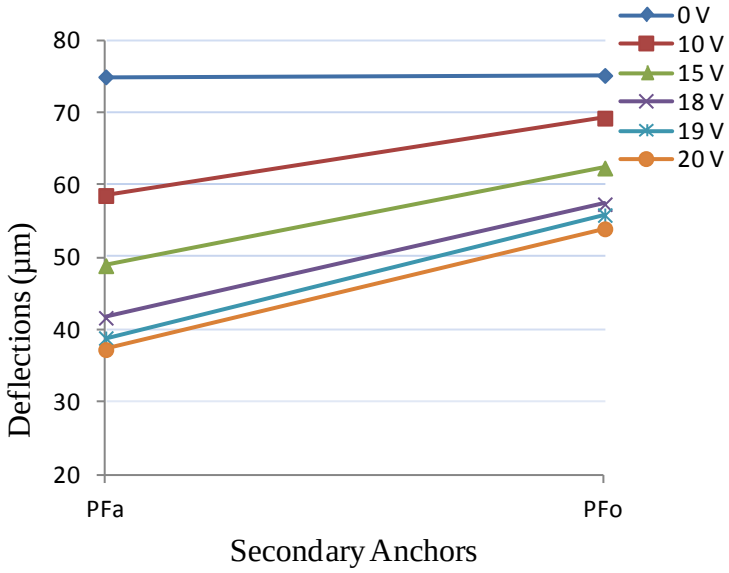

Figure 152: Graph of measured micro-mirror platform deflection results for pull-in test of PolyMUMPs® fabricated 11-beam (corrugated) micro-mirror platform assembly 2; measured on actuation side (PF_a) and side opposite actuation (PF_o)

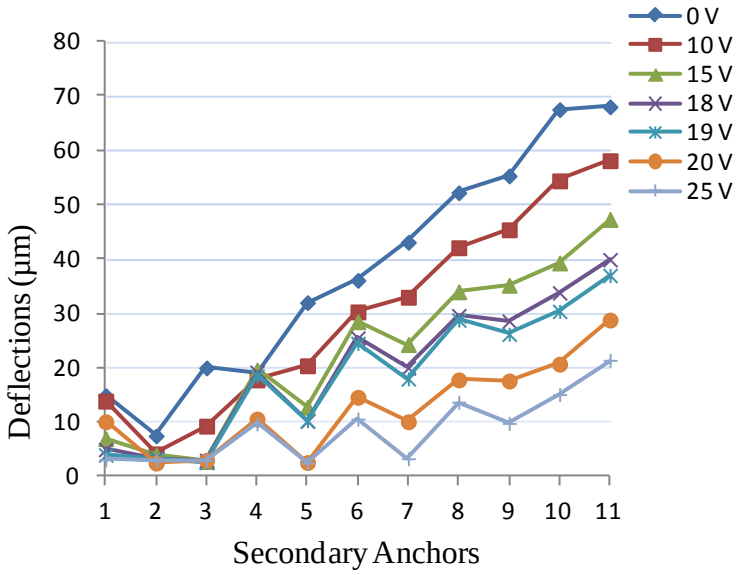

Figure 153: Graph of measured 11-beam (corrugated) "zipper" actuator deflection results for pull-in test of PolyMUMPs® fabricated micro-mirror platform assembly 3; measured at each secondary anchor

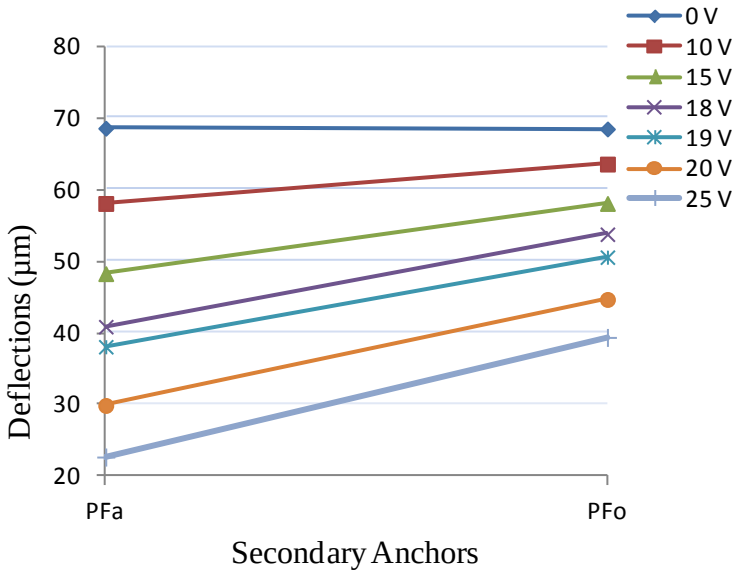

Figure 154: Graph of measured micro-mirror platform deflection results for pull-in test of PolyMUMPs® fabricated 11-beam (corrugated) micro-mirror platform assembly 3; measured on actuation side (PF_a) and side opposite actuation (PF_o)

Table 48: Measured deflection results for pull-in of PolyMUMPs® fabricated micro-mirror platform assembly with four 7-beam (corrugated) “zipper” actuators; (a) device 1 test results, (b) device 2 test results, (c) device 3 test results

	1	2	3	4	5	6	7	PFa	PFo
0 V	10	35	27	40	36	53	49	50	51
10 V	3	3	19	20	30	36	41	41	48
(a) 15 V	3	3	16	11	23	20	31	32	43
18 V	3	3	4	3	19	3	26	27	38
0 V	20	25	27	43	38	58	51	52	54
10 V	16	5	20	25	29	44	44	45	52
15 V	7	2	3	21	14	30	30	33	45
(b) 18 V	3	3	3	21	12	26	27	27	42
19 V	3	2	3	19	12	25	25	26	41
20 V	3	3	2	19	10	22	24	24	39
0 V	4	26	3	36	26	46	45	46	47
10 V	4	22	3	29	17	30	33	33	40
(c) 15 V	3	17	4	17	8	13	18	19	31
18 V	4	12	4	14	3	7	11	12	21
19 V	4	12	4	13	3	6	11	11	20

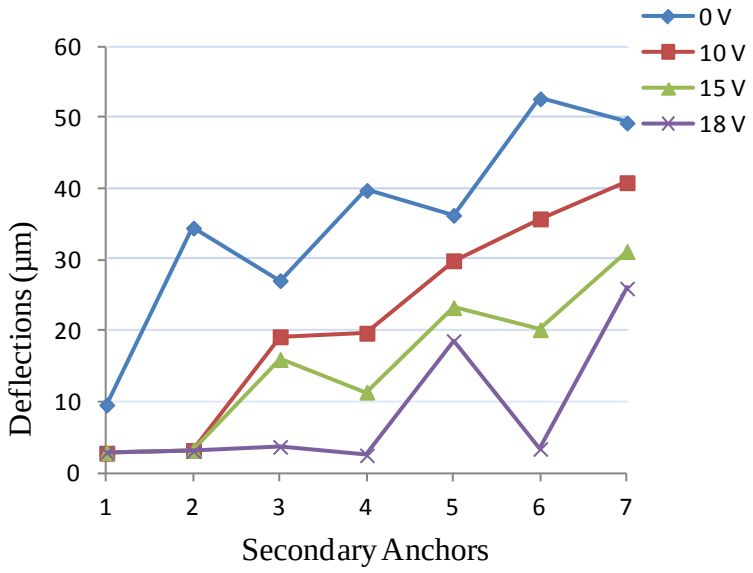

Figure 155: Graph of measured 7-beam (corrugated) "zipper" actuator deflection results for pull-in test of PolyMUMPs® fabricated micro-mirror platform assembly 1; measured at each secondary anchor

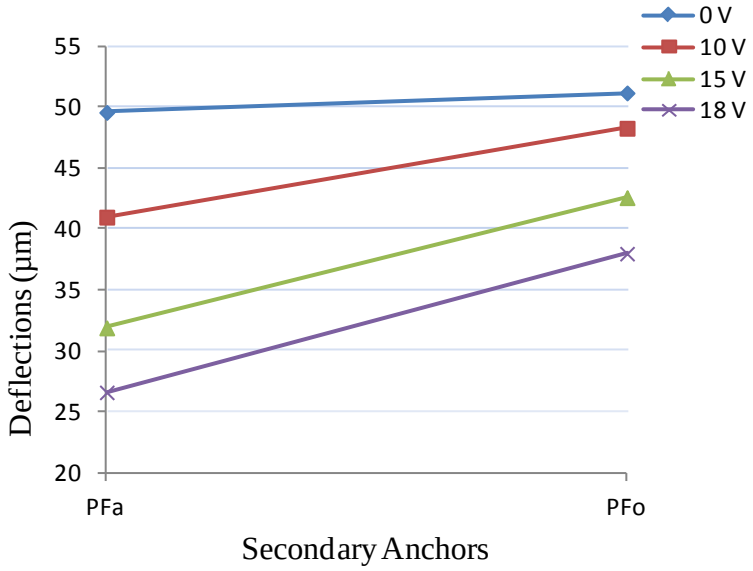

Figure 156: Graph of measured micro-mirror platform deflection results for pull-in test of PolyMUMPs® fabricated 7-beam (corrugated) micro-mirror platform assembly 1; measured on actuation side (PF_a) and side opposite actuation (PF_o)

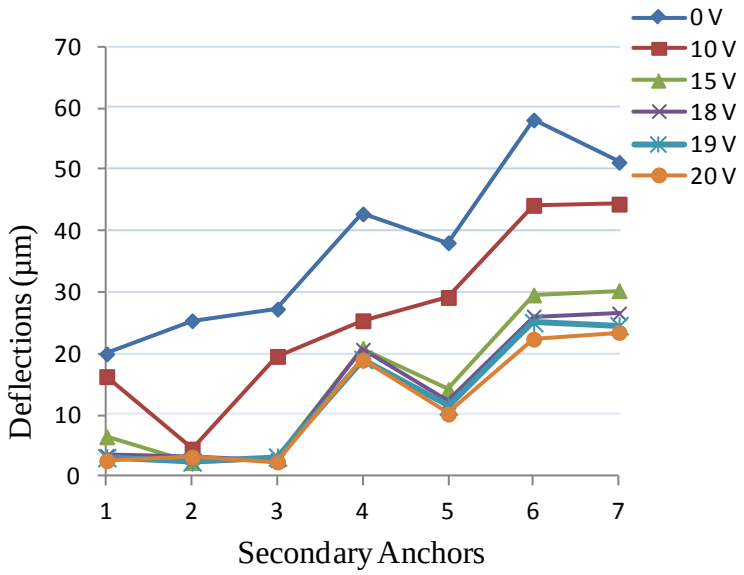

Figure 157: Graph of measured 7-beam (corrugated) "zipper" actuator deflection results for pull-in test of PolyMUMPs® fabricated micro-mirror platform assembly 2; measured at each secondary anchor

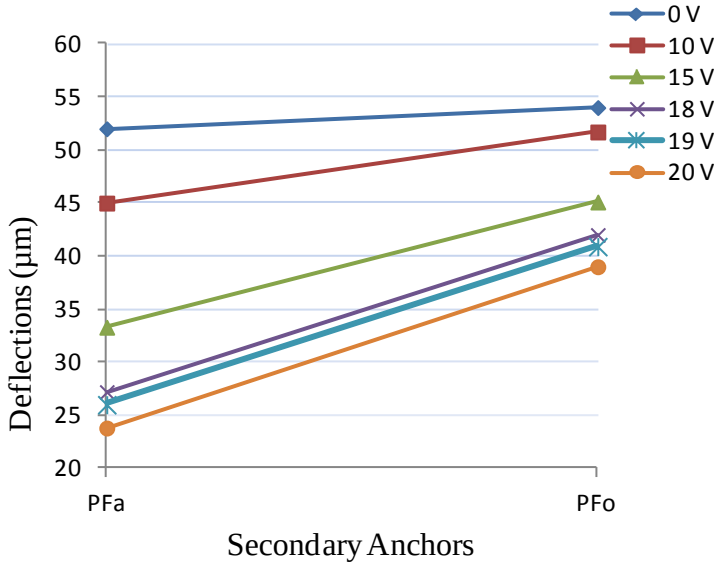

Figure 158: Graph of measured micro-mirror platform deflection results for pull-in test of PolyMUMPs® fabricated 7-beam (corrugated) micro-mirror platform assembly 2; measured on actuation side (PF_a) and side opposite actuation (PF_o)

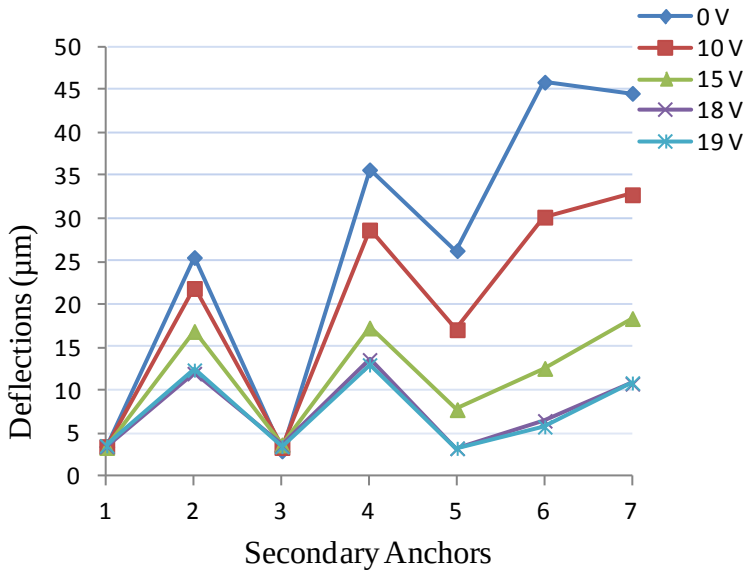

Figure 159: Graph of measured 7-beam (corrugated) "zipper" actuator deflection results for pull-in test of PolyMUMPs® fabricated micro-mirror platform assembly 3; measured at each secondary anchor

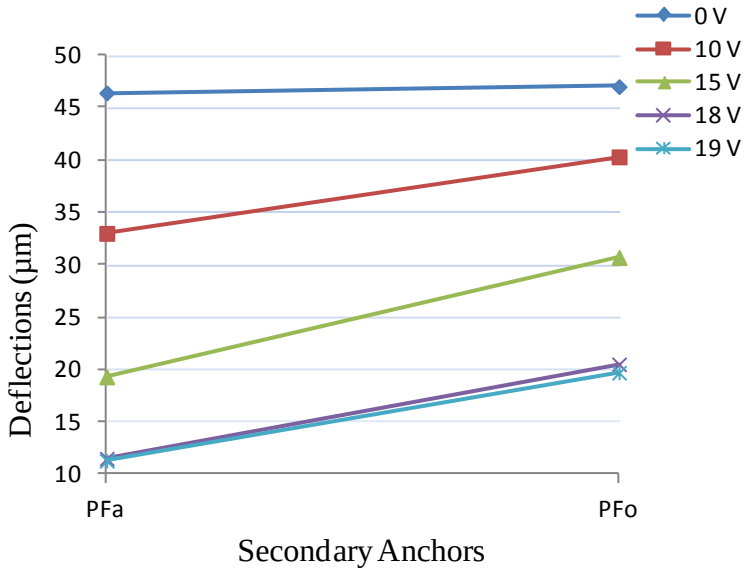

Figure 160: Graph of measured micro-mirror platform deflection results for pull-in test of PolyMUMPs® fabricated 7-beam (corrugated) micro-mirror platform assembly 1; measured on actuation side (PF_a) and side opposite actuation (PF_o)

APPENDIX I. Additional Background: Piezoelectric Material

Introduction

Piezoelectricity, stemming from piezein (Greek for ‘press’ or ‘squeeze’) combined with electricity, describes the electrical polarization which occurs in a material as a direct result of an applied force [81]. Essentially piezoelectric materials are able to convert an applied force, which induces a mechanical strain in the material, into an electrical signal. Conversely, an applied electrical field will induce a mechanical strain in the same material [82].

It is said that piezoelectricity was first conjectured by Alexandre Becquerel, pictured in Figure 161, in the mid to late 1800’s [83]. Even though Alexandre Becquerel

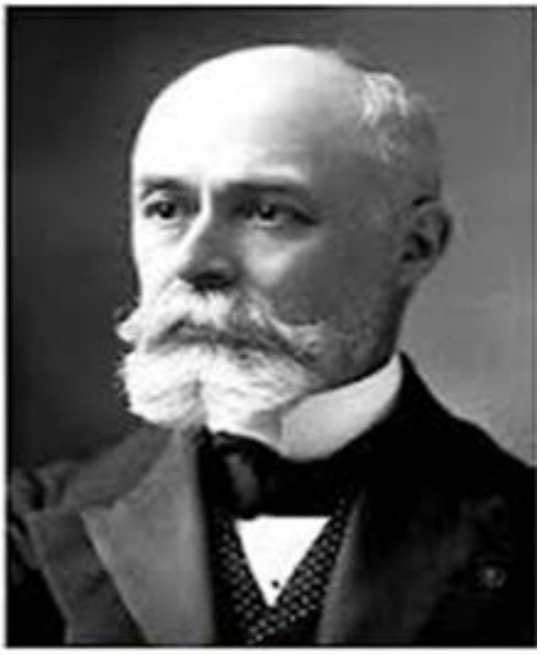

Figure 161: Alexandre Edmond Becquerel [84]

conceptualized the piezoelectric effect in crystals, history credits Pierre and Jacques Curie with the discovery of the effect and its close link to the crystal symmetry of

materials [82]. This is mainly due to the fact that the first experimental demonstration of the connection between electric fields generated in response to applied stresses (piezoelectric phenomena) and the crystallographic structures of particular materials were conducted by the Curie Brothers (Figure 162) with published results in 1880 [85]. The experiments were conducted on materials such as sodium chlorate, tourmaline, topaz,

Figure 162: Brothers and Colleagues, Jacques (left) and Pierre (right) Curie, discoverers of the piezoelectric effect [86]

cane sugar, quartz, and Rochelle salt among others; and produced conclusive measurements of the electrical charges obtained when a piece of crystal was subjected to an external force. This phenomenon is easily described by Equation 1, where $\boldsymbol{P_i}$ is a

$$\boldsymbol{P_i} = \boldsymbol{P_i^0} + \boldsymbol{_{jk}\sum d_{ijk} T_{jk}} \quad (27)$$

component of the polarization vector, $\boldsymbol{P_i^0}$ is the spontaneous polarization, $\boldsymbol{d_{ijk}}$ refers to the piezoelectric coefficient, and $\boldsymbol{T_{jk}}$ is the stress tensor component for a specific

piezoelectric material [82]. The amazing thing is that they were able to do all of this with very basic tools and equipment, by today's standards. Using nothing more than some tin foil, glue, wire, magnets, and a jeweler's saw to prepare the material for testing [85] and a Thomas electrometer (Figure 163) they were able prove that a force applied to specific types of materials can generate electricity [82].

Figure 163: Sir William Thomson's Quadrant Electrometer [87]

Interestingly, the Curie brothers did not envision the inverse effect. A year after the discovery by the Curie Brothers, mathematician Gabriel Lippmann demonstrated the possibility of the application of an electric field inducing a mechanical stress in a piezoelectric crystal [86]. This converse effect is expressed by Equation 28 where $\boldsymbol{S_{jk}}$ is the strain tensor component and $\boldsymbol{S_{jk}}^{\boldsymbol{0}}$ is the spontaneous strain of the specific piezoelectric material and $\boldsymbol{E_l}$ refers to the applied external electric field.

$$\boldsymbol{S_{jk}} = \boldsymbol{S_{jk}}^{\boldsymbol{0}} + {}_{\boldsymbol{l}}\sum \boldsymbol{d_{ijk}}\,\boldsymbol{E_l} \tag{28}$$

The Curie Brothers immediately, experimentally, verified the existence of the inverse effect of their original experiments and continued work in the field to show, through quantitative results, that the piezoelectric effects found in these specific crystal structures are completely reversible [82].

From the initial discovery in the late 1800, developments in the science of piezoelectric have advanced vary sporadically; with periods of rapid progression and periods of slow or no developments [82]. History shows that each time piezoelectric developments seemed to hit a plateau the discovery of a new piezoelectric effect or material would occur and lead to new innovations, sparking explosive developments in that new area of study. The first major development in the field of piezoelectricity, after its initial discovery, occurred in 1917 when Paul Langvin used quartz plates for the emission and detection of underwater sound waves. This was mainly in response to the use of submarines by enemy forces in World War I. The need arose to find and track targets under water, so this device was developed as an ultrasonic submarine detector [88]. This marked the first practical application of a piezoelectric device and opened the fields of ultrasonic and hydro-acoustics, and gave rise to modern sonar [82]. The next great leap occurred in 1934 when Fredrick R. Lack, while working in the radio telephone development at Bell Telephone Laboratories, developed the “AT” cut. This reduced the weight of radio technology of the day and facilitated the development of aviation radio and is still used today in applications across the world. During the 1940’s and 1950’s studies focused on the discovery of new piezoelectric materials. The first major breakthrough came with Bernard Jaffe’s discovery of the strong piezoelectric properties in ceramics; specifically his discovery of the solid solutions of lead zirconate titanate

(PZT) which then lead to the discovery of other piezoelectric materials [82, 89]. In the 1960's the need for single crystals with higher piezoelectric effects arose, leading to the 'polymer boom' and the discovery of lithium tantalite and lithium niobate [47]. Holding true to historical precedence, developments in the science of piezoelectric materials continued to ebb and flow from the 1960's through today.

Currently, piezoelectric actuators and sensors have applications in nearly every technological product today; from televisions, wrist watches, 'smart' cell phones, automobiles, etc. to more sophisticated civil, mechanical, and aerospace engineering structures for control purposes [46, 90]. Future work in the science of piezoelectricity is showing a lot of promise in the field of energy harvesting of the human movements. There are two main focus areas within this topic. One is though the harnessing of biomechanical movement within the body. A piezoelectric device attached to a constantly moving organ, such as the heart, lungs, or diaphragm has been shown to produce enough electricity to run a pacemaker [91, 92]. Figure 164 is an example of one such device which was proven to work by scientist from the University of Illinois and the University of Arizona [91]. The other approach is kinetic energy harvesting, meaning movements external to the body, such as walking, opening doors, and moving turnstiles in a subway. A great example of how this technology occurred when the 2013 Paris Marathon harnessed energy from the runners in the marathon to power the electric signs and display screens throughout the marathon [93]. When more than 40,000 participants ran across the

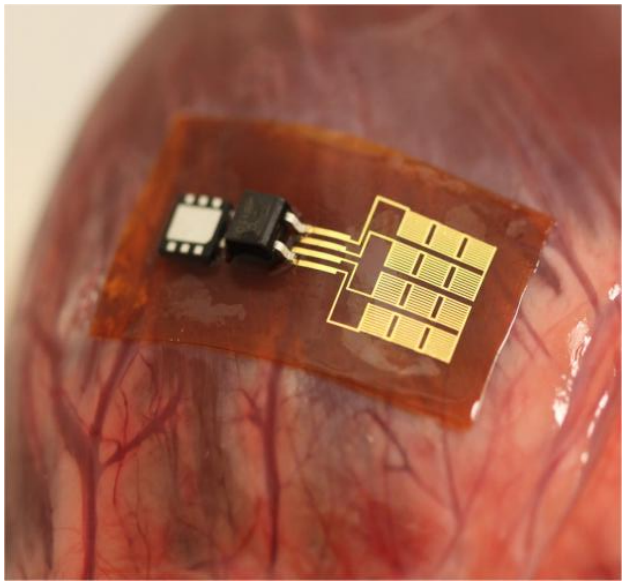

Figure 164: Thin, flexible mechanical energy harvester, with rectifier and micro-battery, mounted on a bovine heart [92]

piezoelectric pads seen in Figure 165, each step a runner took generated approximately 8 watts of energy which resulted in about 7 kilowatt hours of energy in total. Although these concepts have been proven to work, I think it will be a long while before we will see energy saving benefits on a global scale mainly due to the lack of an infrastructure to make it affordable.

Figure 165: Runners crossing piezoelectric pad during 2013 Paris Marathon [93]

At the time of this race, each tile cost over $150 each [93]; not cheap by any means but when added to the expansive bank of batteries required to store and redistribute the energy it becomes clear this is not a realistic solution at this time. That being said, for small scale applications such as piezoelectric power cells in combat boots (to provide a constant power source for small equipment in the field) I think the benefits could be immediate; as long as the fabrication cost are reasonable. Now, armed with an understanding of how and why the science of piezoelectricity came to be, we can dig a little deeper to examine what material properties within certain materials and allow this piezoelectric phenomenon to exist.

Material Properties

The piezoelectric effect can be observed in many naturally-occurring crystals, recall the materials used in the original experiments. It is also found in man-made materials such as PZT and other piezoelectric ceramics [94]. Among these polycrystalline materials, many have a perovskite crystal (tetragonal/rhombahedral) structure very close to cubic. They exhibit simple cubic symmetry with a general formula of $\boldsymbol{A^2 + B^1 + O_3^{2-}}$, as seen in Figure **166**, were A represents a large divalent metal ion such as lead, B represents a tetravalent metal ion such as zirconium, and O represents oxygen. This specific formation of the atoms in piezoelectric ceramics occurs as the material experiences a phase change brought on by cooling from a high-symmetry, high temperature phase to a non-centrosymmetric piezoelectric phase [95]. Centrosymmetric is defined as: having symmetry in relation to a center [96]. Conversely, non-

centrosymmetric refers to crystalline structures with point groups lacking an inversion center [97]. It is this phenomenon which gives the material its piezoelectric properties.

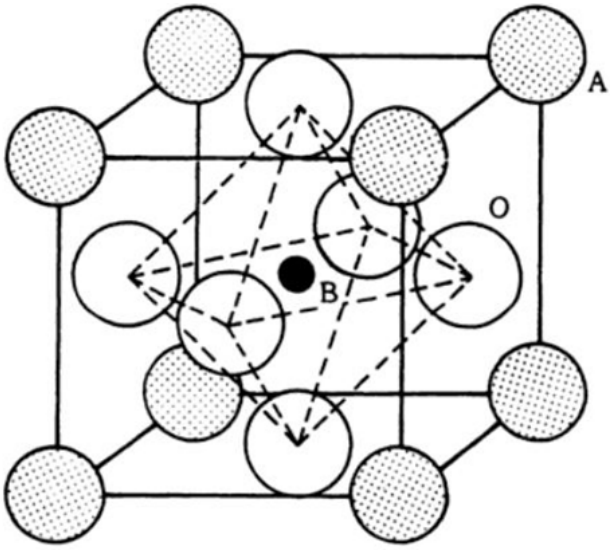

Figure 166: Perovskite Crystal Structure of ABO_3[95]

In addition to the simple form structures seen in Figure 166 much more complex structures can be formed rather easily by adding a fourth element into the structure [95]. This flexibility in material designs becomes very important when fabricating piezoelectric devices. Figure 167 (b) and (c) show these complex structures with a B-site ordering, when B and B' occupy the same relative locations in the ABO_3 structure in a 1 to 1 ratio (Figure 167b) it is said to be 1:1 Ordered, where a 2 to1 ratio (Figure 167c) is a 2:1 or 1:2 Ordered, and so on for more complex orientations. These orientations of ions give each individual material its specific trait and are why some materials are better as sensors while others make better actuators. When the B and B' ions are randomly distributed the structure it becomes a simple structure (Figure 167a) [95].

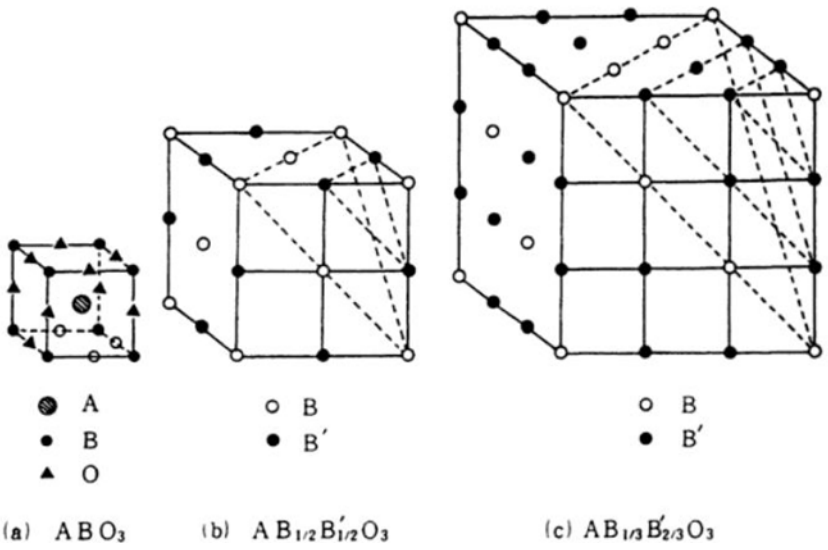

Figure 167: Perovskite structures with various B ion arrangements: (a) simple; (b) 1:1 ordered; (c) ordered [95]

These ion configurations within the material are vital when designing piezoelectric actuators and sensors as they dictate how the material will respond to specific stimuli. One constant which is used to describe behaviors in piezoelectric materials is the piezoelectric coefficient (charge constant) [51]. These coefficients are displayed using a tensor representation following the form $\boldsymbol{d_{ijk}}$ which is representative of a 3-D vector. The d tensor is comprised three layers of symmetrical matrices, as seen in Figure 168 [95]. When two tensors within a material are equal they are said to be

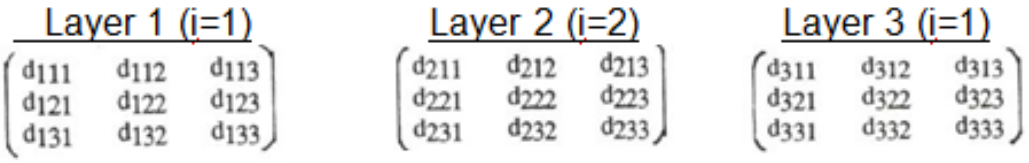

Figure 168: The three layers of symmetrical matrices of the d tensor [95]

crystallographically equivalent and cancel out. This reduces the overall number of independent tensor components. The number of remaining independent tensor determines the point group a material resides in. A point group is a group of geometric symmetries

that keep one or more point fixed, examples can be seen with the Ying/Yang symbols and other simple tessellations [98]. Piezoelectric materials belong to the 20 point group, meaning the lattice of the material has 20 point symmetry with respect to its center. A more common representation of the piezoelectric coefficient is in matrix notation. Since $\boldsymbol{d_{ijk}}$ is symmetric along j and k it can easily be reduced from tensor to matrix notation [95]. Figure 169 shows the tensor notation for the j and k elements of the tensor and what the resulting matrix notation is. The two most common piezoelectric materials having the

Tensor Notation	11	22	33	23,32	13,31	12,21
Matrix Notation	1	2	3	4	5	6

Figure 169: Tensor notation to matrix notation conversions [95]

$\boldsymbol{d_{31}}$ and $\boldsymbol{d_{33}}$ elements [50]. Based on a materials crystalline structure, characterized by the piezoelectric coefficient of the material, we are able to determine the material response. Piezoelectric materials respond to a stimulus (force or electrical field) in one of two ways. The $\boldsymbol{d_{31}}$coefficient, depicted in Figure 170(a), describes the elastic

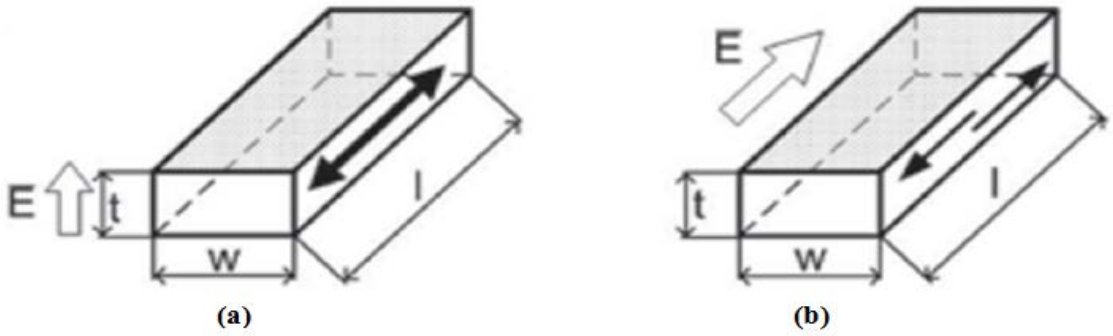

Figure 170: Samples of piezoelectric ceramic materials; (a) perpendicular response, (b) parallel response [51]

polarization generated perpendicular to the direction as the applied stress [50]. Plainly, an electric field applied through the thickness of the material creates an elongation in the

material or inversely, the material is stretched causing an electrical difference across the thickness of the material [8]. The $\boldsymbol{d_{33}}$ coefficient, depicted in Figure 170(b) describes the elastic polarization generated in the same (parallel) direction as the applied stress [50]. More simply put, an electric field applied though the length of the material causes an elongation and vice versa [8].

To more closely examine the piezoelectric response in a material, using a crystalline structure as described in Figure 170(a) deposited atop a polysilicon beam, we will examine the mechanics of composite (bimorph) piezoelectric beams [99]. Figure 171 depicts just such a beam where subscript 1 refers to material properties and dimensions of the piezoelectric material and subscript 2 refers to the same factors in the polysilicon

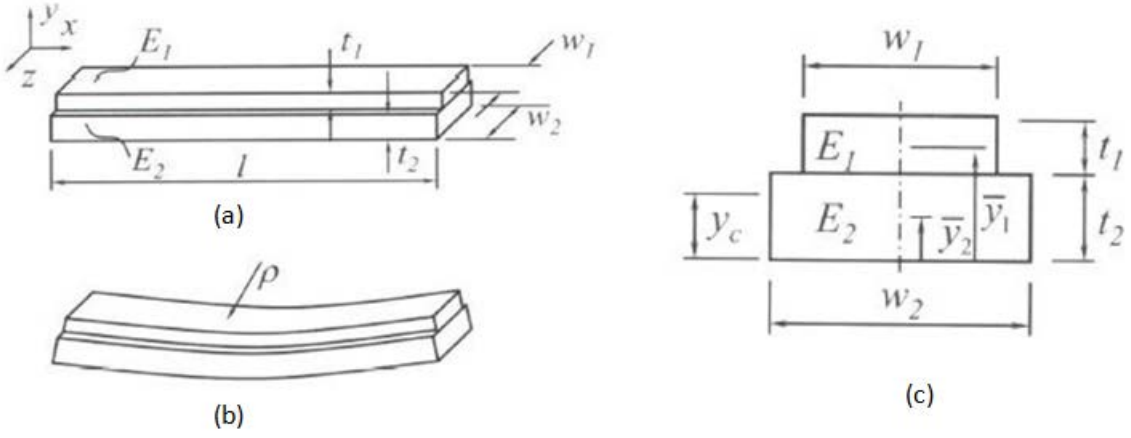

Figure 171: Simple composite (bimorph) beam actuator with piezoelectric layer atop Polysilicon layer; (a) side view of beam without stress effects, (b) side view of beam under stress, (c) front view of beam [8]

material. When a piezoelectric material is to be used as an actuator an important element to its operation to understand is ρ, the radius of deflection (Equation (29)). For this equation some components are dependent on material properties, $\boldsymbol{r = \frac{Young's\ Modulus_1}{Young's\ Modulus_2}}$

and $\boldsymbol{\varepsilon = relative\ strain}$, while others depend of design geometries, $\boldsymbol{p = \frac{t_1}{t_2}}$ and $\boldsymbol{q = \frac{w_1}{w_2}}$ [8].

$$\rho = \frac{(EI)_{eff}}{M_{eff}} = \frac{t_{total}}{2\varepsilon_1}[1 + \frac{1 + pqr}{3(1+p)^2}\left(p^2 + \frac{1}{pqr}\right)] \quad (29)$$

Figure 171(b) illustrates the operation of the beam as a function of the radius of deflection which is important when designing an actuator. From this one can model how a specific composite beam will respond to stimulus and determine the expected deflections of the beam. Choosing specific materials and geometries, a designer can create an actuator to do exactly what is needed.

In order to better understand this effect, the radius of deflection affected by changes in beam widths and layer thicknesses is modeled. But before this it is necessary to step down just a little deeper understand exactly what is happening in the crystal structure of a material which allows for the effect to transpire.

Material Physics

Piezoelectricity is a term used to describe materials that produce and electrical charge due to an applied mechanical stress [50]. This phenomenon happens as a direct result of the arrangement of ions in the crystal lattice structure of the material. A linear change in internal polarization occurs as a result of an applied stress, which causes an electrical field to develop.

When an ordinary crystal with positive and negative ions is compressed the equivalent center of charge remains constant, at the same relative location, and there is no

change in polarization due to the applied stress (Figure 172(a)). Whereas, piezoelectric materials experience a change in the center of charge of their positive and negative ions

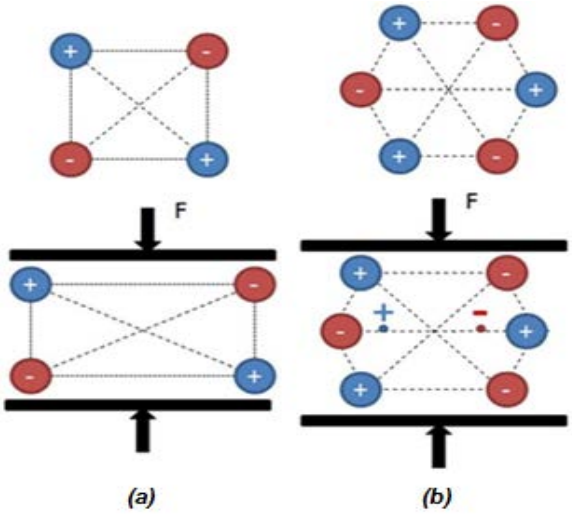

Figure 172: Example 2D crystal structures: (a) square, non-piezoelectric (b) hexagon, piezoelectric [50]

due to the applied stress, which induces the change in polarization that spawns an effective electrical field (Figure 172(b)). Another illustration of this behavior is shown in Figure 173, where the material is polarized parallel to the applied force [94]. Figure 173(a) shows the piezoelectric material sample under no load, 'steady-state' condition.

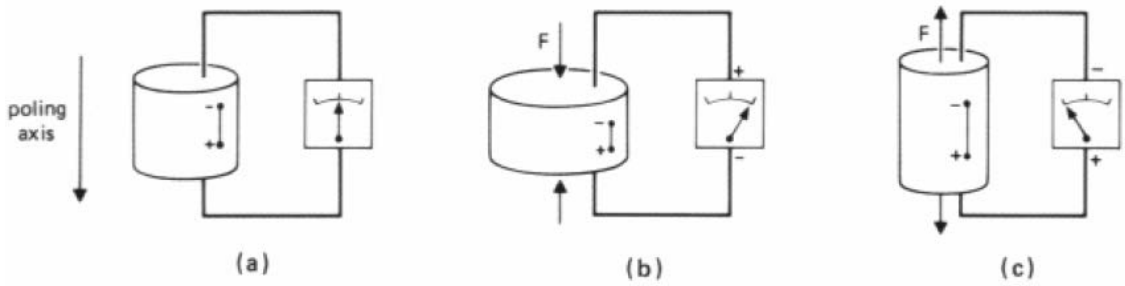

Figure 173: Piezoelectric effect in a cylindrical body of piezoelectric ceramic; (a) steady-state, (b) under compressive force, (c) under pulling/stretching force [94]

While Figure 173(b) shows the material under a compressive external force (tensile strain) which produces a change in the dipole moment and results in a voltage across the electrodes. If the same material were to be stretched rather than compressed, as seen in Figure 173(c), the voltage across the electrodes will have an opposite polarity.

Armed with the understanding of the piezoelectric effect and properties found in these materials modeling of some of these materials can be conducted in order to identify potential uses and impacts to my thesis work. This is done by examining how the radius of deflection can be manipulated to achieve high deflections, by changing beam widths and material thicknesses.

Numerical Analysis

Prior to going through the results it is important to specify how this information is to be used and why it is important, as it relates to the thesis work. This section examines the use of piezoelectric material for two possible applications in this thesis design. First, examines whether or not a piezoelectric material can be used in conjunction with another composite/bimorph material to assist with the pull-in of the beam, by taking advantage of the electric field generated during actuation. Second and the subject of this analysis, would a piezoelectric material used as the composite material be capable of achieving large enough deflections. With an understanding that the radius of deflection will characterize the beam deflection, as the radius of deflection is reduced the beam deflections is increased (due to the curl), the following model approach was taken.

To adequately model the radius of deflection in materials the effects in three of the more common piezoelectric ceramic materials were observed. The materials chosen

were lead zinconate titanate (PZT)[100, 101], aluminum nitride (AlN)[102, 103, 104]and Zinc Oxide (ZnO)[100, 105, 106]. Understanding that the material properties of a piezoelectric material depends greatly on the sample itself, for the purpose of the following models, the values for the material properties were researched and multiple sources were used to determine a good estimate of Young's modulus values for use in computations. Issues arose when determining 'good' relative stress values for each material for use in the computations. It appears that these numbers greatly depend on numerous factors and would require analysis of individual sample to determine. Noting that changes in relative stress of the material only effects the graphical scale for the radius of curvature and how the materials behave with respect to one another, this value in the calculations was fixed. The values for the material properties and thickness for the polysilicon layer was obtained using MEMSCAP® PolyMUMPs™ design constraints and measured results from previous runs.

To further clarify, the goal with this modeling was to observe how the radius of deflection is of PZT, AlN, and ZnO piezoelectric material samples of the same dimensions are affected by changes in those dimensions. For all the matlab models the thickness of the piezoelectric material was stepped from .25μm to 2μm and the beam widths were stepped from 5μm to 40um, the Poly2 beam thickness and width were fixed to 1.5 μm and 40 μm respectively. At first glance Figure 174, Figure 175, and Figure 176 show very similar responses to changes in thickness and width; the important difference being the scale of the y-axis, the radius of curvature results. The lead zinconate titanate (PZT), Figure 174 shows results range from 0 to .07 μm, while Figure 175 shows zinc

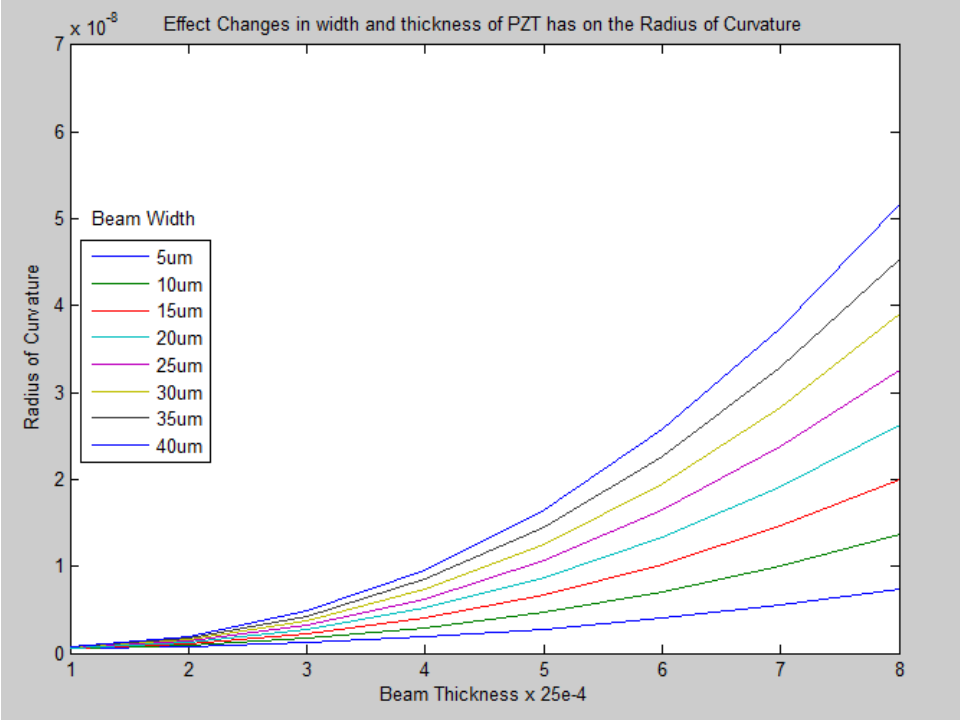

Figure 174: Change in Radius of Deflections of lead zinconate titanate (PZT) material as Width and Thickness are varied

oxide (ZnO) results ranging from 0 to .012 µm, and Figure 176 shows the range of 0 to .25 µm for aluminum nitride (AlN). It is clear from all the results that as the piezoelectric layer thickness is increased the radius of curvature is also increase, leading to smaller deflections. This makes sense, with respect to the piezoelectric material because thinner materials should more easily react to an external electric field (not as rigid as thicker layers).

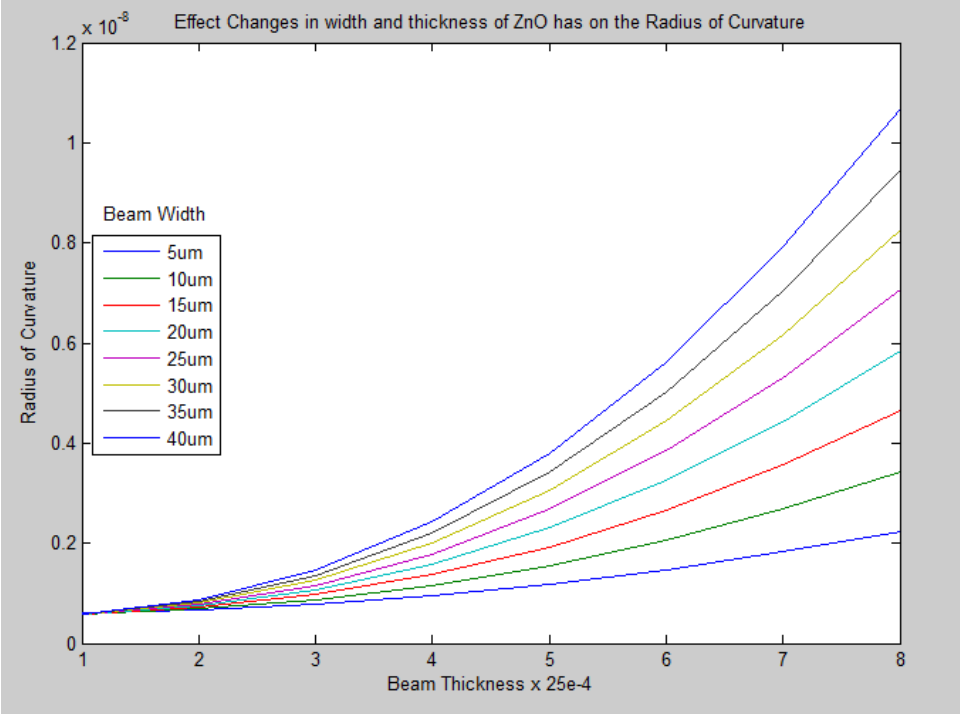

Figure 175: Change in Radius of Deflections of zinc oxide (ZnO) material as Width and Thickness are varied

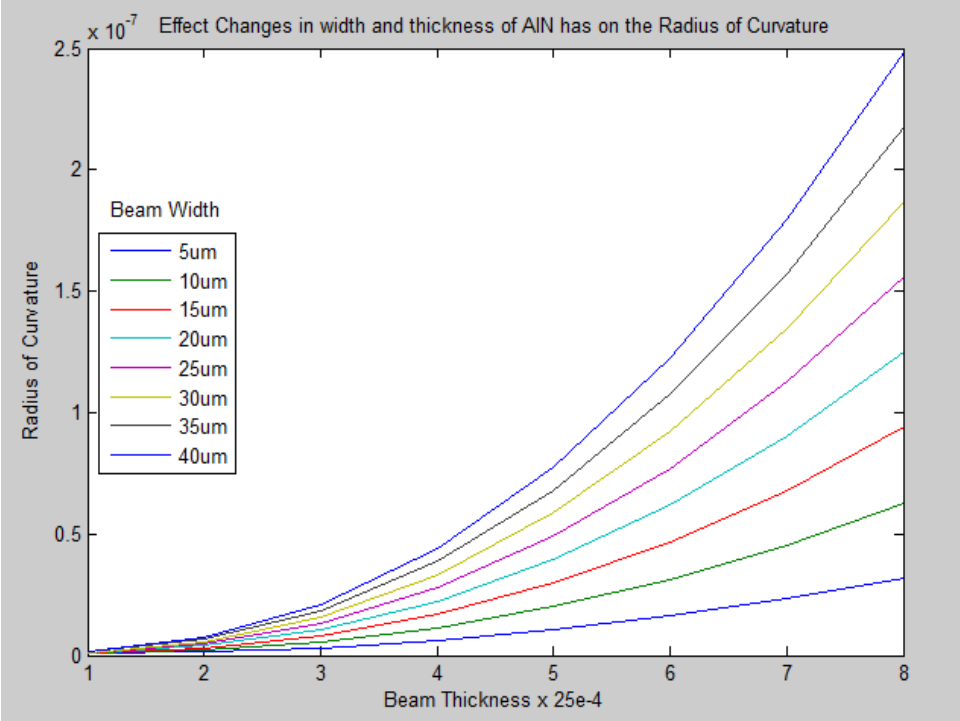

Figure 176: Change in Radius of Deflections of aluminum nitride (AlN) material as Width and Thickness are varied

What does not make sense is that the model should also take into account the flexibility/rigidity of the polysilicon beam, and that does not appear to be the case. It was expected that there would to be a reduction in deflection as the piezoelectric material layer thickness was increased but also expected was that a particular thickness would be required to produce enough the force required to overcome the rigidity of the polysilicon beam. Similarly, thinner beam widths also responded in the same manner. As the width of the piezoelectric material increased, the radius of curvature also increased. As for this aspect of the design, more piezoelectric surface area (wider beams) was expected to result in smaller radius of curvatures. The data plots do show promising results, more analysis is required.

APPENDIX I. Visual Bibliography

The purpose of this visual bibliography is to provide insight into topics applicable to this research and how they are interrelated. The boxes below correlate an actuation method with a topic relevant to this research and contain numbers which correspond to the reference numbers in the bibliography.

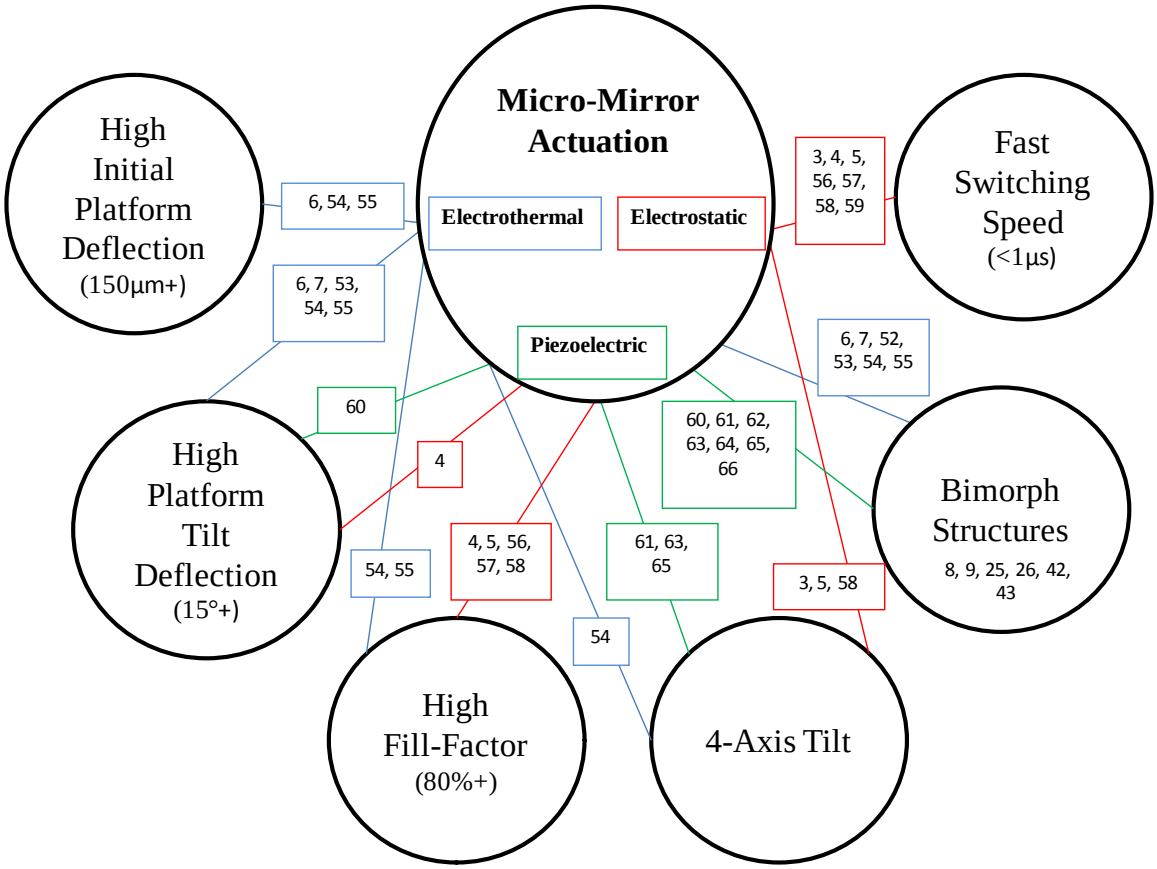

BIBLIOGRAPHY

[1] J. Bryzek, K. Petersen and W. McCulley, "Micromachines on the march," *Spectrum, IEEE,* vol. 31, no. 5, pp. 20-31, 1994.

[2] "What is it?," MEMS & Nanotechnology Exchange, [Online]. Available: https://www.mems-exchange.org/MEMS/what-is.html. [Accessed 14 01 2015].

[3] S. He and R. B. Mrad, "Large-Stroke Microelectrostatic Actuators for Vertical Translation of Micromirrors Used in Adaptive Optics," *IEEE TRANSACTIONS ON INDUSTRIAL ELECTRONICS,*, vol. 52, no. 4, pp. 974-983, 2005.

[4] S. Waldis, F. Zamkotsian, P.-A. Clerc, W. Noell, M. Zickar and N. de Rooij, "Arrays of High Tilt-Angle Micromirrors for Multiobject Spectroscopy," *IEEE JOURNAL OF SELECTED TOPICS IN QUANTUM ELECTRONICS,* vol. 13, no. 2, pp. 168-176, 2007.

[5] I. W. Jung, U. Krishnamoorthy and O. Solaard, "High Fill-Factor Two-Axis Gimbaled Tip-Tilt-Piston Micromirror Array Actuated by Self-Aligned Vertical Electrostatic Combdrives," *JOURNAL OF MICROELECTROMECHANICAL SYSTEMS,*, vol. 15, no. 3, pp. 563-571, 2006.

[6] A. Jain, H. Qu, S. Todd and H. Xie, "A thermal bimorph micromirror with large bi-directional and vertical actuation," *Sensors and Actuators,* vol. A, no. 122, pp. 9-15, 2005.

[7] L. Wu and H. Xie, "124◦ Rotation Angle Electrothermal Micromirror With Integrated Platinum Heater," *IEEE JOURNAL OF SELECTED TOPICS IN QUANTUM ELECTRONICS,* vol. 13, no. 2, pp. 316-321, 2007.

[8] K. B. Lee, Principles of Microelectromechanical Systems, 1 ed., Hoboken,Nj: John Wiley & Sons, Inc., 2011.

[9] G. T. Kovacs, Micromachined Transducers Sourcebook, New York: WCB/McGraw-Hill, 1998.

[10] S. Franssila, Introduction to Micro Fabrication, West Sussex, England: John Wiley & Sons Ltd., 2004.

[11] W. S. Trimmer, Micromechanics and MEMS, New York: IEEE Press, 1997.

[12] K. E. Petersen, "Silicon as a Mechanical Material," *Preceedings of the IEEE,* vol. 70, no. 5, pp. 420-457, 1982.

[13] F. Vollertsen, Z. Hu, H. Schulze Niehoff and C. Theiler, "State of the art in micro forming and investigations into micro deep drawing," *Journal fo Material Processing Techniques,* vol. 151, pp. 70-79, 2004.

[14] U. Engel and R. Eckstein, "Microforming--from basic research to its realization," *Journal of Materials Processing Technology,* Vols. 125-126, pp. 35-44, 2002.

[15] S. A. Campbell, Fabrication Engineering at the Micro- and Nanoscale, 4th ed., New York: Oxford University Press, 2013.

[16] M. J. Madou, Fundamentals of Microfabrication: The Science of Miniaturization, Boca Raton: CRC Press LLC, 2004.

[17] F. Chollet, "SU-8: Thick Photo-Resist for MEMS," MEMScyclopedia, 3 12 2013. [Online]. Available: memscyclopedia.org/su8.html. [Accessed 14 01 2015].

[18] J. Geottert, G. Aigeldinger, Y. Desta, Z. L. Ling and L. Rupp, *Instrumentation for Synchrotron Based Micro Machining at CAMD,* Baton Rouge: CAMD, Louisiana State University.

[19] T.-R. Hsu, MEMS and Microsystems, Hoboken, New Jersey: John Wiley & Sons Inc., 2008.

[20] J. P. McKelvey, Solid State Physics for Engineering and Material Science, Malabar: Krieger Publishing Company, 1993.

[21] S. E. Lyshevski, MEMS and NEMS systems, Devices and Structures, Boca Raton: CRC Press LLC, 2002.

[22] "Misson," Sandia Corporation, 2015. [Online]. Available: http://www.sandia.gov/about/mission/index.html. [Accessed 05 Feb 2015].

[23] "SUMMiT V Five Level Surface Micromachining Technology Design Manual (Version 3.2)," Sandia National Laboratories, Alburquerque, 2012.

[24] J. Carter, A. Cowen, B. Hardy, R. Mahadevan, M. Stonefield and S. Wilcenski, "PolyMUMPs Design Handbook (Revision 11.0)," MEMSCAP Inc..

[25] H. N. Norton, Handbook of Transducers, Englewood Cliffs: Prentice Hall, 1989.

[26] A. D. Khazan, Transducers and Their Elements: Design and Application, Englewood Cliffs: Prentice Hall, 1994.

[27] P. Hauptmann, Sensors: Principles and Applications, Hertfordshire: Prentice-Hall International, 1991.

[28] J. W. Gardner, Microsensors: Principles and Applications, Chicherster: Wiley, 1994.

[29] S. Timoshenko, Strength of Materials Part 1, New York: D. Van Nostrand Company, Inc., 1940.

[30] S. K. Vashist, "A Review of Microcantilevers for Sensing Applications," AZoNetwork, 18 06 2007. [Online]. Available: http://www.azonano.com/article.aspx?ArticleID=1927#_Cantilevers_Use_in. [Accessed 25 02 2015].

[31] X. Feng, Y. Huang, H. Jiang, D. Ngo and A. J. Rosakis, "The Effect of Thin Film/Substrate Radii on the Stoney Formula for Thin Film/Substrate subjected to Nonuniform Axisymmetric Misfit Strain and Temperature," *Mechanics of Materials and Structures*, vol. 1, no. 6, pp. 1041-1053, 2006.

[32] Deepak and Vikas, "Design and Analysis fo Micro-Cantilevers for Energy Harvesting," *International Journal of Advanced Research in Computer Science and Software Engineering*, vol. 3, no. 11, pp. 468-473, 2013.

[33] "HyperPhysics Sound," Georgia State University, [Online]. Available: http://hyperphysics.phy-astr.gsu.edu/hbase/sound/reson.html. [Accessed 26 05 2015].

[34] N. A. Lavrik, M. J. Sepaniak and P. G. Datskos, "Cantilever Transducers as a Platform for Chemical and Bioligical Sensors," *Review of Scientific Instruments*, vol. 75, no. 7, pp. 2229-2253, 2004.

[35] S. Beeby, G. Ensell, M. Kraft and N. White, MEMS Mechanical Sensors, Norwood: Artech House Inc., 2004.

[36] N. O. Lobontiu, Mechanical Design of Microresonators, New York: McGraw-Hill Companies, Inc., 2006.

[37] J. G. Korvink and O. Paul, MEMS: A Practical Guide to Design, Analysis and Applications, Norwich: William Andrew Inc., 2006.

[38] A. Boisen, S. Dohn, S. S. Keller, S. Schmid and M. Tenje, "Cantilever-like Micromechanical Sensors," *Reports on Progress In Physics*, vol. 74, no. 036101, pp. 1-29, 2011.

[39] J. A. Kubby, A Guide to Hands-on-MEMS Designs and Prototyping, Cambridge: Cambridge University Press, 2011.

[40] S. Baglio, S. Castorina and N. Savalli, Scaleing Issues and Design of MEMS, Sussex, England: John Wiley & Sons, Ltd, 2007.

[41] W.-H. Chu, M. Mehregany and R. L. Mullen, "Analysis of tip deflection and force of bimetallic cantilever micoractuators," *Journal of Micromechanical Microengineering,* vol. 3, pp. 4-7, 1993.

[42] J. M. Gene and S. P. Timoshenko, Mechanics of Materials, Boston: PWS Publishing Company, 1990.

[43] S. Timoshenko, "Analysis of Bi-Metal Thermostats," *Journal of the Optical Society of America,* vol. 11, no. 3, pp. 233-255, 1925.

[44] A. M. Moulin, R. J. Stephenson and M. E. Welland, "Micromechanical Thermal Sensor: Comparison of Experimental Results and Simulations," *Journal of Vacuumm Science & Technology B,* vol. 15, pp. 590-596, 1997.

[45] S. Pal and H. Xie, "Fabrication of robust electrothermal MEMS devices using aluminum-tungsten bimorphs and polyimide termal isolation," *Journal of Micromechanics and Micorengineering,* vol. 22, p. 14, 2012.

[46] C. Galassi, M. Dinescu, K. Uchino and M. Sayer, Piezoelectric Materials: Advances in Science, Technology and Applications, a. Carmen Galassi et, Ed., Kluwer Academic Publishers, 2000.

[47] a. Kenji Uchino et, Advanced Piezoelectric Materials, K. Uchino, Ed., Philadelphia, PA: Woodhead Publishing Limited, 2010.

[48] M. C.-Y. Huang, Y. Zhou and B. Cheng, "Monolithic Piezo-Electric Actuated MEMS Tunable VCSEL," College of Engineering, UC Berkeley, 30 Jan 2015. [Online]. Available: https://buffy.eecs.berkeley.edu/PHP/resabs/resabs.php?f_year=2006&f_submit=one&f_absid=101239. [Accessed 02 Feb 2015].

[49] C. J. Chang-Hasnain, "Tunable VCSEL," *IEEE JOURNAL ON SELECTED TOPICS IN QUANTUM ELECTRONICS,* vol. 6, no. 6, pp. 978-987, 2000.

[50] a. Khaled S. Ramadan et, "A review of piezoelectric polymers as functional materials for electromechanical transducers," *Smart Materials ans Structures,* vol. 23, no. 033001, pp. 1-26, 2014.

[51] P. B. Jiří Fialka, "Comparison of Methods of Piezoelectric Coefficient Measurment," *IEEE Transactions on Instrumentation and Measurment,* vol. 62, no. 5, pp. 1047-1057, May 2013.

[52] J. Singh, T. Gan, A. Agarwal, Mohanraj and S. Liw, "3D free space thermally actuated micromirror device," *Sensors and Actuators,* vol. A, no. 123-124, pp. 468-475, 2005.

[53] S. Pal and H. Xie, "Repeatability Study of an Electrothermally Actuated Micromirror," in *IEEE 47th Annual International Reliability, Physics Symposium,* Montreal, 2009.

[54] L. Wu, S. Dooley, E. A. Watson, P. F. McManamon and H. Xie, "A Tip-Tilt-Piston Micromirror Array for Optical Phased Array Applications," *JOURNAL OF MICROELECTROMECHANICAL SYSTEMS,* vol. 19, no. 6, pp. 1450-1461, 2010.

[55] K. Jia, S. R. Samuelson and H. Xie, "High-Fill-Factor Micromirror Array With Hidden Bimorph Actuators and Tip–Tilt-Piston Capability," *JOURNAL OF MICROELECTROMECHANICAL SYSTEMS,* vol. 20, no. 3, pp. 573-582, 2011.

[56] D. Hah, S. T.-Y. Huang, J.-C. Tsai, H. Toshiyoshi and M. C. Wu, "Low-Voltage, Large-Scan Angle MEMS Analog Micromirror Arrays With Hidden Vertical Comb-Drive Actuators," *JOURNAL OF MICROELECTROMECHANICAL SYSTEMS,*, vol. 13, no. 2, pp. 279-289, 2004.

[57] J.-C. Tsai and M. C. Wu, "Design, Fabrication, and Characterization of a High Fill-Factor, Large Scan-Angle, Two-Axis Scanner Array Driven by a Leverage Mechanism," *JOURNAL OF MICROELECTROMECHANICAL SYSTEMS,* vol. 15, no. 5, pp. 1209-1213, 2006.

[58] M. Kim, J.-H. Park, J.-A. Jeon, B.-W. Yoo, I. H. Park and Y.-K. Kim, "High fill-factor micromirror array using a self-aligned vertical comb drive actuator with two rotational axes," *JOURNAL OF MICROMECHANICS AND MICROENGINEERING,* vol. 19, pp. 1-9, 2009.

[59] F. Hu, J. Yao, C. Qiu and H. Ren, "A MEMS micromirror driven by electrostatic force," *Journal of Electrostatics,* vol. 68, pp. 237-242, 2010.

[60] K. H. Koh, T. Kobayashi, F.-L. Hsiao and C. Lee, "Characterization of piezoelectric PZT beam actuators for driving 2D scanning micromirrors," *Sensors and Actuators A: Physical,* vol. A, no. 162, pp. 336-347, 2010.

[61] Y. Zhu, W. Liu, K. Jia, W. Liao and H. Xie, "A piezoelectric unimorph actuator based tip-tilt-piston micromirror with high fill factor and small tilt and lateral shift," *Sensors and Actuators A: Physical,* vol. A, no. 167, pp. 495-501, 2011.

[62] K. H. Koh, T. Kobayashi and C. Lee, "Investigation of piezoelectric driven MEMS mirrors based on single and double S-shaped PZT actuator for 2-D scanning applications," *Sensors and Actuators A: Physical,* vol. A, no. 184, pp. 149-159, 2012.

[63] W. Liu, Y. Zhu, K. Jia, Y. Tang, B. Wang and H. Xie, "A tip–tilt–piston micromirror with a double S-shaped unimorph piezoelectric actuator," *Sensors and Actuators A: Physical,* vol. A, no. 193, pp. 121-128, 2013.

[64] K. Ikegami, T. Koyama, T. Saito and Y. Yasuda, "A biaxial PZT optical scanner for pico-projector applications," in *SPIE Photonic West, 9375-20,* San Francisco, 2015.

[65] S. Gu-Stoppel, J. Janes, H.-J. Quenzer, F. Heinrich and W. Benecke, "A study of intergrated piezoelectric positon sensors for PZT resonant micromirrors," in *SPIE Photonic West 9375-9,* San Francisco, 2015.

[66] S. Lani, D. Z. Bayat and M. Despont, "2D tilting MEMS micro mirror intergrating piesoresistive sensors positon feedback," in *SPIE Photonics West 9375-10,* San Francisco, 2015.

[67] "Simulation-Driven Product Development," ANSYS Inc., 2015. [Online]. Available: http://www.ansys.com/Products. [Accessed 25 4 2015].

[68] "Multiphysics Solutions," ANSYS Inc., 2015. [Online]. Available: http://www.ansys.com/Products/Simulation+Technology/Multiphysics. [Accessed 25 4 2015].

[69] "ANSYS Workbench Platform," ANSYS Inc, 2015. [Online]. Available: http://www.ansys.com/Products/Workflow+Technology/ANSYS+Workbench+Platform. [Accessed 25 4 2015].

[70] "MEMS Module," COMSOL Inc., 2015. [Online]. Available: http://www.comsol.com/mems-module. [Accessed 25 4 2015].

[71] "COMSOL Multiphysics," COMSOL Inc., 2015. [Online]. Available: http://www.comsol.com/comsol-multiphysics. [Accessed 25 4 2015].

[72] "MEMS Solution," Coventor Inc., [Online]. Available: http://www.coventor.com/mems-solutions/. [Accessed 25 4 2015].

[73] "Our Products," Coventor Inc, [Online]. Available: http://www.coventor.com/mems-solutions/products/. [Accessed 25 4 2015].

[74] "www.memscap.com," MEMSCAP Inc., 2011-2012. [Online]. Available: http://www.memscap.com/products/mumps/polymumps/reference-material. [Accessed 24 12 14].

[75] A. Cowen, B. Hardy, R. Mahadevan and S. Wilcenski, "www.memscap.com," 2011-2012. [Online]. Available: http://www.memscap.com/__data/assets/pdf_file/0019/1729/PolyMUMPs-DR-13-0.pdf. [Accessed 24 12 2014].

[76] S.-H. Lim, J. Choi and R. Horowitz, "Design and Fabrication of a Novel Bimorph Microoptomechanical Sensor," *Journal of Microelectomechanical Systems*, vol. 14, no. 4, pp. 683-690, 2005.

[77] "NewView 7300," Zygo Metrology Solutions, [Online]. Available: http://www.zygo.com/?/met/profilers/newview7000/. [Accessed 25 04 2015].

[78] "Pattern Transfer," MEMSnet, [Online]. Available: https://www.memsnet.org/mems/processes/lithography.html. [Accessed 15 01 15].

[79] "Molecular Beam Exipaxy," UCL Department of Electronic & Electrical Engineering, [Online]. Available: http://www.ee.ucl.ac.uk/about/MBE. [Accessed 15 01 2015].

[80] R. C. Jaeger, Introduction to Microelectronic Fabrication, Addison-Wesley Publishing Company, Inc., 1993.

[81] Oxford, May 2014. [Online]. Available: www.oxforddictionaries.com/us/definition/american_english/piezoelectricity.

[82] a. George W. Taylor et, Piezoelectricity, vol. 4, a. George W. Taylor et, Ed., Gordon and Breach Science Publishers, 1985.

[83] M. W. Davidson, "Science, Optics & You," Molecular Expressions, 04 October 2004. [Online]. Available: micro.magnet.fsu.edu/optics/timeline/people/becquerel.html. [Accessed 14 05 2014].

[84] Unknown, "Colego Web," 6 1 2012. [Online]. Available: http://www.colegioweb.com.br/trabalhos-escolares/quimica/radioatividade/descoberta-da-radioatividade.html. [Accessed 15 5 2014].

[85] Piezo Systems, Inc., May 2014. [Online]. Available: www.piezo.com/tech4history.html.

[86] American Physical Society-Physics, May 2014. [Online]. Available: http://www.aps.org/publications/apsnews/201403/physicshistory.cfm.

[87] University of Nebraska-Lincoln, "Historical Scientific Instrument Gallery (electrostatics)," [Online]. Available: www.unl.edu/physics/history/histinstr/electrostatics.html. [Accessed 15 05 2014].

[88] Unknown, May 2014. [Online]. Available: http://en.wikipedia.org/wiki/Piezoelectricity.

[89] B. Jaffe, W. R. Cook and H. L. Jaffe, Piesoelectric Ceramics, New York, NY: Academic Press Inc., 1971.

[90] J. Yang, Special Topics in the Theory of Piezoelectricity, New York, NY: Springer Science + Business Media, 2009.

[91] C. Dagdeviren, B. D. Yang, Y. Su and a. et, "Conformal piezoelectric energy harvesting and storage form motion of the heart, lung and diaphram," *Proceedings of the National Academy of Science*, vol. 111, no. 5, pp. 1927-1932, 2014.

[92] B. Yirka, "Phys.org," Science X network, 21 01 2014. [Online]. Available: http://phys.org/news/2014-01-team-implantable-piezoelectric-nanoribbon-devices.html. [Accessed 31 05 2014].

[93] L. Zimmer, "Energy," inhabitat, 10 4 2013. [Online]. Available: http://inhabitat.com/kinetic-energy-harvesting-tiles-generate-power-from-paris-marathon-runners/. [Accessed 31 05 2014].

[94] J. W. waanders, Piezoelectric Ceramics: Properties and Applications, N.V. Philips' Gloeilampenfabrieken, 1991.

[95] K. Uchino, Piezoecletric Actuators and Ultrasonic Motors, H. L. Tuller, Ed., Kluwer Academic Publishers, 1997.

[96] unknown, "Dictionary.com Unabridged," Random House, Inc, 2014. [Online]. Available: http://dictionary.reference.com/browse/centrosymmetric. [Accessed 31 05 2014].

[97] unknown, "Centrosymmetry," Wikipedia, 2 2 2014. [Online]. Available: http://en.wikipedia.org/wiki/Centrosymmetry. [Accessed 31 5 2014].

[98] unknown, "Point Groups," Wikipedia, 26 05 2014. [Online]. Available: http://en.wikipedia.org/wiki/Point_group. [Accessed 01 06 2014].

[99] J. Yang, The Mechanics of Piezoelectric Structures, J. Yang, Ed., Hackensack, NJ: World Scientific Publishing, 2006.

[100] A. S. a. X. J. Avula, "Analytical and Computational Solution to Piezoelectric Bending: A Comparative Study," *NSTI-Nanotech* , vol. 3, pp. 189-192, 2007.

[101] MEMS & Nanotechnology Exchange, "Material: Lead Zirconate Titanate (PZT)," [Online]. Available: https://www.memsnet.org/material/leadzirconatetitanatepzt/. [Accessed 15 5 2014].

[102] MEMS & Nanotechnology Exchange, "Material: Aluminum Nitride (AlN)," MEMS net, [Online]. Available: https://www.memsnet.org/material/aluminumnitridealnbulk/. [Accessed 15 5 2014].

[103] a. D. Gerlich et, "Elastic Properties of Aluminum Nitride," *Journal of Physics and Chemical Solids*, vol. 47, no. 5, pp. 437-441, 1986.

[104] M.-A. Dubois and P. Muralt, "Stress and piezoelectric properties of aluminum nitrice thin films deposited onto metal electrodes by pulsed direct current reative sputtering," *Applied Physics*, vol. 89, no. 11, pp. 6389-6395, 2001.

[105] Unknown, "Material: Zinc Oxide (ZnO)," MEMS & Nanotechnology Exchange, [Online]. Available: http://www.memsnet.org/material/zincoxideznobulk/. [Accessed 01 06 2014].

[106] Z.-H. Hong, T.-H. Fang and S.-F. Hwang, "Atomic-level stresss and induced growth of wurtzite zinc oxide using molecular dynamics simulation," *Physics D: Applied Physics*, vol. 44, pp. 1-9, 2011.

REPORT DOCUMENTATION PAGE

Form Approved
OMB No. 074-0188

PLEASE DO NOT RETURN YOUR FORM TO THE ABOVE ADDRESS.

1. REPORT DATE *(DD-MM-YYYY)*	**2. REPORT TYPE**	**3. DATES COVERED** *(From – To)*
18-06-2015	Master's Thesis	August 2013 – June 2015

TITLE AND SUBTITLE

Electrostatically Driven Large Aperture Micro-Mirror Actuator Assemblies for High Fill-Factor, Agile Optical Phase Arrays

5a. CONTRACT NUMBER

5b. GRANT NUMBER

5c. PROGRAM ELEMENT NUMBER

6. **AUTHOR(S)**

Walton, John P.K., Captain, USAF

5d. PROJECT NUMBER

15G232

5e. TASK NUMBER

5f. WORK UNIT NUMBER

7. PERFORMING ORGANIZATION NAMES(S) AND ADDRESS(S)

Air Force Institute of Technology
Graduate School of Engineering and Management (AFIT/EN)
2950 Hobson Way, Building 640
WPAFB OH 45433-8865

8. PERFORMING ORGANIZATION REPORT NUMBER

AFIT-ENG-MS-15-J-003

9. SPONSORING/MONITORING AGENCY NAME(S) AND ADDRESS(ES)

Air Force Research Laboratory's Sensor Directorate
2241 Avionics Circle, Bldg 600, WPAFB, OH. 45433-7318
(937)528-8993 / lavern.starman.1@us.af.mil
ATTN: Dr. LaVern A. Starman

10. SPONSOR/MONITOR'S ACRONYM(S)

AFRL/RYDP

11. SPONSOR/MONITOR'S REPORT NUMBER(S)

12. DISTRIBUTION/AVAILABILITY STATEMENT

DISTRUBTION STATEMENT A. APPROVED FOR PUBLIC RELEASE; DISTRIBUTION UNLIMITED.

13. SUPPLEMENTARY NOTES

14. ABSTRACT

Aircraft laser beamsteering is accomplished using a single gimbaled mirror housed inside a turret, which protrudes from the fuselage and causes unwanted turbulence, vibrations, and weight. The Air Force is currently investigating the use of microelectromechanical systems (MEMS) micro-mirror arrays to replace aircraft beamsteering technology. MEMS micro-mirror arrays provide a unique solution to address these issues. Unfortunately, current MEMS micro-mirror technology cannot meet all the beamsteering requirements in a single assembly. These include high fill-factor, large aperture, 25 degrees of out-of-plane deflection, 4-axis tilt, and actuation speeds below 1 ms. In this research, a novel MEMS actuation scheme to address all these requirements using electrostatically driven bimorph cantilever beams was designed, modeled, fabricated, and characterized. Modeling results show a linear relationship between the number of cantilever beams and maximum deflection. Characterization of fabricated micro-mirror assemblies supports the modeling for individual actuators as well as for micro-mirror platform assemblies. Fabricated devices reached vertical deflections greater than 170 μm with pull-in voltages of 20 V and an optical range of 16 degrees. These large deflections, low pull-in voltage, and reasonable optical range shown in this research demonstrate the feasibility of using MEMS micro-mirror arrays to address aircraft beamsteering issues.

15. SUBJECT TERMS

micro-mirror array, beam steering, electrostatic, high deflection, low actuation voltage

16. SECURITY CLASSIFICATION OF:			**17. LIMITATION OF ABSTRACT**	**18. NUMBER OF PAGES**	**19a. NAME OF RESPONSIBLE PERSON**
a. REPORT	**b. ABSTRACT**	**c. THIS PAGE**			Ronald A. Coutu, Jr., PhD, AFIT/ENG
U	**U**	**U**	**UU**	245	**19b. TELEPHONE NUMBER** *(Include area code)* (937) 255-3636, ext 7230 ronald.coutu@afit.edu

Standard Form 298 (Rev. 8-98)
Prescribed by ANSI Std. Z39-18